FINITE ELEMENT MODELLING OF CREEP AND INSTABILITY OF LARGE ICE MASSES

By

© DIETER FRANZ EUGEN STOLLE, B.ENG., M.ENG.

A Thesis

Submitted to the School of Graduate Studies

in Partial Fulfilment of the Requirements

for the Degree

Doctor of Philosophy

McMaster University

September 1982

CREEP AND INSTABILITY OF LARGE ICE MASSES

DOCTOR OF PHILOSOPHY (1982) McMASTER UNIVERSITY

(Civil Engineering) Hamilton, Ontario

TITLE: Finite Element Modelling of Creep and Instability of Large Ice Masses

AUTHOR: Dieter Franz Eugen Stolle, B.Eng. (McMaster University), M.Eng. (McMaster University).

SUPERVISOR: Dr. F. A. Mirza

NUMBER OF PAGES: xx, 213.

ABSTRACT

Detailed descriptions of finite element models for deformation, temperature and instability analyses of large ice masses are presented. Two non-Newtonian creeping flow models are developed for steady-state creep situations; one enforces incompressibility, the other near incompressibility. The third creep model incorporates a large displacement formulation and an implicit time-marching scheme for transient creep analysis. To allow for basal sliding, a time-dependent sliding element is also developed. In addition to the creep models above, a transient heat transfer model is presented. By stepwise uncoupling of the stress and temperature dependent creep, it is possible to carry out transient thermal creep analysis for surging of the Barnes Ice Cap. An upwind scheme for triangular elements is given for thermal analysis where the influence of thermal advection is required.

It is demonstrated that the three finite element creep models predict similar steady-state creep behaviour for simple ice masses with simple boundary conditions. For more complex problems, agreement of the computed velocities by the models is found to be very sensitive to the boundary conditions at the ice-bedrock interface. Results from the finite element simulations suggest that it may be premature to assume that the influence of elastic strains is negligible.

The thermal regime of the Erebus Glacier Tongue is studied assuming steady-state conditions. It is shown that the temperature field is mainly influenced by the near horizontal thermal advection. Reasonable velocity fields for the thermal analysis could only be attained by assuming that the ice is not frozen to bedrock at the transition from a land-based glacier to a floating glacier.

Finally, a basal instability model is presented. In this model, the basal shear resistance is reduced according to the excess sliding energy dissipated above some threshold value. The time for a surge to propagate is characterized by a lubrication factor incorporated in the basal instability model. It is confirmed that a geothermal flux approaching 1.9 HFU is required to bring most of the south-west ice-bed interface of the Barnes Ice Cap to pressure melting which would allow for basal sliding and instability. Furthermore, it is shown that the temperature changes during a surge are negligible. The numerical examples analyzed and presented indicate the appropriateness of the analytical modelling and versatility of the finite element method for incorporating complex material properties and boundary conditions.

ACKNOWLEDGEMENTS

In presenting this thesis, I wish to express my sincere appreciation to the following individuals and organizations:

- My supervisor, Dr. F. A. Mirza, for his valuable advice and support during the research and preparation of this thesis.

- Drs. J. J. Emery, J. L. Duncan and R. M. Korol, members of my supervisory committee, for their valuable advice.

- G. Holdsworth, of Environment Canada, for providing data on the Erebus Glacier Tongue, Antarctica and the Barnes Ice Cap, Baffin Island, Canada.

- Marlene Fletcher, for her time in typing and proofreading this thesis.

- The financial support from McMaster University in the form of a McMaster Alumni Scholarship and the Natural Sciences and Engineering Research Council, grant number A-1003, for supporting the research work reported in this thesis are deeply appreciated.

- Finally, a special thank you to my wife, Barbara, for her help, patience and encouragement toward the completion of this thesis.

TABLE OF CONTENTS

TABLE OF CONTENTS (Continued) PAGE

TABLE OF CONTENTS (Continued) PAGE

TABLE OF CONTENTS (Continued)

TABLE OF CONTENTS (Continued)

LIST OF FIGURES

LIST OF TABLES

CHAPTER 1

INTRODUCTION

1.1 Ice Dynamics

The study of ice dynamics involves determining the state of stress and the velocity field within a glacier or an ice sheet due to self-weight. The dynamic response of a large ice mass depends on the geometry, mass balance, energy balance, material properties, and boundary conditions. An understanding of ice dynamics is of both practical and academic interest; see Paterson [80] for a brief summary for the motivation behind the need for understanding the movements of glaciers and large ice sheets.

An analysis or modelling of large ice mass behaviour requires consideration of the mass and momentum conservation principles. Since these pheonomena are coupled, they require simultaneous treatment. Except for a few highly idealized problems, it is most often not possible to develop closed form solutions that can describe dynamic behaviour of a large ice mass. In order to render a manageable form for analysis of a very difficult problem, assumptions based on field experience are necessary. Some of the simplifications adopted are described in the following text.

1.2 Review of Ice Dynamics

A reasonable understanding of the mechanics of large ice mass flow has been accomplished only over the past three decades. The velocities observed at the surface can be partly due to sliding at the ice-bedrock interface and partly due to process of continuous internal deformation due to creep. Orwan [78] was the first to suggest that glacier flow can be treated as a problem in plasticity. Based on the experimental results by Glen [27, 28], it was found that ice deformation can be expressed by a power law relationship between strain rate and stress. The recognition that ice creep is similar to that of other crystalline materials at high temperatures has enhanced the possibilities to model (mathematically) ice deformation within large ice bodies. Nye [71, 72] completed extensive studies on the mechanics of glaciers for both plastic and creep modes of deformation. He also extended his analyses to include the influence of the multiaxial state of stress that may be known [74].

By taking advantage of the known geometries of many glaciers, early analyses of ice deformation were limited to planar flow of a parallel-sided slab, which has large length and width compared to the thickness, and moves down an inclined plane for which an analytical solution can be found. It was assumed that the deformation of these bodies was essentially due to shear. Nye [72] considered two modes of deformation, i.e., pure shear flow and shear flow with uniform longitudinal straining. To facilitate analysis it was assumed that the ice mass is homogeneous, isotropic and isothermal. Simplified analyses have also

been completed for other geometries where certain symmetry conditions are used to reduce the problem size (see, e.g., Budd [7]).

The solution of the equilibrium equations for more complex geometries, where the surface and bed may be irregular, is extremely difficult. Much emphasis has been placed on reducing the equilibrium equations to a suitable form for approximate analyses for cases where variations in longitudinal stress along the glacier length are important [18], [75] and [8]. These approximations impose restrictions on the type of flow behaviour that can be analysed and lead to a loss of generality: equations are applied in a piecewise (or stripped) manner along a flow line without maintaining strict continuity of the velocity field; a rigorous coupling between the stress and velocity fields is not enforced; constitutive equations are introduced between vertically averaged stress and strain rates and a weighted mean temperature and density are required to account for spatial variations in temperature and density. The weighting of flow parameters, to account for temperature variations, tends to reflect shear deformation in the basal layers where temperatures are generally the highest (see reference [8]). For more details, the reader is referred to a recent synthesis of articles on this topic by Colbeck [17].

The simplified analytical procedures do offer valuable analytical information on glacier flow behaviour which can be verified through field studies. These analyses allow one to relate the surface velocity distribution to general features of an ice mass such as surface slope, ice thickness, basal boundary conditions, etc. However, these simpli-

fied analyses can sometimes lead to erroneous conclusions. Most recently, Hutter et al. [48] formulated the ice dynamics problem in a more rigorous manner based on the non-Newtonian fluid model and a continuum approach. Their results indicate that the basal shear stress depends on the sliding law and the spatial temperature distribution in the ice mass. Furthermore, it was stressed that under no circumstances is it allowable to disregard the temperature variations in cold ice. Unfortunately their study was restricted to a very idealized problem. The analytical modelling of more realistic problems requires sophisticated numerical methods for a resolution.

1.3 Instability of Glaciers and Large Ice Masses

In contrast to the apparently stable behaviour of most ice masses, a small group of glaciers undergo a rapid change in velocity and geometry within a short period of time after having been stable for a large number of years. These periods of fast flow, or instability, have often been referred to as catastrophic advances or surges [79]. Very few surging glaciers have been well documented in the literature and therefore little is known about the mechanical properties and thermal regimes of these ice masses prior to surging. The lack of data for these ice masses has been attributed to the rare occurences and short durations of such events (e.g., one to two years), the remoteness of their location, and the inaccessibility of the glacier surface during instability [79]. A brief summary of what is known about surging is presented in Appendix A1.

While an understanding of the mechanics of large ice mass instability is somewhat of academic interest, practical concerns have been indicated for instabilities of the major ice masses. It has been suggested that instability of the Antarctica ice cover can produce a world wide climatic change by reducing the earth's albedo and can also lead to flooding of many major ocean ports [80]. Surging has been most often identified with valley glaciers. However, instabilities have been reported for certain ice caps in Iceland and Svalbord by Thorarinsson [92], Liestol [54], and Schytt [91]. Evidence suggests that the Barnes Ice Cap, Baffin Island, Canada, which is of particular interest in this study, is also a surging ice cap [59] and [36].

1.3.1 Instability Mechanisms

There are two important aspects which should be considered in the study of instability: the conditions necessary for the attainment of high velocities; and how these velocities are maintained while the driving mechanism continuously decreases as the surge progresses, i.e. thickness and surface slope decrease [64]. A number of proposed theoretical explanations, based on mechanical or boundary instabilities, have been developed and some include: nonunique longitudinal ice thickness profile [87]; basal temperature variations with time [86, 87]; and change in flow properties due to dynamic recrystallization [50]. These explanations address possible trigger mechanisms but do not satisfy the conditions for surge propagation set forth by Meier [64].

Weertman [95, 97] advanced a theory based on instability at the

ice-bed interface due to formation of a thick water layer. Such instability can account for the high velocities observed for surging glaciers. Lliboutry [56] suggested that the basal instability can also result from excessive cavitation between ice and the bedrock at critical sliding velocities. For further details on surge mechanisms see Appendix A2.

Most surge models concentrate on accounting for the cyclic characteristic of a surging glacier rather than on detailed modelling of the flow behaviour within a surging ice mass. These models recognize that instability in the lower ice layer is required to achieve a catastrophic advance (see Budd [9] and Clark [14]). Budd [9], for example, introduced a numerical model describing the net dynamic changes during a surge cycle. The main purpose of his study was to highlight the essential features of a surge without dwelling in detail on the processes responsible for the advance, i.e. he concentrated on the cyclic response of a glacier given the bed topography and accumulation-ablation pattern. To maintain simplicity of his model, Budd made simplifying assumptions regarding the velocity distribution, flow law, temperature profile (temperate) and the reduction in basal shear resistance.

Budd was able to show that for a given bedrock profile, a glacier can fall into one of the following three categories depending on the mass balance: ordinary glacier - insufficient mass flux to go beyond the slow mode; fast glacier - sufficient mass flux to maintain a fast mode; and surging glacier - sufficient mass flux to reach a fast mode but not enough to maintain it. An important factor, not considered

by Budd, is the role of the temperature distribution. Clarke [14] indicated that even if the basal temperature variation with time is not responsible for a surge initiation, the temperature distribution in a cold ice mass may play an important role in the timing of the surge cycle.

1.4 Purpose and Scope of Study

The purpose of this study is to develop a numerical model that would be capable of simulating the creep and temperature responses of glaciers and ice sheets with emphasis on the model's ability to accomodate instability. To meet this objective, the finite element method has been used for determining responses of large ice masses which can be modelled as two-dimensional flow problems. The models developed have the advantage of treating ice dynamic problems as a continuum in which rigorous coupling is enforced between the stress and the velocity fields. These models demonstrate flexibility in handling glaciers or ice sheets of arbitrary geometries, a wide range of material properties and complicated boundary conditions.

A major difficulty in ice dynamics is to find the constitutive relationships which govern the motion of large ice masses. Chapter 2 reviews some of the available creep and sliding relationships.

Past emphasis in glaciology has concentrated on treating ice as a nonlinear incompressible fluid. Analyses of ice deformations based on such an approximation have been most suitable for steady-state flow.

Three creep models are developed herein: Model A adopts the incompressible fluid dynamic approach in which mean normal stress and velocities are primary variables; Model B approximates incompressibility through a constitutive relationship similar to that used in elasticity; and Model C uses a large displacement formulation where compressibility of the velocity field is introduced through the assumed elastic compliance of ice. Models A and B yield steady-state solutions while Model C is suited for transient responses. Model C has also been tailored for studying surges. An implicit time-marching scheme, outlined by Kanchi et al. [53], is used to eliminate numerical instability problems. A sliding element has been developed to accomodate basal sliding or high shear deformation gradients within the basal ice layer.

In addition to the creep models a finite element, transient thermal model is also developed. By interactive coupling of the creep and temperature algorithms, it is possible to update the temperature field due to changes in strain heating and boundary conditions. The new temperature distribution is then used to compute the creep response. Details of the finite element models are presented in Chapter 3.

To demonstrate some of the many potential applications of the finite element models, the dynamic behaviour of three ice masses is investigated in this thesis: an idealized double slope problem; Erebus Glacier Tongue (EGT), Antarctica; and Barnes Ice Cap (BIC), Baffin Island, Canada. Particular emphasis is placed on the surge behaviour of BIC. The following factors that influence the dynamics of large ice masses are addressed: the influence of initial (or residual) stresses

on the history of ice deformation; the effect of compressibility on the velocity field; the effect of sliding and thermal regime on the dynamic response; and the effect of basal shear resistance and temperature distribution on the surging of BIC. The importance of thermal advection on the temperature fields is illustrated for both EGT and BIC examples. The time required for the temperature field of BIC to adjust to changes in boundary conditions and velocity field is also investigated.

Chapter 4 deals exclusively with the double slope problem while Chapter 5 summarizes the results of the finite element simulations of EGT and BIC. Conclusions and recommendations are presented in Chapter 6.

CHAPTER 2

CONSTITUTIVE PROPERTIES OF ICE AND SLIDING MECHANISMS

2.1 General

A major difficulty in the analysis of large ice masses is the selection of appropriate creep relationships. Most often the field data available are sparse and at present time one has to rely on information available in the literature. The selection of a creep law is difficult due to the large number of laws available. Also the predicted velocities for a particular ice problem can vary by several orders of magnitude depending on the choice of a flow law [23]. In this chapter a survey of creep relationships for ice is presented. Also reviewed are mechanisms and relationships for sliding at the ice-bed interface.

2.2 Creep Deformation

2.2.1 General Approaches

Three general approaches are available for the development of creep relationships: fundamental approach; rheological approach; and empirical approach [22]. These approaches usually deal with the primary and secondary creep stages. The fundamental approach relates the deformation of a material to micromechanistic processes using rate-process or dislocation theory. For details on fundamental processes responsible for creep deformation of ice, the reader is referred to Barnes et al.

[3] and Michel [67]. Rheological models describe creep behaviour using a combination of springs, dashpots and sliders. Although this approach gives useful approximate mathematical models, these are often highly idealized [22]. The empirical approach has been used more often in ice mechanics.

2.2.2 Mechanical Behaviour of Polycrystalline Ice

The creep response of polycrystalline ice is similar to that of metals, i.e. polycrystalline ice can exhibit primary, secondary and tertiary stages of creep as shown in Figure 2.1(a). Due to the high homogolous temperature of natural ice it is generally assumed that the long-term deformation of large ice masses is due to steady-state creep which can be approximated by the minimum strain rate as illustrated in Figure 2.1(b). Various flow laws have been developed using the empirical approach based on either laboratory or insitu data. While laboratory tests can be more carefully controlled, field measurements reflect the insitu material properties which are dependent on the loading and temperature histories. The minimum flow rate for glacier ice is believed to be larger than that observed in the laboratory as shown in Figure 2.1(b). Mellor [66] provides a summary on the current state of knowledge of the mechanical properties of polycrystalline ice.

Glen [27, 28] performed laboratory tests on polycrystalline ice and determined the flow law to be of the form,

$$\dot{\varepsilon} = A\sigma^n \qquad (2.1)$$

where $\dot{\varepsilon}$ is the uniaxial strain rate, σ is the uniaxial compressive stress, and A and n are constants. The power law may also be expressed in terms of shear strain rate and shear stress. Measured values for the index "n" are in the range of 1.9 to 4.5 with a mean value of approximately three [79]. Glen [28] indicated that the index appears to increase with an increase in stress. Various researchers suggest that the index approaches unity for stresses below 0.1 MPa, and the field data at these low stresses support a value closer to three (see reference [37]). The constant A depends on temperature, ice fabric, texture, etc.

Meier [63] proposed a multiaxial flow law of the form,

$$\dot{\varepsilon}_{OCT} = 0.018\ \sigma_{OCT} + 0.013\ \sigma_{OCT}^{4.5} \qquad (2.2)$$

which is based on the velocity distributions within temperate glaciers and on laboratory tests. The octahedral shear strain rate $\dot{\varepsilon}_{OCT}$ is expressed as per annum and the octahedral shear stress σ_{OCT} is expressed in bars (1 bar = 0.1 MPa). Meier included the linear term in order to accommodate the low stresses that are encountered in glaciers. Other creep laws are available but are not reviewed here. The reader is referred to a summary of creep flow laws given by Budd [7].

Various temperature dependencies of creep laws have been proposed to account for the influence of temperature on strain rate. The

rate-process relationship (Arrhenius) used by Glen [28] has received the widest acceptance in glaciology and is given by

$$\dot{\varepsilon} = B(\sigma) \exp(-Q/RT) \qquad (2.3)$$

where R is the gas constant, Q is the apparent activation energy, T is the absolute temperature and $B(\sigma)$ is a stress dependent function such as the power law. The main criticism of Equation (2.3) is that it grossly underestimates the creep strain rates for ice at temperatures approaching the melting point. The difference between the actual flow rates and the flow rates predicted by Equation (2.3) has been attributed to a change in the activation energy and increased grain-boundary sliding due to the presence of water at temperatures above -10°C [3]. To approximate the influence of an 'apparent' temperature sensitive activation energy, the following activation energies have been adopted in this study.

$$Q = 120 \text{ kJ/mol for } T < -8°C \qquad (2.4.a)$$

$$Q = 78 \text{ kJ/mol for } T > -8°C \qquad (2.4.b)$$

A summary of activation energies and power law indices determined by various researches is given by Homer and Glen [43].

2.2.3 Creep Under a Multiaxial State of Stress

From a practical viewpoint, laws are generally required to reflect a multiaxial state of stress. Using the von-Mises yield criter-

ion, usually employed for generalization of the constitutive laws in plastic flow problems (see, e.g., Johnson and Mellor [49]), the components of creep strain $\Delta\varepsilon_{ij}^{c}$ during time interval Δt_n for a homogeneous and isotropic material are given by

$$\Delta\varepsilon_{ij}^{c} = \frac{3}{2} \frac{\Delta\varepsilon_{e}^{c}}{\sigma_e} S_{ij} \tag{2.5}$$

where S_{ij} are the deviatoric stress components defined as

$$S_{ij} = \sigma_{ij} - \delta_{ij} \frac{\sigma_{kk}}{3}, \tag{2.6}$$

in which δ_{ij} is the Kronecker delta, and σ_e and $\Delta\varepsilon_{e}^{c}$ are the equivalent stress and the equivalent creep strain increment, respectively, which are defined in the following equations.

$$\Delta\varepsilon_{e}^{c} = \left(\frac{2}{3} \Delta\varepsilon_{ij}^{c} \Delta\varepsilon_{ij}^{c}\right)^{1/2} \tag{2.7.a}$$

$$\sigma_e = \left(\frac{3}{2} S_{ij} S_{ij}\right)^{1/2} \tag{2.7.b}$$

Summation is implied over the repeated indices. Dorn's definitions for equivalent stress and equivalent strain increment are adopted since they preserve the form of an uniaxial creep law when generalized to a multiaxial state of stress. The product of the equivalent stress and the equivalent strain increment gives the energy dissipated during time Δt_n,

i.e. $\sigma_e \Delta\varepsilon_e^c = \sigma_{ij}\Delta\varepsilon_{ij}^c$.

For steady-state creep in ice mechanics, one can assume that the elastic strains are negligible and that the flow of ice can be modelled as a creeping, incompressible flow problem obeying the following creep law:

$$\dot{\varepsilon}_{ij}^c = \frac{1}{2\mu} S_{ij} \qquad (2.8.a)$$

where μ is an equivalent strain-rate dependent viscosity and $\dot{\varepsilon}_{ij}^c$ is the creep strain rate. In view of the form of Equation (2.8.a) the viscosity μ depends on the current equivalent stress σ_e and the creep strain rate $\dot{\varepsilon}_e^c$.

$$\mu = \frac{1}{3} \frac{\sigma_e}{\dot{\varepsilon}_e^c} \qquad (2.8.b)$$

For the development of Equation (2.5) the following assumptions are made: increments of creep strain depend on the current values of the deviatoric stress components; the principle axes of stress and strain increment tensors coincide; and no volume change occurs due to creep strains. Experimental evidence from creep of metals indicates that the assumptions leading to Equation (2.5) (or (2.8.a)) are not strictly correct. However this relationship appears to be sufficiently accurate from a practical viewpoint.

If the elastic strains are included, the Prandtl-Reuss approximation for strain increments can be used, i.e.,

$$\Delta\varepsilon_{ij} = \Delta\varepsilon_{ij}^{E} + \Delta\varepsilon_{ij}^{C} \tag{2.9}$$

where $\Delta\varepsilon_{ij}$ is the total strain increment and $\Delta\varepsilon_{ij}^{E}$ is the elastic strain increment. The inclusion of the elastic strain increments allows for changes in volumetric strain which is caused by changes in the current spherical stress. Since it is assumed that the ice is homogeneous and isotropic only two parameters are necessary to completely define the elastic response: elastic modulus E; and Poisson's ratio ν. It is further assumed that the elastic response is linear and that the material properties are constant. The elastic modulus and Poisson's ratio used in this study are 9.1×10^3 MPa and 0.34, respectively. A review of elastic constants is given by Emery and Nguyen [23]. For more details on the engineering properties of fresh water ice, the reader is referred to Gold [32].

2.3 Basal Sliding

2.3.1 Factors Influencing Sliding

The attempts to understand basal sliding have been mainly due to theoretical considerations. A direct verification of the theoretical concepts involved is generally not possible. Much field data on sliding is extracted from surface velocity measurements and then separating the velocity thought to be due to internal deformation only [79]. For the

few cases where sliding has been observed at the ice-bed interface (for example at ice-falls), the conditions are not typical of those expected at the base of glaciers or ice sheets (see Kamb and LaChapelle [51]). Factors that are believed to influence basal sliding include: temperature at the ice-bed interface; state of stress at the interface; rheology of basal ice; morphology of the bed surface; nature of the ice-bed interface, i.e. presence of cavities, water, debris, etc.; and subglacial hydrology [99].

2.3.2 Sliding Mechanisms

Weertman [93] was the first researcher to attempt a mathematical model for sliding over an undeformable bed. Two processes were considered by which ice can move past obstacles posed by the bedrock: pressure melting where ice melts on the upstream side of an obstacle and refreezes on the downstream side; and enhanced creep due to stress concentrations around an obstacle. Obstacles (or bedrock irregularities) are the perturbations about the mean bed surface. Sliding is possible only if the basal ice is temperate. The pressure melting mechanism dominates for small obstacle sizes while creep enhancement dominates around the larger obstacles. Since a glacier bed consists of a continuous spectrum of obstacle sizes, Weertman indicated that sliding is likely to be controlled by one obstacle size where both processes contribute equally to sliding. The smaller obstacles limit the creep process and the larger ones limit the regelation process. Weertman referred to the transition obstacle (or wavelength) as the controlling obstacle size since much of the drag comes from obstacles of this size.

Kamb and LaChapelle [51] confirmed the existence of both mechanisms in a tunnel going to the bedrock in Blue Glacier, U.S.A. They observed that most of the differential movement occurs in the lowest 50 cm of basal ice. They also observed that the regelation thickness varies between 0 and 30 mm and that the controlling obstacle size is approximately 50 cm. Based on theoretical considerations, Kamb [52] estimated that the transition wavelength is in the range of 0 to 80 cm with a mean regelation thickness in the range of 2 to 15 mm. The transition wavelength decreases with an increase in basal shear stress for a nonlinear creep flow law. Kamb noticed a lack of roughness at scales less than the transition wavelength. This apparent lack of roughness for smaller obstacle sizes was attributed to extensive glacial abrasion or possible ice-bedrock separation. For a bed, where roughness is absent at wavelengths less than λ which is longer than the transition wavelength, sliding is dominated by creep enhancement. Although most glaciologists agree that the two mechanisms suggested by Weertman contribute to basal sliding, at the same time they disagree on the relative importance of these mechanisms.

2.3.3 Sliding Relationships

As for most sliding theories it is assumed that the basal ice is clean and rests on a fixed undeformable bed, the basal ice remains in intimate contact with the bed, the bed offers no tangential shear resistance due to a thin water film from regelation, the rheology of the basal ice is similar to that of ice lying directly above, and the clas-

sical regelation theory is applicable for the pressure melting mechanism. Although limitations do exist regarding these assumptions, the above simplifications are required to yield a relationship between sliding velocity, basal shear stress and the bed roughness. Raymond [85] discusses some of the limitations of these assumptions. Other recent references on theories of basal sliding include those by Weertman [94], Lliboutry [57] and Fowler [25].

As indicated previously, Weertman [93] was the first researcher to address the problem of sliding. To simplify his analysis and to illustrate the relative importance of the two sliding mechanisms, he chose a highly idealized bed consisting of cubic obstacles. In his original treatment he assumed that only the controlling obstacle size is important for sliding. Later on, Weertman [96] relaxed his assumption of cubic obstacles and allowed for a discrete spectrum of obstacles that varied according to a geometric progression. By assuming that roughness is constant for all obstacle sizes and that the ice rheology is given by a power law, Weertman obtained the following relationships for basal sliding velocity v_b:

$$v_b \propto \tau_b^{\frac{n+1}{2}} \tag{2.10}$$

when both mechanisms are important, and

$$v_b \propto \tau_b^{n} \tag{2.11}$$

when creep enhancement dominates. The index n is the power from the creep relationship and τ_b is the average basal shear stress. For Equation (2.10) the controlling obstacle size contributes between 40 and 50 percent to the total drag or shear resistance.

Nye [76] and Kamb [52] gave a mathematically rigorous treatment of basal sliding for linear ice rheology using methods of Fourier analysis which can handle arbitrary bedrock morphology. Kamb extended his treatment of sliding to include nonlinear ice rheology by using an approximate method for estimating sliding due to creep. While the Fourier analysis can be completed for an arbitrary spectral content, most results are expressed assuming constant roughness for all wavelengths. This feature is referred to as white roughness [52]. The dependence of sliding velocity on shear stress for white roughness and for a truncated white roughness is given by Equations (2.10) and (2.11), respectively. Many of the qualitative results obtained by the more advanced theories proposed by Nye, Kamb and Fowler are the same as those given by Weertman's more simplified analysis.

2.3.4. Influence of Water, Ice-bed Separation and Till

The influence of water, ice-bed separation and till have not been considered in the developing of the sliding relationships presented previously. A major influence on sliding, which remains a controversial topic, is the hydrology at the ice-bed interface (see e.g. Lliboutry [57] and Weertman [98]). The presence of water can lead to easier separation between the glacier sole and the bedrock. Cavities,

initially predicted by Lliboutry [55], are believed to form first on the downstream side of the controlling obstacles where negative pressure deviations are the greatest. It has been shown theoretically [52] and verified through field observations [51] that separation is expected at ice-falls where the ice is thin and slopes are steeper. Separation is also predicted for typical surface slopes for glaciers if the cavity water pressure exceeds one half of the overburden ice pressure. The formation of cavities [52] or the buildup of a thick water layer [95, 97] have the influence of smoothening the bed profile as seen by the glacier sole. As a consequence, the sliding velocity increases due to lack of roughness at the transition and shorter wavelengths. As mentioned in Chapter 1, it has been suggested that a buildup of a water layer or extensive cavitation may be responsible for surging.

If the basal shear stress and porewater pressure are sufficiently high, any till at the ice-bedrock interface may also deform. Boulton and Jones [5] showed that ice sheets resting on deformable beds will in general be thinner due to reduced shear strength at the base. An important consideration, not given much attention in sliding theories, is friction due to debris locked in the ice that makes contact with the bedrock. The main influence of friction is to reduce the sliding velocity. Based on observations and direct measurements at the ice-bed interface of a glacier, Boulton et al. [6] indicated that the concentration of debris, commonly found within a basal ice layer, is sufficiently high and that a significant contribution to drag at the ice-bed interface of an ice mass can be due to this.

For this study, the sliding relationship is assumed to be of the following form

$$v_b = C' \tau_b^{\,m} \qquad (2.12)$$

where C and m are constants that depend on the bed roughness as seen by the glacier sole and the ice-rock thermal properties. In view of the uncertainties associated with the development of sliding laws and to maintain simplicity, a linear sliding law has been used in this study. The constant C for the Barnes Ice Cap example is determined through a parameteric study. It should be noted that the creep models developed in this study are also capable of accomodating nonlinear sliding laws.

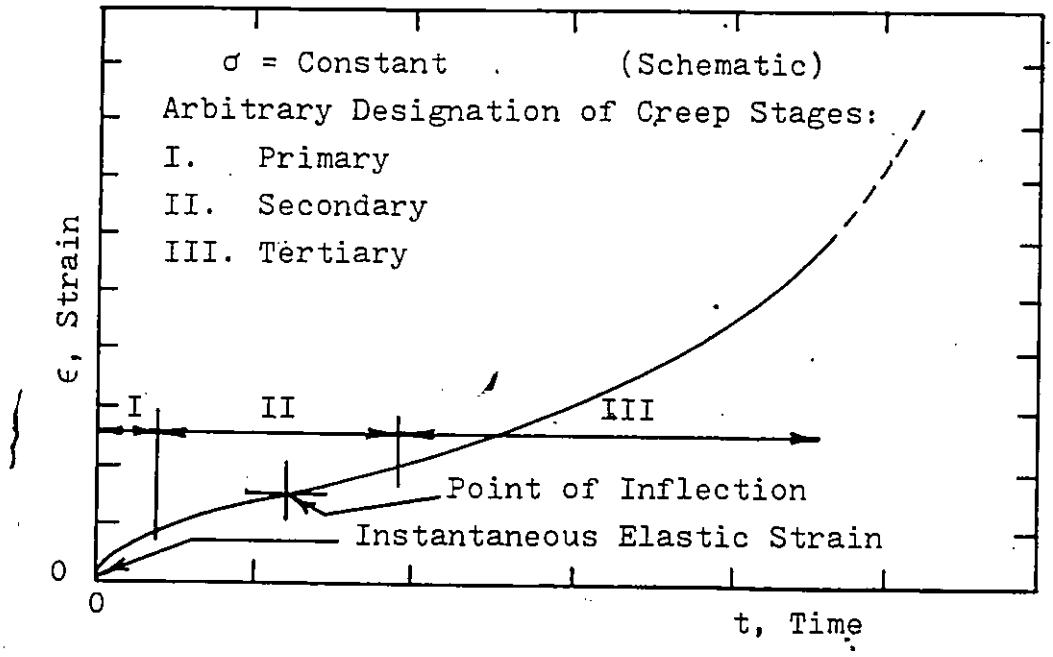

FIGURE 2.1 (a) TYPICAL CREEP CURVE FOR A CONSTANT STRESS TEST ON ICE.

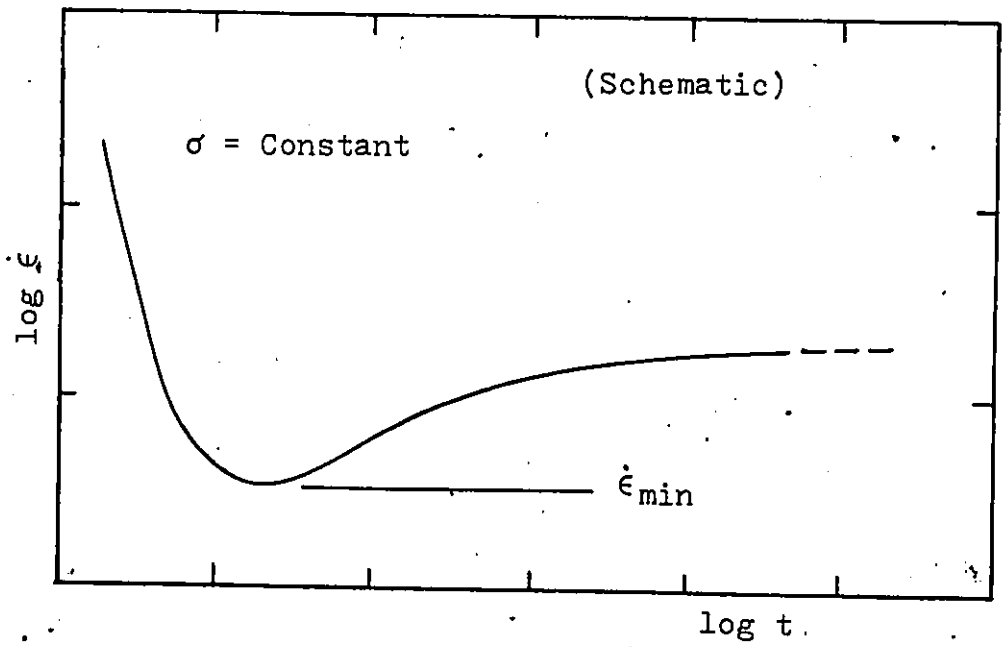

FIGURE 2.1 (b) ALTERNATIVE CREEP CURVE FOR ICE (see reference [66]).

CHAPTER 3

ANALYTICAL AND FINITE ELEMENT MODELLING

3.1 Introduction

The finite element method presents a simple and practical tool to solve continuum problems of complex geometry, boundary conditions and material properties, for which close form solutions may not exist. The ability of this numerical method to predict the response of natural ice masses due to gravity and thermal loading depends on the suitability of the analytical model and correctness of the input information. The accuracy of the numerical solution when compared with an available analytical solution depends on the refineness of the finite element mesh, the grid arrangement and the length of the time steps for the transient part. Several texts on the finite element method (see Bathe and Wilson [4], Zienkiewicz [103], etc.) are available, thus details of the method are not presented in this thesis.

This chapter describes the finite element models that are used for computing the temperature and velocity distributions within an ice mass. The analysis is restricted to planar flow and isotropic material properties. Various assumptions made for the models are outlined as they occur. Both, tensor and matrix notations are used interchangeably, when and where it is convenient to maintain compactness and clarity.

3.2 Steady-State Creeping Flow

3.2.1 Incompressible Non-Newtonian Flow (Model A)

The stress history of large ice masses is generally not known. To avoid this difficulty, non-Newtonian fluid rheology has been assumed for the ice flow properties and the analysis procedure is analogous to steady-state creeping flow under gravity loads and surface tractions. This modelling, of course, assumes that the elastic strains are negligible. This approach has been used extensively in the past and has lead to models which predicted velocities in good agreement with the measured velocities (see e.g., Hooke et al. [46]). Model A, which is presented in this section, is consistent with the fluid mechanics approach most often adopted by the glaciologists. Glacier ice is treated as an incompressible fluid where the viscosity depends on the strain rate and temperature.

The equilibrium of an ice mass can be written in an integral equation form which is usually the basis for the finite element formulation. Several methods are available to reduce the differential equilibrium equations to suitable integral equations, variational principles [46], Gälerkin method, and virtual work principles [77]. The primitive variable approach used here is based on the principle of virtual velocities [61]:

$$\int_{\Omega} \sigma_{ij}\, \delta\dot{\varepsilon}_{ij}\, d\Omega - \int_{\Omega} b_i\, \delta v_i d\Omega - \int_{\Gamma_t} \bar{T}_i \delta v_i d\Gamma = 0 \qquad (3.1)$$

where $\delta\dot{\varepsilon}_{ij}$ and δv_i are the virtual rate of deformation and virtual velocity tensors which are compatible, b_i are the body forces, Ω is the volume and $\bar{T}_i$ are the surface tractions applied on part of the boundary Γ_t. The primitive variables are the mean normal stress σ_m and the velocities v_i. On the portion of the boundary where velocities are specified, the virtual velocities vanish.

The stress tensor σ_{ij} is related to σ_m and the rate of deformation tensor as

$$\sigma_{ij} = \sigma_m \delta_{ij} + 2\mu\, \dot{\varepsilon}_{ij} \tag{3.2}$$

where δ_{ij} is the Kronecker delta and μ is the deformation rate and temperature dependent viscosity. The components of the rate of deformation tensor $\dot{\varepsilon}_{ij}$ are given in terms of the velocity gradients by,

$$\dot{\varepsilon}_{ij} = \frac{1}{2}\left(\frac{\partial v_i}{\partial x_j} + \frac{\partial v_j}{\partial x_i}\right). \tag{3.3}$$

All derivatives are with respect to the spatial coordinates x_i. It should be noted that the rate of deformation tensor is often referred to as the strain rate tensor.

A second virtual work rate equation is required to enforce incompressibility and is of the following form.

$$\int_{\Omega} \delta\sigma_m \, v_{i,i} \, d\Omega = 0 \tag{3.4}$$

This equation states that the internal work rate due to a virtual mean normal stress ($\delta\sigma_m = \frac{\delta\sigma_{kk}}{3}$) acting on an incompressible flow field is zero [101].

The finite element approximation for velocity, strain rate and mean normal stress can be chosen as

$$\{v\} = [N] \{\bar{v}\}; \qquad v_i = \langle N_i \rangle \{\bar{v}\} \tag{3.5}$$

$$\{\dot{\varepsilon}\} = [B] \{\bar{v}\}; \qquad \dot{\varepsilon}_{ij} = \langle B_{ij} \rangle \{\bar{v}\} \tag{3.6.a}$$

with

$$\langle B_{ij} \rangle = \frac{1}{2}(\langle N_i \rangle_{,j} + \langle N_j \rangle_{,i}) \tag{3.6.b}$$

and

$$\sigma_m = \langle \bar{N} \rangle \{\bar{\sigma}_m\} \tag{3.7}$$

where [N] contains the interpolation functions for the velocity vector $\{v\}$, [B] is the strain rate matrix, $\langle \bar{N} \rangle$ contains the interpolation functions for the mean normal stress, $\{\bar{v}\}$ contains the velocity nodal degrees of freedom and $\{\bar{\sigma}_m\}$ contains the mean normal stress nodal degrees of freedom. The symbol < > denotes a row matrix, e.g. $\langle B_{ij} \rangle$ is the row matrix of [B] that corresonds to $\dot{\varepsilon}_{ij}$.

After performing appropriate substitutions of Equations (3.1) to (3.7), the virtual work rate statements (Equations (3.1) and (3.4)) reduce to the following matrix form:

$$\begin{bmatrix} [K_u] & [K_p] \\ [K_p]^T & [0] \end{bmatrix} \begin{Bmatrix} \bar{v} \\ \bar{\sigma}_m \end{Bmatrix} = \begin{Bmatrix} \{F\} \\ \{0\} \end{Bmatrix} \tag{3.8.a}$$

where

$$[K_u] = \int_\Omega \langle B_{ij}\rangle^T 2\mu \langle B_{ij}\rangle d\Omega \tag{3.8.b}$$

$$[K_p] = \int_\Omega \langle N_i\rangle^T_{,i} \langle \bar{N}\rangle \, d\Omega \tag{3.8.c}$$

and

$$\{F\} = \int_\Omega \langle N_i\rangle^T b_i d\Omega + \int_{\Gamma_t} \langle N_i\rangle^T \bar{T}_i \, d\Gamma. \tag{3.8.d}$$

For the finite element modelling, a quadratic velocity variation and a linear mean normal stress (pressure) were assumed within each triangular element. The lower order of interpolation for pressure is consistent and does not lead to singular matrices when using the standard matrix equation solvers. For details on the choice of interpolation functions the reader is referred to Mirza [68] and Argyris et al. [2]. In solving a complete flow problem the usual assemblage procedure for finite elements was used [103]. Care is taken when using the primitive variable formulation to ensure that there are at least twice as many velocity unknowns as mean normal stress unknowns in order not to impose over-constraints.

Since the viscosity is strain rate dependent, a direct iteration scheme has been used to carry out the nonlinear analysis [103]. Conver-

gence of this algorithm, based on the root-mean-square error of velocities for successive iterations, depends on the complexity of the problem, i.e. the number of nodes, geometry, etc. Solution by the discrete least square method (which renders a positive definite matrix) in conjuntion with the Choleski square root method, has been used to solve for the unknowns during each iteration.

3.2.2 Alternative Formulation for Incompressibility (Model B)

A second steady-state creep flow model has been developed following somewhat the penalty function approach [103]. This approach is based on a direct comparison between the constitutive relationships for nearly incompressible linear elasticity and fluid flow. The constitutive relationship between elastic stresses and strains is given by

$$\sigma_{ij} = \frac{2\nu G}{(1-2\nu)} \varepsilon_{kk} \delta_{ij} + 2G \varepsilon_{ij} \qquad (3.9)$$

where ε_{ij} is the strain tensor, G the shear modulus and ν is Poisson's ratio. For a nearly incompressible elastic solid ε_{kk} approaches zero when ν approaches half. Herrmann [35] formulated a variational theorem for incompressible and nearly incompressible materials in terms of displacements and mean normal stress. A similar approach can be adopted by replacing the strains in Equation (3.9) with rates of deformation and by formulating the finite element model for creeping nonlinear viscous flow in terms of deformation rates alone. Due to dominance of the volumetric strain contribution to σ_{ij} in Equation (3.9) as Poisson's ratio

approaches half, a reduced numerical integration has been applied to this term when formulating the finite element matrices. A caution here that the mean normal stress cannot be computed directly when using a penalty function approach.

Since the major difference between Models A and B is the formulation of the element matrices, both models are available as options in a single finite element program. A comparison of the velocity fields computed from both models, helps determine the influence of volumetric compliance on the flow field for large ice masses.

3.2.3 Sliding Boundary Condition

Sliding at the ice-bed interface can be incorporated into a finite element model in two ways: assume that sliding is due to high deformation gradients in a finite basal layer which is accomodated by a layer of elements with suitable rheological properties; or introduce boundary conditions analogous to springs at the boundary as used in elastic analysis. The introduction of an additional layer of elements increases the number of unknowns and the matrix band width which ultimately leads to larger computer storage requirements and greater computation costs. If many element layers are to be used to model the basal layer, one can encounter problems of bad aspect ratios for the elements near the base which are further compounded by the fact that such elements would have much smaller stiffnesses. The spring analogy is used in this study in view of the disadvantages mentioned above.

Consider a segment of the boundary where ice slides over a bedrock as illustrated in Figure (3.1). The surface force that resists sliding is represented by the tangential surface traction $\tilde{T}_1$ (formerly τ_b) which is given by a modified version of Equation (2.12), i.e.

$$\tilde{T}_1 = \tilde{k}_{11} \tilde{v}_1 \qquad (3.10.a)$$

where $\tilde{v}_1$ (formerly v_b) is the tangential velocity and $\tilde{k}_{11}$ is a velocity dependent parameter that incorporates resistance to sliding.

$$\tilde{k}_{11} = \tilde{v}_1^{\left(\frac{1}{m} - 1\right)} C^{\left(-\frac{1}{m}\right)} \qquad (3.10.b)$$

For the moment it is assumed that the normal surface traction $\tilde{T}_2$ is related to a normal velocity $\tilde{v}_2$ by a relationship similar to Equation (3.10.a), i.e. no coupling between the normal and tangential actions.

Equation (3.10.a) can be rewritten in a more general form as

$$\tilde{T}_i = \tilde{k}_{ij} \tilde{v}_j. \qquad (3.11)$$

and $\tilde{k}_{ij} = 0$ if $i \neq j$.

In order to introduce this boundary condition into the virtual work rate statement, both sides of Equation (3.11) are integrated along the bound-

ary, after multiplying by a virtual velocity $\delta\tilde{v}_i$ yielding,

$$\int_{\bar{\Gamma}} \delta\tilde{v}_i\tilde{T}_i d\Gamma = \int_{\bar{\Gamma}} \delta\tilde{v}_i\tilde{k}_{ij}\tilde{v}_j d\Gamma = \int_{\bar{\Gamma}} \delta v_i T_i d\Gamma \qquad (3.12)$$

where $\bar{\Gamma}$ is part of the boundary with sliding on it. Adding Equation (3.12) to (3.1), for incorporating the sliding boundary, yields

$$\int_{\Omega} \delta\dot{\varepsilon}_{ij}\sigma_{ij} d\Omega + \int_{\bar{\Gamma}} \delta\tilde{v}_i\tilde{k}_{ij}\tilde{v}_i d\Gamma - \int_{\Omega} \delta v_i b_i d\Omega - \int_{\Gamma_t} \delta v_i \bar{T}_i d\Gamma = 0. \qquad (3.13)$$

To simplify integration along a curved boundary, matrix transformations are employed, see Figure (3.2). In order to prevent a velocity component normal to the bedrock surface, the normal velocities at the boundary are fixed at zero.

3.3 Large-Displacement Nonlinear Creep Model (Model C)

3.3.1 Theoretical and Practical Considerations

Application of the finite element method to include the transient creep response of ice masses due to changes on the boundary and/or due to various changes in the interior has presented difficulties in the past regarding accuracy and computational efficiency. This is particularly true for simulation of long-term creep [1]. The finite element model presented in this section is an extension of the model developed by Emery and Mirza [24]. The following model incorporates the influence of geometric nonlinear effects, time-dependent sliding and an implicit

time-marching scheme for creep [53]. The implicit time-marching scheme allows for longer time steps than is possible with an explicit scheme and yet maintaining a better accuracy.

To accommodate geometric nonlinearities, an updated Lagrangian approach has been adopted. The strain is given by Green's tensor as,

$$\varepsilon_{ij} = \frac{1}{2}\left(\frac{\partial u_i}{\partial X_j} + \frac{\partial u_j}{\partial X_i} + \frac{\partial u_k}{\partial X_i}\frac{\partial u_k}{\partial X_j}\right) \qquad i,j,k = 1,2,3 \qquad (3.14)$$

where u_i is the displacement in the x_i direction. All derivatives are with respect to the initial (which may be updated) reference configuration denoted by the position vector $\vec{X}$ as shown in Figure (3.3). The second Piola-Kirchhoff stress s_{ij}^{PK} is the conjugate to ε_{ij} [62],

$$s_{ij}^{PK} = \det\left(\frac{\partial \vec{x}}{\partial \vec{X}}\right) \frac{\partial X_i}{\partial x_k} \sigma_{k\ell} \frac{\partial X_j}{\partial x_\ell} \qquad (3.15)$$

where the determinant reduces to ρ_0/ρ, the initial density to deformed configuration density ratio, and $\vec{x}$ is the position vector of a point according to the deformed configuration.

A concise formulation of equilibrium, consistent with the Lagrangian formulation, is given by the virtual work equation cited by McMeeking and Rice [62].

$$\int_{\Omega_0} \delta\varepsilon_{ij}\, s_{ij}^{PK}\, d\Omega - \int_{\Omega_0} \delta u_i b_i d\Omega - \int_{\Gamma_t} \delta u_i\, \bar{T}_i d\Gamma = 0 \qquad (3.16)$$

where δu_i and $\delta\varepsilon_{ij}$ are the virtual displacements and strains, respectively, and the force terms are nominal. For practial purposes it is possible to replace the Piola-Kirchhoff stress by Cauchy stress σ_{ij} by ensuring that

$$\left| \frac{\partial X_i}{\partial x_k} - \delta_{ik} \right| \ll 1. \qquad (3.17)$$

This constraint can be satisfied by the frequent updating of geometry during an incremental analysis.

3.3.2 Finite Element Equivalent of Model C

Details of the reduction of Equation (3.16) to its finite element equivalent is given by Zienkiewicz [103] and Kanchi et al. [53];

$$\int_{\Omega_0} [B_n]^T \{\sigma_n\} d\Omega - \{R_n\} = \{0\} \qquad (3.18)$$

where $\{R_n\}$ is the consistent load vector due to body forces, temperature loads, etc., $[B_n]$ is the kinematic strain matrix due to large displacements and $\{\sigma_n\}$ is the stress vector during the nth iteration. The strain matrix $[B_n]$ arises from the relationship between the strains and the nodal displacements,

$$\{\varepsilon_n\} = [B_n]\ \{\delta_n\} \tag{3.19.a}$$

$$\langle B_{ij}\rangle = \frac{1}{2}\left[\langle N_i\rangle_{,j} + \langle N_j\rangle_{,i} + \{\delta_n\}^T\langle N_k\rangle_{,i}^T\langle N_k\rangle_{,j}\right]. \tag{3.19.b}$$

The matrices $\langle N_i\rangle$ and $\langle B_{ij}\rangle$ are rows of $[N]$ and $[B_n]$ defined so that

$$u_i = \langle N_i\rangle\ \{\delta_n\} \tag{3.20}$$

$$\varepsilon_{ij} = \langle B_{ij}\rangle\ \{\delta_n\} \tag{3.21}$$

where $[N]$ and $\{\delta_n\}$ contain the shape functions and the nodal displacements, respectively.

Equation (3.18) can be reduced to an increment form in the following manner:

$$\int_{\Omega_0} \left([B_n]^T\{\Delta\sigma_n\} + \Delta[B_n]^T\{\sigma_n\}\right)d\Omega - \{\Delta R_n\} = \{0\} \tag{3.22.a}$$

where

$$\int_{\Omega_0} \Delta[B_n]^T\{\sigma_n\}d\Omega = [K_{\tau n}]\{\Delta\delta_n\} \tag{3.22.b}$$

and $[K_{\tau n}]$ is often referred to as the initial stress matrix [103] and $\{\Delta\delta_n\}$ is the displacement increment due to changes in the external load

and/or creep loading during the nth creep increment.

The stress increment $\{\Delta\sigma_n\}$ is obtained using linear elastic compliance matrix [D] as

$$\{\Delta\sigma_n\} = [D]\ \{\Delta\varepsilon_n^E\};\ \text{or}\ \Delta\sigma_{ij}^n = D_{ijkl}\Delta\varepsilon_{kl}^{En} \tag{3.23}$$

where $\{\Delta\varepsilon_n^E\}$ or $\Delta\varepsilon_{k\ell}^{En}$ are the incremental elastic strains. By adopting the Prandtl-Reuss flow rule (introduced in Chapter 2) the stress increments can be expressed in terms of the total strain increments $\{\Delta\varepsilon_n\}$ and the creep strain increments $\{\Delta\varepsilon_n^c\}$ in the following manner:

$$\{\Delta\varepsilon_n\} = [B_n]\ \{\Delta\delta_n\} \tag{3.24}$$

$$\{\Delta\varepsilon_n^c\} = \Delta t_n(\{\dot{\varepsilon}_n^c\} + \theta[H_n]\ \{\Delta\sigma_n\}) \tag{3.25.a}$$

or

$$\Delta\varepsilon_{ij}^{cn} = \Delta t_n[\dot{\varepsilon}_{ij}^{cn} + \theta H_{ijkl}^n\Delta\sigma_{kl}^n] \tag{3.25.b}$$

where

$$H_{ijkl}^n = \frac{\partial\dot{\varepsilon}_{ij}^{cn}}{\partial\sigma_{kl}^n}\ . \tag{3.25.c}$$

The fourth tensor H_{ijkl}^n is symmetric in i,j and k,l if the flow law is associative. In Equations (3.25) θ is a dimensionless parameter that indicates the degree of implicitness. Equations (3.25) are the implicit expression for the creep strain increment [53]. For $\theta = 0$ the

scheme is fully explicit (Euler scheme), and for $\theta > 0$ the scheme is implicit. The scheme is fully implicit for $\theta = 1$. The Crank-Nicolson scheme $\theta = \frac{1}{2}$, is used for the numerical examples to be presented in this study. The creep strain rate $\dot{\varepsilon}_{ij}^{cn}$ at any time t_n is given by Equation (2.8.a).

The relationship between the stress increments and the strain increments is obtained by manipulating Equations (3.23) through (3.25), yielding

$$\{\Delta\sigma_n\} = [C_n]^{-1} \{[B_n] \{\Delta\delta_n\} - \Delta t_n \{\dot{\varepsilon}_n^c\}\} \tag{3.26.a}$$

where $[C_n]$ is the compliance matrix given by

$$[C_n] = [D]^{-1} + \theta\Delta t_n [H_n]. \tag{3.26.b}$$

The compliance matrix depends on the time increment and stresses. For plane strain conditions the strains perpendicular to the plane of flow are zero. Thus, the following constraints for incompressible creeping plane strain flow are imposed:

$$\Delta\varepsilon_{33} = \Delta\varepsilon_{33}^E + \Delta\varepsilon_{33}^C = 0 \tag{3.27.a}$$

and

$$\Delta\varepsilon_{33}^C = -(\Delta\varepsilon_{11}^C + \Delta\varepsilon_{22}^C). \tag{3.27.b}$$

The compliance matrix for plane strain conditions is given in Appendix A4.

Substituting the incremental stress-strain law (Equation (3.26.a)) into Equation (3.22.a) gives:

$$\left([K_{cn}] + [K_{\tau n}]\right) \{\Delta\delta_n\} - \{\Delta\bar{R}_n\} = \{0\} \qquad (3.28.a)$$

where $[K_{cn}]$ part of the stiffness matrix is given by

$$[K_{cn}] = \int_{\Omega_0} [B_n]^T [C_n]^{-1} [B_n] d\Omega \qquad (3.28.b)$$

The influence of creep due to the nth creep increment is introduced as an intial strain through the load vector increment

$$\{\Delta\bar{R}_n\} = \{\Delta R_n\} + \Delta t_n \int_{\Omega_0} [B_n]^T [C_n]^{-1} \{\dot{\varepsilon}_n^c\} d\Omega. \qquad (3.28.c)$$

The usual finite element procedure for assembling the element stiffness matrices is used. Since the stiffness matrix assembled during each creep iteration is symmetric, banded and positive definite, the Choleski square-root method is used to decompose the coefficient matrix. After solving for the displacement increments, these are substituted back into Equation (3.26.a) to calculate the stress increments $\{\Delta\sigma_n\}$ and hence the updated stresses as $\{\sigma_{n+1}\} = \{\sigma_n\} + \{\Delta\sigma_n\}$. The displacement and strains are updated in a similar manner, i.e., $\{\delta_{n+1}\} = \{\delta_n\} + \{\Delta\delta_n\}$,

$$\{\varepsilon_{n+1}\} = \{\varepsilon_n\} + \{\Delta\varepsilon_n\}, \text{ etc.}$$

The updated stresses when substituted into Equation (3.18) after time t_{n+1} may indicate that the equilibrium is not satisfied thus leading to a residual load vector. This residual load vector is due to the first order approximation of the equilibrium equations and can be reduced to an acceptable tolerance through an iterative process. In this study the residual forces are added to the next load increment which avoids excessive iterations and at the same time can help achieve a reduction in error [53] and drifting.

To ensure numerical stability of the iterative solution, the time increment should be small enough so that changes in displacements and stresses are not too large. To obtain an improved accuracy with minimal computational effort, two stability criteria are used [12].

(1) The time increment is based on a percentage of the previous time increment, i.e. $\Delta t_{n+1} = \lambda \Delta t_n$ where λ is usually less than 1.5 for an implicit scheme.

(2) A limitation can be imposed on the maximum time interval Δt_c given by Corneau [19]:

$$\Delta t_c = \frac{4(1+\nu)}{3En} \cdot \frac{\sigma_e}{\dot{\varepsilon}_e^c} \qquad (3.29.a)$$

for a power creep law using an explicit scheme. The terms in this equation are the same as defined previously. A

modified form of this equation is used in this study, i.e.

$$\Delta t_{n+1} < F\Delta t_c \qquad (3.29.b)$$

where F is a factor such that: $F = 1.0$ for $\theta < 1/2$; and $F > 1.0$ for $\theta > 1/2$.

3.3.3 Sliding Boundary Element

A simple method of simulating time-dependent basal sliding is to introduce a thin 'soft' ice layer with appropriate material properties. To simulate basal failure for a limiting shear stress, joint elements [33] can be introduced at potential tension zones and ice-rock interfaces [24]. To avoid numerical difficulties associated with the introduction of a thin soft ice layer the Goodman joint element is extended in this study to include time-dependent sliding response at the ice-bedrock interface. The assumptions regarding the development of this element include:

(1) movement at the ice-bed interface is parallel to the mean bed;

(2) only the basal shear stress governs the sliding velocity;

(3) the change in slope of the bedrock is gradual; and

(4) the boundary also has some elastic resistance.

The virtual work principle is used to relate the surface

tractions $\tilde{T}_i^n$ to the internal stresses $\tilde{\sigma}_i^n$ or $\{\tilde{\sigma}_n\}$ of the joint element. The tilda above the symbols indicates a coordinate system in which the subscripts 1 and 2 are the tangential and normal directions to the bedrock, respectively, as shown in Figure (3.4). It is required that:

$$\int_{\bar{\Gamma}} \delta\tilde{u}_i^n \tilde{T}_i^n = \int_{\bar{\Gamma}} \delta\tilde{w}_i^n \tilde{\sigma}_i^n d\Gamma = \int_{\bar{\Gamma}} \delta\{\tilde{w}_n\}^T \{\tilde{\sigma}_n\} d\Gamma \qquad (3.30.a)$$

or in an incremental form as

$$\int_{\bar{\Gamma}} \delta\tilde{u}_i^n \, \Delta\tilde{T}_i^n \, d\Gamma = \int_{\bar{\Gamma}} \delta\tilde{w}_i^n \, \Delta\tilde{\sigma}_i^n \, d\Gamma = \int_{\bar{\Gamma}} \delta\{\tilde{w}_n\}^T \{\Delta\tilde{\sigma}_n\} d\Gamma \qquad (3.30.b)$$

$$\tilde{w}_i^n = \tilde{u}_i^{In} - \tilde{u}_i^{Rn}; \quad \delta\tilde{w}_i^n = \delta\tilde{u}_i^{In} - \delta\tilde{u}_i^{Rn} \qquad (3.30.c)$$

where $\tilde{u}_i^{In}$ and $\tilde{u}_i^{Rn}$ are displacements of the ice and bedrock, respectively. All the other symbols have the same meaning as defined previously. The displacements in the ice and bedrock are related to the nodal displacements $\{\delta_n\}$ by

$$\tilde{u}_i^{In} = \langle N_i^I \rangle \{\delta_n\} \qquad (3.31.a)$$

$$\tilde{u}_i^{Rn} = \langle N_i^R \rangle \{\delta_n\}, \qquad (3.31.b)$$

respectively, where $\langle N_i^I \rangle$ and $\langle N_i^R \rangle$ are the shape functions. Equation (3.30.c) can be written as:

$$\tilde{w}_i^n = (\langle N_i^I \rangle - \langle N_i^R \rangle) \{\delta_n\} = \langle \bar{N}_i \rangle \{\delta_n\}. \tag{3.32}$$

The constitutive relationship between the stress increments $\{\Delta\sigma_n\}$ and the relative elastic displacement increments $\{\Delta w_n^E\}$ is

$$\begin{Bmatrix} \Delta\tilde{\sigma}_1^n \\ \Delta\tilde{\sigma}_2^n \end{Bmatrix} = \begin{bmatrix} \tilde{k}_{11} & 0 \\ 0 & \tilde{k}_{22} \end{bmatrix} \begin{Bmatrix} \Delta\tilde{w}_1^{En} \\ \Delta\tilde{w}_2^{En} \end{Bmatrix} \tag{3.33}$$

where $\tilde{k}_{ij}$ are the elastic stiffness constants in the matrix. Imposing additivity of the elastic and inelastic displacement increments gives

$$\Delta\tilde{w}_i^n = \Delta\tilde{w}_i^{En} + \Delta\tilde{w}_i^{Sn} \tag{3.34}$$

where $\Delta\tilde{w}_i^n$ and $\Delta\tilde{w}_i^{Sn}$ are the total and the irrecoverable sliding displacement increments, respectively. With the introduction of an implicit time-marching scheme as outlined before and by allowing sliding only parallel to the bedrock, Equation (3.33) can be rewritten as

$$\begin{Bmatrix} \Delta\tilde{\sigma}_1^n \\ \Delta\tilde{\sigma}_2^n \end{Bmatrix} = \begin{bmatrix} \tilde{k}_{11}^{*n} & 0 \\ 0 & \tilde{k}_{22} \end{bmatrix} \begin{Bmatrix} \Delta\tilde{w}_1^n - \tilde{v}_1^n \Delta t_n \\ \Delta\tilde{w}_2^n \end{Bmatrix} \tag{3.35.a}$$

with
$$\tilde{k}_{11}^{*n} = \tilde{k}_{11}/\left(1 + \Delta t_n \, \theta \, \tilde{k}_{11} \frac{\partial \tilde{v}_1^n}{\partial \tilde{\sigma}_1^n}\right) \tag{3.35.b}$$

where $\tilde{v}_1^n$ and $\tilde{\sigma}_1^n$ are the basal sliding velocity v_b and the basal shear stress τ_b, respectively, as in Equation (2.12). Note that the derivation of Equation (3.35.b) is similar to derivation of Equation (3.26.a) and is not repeated here. The incremental finite element equations for sliding are obtained by substituting Equation (3.35.a) into (3.30.b) and by expressing the displacement increments in terms of shape functions and nodal degrees of freedom as in Equations (3.31). Since the basal boundary is usually irregular, matrix transformations are required when formulating the local stiffness matrices and again when transforming back to the global coordinate system before assembling the global stiffness matrix.

If the deformation of the bedrock is negligible compared to that of the ice, the joint element formulation is not required and sliding can be introduced as a boundary condition similar to the procedure followed in Section 3.2.3. It should be pointed out here that the basal ice layer has been assumed to be incompressible. Thus the degrees of freedom normal to the bedrock are fixed at zero. The computed displacement increments, when substituted back into Equation (3.35.a), give the stress increments $\{\Delta\tilde{\sigma}_n\}$ and thus the updated stress state $\{\tilde{\sigma}_{n+1}\} = \{\tilde{\sigma}_n\} + \{\Delta\tilde{\sigma}_n\}$.

3.4 Transient Temperature Modelling

3.4.1 General

The assumption of isothermal ice masses in the past has been an over-simplification of rather complicated ice dynamic problems. To avoid this a finite element model for computing temperature variations due to thermal conduction and advection due to ice movement has been developed.

The time-dependent heat balance equation can be written directly in an integral form in the following manner [102].

$$\int_{\Omega} [\frac{\partial \delta T}{\partial x_i} K \frac{\partial T}{\partial x_i} + C_p \rho \, \delta T \frac{DT}{Dt}] d\Omega - \int_{\Omega} \delta T Q d\Omega + \int_{\Gamma_q} \delta T q d\Gamma = 0 \quad (3.36)$$

where T and δT are real and virtual temperatures within the region Ω, respectively; K is the conductivity; C_p the specific heat; ρ is the density; Q is the rate of heat generation; D/Dt is the Eulerian derivative $(\frac{\partial}{\partial t} + v_i \frac{\partial}{\partial x_i})$; q is the heat input per unit area on boundary Γ_q; and $\delta T = 0$ on Γ_T where T is specified. For a transient analysis the initial conditions must also be specified, i.e.

$$T(x_1, x_2, t = 0) = T_0(x_1, x_2). \quad (3.37)$$

3.4.2 Finite Element Model

Application of the finite element method to heat transfer analysis in solids is well established and is presented first. For this development the advective terms in the Eulerian derivative have been deleted. Temperature within the region of interest is given by;

$$T = N_i(x\ y)T_i(t) \qquad \text{or} \qquad T = [N]\ \{T'\} \tag{3.38}$$

where [N] contains the shape functions and $\{T'\}$ is the nodal temperature vector which is a function of time. The finite element equation for heat balance is obtained by substituting Equation (3.38) into (3.36) yielding

$$[\bar{C}_n]\ \{\frac{\partial T'}{\partial t}\} + [\bar{H}_n]\ \{T'\} + \{Q_n\} = \{0\} \tag{3.39.a}$$

where $[\bar{H}_n]$ is the heat conductance matrix, $[\bar{C}_n]$ is the heat capacitance matrix and $\{Q_n\}$ is the temperature load vector. These are given by

$$\bar{H}_{ij} = \int_\Omega K(N_{i,x}\ N_{j,x} + N_{i,y}\ N_{j,y})\ d\Omega \tag{3.39.b}$$

$$\bar{C}_{ij} = \int_\Omega C_p\rho\ N_i N_j\ d\Omega \tag{3.39.c}$$

$$Q_i = -\int_\Omega N_i Q d\Omega + \int_{\Gamma_q} N_i q d\Gamma. \tag{3.39.d}$$

The time integration of Equation (3.39.a) is carried out by approximating the time derivative using either the finite differences or the finite element approximations and carrying out time marching using a recursion scheme similar to that adopted in the creep model. The temperature in the second term of Equation (3.39.a) is replaced by,

$$\{T'\} = (1 - \theta)\ \{T'\}^{n} + \theta\{T'\}^{n+1} \tag{3.40}$$

where $\{T'\}^{n}$ is the temperature at time t_n, $\{T'\}^{n+1}$ is the temperature at time t_{n+1} and θ controls the degree of implicitness. The temperature at the end of the nth time increment is computed by solving the following equation:

$$\left([\bar{C}_n]/\Delta t_n + \theta[\bar{H}_n]\right)\{T'\}^{n+1} + \left(-[\bar{C}_n]/\Delta t_n + (1 - \theta)[\bar{H}_n]\right)\{T'\}^{n} + \{Q_n\} = \{0\} \tag{3.41}$$

where $\{Q_n\}$ is computed at time $t'_{n+\theta}$. Zienkiewicz and Parekh [100] have derived this equation through a more elaborate approach where the time domain is also discretized by the finite element approximations. For further details on time-marching procedures, their stability and their accuracy the reader is referred to Donea [21], Zlamal [104] and Zienkiewicz [103]. The Crank-Nicholson scheme ($\theta = 1/2$) has also been adopted for the transient thermal analysis as was done for the creep analysis.

3.4.3 Influence and Treatment of Heat Advection

Past experience with the finite element approximation of thermal advection indicates severe spatial oscillations of the solution when the advection terms dominate. The influence of advection in heat transfer analysis is characterized by the Peclét number which is defined as

$$P_e = \frac{v\ell}{\kappa} \tag{3.42}$$

where v is the entry velocity, ℓ is a typical dimension and κ is the thermal diffusivity $\frac{K}{(C_p\rho)}$. The spatial oscillations are due to different mathematical characteristics of the first and second order operators, i.e. $v_i \frac{\partial T}{\partial x_i}$ and $\nabla^2 T$, involved in the heat balance equation and the specified boundary conditions.

To suppress the undesirable oscillations, either the grid density must be increased where rapid temperature changes are expected or upwind finite elements should be used. The concept of upwind finite elements was introduced by Christie et al. [13] who applied this technique to one-dimensional problems. Heinrich et al. [34] extended the one-dimensional treatment to two-dimensional problems using quadrilateral finite elements. To avoid cumbersome integrations due to non-symmetric weighting functions, an alternative and much simpler way to incorporate upwinding was introduced by Hughes [47]. Hughes' approach to upwinding has been employed with some modifications for the triang-

ular elements and is used in this study.

The finite element approximation of the Eulerian derivative is obtained by using the Galerkin method in the following manner:

$$\int_{\Omega} C_p \rho \, [N]^T \frac{D[N]\{T'\}}{Dt} = \int_{\Omega} C_p \rho [N]^T \left([N] \frac{\partial \{T'\}}{\partial t} + v_i \frac{\partial [N]}{\partial x_i} \{T'\} \right) d\Omega \qquad (3.43)$$

Hughes proposed that an upwind scheme for a one-dimensional problem can be introduced by approximating the advective term using a special numerical integration technique, e.g. for a single point numerical integration

$$\int_{\Omega_e} [N]^T v_1 [N]_{,1} d\Omega = [N(\bar{\alpha})]^T v_1(O_e) [N(\bar{\alpha})]_{,1} J(O_e) W \qquad (3.44)$$

where O_e is the origin of the isoparametric coordinates in the eth element, J is the Jacobian determinant of the isoparametric transformation, W is a weight factor equal to 2 for a one-dimensional problem and $\bar{\alpha}$ is the coordinate which determines the degree of upwinding. The optimized value for $\bar{\alpha}$ is given by

$$\bar{\alpha} = \coth\left(\frac{Pe}{2}\right) - \frac{2}{Pe} . \qquad (3.45)$$

The value of $\bar{\alpha}$ ranges from -1.0 to 1.0 which corresponds to the limits of the isoparametric coordinate system on either side as shown in

Figure (3.5). For one-dimensional problems Hughes' approach reduces the finite element equations to those given by Christie et al. [13].

The degree of upwinding for a one-dimensional problem depends on the location of the upwind integration coordinate relative to the Gauss-Quadrature integration point. Following this reasoning, an upwind scheme for triangular elements is proposed. For numerical integration of a triangular element, three integration points (described by area coordinates) are used as shown in Figure (3.6). Upwinding is implemented in the following manner.

(1) Resolve the velocity into components along edge 1-2 and perpendicular to it (see Figure (3.6)).

(2) Compute $\bar{\alpha}$ in the direction perpendicular to edge 1-2.

(3) Determine $\bar{L}_3$ based on $\bar{L}_3 = \bar{\alpha} L_3^{max}$. L_3^{max} is the area coordinate L_3 where the velocity vector pierces one of the other edges as shown. If $\bar{\alpha} < 0$, then $\bar{L}_3 = 0$.

(4) Compute $\bar{\alpha}$ parallel to edge 1-2.

(5) Determine $\bar{L}_1$ and $\bar{L}_2$ based on $\bar{L}_2 = \frac{(1 - \bar{L}_3)}{2}(1 + \bar{\alpha})$ and $\bar{L}_1 = 1 - \bar{L}_2 - \bar{L}_3$.

(6) Repeat steps (1) through (5) for the other two integration points.

(7) Complete numerical integration as follows:

$$\sum_{i=1}^{3} [N(\bar{L}_i)]^T \left(v_1 (O_e)_i [N(\bar{L}_i)]_{,1} + v_2 (O_e)_i [N(\bar{L}_i)]_{,2} \right) J(O_e)_i W_i . \qquad (3.46)$$

This upwind scheme was tested on problems for which solutions are available in the literature. It can be observed that this approach suppresses the spatial oscillations as illustrated through an example in Figure (3.7). The efficiency of the upwinding scheme may also depend on the grid arrangement.

3.5 Summary

The analytical and finite element models developed for analyses of large ice masses have been presented. All models developed in this study have been tested by comparing the computer solutions obtained from analytical solutions for problems where closed form solutions are available. Excellent agreements were achieved between solutions from the models developed herein and those available in the literature.

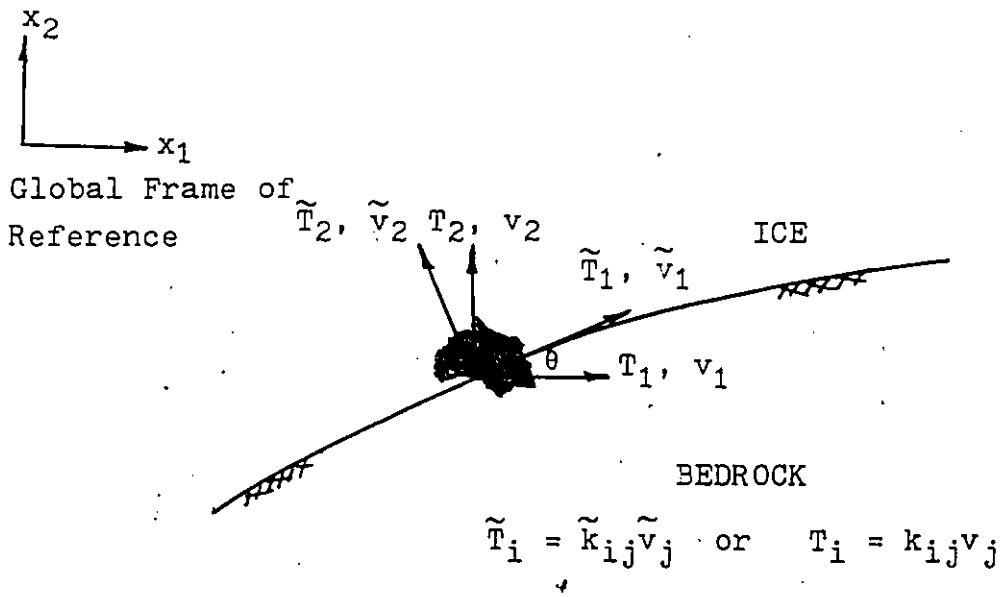

FIGURE 3.1 SLIDING BOUNDARY FOR MODELS A AND B.

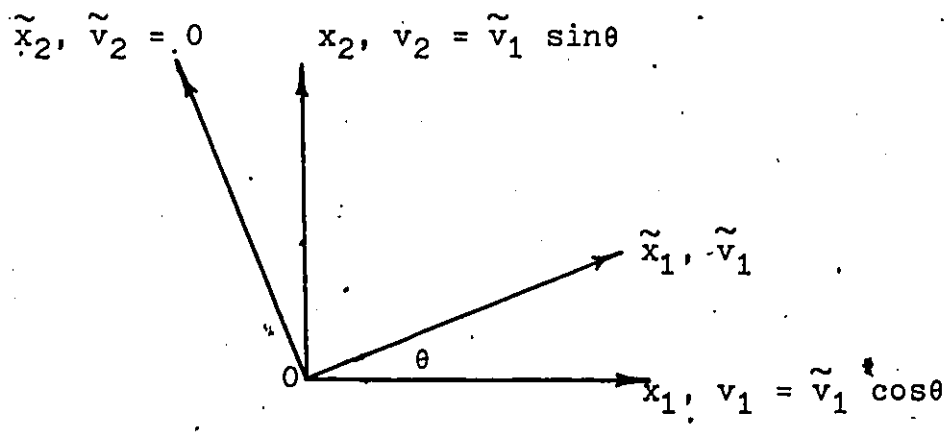

FIGURE 3.2 VELOCITY TRANSFORMATIONS AT SLIDING BOUNDARY.

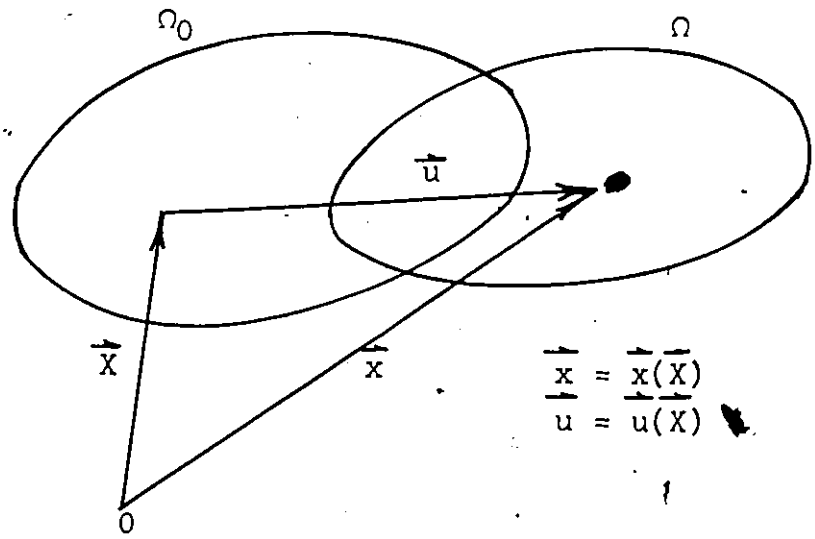

FIGURE 3.3 LAGRANGIAN DESCRIPTION: All material positions are defined with respect to position vectors $\{\vec{X}_1, \vec{X}_2, \ldots \vec{X}_n\}$.

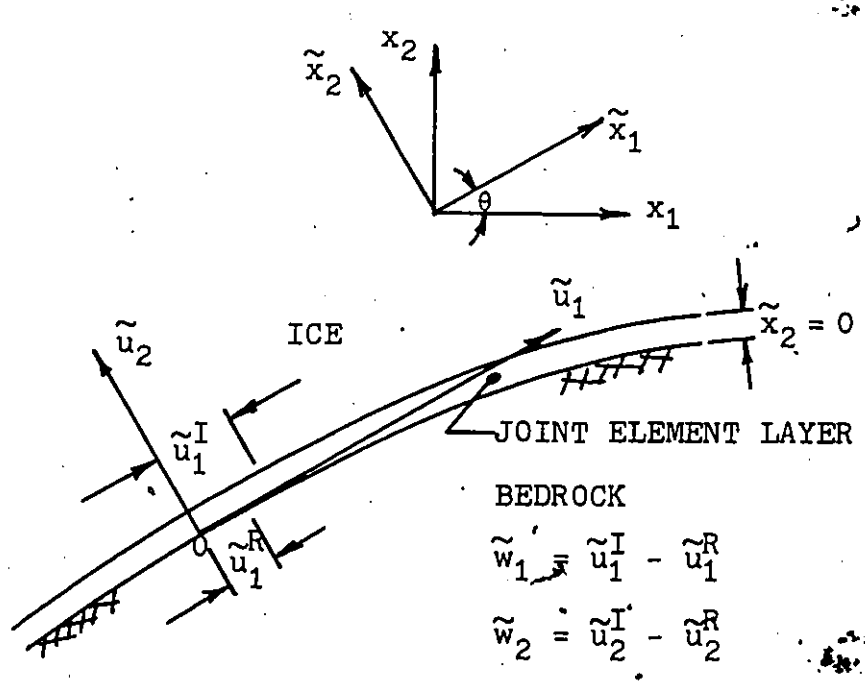

FIGURE 3.4 SLIDING BOUNDARY FOR DISPLACEMENT FORMULATION .

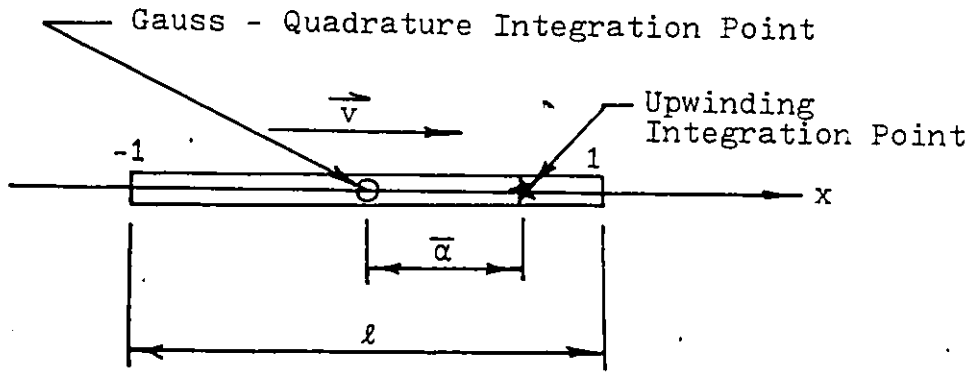

FIGURE 3.5 UPWINDING WITH NUMERICAL INTEGRATION.

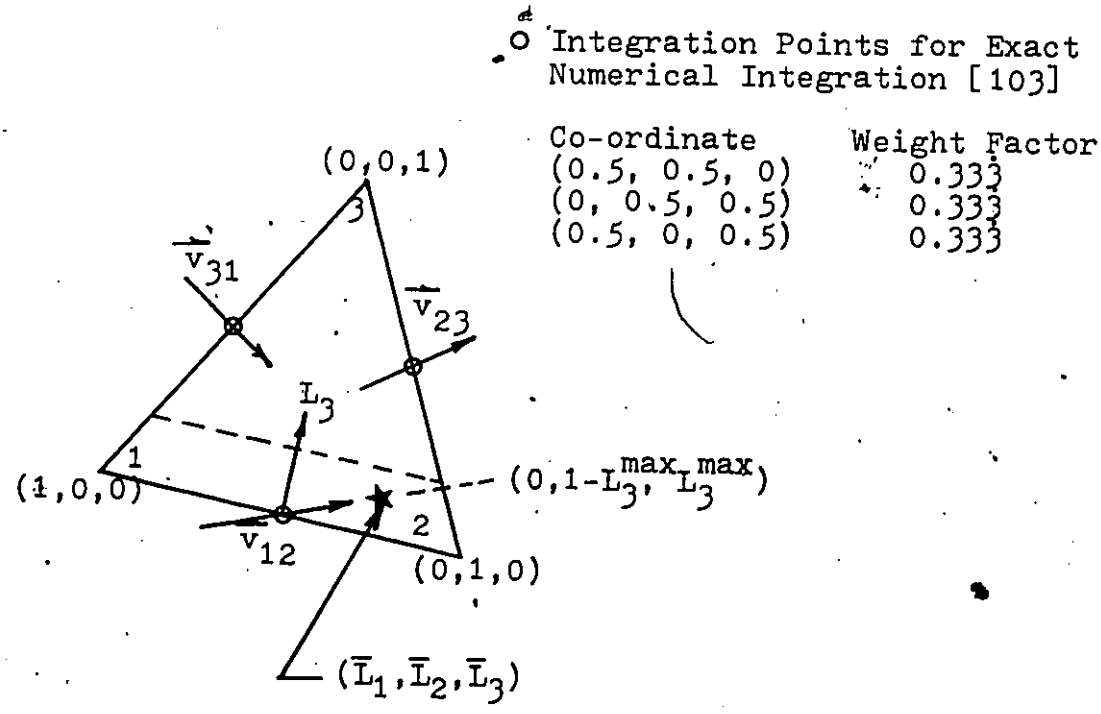

FIGURE 3.6 ILLUSTRATION OF UPWINDING SCHEME FOR TRIANGULAR ELEMENT.

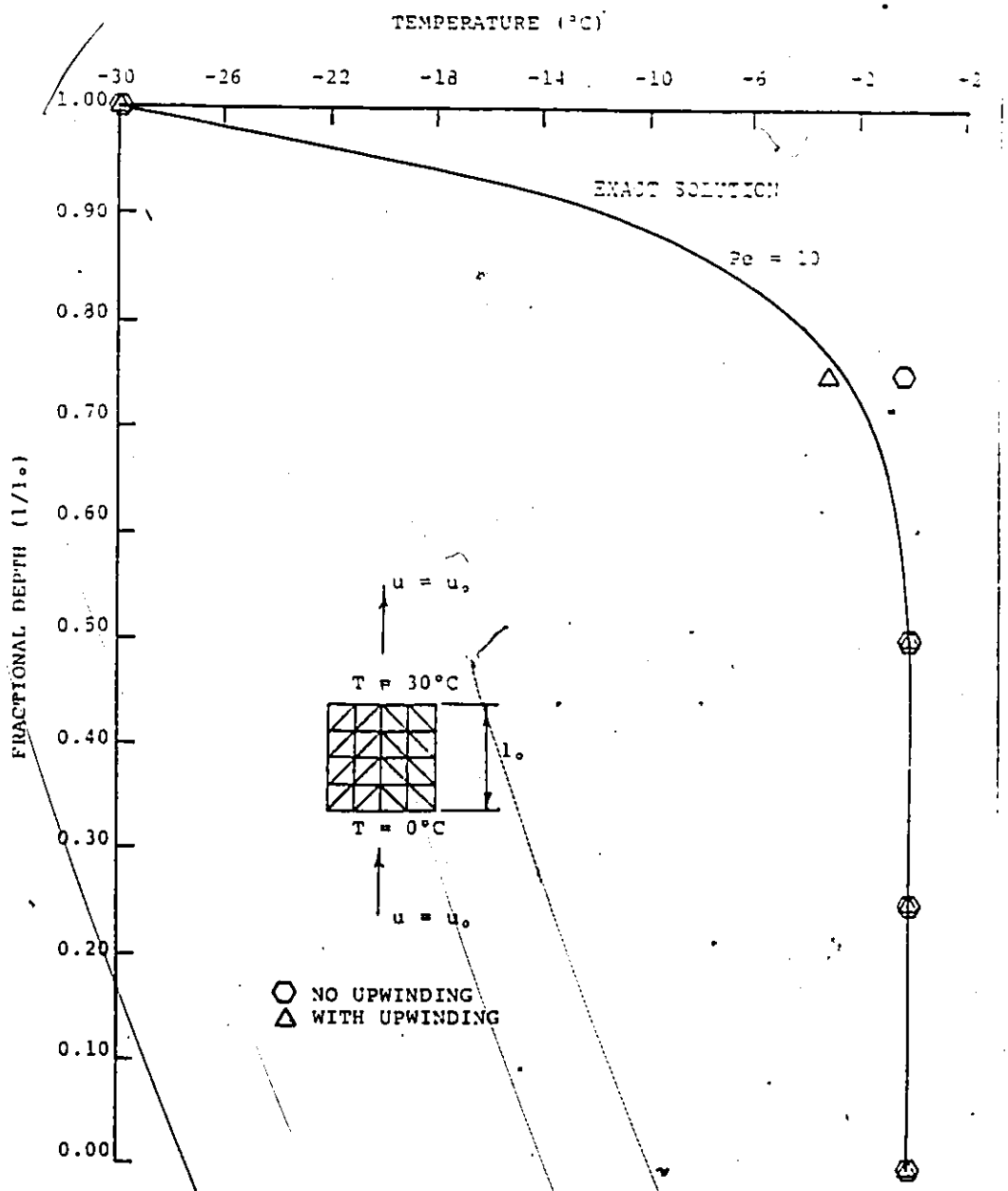

FIGURE 3.7 INFLUENCE OF UPWINDING ON A SIMPLE ONE-DIMENSIONAL PROBLEM FOR PECLET NUMBER, Pe = 10.

CHAPTER 4

APPLICATIONS OF FINITE ELEMENT MODELS TO DOUBLE SLOPE ICE MASS

4.1 Introduction

The finite element models presented in the previous chapter are used to study the creep behaviour of an idealized, double-slope ice mass. Both steady-state and transient analyses are considered. Although the computer programs can be modified to handle any complex material properties, it is assumed that the material properties are homogeneous and isotropic. Furthermore, the ice mass is assumed to remain intact, i.e. no geometric discontinuities occur due to cracking. The possibilities of tensile failure and subsequent crack propogation in ice bodies have been studied by Nguyen [70] and Chan [12]. In cases where a possible yielding can occur within an ice mass, an elasto-plastic response is incorporated as an option into the large displacement finite element model (Model C).

4.2 Double Slope Example

Before simulating responses of natural ice masses, the limitations of the models were investigated by studying a simple double slope ice problem. This problem, shown in Figure 4.1, demonstrates the relative performances of these models within the framework of the finite element approximations. Influences of flow parameters, sliding, initial

stress state and compressibility on the flow field are examined. At the end of this chapter a surge model based on basal instability is also presented for the double slope ice mass. This model relates basal sliding resistance to energy dissipated through sliding, which is similar to an approach advanced by Budd [9].

Constant stress triangular elements (CST's) are used for the transient creep model (Model C) and linear stress triangular elements (LST's) for the steady-state behaviour of large ice masses (Models A and B) with incompressibility constraints. The decision to use the constant stress triangular elements (CST's) was based on the fact that the ice properties to be used can have reasonably large errors in their estimations thus undermining the accuracies of high performance elements. A higher order element is required for Models A and B due to the incompressible and near incompressible formulations, respectively. Since incompressibility is introduced through the constitutive relationship in Model B, a very large bulk modulus is obtained by allowing Poisson's ratio to approach half. In this study a Poisson's ratio of 0.49995 has been found to perform the best.

4.2.1 Elastic Solution

A direct comparison of velocities and stresses as predicted by the various models is difficult unless the transient response approaches a near steady-state condition while the displacements remain small enough to not alter the geometry. All programs were developed so as to allow for a linear elastic solution as an option. Since the finite

element applications to elasticity problems are well understood, the comparison of the elastic responses predicted by the LST and the CST elements serves to give an indication of the closest agreement that one should expect of these models for the double slope example. The same number of nodes and grid patterns were used for both programs, only the number of elements was changed; i.e. 4 CST elements for one LST element. The elastic analyses were completed by allowing no movement at the ice-bed interface and by forcing the horizontal displacements to be zero at the upstream boundary as shown in Figure 4.1. The material properties used for elastic and creep analyses are presented in Table 4.1.

A comparison of strain energies, computed by each model, indicates that the LST element predicted a higher strain energy as expected. It is well known that the strain energy of the exact solution represents an upper bound. The computed displacement and stress profiles at the knee of the double slope are shown in Figures 4.2(a) and (b), respectively. These profiles demonstrate that a close agreement exists between solutions from both programs. The smaller displacements predicted by the CST program are in accordance with the lower strain energy.

Since the stresses vary linearly over the LST element, a continuous curve can be fitted through the averaged nodal values quite appropriately. For the CST elements, the stresses are assumed to correspond to values at the centroids of the elements adjacent to the x = 200 m section. The vertical stress variation can often be approximated by

TABLE 4.1 CONSTITUTIVE PROPERTIES OF ICE FOR DOUBLE SLOPE PROBLEM

Unit Weight for Ice:	$\gamma = 8.952\ kN/m^3$
Elastic Properties:	Elastic Modulus $E = 9.075 \times 10^6$ kPa
	Poisson Ratio $\nu = 0.34$
Flow Laws:	
Hooke's Parameters:	$\dot{\varepsilon}_e^c = 0.0327\ \sigma_e^{1.65}$
Linear Law:	$\dot{\varepsilon}_e^c = 0.01\ \sigma_e$
Nye's Parameters:	$\dot{\varepsilon}_e^c = 0.0374\ \sigma_e^{3.07}$
Basal Sliding Law:	$\tilde{T}_1 = 10.0\ \tilde{v}_1$
Basal Sliding Law for Instability:	$\tilde{T}_1 = f(\tilde{v}_1)\tilde{v}_1$ - The function $f(\tilde{v}_1)$ allows for a reduction in shear resistance with time.
Units:	$\dot{\varepsilon}_e^c(yr^{-1})$; $\tilde{T}_1$(kPa); σ_e(bars, 1 bar = 0.1 MPa); $\tilde{v}_1(m \cdot yr^{-1})$

Note: Hooke's parameters are adopted in the power creep law for sliding and basal instability simulations.

$$\sigma_{22} = \rho g\, x_2 \cos \alpha; \qquad \alpha_1 < \alpha < \alpha_2 \tag{4.1}$$

where α_1 and α_2 are the upper and lower surface slope angles, respectively. This equation appears to be consistent with the stress variations produced from the computer generated results. Since α_1 and α_2 are relatively small, Equation (4.1) represents the vertical stress due to the overburden ice. Good agreement is also obtained between the stresses computed using the CST and LST programs.

4.2.2 Creep Response without Basal Sliding

In order to solve the time-dependent boundary value problems both boundary conditions and initial conditions are required. Often the boundary conditions are known as part of the problem statement. The initial conditions in terms of insitu stresses for large ice masses are generally not known and have to be assumed or approximated. One way of overcoming this difficulty in ice dynamics has been to assume a non-Newtonian fluid rheology for ice in which creep history is not important. Of course, this would be the case of steady-state creep. In previous transient finite element simulations of large ice masses it has been assumed that the influence of initial stresses is minor due to the relatively high flow rates of ice. In order to investigate the sensitivity of stress history due to creep on deformations of large ice masses, hypothetical initial conditions are generated and creep simulations are carried out. The initial conditions are determined by first computing the elastic state of stress and then redefining the lateral stress σ_{11} as

$$\sigma_{11} = k_0 \sigma_{22} \tag{4.2}$$

where k_0 is a constant relating the vertical stress to the horizontal stress.

Figures 4.3(a) and (b) clearly indicate that for different initial stress conditions the same nearly steady-state creep flow is attained in a relatively short period of time. While the influence of initial stress does not appear to be important for long term analysis under gravity loading, the influence of creep history can enter through the constitutive relationships of ice which depend on ice fabric, texture and grain size. Since a finite time length is required to reach steady flow, the influence of stress history may be important for ice shelves which undergo cyclic loading and never reach a steady flow situation.

The time to reach steady flow is different for the various flow laws that have been used, as shown in Figures 4.4(a) and (b). For all simulations the horizontal velocity at node 25 and the equivalent stress in element 19 reach steady conditions at different times. This observation suggests that the entire ice mass does not reach near steady-state conditions at the same time.

Unlike the horizontal velocities the vertical velocities do not reach steady-state as shown in Figure 4.5. The vertical velocities predicted by Model C become superfluously small. A comparison of the

vertical velocity variations from each of the models, shown in Figure 4.6, indicates that the steady-state vertical velocities from Models A and B are much larger than those predictd by the transient Model C. The smaller velocities predicted by Model C are attributed to the lack of sensitivity of the CST elements [103] when incompressibility due to dominant creep strains becomes important. Due to this insensitivity less longitudinal straining is observed for the transient model resulting in smaller horizontal and vertical velocities.

As creep proceeds, starting from an elastic stress state where

$$\sigma_{33} = \nu(\sigma_{11} + \sigma_{22}), \tag{4.3}$$

the out of plane stress σ_{33}, near steady-state, approaches average of the other two;

$$\sigma_{33} \approx \frac{1}{2}(\sigma_{11} + \sigma_{22}). \tag{4.4}$$

For a stress field where σ_{33} is approximated by Equation (4.4), only the in plane deformations occur and

$$\Delta\varepsilon_{33}^{E} = -\Delta\varepsilon_{33}^{C} = \Delta\varepsilon_{11}^{C} + \Delta\varepsilon_{22}^{C} \approx 0. \tag{4.5}$$

The velocity field which is dominated by changes in creep strains can be artificially constrained, as indicated by Equation (4.5), when using the CST elements. The period of time for this constraint to develop depends

on the rate of creep straining. For ice, this period is of the order 10^2 to 10^4 minutes whereas for rocks, this period is much longer.

The question arises as to how this constraint develops for the double slope ice mass. Consider the elements at the base of the ice mass where the slope breaks as shown in Figure 4.7. In order to maintain constant volume for elements 17 and 25 when the creep strains dominate, nodes 22 and 27 must move parallel to the bed as shown in the figure. Since element 26 must also satisfy incompressibility, an additional constraint is imposed on the velocities at nodes 22 and 27. Such constraints, originating at the base, propagate through the ice mass resulting in a negligible vertical velocity at node 25. The horizontal velocities at the surface are due to shear strains which are not affected by the incompressibility. This additional constraint does not develop when higher order elements are used.

For ice bodies, in which either shear dominates or sliding at the ice-bed interface is important, the additional constraint should not develop. Although care must be taken when selecting a finite element mesh for creep analyses to ensure that any potential overconstraining modes are eliminated [2]. While the differences in the computed velocities from Models A and C are primarily due to the overconstraint developed at the lower boundary, a comparison of the steady-state velocities given by Models A and B suggests that part of the difference may be attributed to the compressibility, no matter how small, in the flow field for Model C due to the elastic action. The influence of compressibility is discussed in the next section.

The transient response of the stress state in element 19 for the different flow parameters is shown in Figure 4.8. This figure shows clearly that the normal stresses for all simulations begin to diverge at the onset of incompressibility due to dominant creep strains. Since both the shear and equivalent stresses remain relatively steady, the divergence of the normal stresses is believed to be due to divergence of the mean normal stress given by

$$\sigma_m = \frac{1}{3}\sigma_{ii} = \frac{E}{3(1-2\nu)}\varepsilon_{ii}^{E} \qquad (4.6.a)$$

or in the incremental form by

$$\Delta\sigma_m = \frac{E}{3(1-2\nu)}\Delta\varepsilon_{ii}^{E}. \qquad (4.6.b)$$

When the creep strains dominate, the volumetric elastic strain increment is expected to become negligible if the geometry of the problem does not change. Since the mean normal stress is independent of creep strains, its value should remain constant. Several computer simulations have been completed using the small deflection theory where an updating of geometry is not allowed. These analyses allowed determination of the steady-state creep flow conditions through successive approximations starting from an elastic stress state. It has been found that unless a problem is statically determinate, the mean normal stress diverges. This suggests that the divergence is mainly due to the artificial constraint just discussed and partially due to numerical round-off errors

when computing $\Delta\varepsilon_{ii}^{E}$. Of course, for statically determinate problems the stresses can be computed independent of the strain field. Although drawbacks exist for computation of the mean normal stress, a solution of the displacement (or velocity) field is not influenced since creep is not influenced by the mean normal stress. One should be able to approximate the mean normal stress field by satisfying the following equation

$$\nabla^2\sigma_m = 0 \qquad (4.7)$$

The stress profiles predicted by Model A at the knee of the double slope for a linear creep law are shown in Figure 4.2(b). While the vertical stresses do not change by much, the horizontal stresses do change substantially when compared with the elastic stresses.

4.2.3 Creep Response with Basal Sliding

In the previous simulations, a comparison of the velocities and stresses predicted by the various creep models was difficult due to the incompressibility constraint which develops in the transient model when creep strains become dominant. This constraint was eliminated for the following simulations by allowing basal sliding. The simulations were completed by using Hooke's parameters in the power creep law and a linear sliding law. The constant in the sliding law was chosen to allow for an appropriate sliding velocity of the same magnitude as those velocities caused by the internal creep strain rates.

It has been indicated that changes in the creep flow field are observed when incompressibility is approximated as done for Models B and C. The influence of near compressibility (as opposed to full incompressibility, Model A) is not noticeable when sliding is allowed at the ice-bed interface as shown in Figures 4.9(a) and (b). Figure 4.9(a) shows that the computed velocities by Models A and B at the knee of the double slope are essentially the same. The slightly lower velocities predicted by Model C are attributed to the use of CST elements for this model. The variations in basal shear stress shown in Figure 4.9(b) indicate that the general sliding behaviour, as predicted by Models A, B and C, is also similar. While good agreement of the computed velocities is achieved for this relatively simple double slope ice mass, the analysis of a more difficult problem (presented in Appendix A5) in which the basal boundary is quite complex indicates that compressibility of the velocity field may be important. In this more complex example it is shown that the agreement of computed velocities by the various models is very sensitive to the specification of the basal boundary.

The transient responses from Model C, shown in Figures 4.10(a), (b) and (c), again demonstrate that steady flow conditions are attained in a relatively short period of time. The important observation from these figures is that the vertical velocities also become relatively steady unlike for the case of no basal sliding. Both the horizontal and the vertical velocities approach values close to that predicted by Models A and B. A comparison of the equivalent stress σ_e and the shear

stress σ_{12} clearly indicates that the longitudinal straining dominates in this example. The normal stress variations are not shown since they diverge after onset of incompressibility as explained before for the case of no basal sliding.

Figure 4.11 illustrates the change in geometry of the double slope example over a period of thirteen years. The gross deformations are modelled by the constant updating of geometry. It should be noted that the displacements at the base are parallel to the local bedrock which helps illustrate the ability of the transient model to accomodate irregular bedrock geometry.

4.3 Large Ice Mass Instability

Previous investigations on surging of large ice masses suggest that basal instability appears to be the main mechanism by which a surge propagates. Clarke [14] indicated that the temperature variation influences the time of surge for a cold glacier rather than it being the essential mechanism for surge initiation and propagation. The transient finite element model (Model C) developed in Chapter 3 is extended to allow for basal sliding instability. The change in temperature during a surge and plastic yielding can also be accounted for in Model C. The influence of mass balance is not incorporated into this model, and the surge analyses are completed by starting from assumed presurge profiles. In this section only the basal instability is studied. The change in temperature profile for an ice mass during a surge and the possibility of mechanical instability are discussed in Chapter 5.

The sliding element introduced in Chapter 3 incorporates a sliding law that relates basal shear stress to the sliding velocity by,

$$\tilde{T}_1 = \tilde{k}_{11} \tilde{v}_1 \tag{4.8}$$

where $\tilde{k}_{11}$ is the sliding stiffness. To implement basal instability, it is assumed that a loss in sliding resistance is due to buildup of a sufficiently thick water layer due to the excess energy dissipation at the ice-bed interface. Since the interface may consist of a debris layer, it may mobilize if sufficient ice at the sole melts and if the layer becomes saturated. An important consideration, which can reduce the shear resistance of a debris layer, is the buildup of a sufficient water pressure head.

The bed or ice-bed interface of ice masses would likely have some permeability [57] so that a certain critical amount of energy must be dissipated to melt enough water to ensure that more water is produced locally than can run off. This excess water leads to the buildup of a water layer under the ice mass. Since the hydraulics at the ice-bed interface is not well understood, it is assumed that the runoff does not alter the sliding resistance. Only the water produced at the ice-bed interface is considered for reduction in sliding resistance.

To account for reduction in the basal shear resistance, it is suggested that the sliding parameter in Equation (4.8) be defined by:

$$\tilde{k}_{11} = k' + k^*/(1 + \langle \sum_i \phi_i (\tilde{T}_1 \tilde{v}_1 - q_0)_+ \Delta t_i \rangle) \qquad (4.9)$$

where k^* is the initial shear resistance when no water has collected at the base; $\tilde{T}_1 \tilde{v}_1$ is the local energy dissipation rate per unit area; q_0 is the threshold energy dissipation rate per unit area which also accounts for the basal permeability; k' is a lower limit on the sliding parameter; Δt_i is the time increment during the ith creep iteration; and ϕ_i is a lubrication factor.

Equation (4.9) is a modified form of shear resistance reduction proposed by Budd [9]. In this study the influence of shear resistance reduction is introduced through a constitutive relationship rather than directly to the stresses as was done by Budd. It is implied that the summation within the brackets < > cannot be less than zero. The lubrication and threshold energy dissipation parameters, both influence the surge timing. These parameters can change with position under the ice mass and with time due to changes at the ice-bed interface as a surge propagates. For the examples studied herein, q_0 is assumed to be zero, i.e. all computer simulations are started with near ripe conditions for a surge in order to economize on computational costs incurred. The lubrication factor was estimated to be approximately

$$\phi_0 = 1.27 \times 10^{-6} \left(\frac{m^2}{kN} \cdot \frac{yr}{m} \cdot \frac{1}{min}\right) \qquad (4.10)$$

for a surge propagation lasting between one and two years. A minimum value for the sliding parameter was chosen to be 0.01 kN/(m•yr). It should be emphasized that if a more realistic sliding model is available for surging, it can be incorporated into the finite element algorithm. The shear model adopted in this study is chosen for its simplicity.

The double slope example is used to illustrate the influence of lubrication factor on the timing of the surge propagation for this particular ice mass. All lubrication factors are expressed as fractions of the value given in Equation (4.10). Figures 4.12(a) and (b) show the changes in horizontal velocity at node 25 and in stress within element 19 as the surge propagates. Unlike the previous examples, the horizontal velocity, shear stress and equivalent stress do not reach steady-state values. Instead, the velocity and equivalent stress increase due to a reduction in the shear resistance at the ice-bed interface. Shorter times for increases in the velocity and equivalent stress are observed as the lubrication factor is increased. The time lag between the velocity increase and the equivalent stress increase demonstrates that different parts of the ice mass respond to a reduction in basal shear stress at different times. A decrease in shear stress while the equivalent stress increases indicates that the surge propagation is due to increased longitudinal straining as anticipated.

4.4 Summary

The scope and limitations of the three creep flow models have been demonstrated through applications to the double slope ice mass. It

is shown that by avoiding the undesireable numerical difficulties (e.g. for Model C) all models demonstrate close agreement among the computed solutions. Due to the relatively simple geometry and boundary conditions of the double slope problem, influences of compressibility on the creep flow field are not apparent when using Models A, B, and C. Basal sliding instability has been incorporated into Model C and has been applied to study surging of the double slope ice mass. The sliding parameter has been so defined that the time for surging can be controlled.

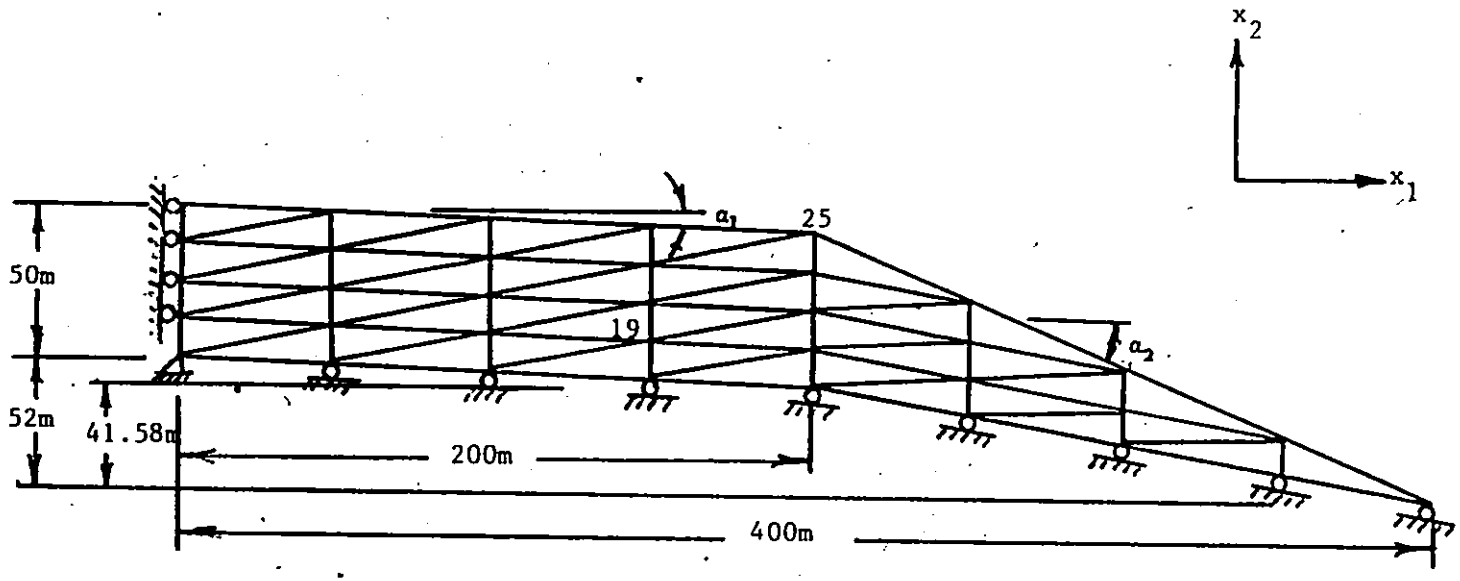

FIGURE 4.1 DOUBLE SLOPE PROBLEM - Finite element grid for CST element and non-variable boundary conditions.

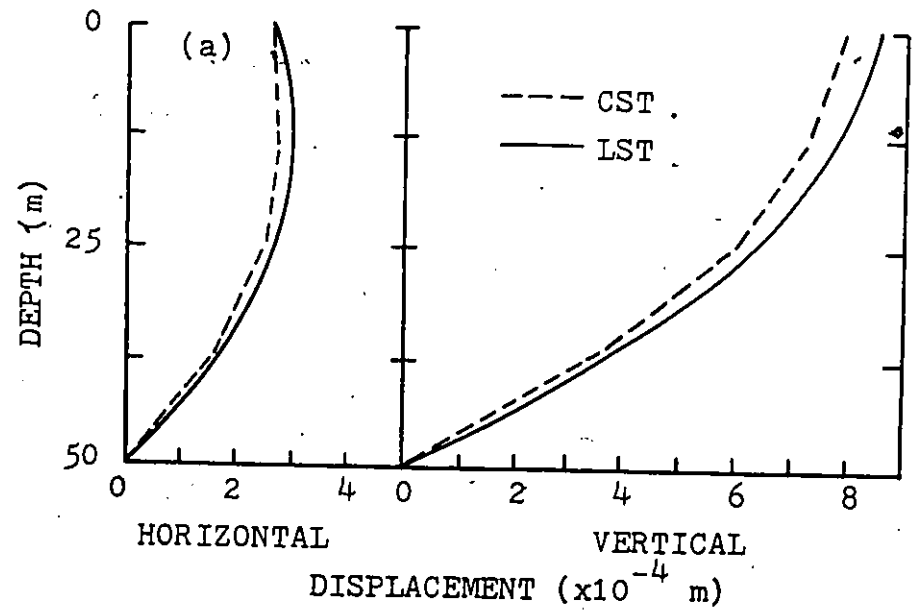

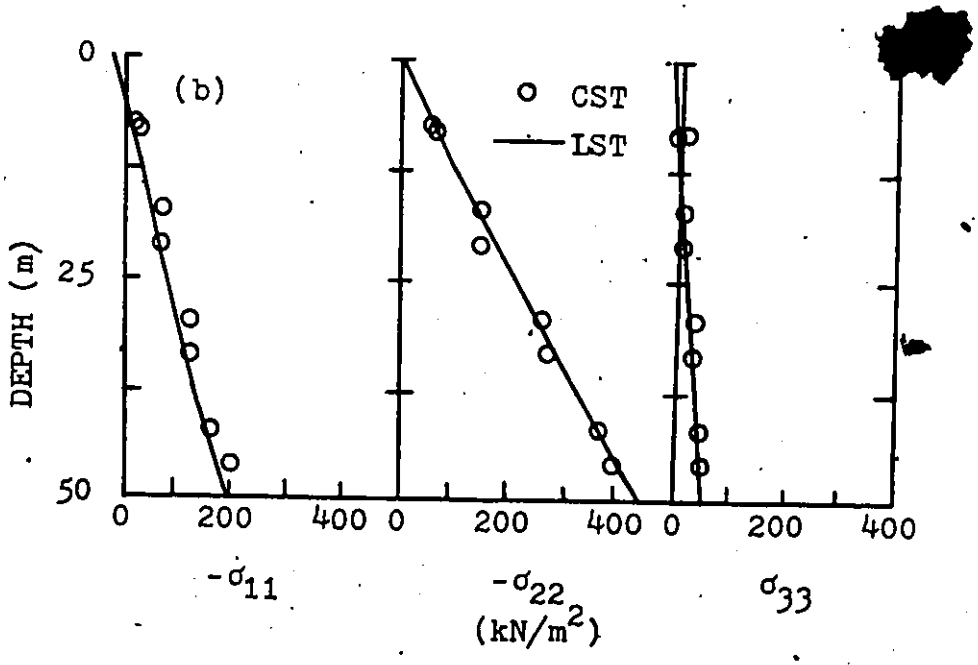

FIGURE 4.2 DOUBLE SLOPE PROBLEM - (a) Elastic Displacements and (b) Stresses at x_1 = 200 m.

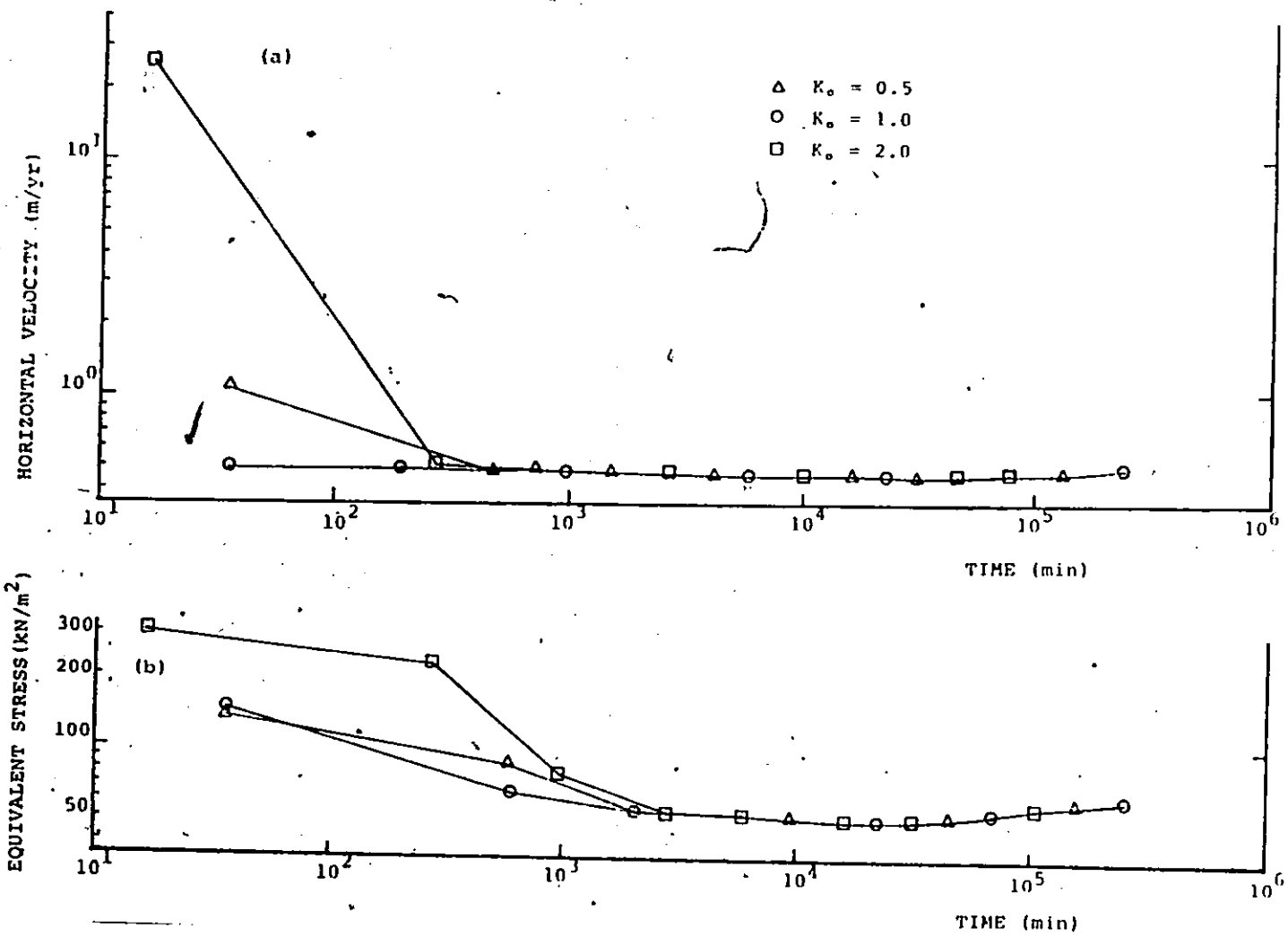

FIGURE 4.3 DOUBLE SLOPE PROBLEM - Influence of initial state of stress on: (a) Horizontal surface velocity at node 25, and (b) Equivalent stress in element 19, when using a linear creep law (Model C).

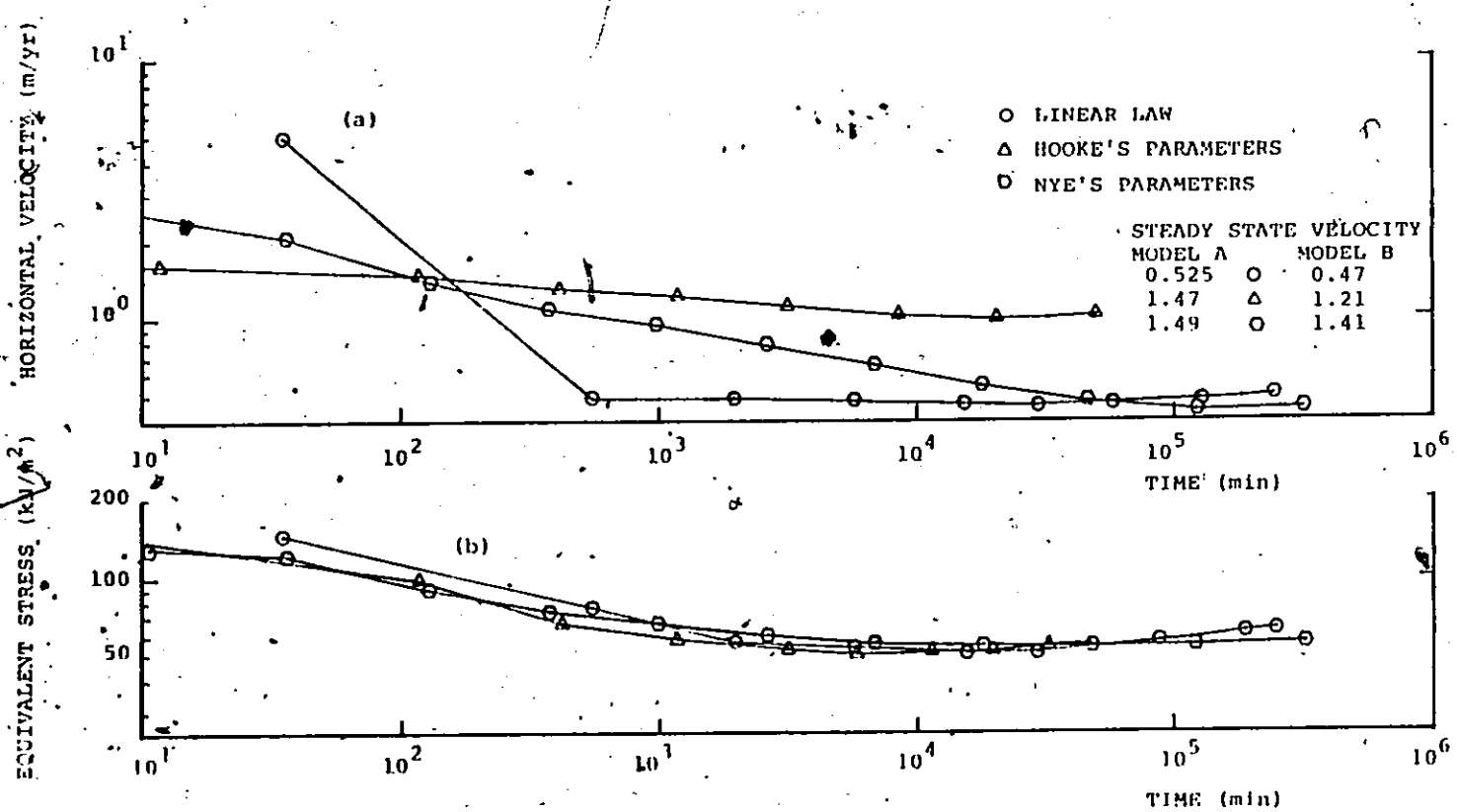

FIGURE 4.4 DOUBLE SLOPE PROBLEM - Influence of creep law on:
(a) Horizontal surface velocity at node 25, and
(b) Equivalent stress in element 19 (Model C).

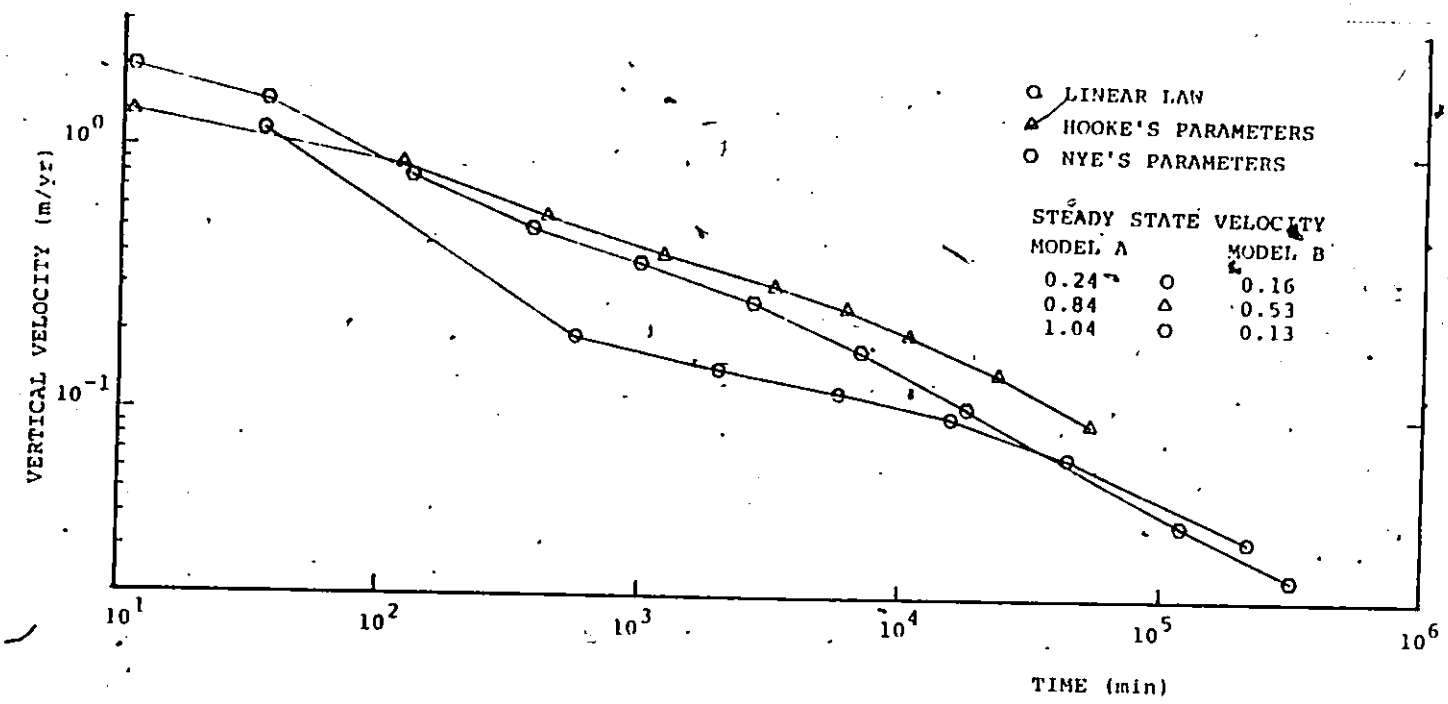

FIGURE 4.5 DOUBLE SLOPE PROBLEM - Influence of creep law on vertical surface velocity at node 25 (Model C).

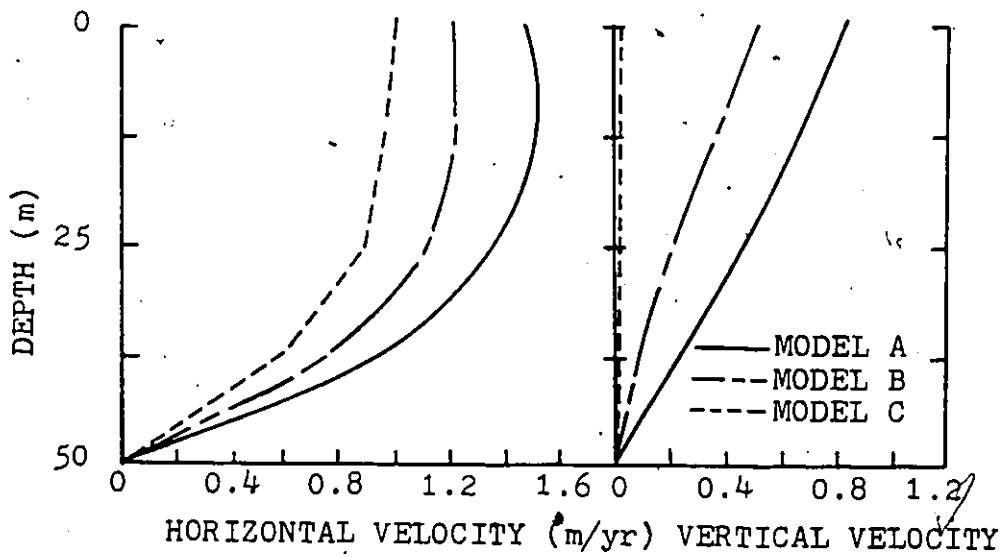

FIGURE 4.6 DOUBLE SLOPE PROBLEM - Velocity profiles, using Hooke's parameters, at x_1 = 200 m .

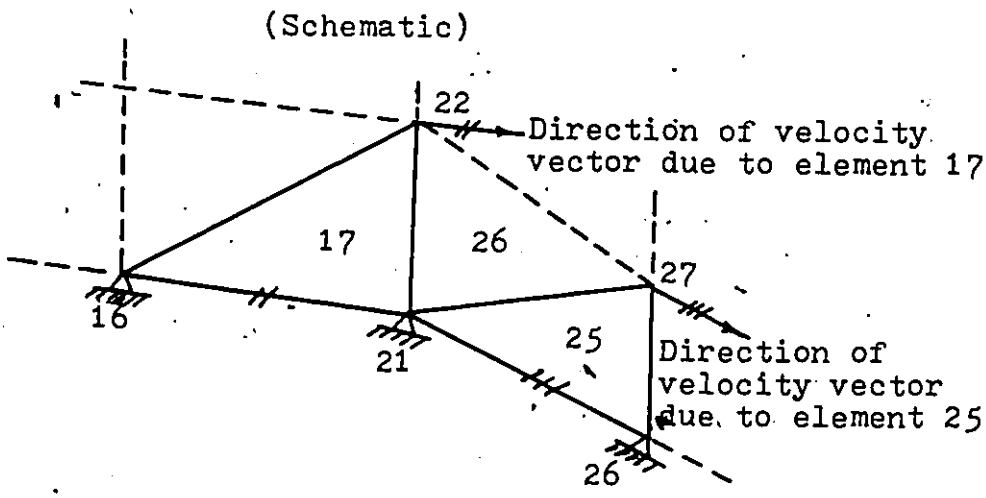

FIGURE 4.7 DOUBLE SLOPE PROBLEM - Direction of constrained velocities at the basal boundary. (Model C)

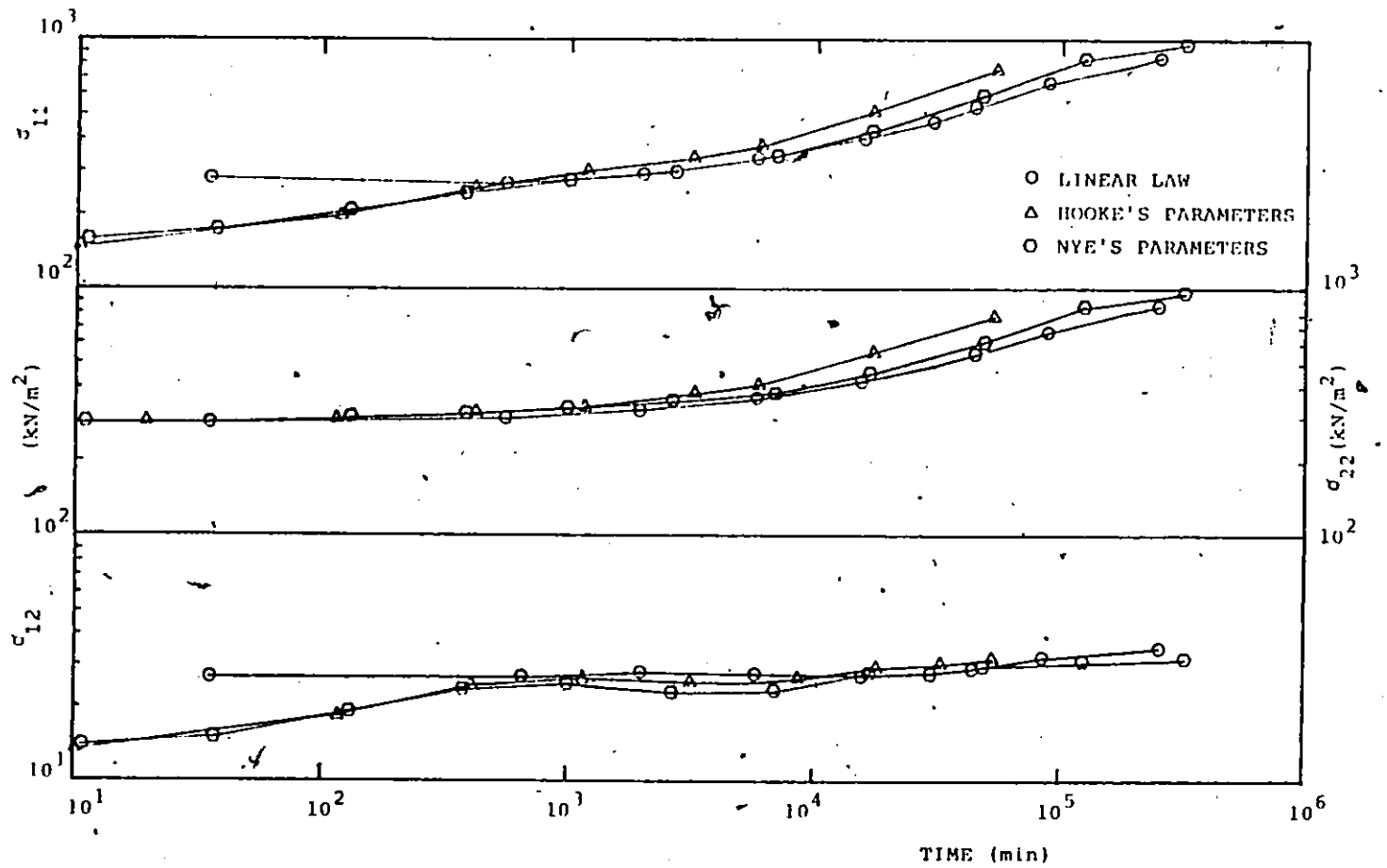

FIGURE 4.8 DOUBLE SLOPE PROBLEM - Stresses in element ~~19~~ with respect to time (Model C).

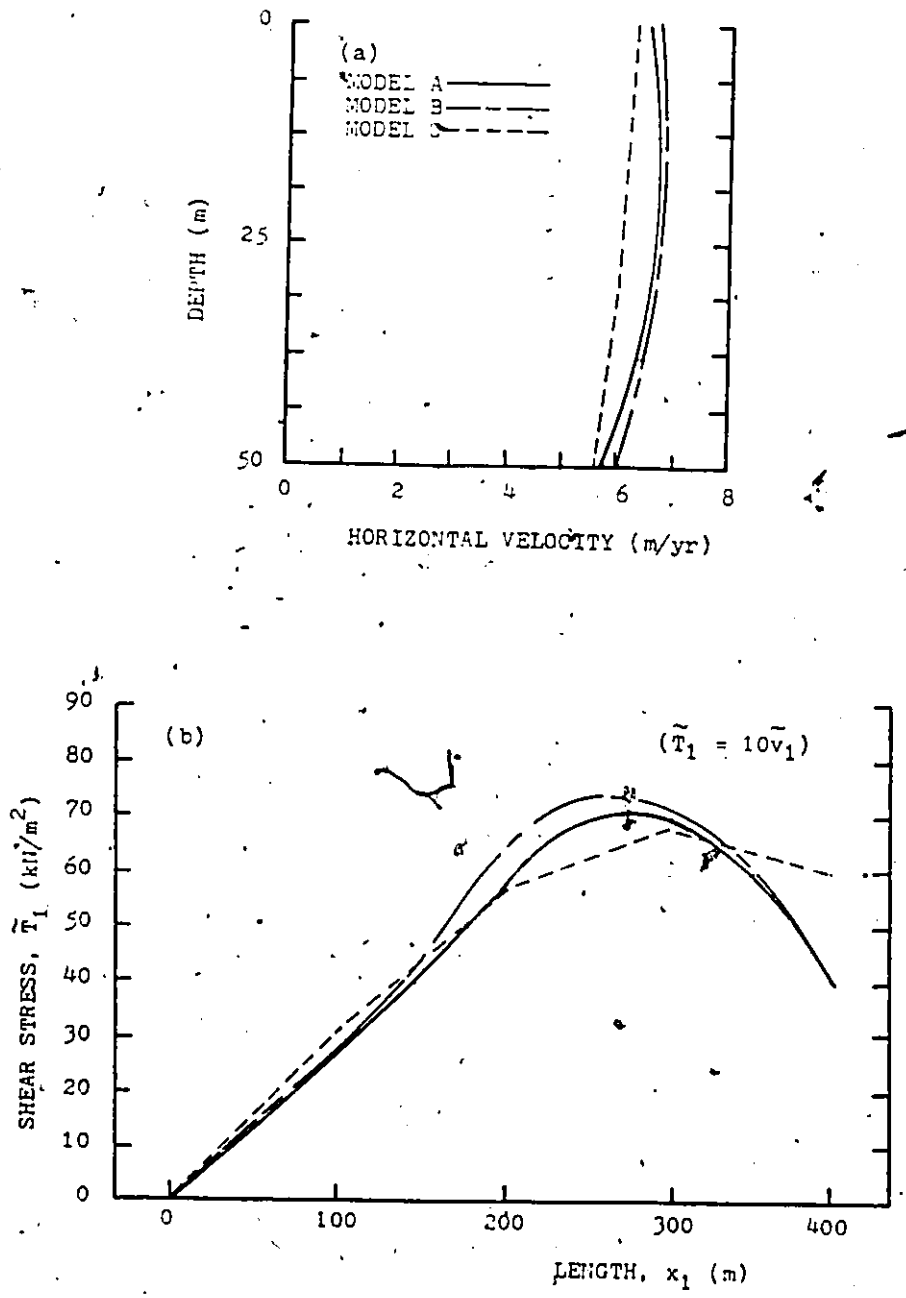

FIGURE 4.9 DOUBLE SLOPE PROBLEM: (a) Horizontal velocity profiles at x_1 = 200 m, and (b) Shear stresses at basal boundary, when sliding is allowed.

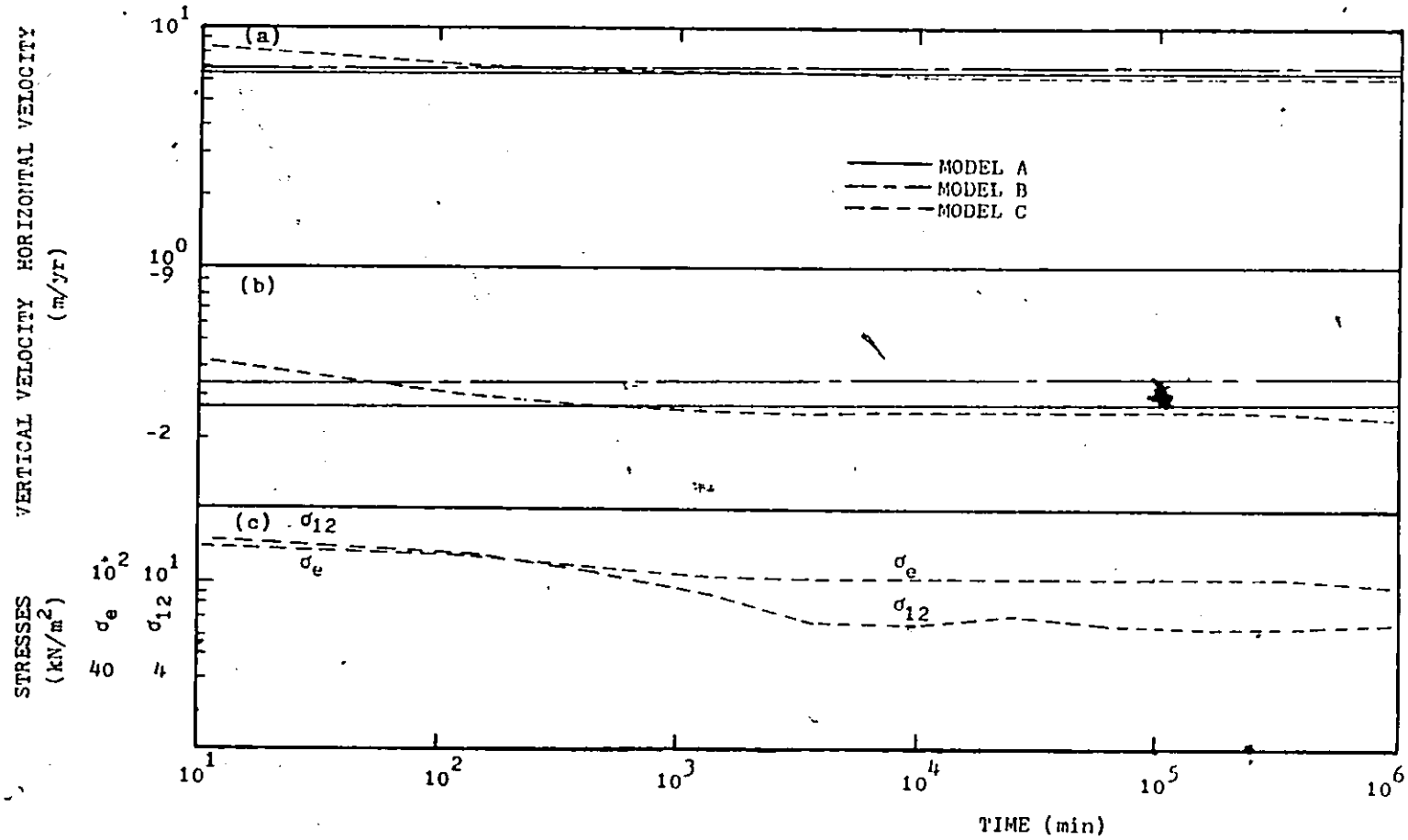

FIGURE 4.10 DOUBLE SLOPE PROBLEM: (a) Horizontal surface velocity and (b) Vertical surface velocity at node 25, and (c) Stresses in element 19, when sliding is allowed at the basal boundary.

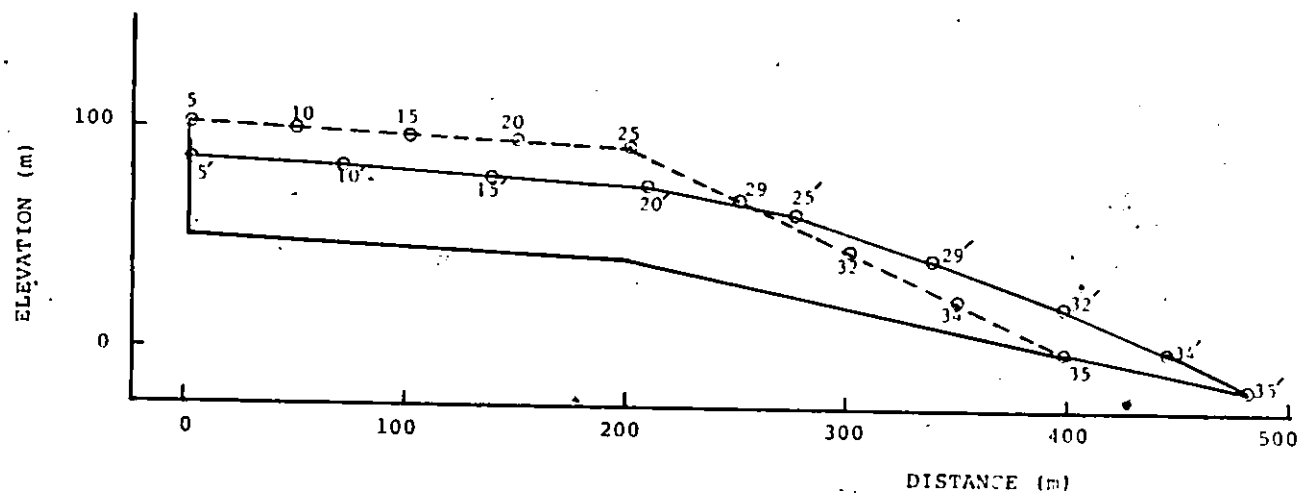

FIGURE 4.11 DOUBLE SLOPE PROBLEM - Profile after creeping 7×10^6 min.

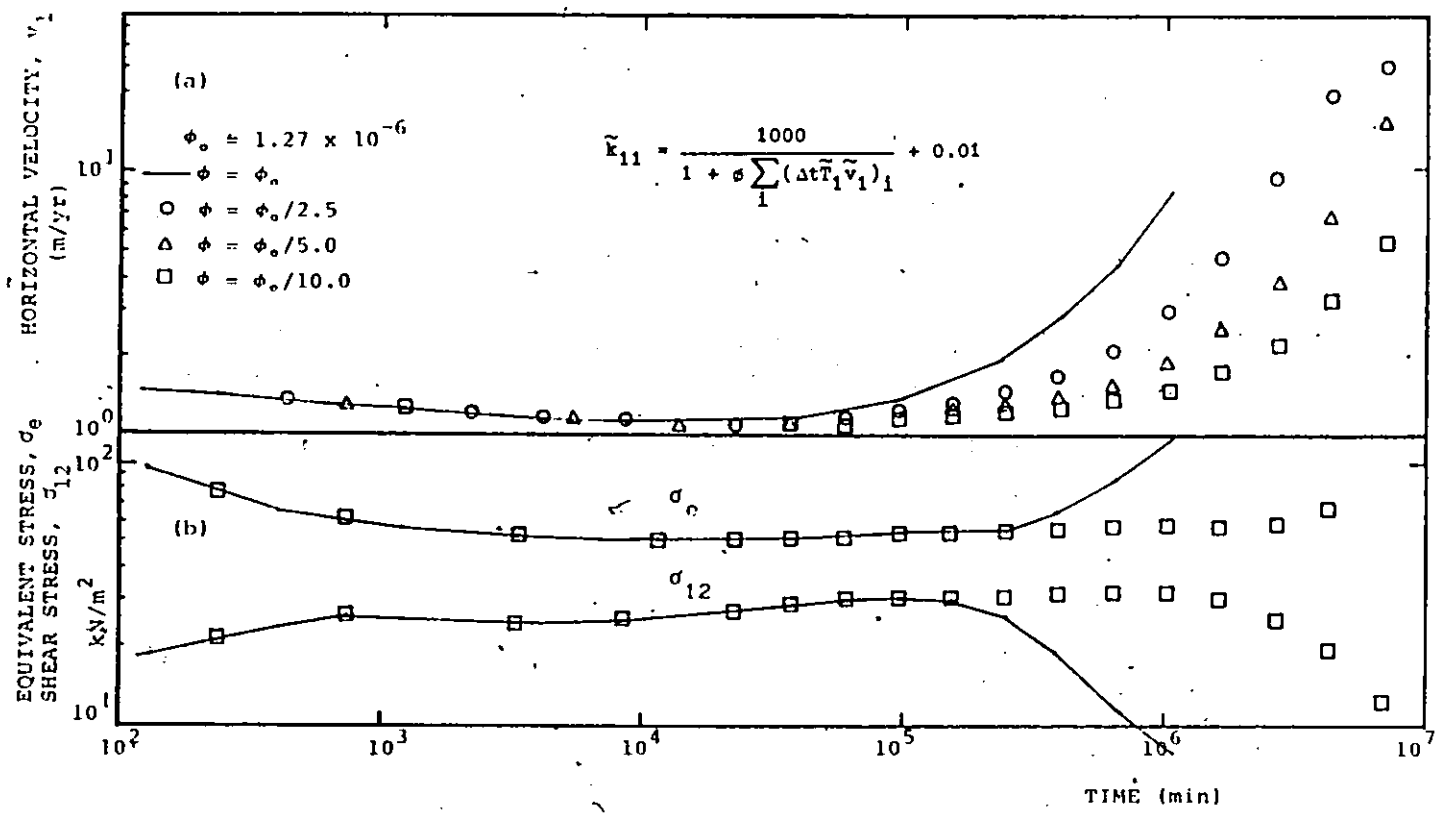

FIGURE 4.12 DOUBLE SLOPE PROBLEM: (a) Horizontal surface velocity at node 25, and (b) Stresses in element 19, during instability of ice mass (Model C).

CHAPTER 5

FINITE ELEMENT SIMULATIONS OF EREBUS GLACIER TONGUE (EGT) AND BARNES ICE CAP (BIC)

5.1 Introduction

The finite element models presented in the previous chapters are used to simulate the creep and temperature behaviour of two well known ice masses: Erebus Glacier Tongue (EGT), Antarctica; and the Barnes Ice Cap (BIC), Baffin Island, Canada. The locations for EGT and BIC are shown in Figures 5.1(a) and (b), respectively. The Erebus Glacier Tongue, which is believed to be floating along its entire length, extends more than 12 km into the McMurdo Sound. The tongue has a history of reaching a critical length (approximately 12 to 13 km) at which time it becomes unstable and undergoes extensive calving that reduces its length to approximately 8 km [37].

The Barnes Ice Cap is a medium-sized sub-polar ice cap that is a remnant of the Laurentide Ice Sheet. Convincing evidence for a surge along the south-west side of the south dome, shown in Figure 5.1(b), has been presented by Holdsworth [36]. In this region, the ice cap sits on temperate basal ice, except at the margin where the ice is frozen to its bedrock [16]. Emphasis, in the current study, is placed on modelling a surge on the south-west side of BIC by assuming basal instability and by taking into account the changes in the temperature field during the surge. The pre-surge ice mass profile at the beginning of the surge has

been provided by Holdsworth of Environment Canada [41]. Regarding the post-surge profile, the finite element simulations for creep and thermal regimes are presented in Appendix A5.

The analyses of EGT and BIC are completed by assuming homogeneous and isotropic material properties. Although, the models have the capabilities of handling nonuniform material properties. Model C (transient creep model) can be modified to allow for time-dependent changes in material properties due to changes in stress and temperature fields.

5.2 Erebus Glacier Tongue (EGT)

The aim of the EGT study is to determine the temperature distribution within the ice mass based on information that had been provided by Holdsworth [42], shown in Figure 5.2. Since the glacier tongue has a history of reaching a critical length and then calving, therefore it is not in steady-state. It is shown that provided the upstream temperature profile is known, steady-state assumptions may be quite reliable for computing the temperature distribution within most of the ice mass at any given time. In order to predict the temperature distribution it is necessary to first estimate the velocity field within the glacier tongue.

5.2.1 Creep Analysis of EGT

The creep of floating ice masses is different from that of land-

based glaciers [illegible] that the deformation is essentially one of longitudinal extension rather than shearing [94]. Model A (incompressible, non-Newtonian creeping flow) is used to complete the steady-state creep flow simulation along the centre line of the glacier tongue. An isothermal temperature field is assumed when completing the creep simulations. Since the glacier tongue is not confined laterally except for hydrostatic pressure due to sea water, it spreads as well. Thus the plane strain assumption provided for in Model A, is not consistent with the actual creep flow behaviour. To overcome this difficulty it is assumed that the lateral strain rate $\dot{\varepsilon}^c_{33}$ is a fraction $\bar{\alpha}$ of the longitudinal strain rate $\dot{\varepsilon}^c_{11}$. The vertical strain rate $\dot{\varepsilon}^c_{22}$ follows from incompressibility and is given by

$$\dot{\varepsilon}^c_{22} = -(1 + \bar{\alpha})\dot{\varepsilon}^c_{11}; \quad \bar{\alpha} > 0. \tag{5.1}$$

For the case when $\bar{\alpha} = 1$ Weertman [94] shows that the influence of the lateral straining is to increase the longitudinal strain rate by approximately 10 percent. In view of Weertman's observation and the condition expressed by Equation (5.1), the relative vertical velocities ($v_{TOP} - v_{BOTTOM}$) within the glacier tongue are approximately double that given by a plane strain analysis.

The boundary conditions for the creep analysis are shown in Figure 5.3. Three cases are studied to determine a suitable velocity field which is later used for the temperature analysis: Case A - the vertical surface velocity is to maintain steady-state flow and the hori-

zontal velocity is constant along the upstream boundary; Case B - the vertical surface velocity is ten times that used in Case A and again the upstream horizontal velocity is constant; and Case C - the vertical surface velocity is ten times that used in Case A and the upstream horizontal velocity varies according to a cubic relationship such that the velocity is zero at the ice-bedrock interface and reaches the measured horizontal velocity at the surface. The material properties for the creep and temperature analyses are given in Table 5.1.

TABLE 5.1 PHYSICAL PROPERTIES OF ICE USED FOR EREBUS GLACIER TONGUE

Unit Weight for Ice:	Assumed consant, $\gamma = 8.592\ kN/m^3$
Flow Law:	$\dot{\varepsilon}_e^c = 0.0035\ \sigma_e^{3.0}$ [37].
	where $\dot{\varepsilon}_e^c$ is in yr^{-1} and σ_e in bars (0.1 MPa)
Conductivity:	$2.195\ W \cdot m^{-1} \cdot {}^\circ C^{-1}$
Heat Capacity:	$1.77 \times 10^6\ W \cdot sec \cdot m^{-3} \cdot {}^\circ C^{-1}$

The main uncertainty in the EGT study is the upstream boundary condition. Sanderson [89] discusses the two important processes at the transition zone (from land-based to floating): the velocity distribution changes from that of a land-based glacier where velocity decreases

with depth to that of a floating glacier where the horizontal velocity is nearly constant with depth; and the temperature distribution undergoes a large change when the colder ice comes in contact with sea water rather than rock. Due to a lack of understanding of the transition process, Sanderson encountered modelling difficulties near the transition zone.

Figure 5.4(a) shows that a constant horizontal velocity at the upstream boundary leads to more realistic vertical velocities than is observed when the ice is frozen to the bedrock at the upstream boundary. The influence of changing the specified vertical surface velocity distribution is small due to the small magnitude of the vertical velocities relative to the horizontal velocities. Higher downward vertical surface velocities only decrease the upward vertical velocities at the bottom. The results for Case C indicate unusually high vertical velocities at the bottom. Moreover the stresses near the transition zone suggest that ice fracture is imminent when the ice is frozen to the bedrock, i.e. $|(\sigma_{11} - \sigma_{22})| > 1.8$ MPa. According to the information on the mass balance at the bottom, melting is expected along most of the glacier tongue. The computed vertical velocity at the ice-water interface for Case C is definitely not consistent with the conditions that are proposed by Holdsworth [42]. These creep simulations suggest that the transition from a land-based glacier to a floating glacier is gradual and that no sharp boundary exists.

The dominance of longitudinal extension, first proposed by Weertman [94], is confirmed by the finite element simulation of EGT in

this study. A comparison of the shear stress with the deviatoric stress (S_{11}) indicates that there is little shearing along the tongue except near the transition zone as shown in Figure 5.5. The higher shear stresses near the transition zone are attributed to the manner in which the upstream boundary condition is specified. Physically, higher shear stresses are expected in this region due to transition from a land-based to a floating glacier and greater convergence rates of the upper and lower ice mass boundaries. These results also compare well with those of Sanderson and Doake [90] who have shown that the shear stresses are small when compared with the direct deviatoric stresses along the glacier tongue.

5.2.2 Thermal Analysis of EGT

Temperature is specified all over the boundary by using the information given in Figure 5.2. The specified surface temperatures are those measured at the 10 m depth while the bottom and the downstream temperature boundary conditions correspond to the phase equilibrium temperature for ice and salt water as indicated in the figure. The upstream temperature is an estimated distribution provided by Holdsworth [42]. The influence of strain heating and thermal advection are included in the temperature analyses by using the strain heating and velocity fields obtained from the creep analyses. Also included in some of the simulations is the heat release due to freezing of sea water at the 10.5 km section. For these simulations the latent heat is introduced as a surface flux at the boundary.

In the absence of thermal advection, it is observed that the strain heating does not change the temperature distribution by much (see Figures 5.6(a) and (b)) in the regions away from localized freezing. However the latent heat due to freezing does have a profound local effect on the temperature field (see Figure 5.6(b)). The following observations are made when advection is included.

1. The heat released during freezing has little influence on the temperature field when advection dominates. See Figures 5.6(c) and (d).
2. Thermal advection in the horizontal direction is the dominating factor that determines the spatial temperature variation throughout EGT. Changes in the vertical advection only result in minor changes in the temperature field. See Figures 5.6(d) and (e) for comparison when the vertical velocities have been doubled.

The spatial temperature variation is extremely sensitive to the upstream boundary conditions which, if not appropriately defined, can lead to erroneous results. Unfortunately no field measurements are available for comparison of the computed and measured temperatures. Even though the glacier tongue is not in steady state, the steady-state analysis is believed to give a reasonable description of the temperature variation within most of the glacier tongue because of a reasonable estimation of the velocity field and importance of advection; i.e. a particle entering the tongue travels through the tongue with only small changes in its temperature due to conduction.

5.3 Surge Simulations of Barnes Ice Cap (BIC)

5.3.1 Overview

Finite element surge simulations have been carried out along section N-O-SS, shown in Figure 5.1, of the Barnes Ice Cap due to suitability of the plane strain flow assumptions along this section. Furthermore, ample evidence exists that supports the hypothesis of instability having taken place on the south-west side of the ice cap, and reasonable information on the thermal regime of the ice cap is available from which some conclusions can be drawn regarding mechanisms for surge propagations.

Convincing evidence for instability having taken place on the south-west side of section N-O-SS is presented by Holdsworth [36]. This evidence is grouped under: (a) ice-surface morphology; (b) marginal-morraine geometry and chronology; (c) basal conditions as determined from flow-rate, ice depth and shallow temperature data; and (d) geological-hydrological observations [16]. Classen [16], by thermal drilling and deep ice-temperature measurements along the flow line of interest, confirmed that temperate basal ice exists. This temperate basal ice on the south-west side is favourable for basal instability. Factors that contribute to higher temperatures on the south-west side of the divide include: lower average surface elevation when compared to the north-east side; more direct solar radiation [39] and the possibility of a higher geothermal flux [40].

It is the opinion here that the events leading to instability are more complex than initially realized and that surging of BIC is not a cyclic phenomenon as is often associated with valley glaciers. According to Holdsworth [39], instability may be attributed to an outward spreading of temperate basal ice. This reduces the passive resistance that prevents the advancement of the ice cap margin. Once the contact area between the ice frozen to the bedrock reduces to a critical size, determined by the ice strength properties, the basal ice yields or flows and a surge propagates.

The south-west side of the ice cap has a negative mass balance that is greater than the vertical emergence flux [39] hence suggesting that the ice cap is receding. Field studies show the existence of recessional morraines which indicate that this has been the case for several centuries [58]. Recent computer simulations by Mahaffy [60] support the hypothesis that the south dome is retreating. Based on this information it is felt that the onset of instability may have been partially caused by a loss in passive resistance at the toe of the ice cap as a result of a receding margin. However, in order to model the surge initiation, factors influencing the ice cap dynamics and energy balance must be incorporated into a single model.

Due to the unknown length of time for instability to develop and the limitations of Model C described in the previous chapter, only the initial stages of surge propagation are modelled. The influence of seasonal changes and mass balance are considered to be negligible during the short period of a surge propagation. The study on instability is

divided into two parts: (a) preliminary investigation to establish initial conditions based on steady-state analysis; and (b) actual simulation of instability with starting conditions that are favourable for a surge. Instability is assumed to be due to a local reduction of basal shear resistance according to the model presented in Chapter 4. Interaction between the ice temperature and velocity fields is included in the non-isothermal simulations.

5.3.2 Preliminary Investigation of BIC (Pre-surge)

The finite element idealizations for the pre-surge profile of BIC are shown in Figure 5.7. These idealizations are developed from the information provided by Holdsworth [41] which is presented in Appendix A6. The material properties, used for modelling surges of BIC, are presented in Table 5.2. As was done previously, it is assumed that the ice is homogeneous and isotropic.

5.3.2(a) Creep Analysis

In order to estimate a velocity field for a steady-state thermal analysis of BIC, an isothermal creep simulation has been completed using Model C. It is assumed that the pre-surge temperature field adjusted itself to steady-state conditions with very little sliding occuring at the ice-bed interface. The surface velocities and the basal stress variations from the creep simulation are given in Figures 5.8 and 5.9, respectively. The velocities and stresses reported are before the mean

TABLE 5.2 PHYSICAL PROPERTIES OF ICE FOR SURGING OF BARNES ICE CAP

Unit Weight	$\gamma = 8.952\ kN/m^3$
Elastic Modulus	$E = 9.075 \times 10^3$ MPa
Poisson's Ratio	$\nu = 0.34$
Flow Law (Hooke's Parameters)	$\dot{\varepsilon}_e^c = 0.0327\ \sigma_e^{1.65}$
Sliding Law	$\tilde{T}_1 = \tilde{k}_{11}\tilde{v}_1$
Thermal Conductivity	$K = 2.1\ W \cdot m^{-1} \cdot {}^\circ C^{-1}$
Heat Capacity	$C = C_\rho \rho = 2.1 \times 10^6\ W \cdot sec \cdot m^{-3} \cdot {}^\circ C^{-1}$

Flow Law including temperature variation (1)

$$\dot{\varepsilon}_e^c = f(\sigma_e)\ \exp\left(-\frac{Q}{RT}\right)$$

$$Q = 78\ kJ/mol \text{ for } T > 265^\circ K$$

$$Q = 120\ kJ/mol \text{ for } T < 265^\circ K$$

Units: $\dot{\varepsilon}_e^c (yr^{-1})$; σ_e(bars, 1 bar = 0.1 MPa); $\tilde{T}_1$ (kPa); $\tilde{v}_1$ $(m \cdot yr^{-1})$

(1) Constant for power flow law is adjusted to correspond to strain-rates at 265°K.

normal stress started to drift. The surface velocities and shear stresses are larger on the south-west side than on the north-east side. An observation of the vertical surface velocity profile and the bedrock topography illustrates the influence of bedrock topography on the vertical velocity, Figure 5.8. In areas where the ice must climb over the obstacles, the downward velocities decrease. The model predicts that the dynamic divide is 600 m north-east of the topographic divide at the 16 km section.

The pressure variation shown in Figure 5.9 resembles the overburden stress distribution due to the self weight of ice. It should be noted that if the basal ice is at the pressure-melting point beneath the south-west slope, and if the bedrock is impermeable, water can collect to reduce the basal sliding resistance in the areas of local pressure minimums. This buildup of a water layer can aid the onset of instability [88].

5.3.2(b) Temperature Analysis

To perform the non-isothermal surge simulations an initial temperature distribution is required. Since no data is available on the pre-surge temperature field of BIC, it is assumed that the ice cap adjusted to a near steady-state before the surge [41]. The steady-state temperature simulations are completed by using the velocity, strain heating and pressure fields from the isothermal creep analysis. Although the computed temperature and creep responses are not strictly compatible it is believed that the computed temperature field is reason-

able in view of the lack of information on the pre-surge conditions. One can perform iterations by alternately carrying out the creep and thermal analyses to arrive at a converged thermal regime, non-isothermal, if very accurate data are available regarding physical properties of ice, geometry and boundary conditions.

The boundary conditions for the steady-state temperature simulation are given in Figure 5.10. The geothermal flux is increased in four equal intervals from 0.95 HFU to 1.9 HFU. It is observed that for an appreciable portion of the base to reach pressure melting the geothermal flux must be sufficiently high, i.e. 87.5 percent of 1.9 HFU (Figure 5.10). This observation is consistent with the hypothesis that the geothermal flux is higher on the south-west side than on the north-east side of the current divide [41]. Figure 5.11 shows the temperature distribution that is used for the non-isothermal surge simulations.

Since the south-west margin of BIC is forzen to the bedrock as indicated by the temperature contours in Figure 5.11, the basal ice must yield for a surge to propagate. To digress from the main theme of creep analysis presented in this thesis, potential zones of yielding have been identified using the equivalent stress criterion. An equivalent yield stress of 0.15 MPa has been assumed. Figure 5.7(a) shows the zone of potential yielding of ice. This yield zone is in the same region where the ice is frozen to the bedrock. To simplify the surge analyses, no distinction is made between the loss in shear resistance due to lubrication by melt water and ice yielding. Since the basal shear stress at the margin is larger than it is elsewhere, the sliding law becomes

faster (through a reduction in $\tilde{k}_{11}$) under larger shear stresses. This is similar to, but not exactly the same as choosing a faster creep law for higher equivalent stresses in the basal zone.

5.3.2(c) Preliminary Creep and Surge Simulations

For simpler cases where no sliding is allowed at the ice-bed interface, creep simulations from both finite element idealizations predict similar responses. However, when Grid A is used for the surge simulations, it is observed that velocity reversals occur at the ice-bed interface near the 26 km section. These reversals prevent the surge from propagating farther upstream, thus limiting its extent as shown in Figure 5.12. No such reversals are observed when the finer Grid B is used. Due to this grid sensitivity all subsequent simulations are completed with Grid B.

5.3.3 Surge Simulations

It has been shown in Chapter 4 that the timing for a surge propagation can be characterized by a lubrication factor. Equally important is the initial shear resistance k^* at the ice-bed interface. Four surge simulations are completed to investigate the sensitivity of a surge to the initial bed resistance, lubrication factor and the temperature field of the ice cap. The details of the basal boundary conditions for these simulations are given in Table 5.3. The determination of values of the sliding parameters for surging is a very difficult problem in itself.

TABLE 5.3 SLIDING INPUTS FOR SURGE SIMULATIONS

$$\hat{k}_{11} = \left(\frac{k^*}{1 + \phi < \sum_i (\hat{T}_1 \cdot \hat{v}_1 \ \Delta t)_i}\right) + 0.01 \qquad (1)$$

$$\phi_0 = 1.27 \times 10^{-6} \frac{m^2}{kN} \cdot \frac{yr}{m} \cdot \frac{1}{min}$$

ISOTHERMAL TEMPERATURE DISTRIBUTION

Case 1	$\phi = 2.5\ \phi_0$	
	$k^* = 1000.0\ kN \cdot m^{-3} \cdot yr$	$x_1 > 13$ km
Case 2	$\phi = 2.5\ \phi_0$	
	$k^* = 100.0\ kN \cdot m^{-3} \cdot yr$	$13\ km < x_1 < 24$ km
	$100.0 < k^* < 1000.0$	$24\ km < x_1 < 25$ km
	$k^* = 1000.0\ kN \cdot m^{-3} \cdot yr$	$x_1 > 25$ km

NON-ISOTHERMAL TEMPERATURE DISTRIBUTION

Case 3	$\phi = 2.5\ \phi_0$	
	$k^* = 100.0\ kN \cdot m^{-3} \cdot yr$	$13\ km < x_1 < 24$ km
	$100.00 < k^* < 1000.0$	$24\ km < x_1 < 25$ km
	$k^* = 1000.0\ kN \cdot m^{-3} \cdot yr$	$x_1 > 25$ km
Case 4	$\phi = 2.5\ \phi_0/33.33$	
	$k^* = 3.0\ kN \cdot m^{-3} \cdot yr$	$13\ km < x_1 < 24$ km
	$3.0 < k^* < 30.0$	$24\ km < x_1 < 25$ km
	$k^* = 30.0\ kN \cdot m^{-3} \cdot yr$	$x_1 > 25$ km

Units: $\hat{T}_1$ (kN/m^2); $\hat{v}_1(m/yr)$; $\Delta t_i(min)$

Therefore, it is necessary to make assumptions regarding these parameters. All sliding parameters are chosen so as to allow most of a surge to be completed within a two-year period. By no means are these parameters and their distributions optimized. Perhaps the most relevant parameters are those in Case 4. The initial sliding resistance ($k^* = 3.00$) for this case has been found to give a reasonable sliding behaviour for the post-surge BIC simulations that are presented in Appendix A5. The higher initial shear resistance toward the margin ($k^* = 30.0$) is intended to represent the greater resistance that is expected to exist near the margin during the early stages of a surge.

In addition to the numerical difficulties that are encountered when the coarser grid, Grid A, is used, numerical oscillations appear even when Grid B is employed. These oscillations are a result of the high strain gradients that develop along the ice-bed interface as a surge propagates and the insentivitity of the finite element mesh to model these high gradients. It should be pointed out that the strains are constant within each constant stress triangular element thus strain gradients are poorly approximated. The severity of these numerical oscillations is also related to the rate at which the basal shear resistance is reduced. The oscillations are least severe for Case 4 where the high basal shear resistance gradients are suppressed by starting the simulations with lower basal resistances and by allowing for a more gradual decrease in the basal shear resistance due to a lower lubrication factor along the ice-bedrock interface.

Although some of the quantitative results may be questionable,

some general conclusions can be made. It is quite clear from Figure 5.13, that the advancements of the south-west margin during the surge simulations and the timing are distinctly influenced by both the initial basal shear resistance and the temperature field. The influence of the temperature field on sliding enters through coupling between the internal deformation (creep) and stresses in the basal layer. Figures 5.14(a) to (d) show the basal shear resistance at various times during a surge for different initial basal resistance and temperature fields. Also shown in Figure 5.15 is the change in shear stress at the ice-bedrock interface at various times during the surge for Case 4. During the initial stages of this simulation, the maximum shear stress is less than 0.2 MPa which is less than that required for the ice to yield. An increase in the peak shear stress could have been achieved by reducing the distance over which the inital sliding resistance (k^*) is equal to 30.0 $KN \cdot m^{-3} \cdot yr$ (see Figure 5.14(d)). The general decrease in basal shear stress as the surge progresses is attributed to a decrease in shear resistance at the ice-bed interface, a lowering and flattening of the ice surface and an increase in the ice-bedrock contact area.

The change in the horizontal surface velocity at node 165, Figure 5.7(b), with time is shown in Figure 5.16. The velocity oscillations appear to be mainly of numerical rather than physical origin, Despite the oscillatory behaviour there is a general decrease in velocity (for each case) after having undergone large deformations. The decrease in velocity is believed to be due to spreading and lowering of the ice surface and an increase in the ice-bed contact area. For Case 4, where the surge propagation is more gradual, the peak velocity is

lower than those for the other cases. The ice cap margin advances 1.7 km when the velocity reaches its highest value. The higher peak velocities for the other surge simulations are partially attributed to numerical oscillations of these simulations as mentioned earlief.

The changes in equivalent stresses at various locations within the ice cap are shown in Figures 5.17(a), (b) and (c). The equivalent stress changes in element 29 represent the transient behaviour of the north-east margin during the surge. For Case 1 numerical instability develops after 350,000 minutes. It is apparent from Figure 5.17(a) that the numerical instability is not only realized in the surge zone where the rapid changes are occurring, but throughout the whole ice mass. For other simulations (Cases 2, 3 and 4) the slow increase of the equivalent stress in element 29 appears to be due to surging on the south-west side. The increase of equivalent stress in elements 145 and 244 is much greater; see Figures 5.17(b) and (c). This indicates that the equivalent stress increases much more rapidly in the surge zone as expected.

A comparison of the equivalent stresses in elements 145 and 244 indicates that the surge starts to propagate first in the middle of the ice mass and then spreads toward the margin for Cases 2, 3, and 4. This is because the initial basal shear resistance at the margin for the last three cases is much greater than that near the middle. The increase in equivalent stress during surging reflects the increase in longitudinal extension as a result of the loss in basal shear resistance. The eventual decrease of equivalent stress suggests that the ice cap is trying to stabilize.

The change in the profile of BIC at different stages during the surge for Case 2 is shown in Figures 5.18(a) to (c). The other simulations attain similar profiles during surging, only the times to reach similar configurations are different. These figures demonstrate how the surface of the ice cap lowers and flattens as the margin advances. Figures 5.19(a) and (b) indicate temperature contours for Cases 3 and 4, respectively. The temperature distributions are plotted with respect to the initial ice cap configuration so that comparisons can be made with the initial temperature field, see Figure 5.11. The influence of pressure melting has not been included for these simulations since large temperature changes are not anticipated. The unusually large increase in temperature for Case 3, shown in Figure 5.19(a), along the south-west margin ice-bed interface is due to a large amount of heat being dissipated within the basal ice layer. This large amount of frictional heat is produced because of the concentration of shear stresses at the margin and high sliding velocities. The magnitude of the shear stresses and consequently the heat dissipated are somewhat magnified due to undesired numerical oscillations. Conservative estimates for temperature increases at the ice-bed interface indicate that the temperature increase should be limited to 0.07°C at most. Within the core of the ice mass where the severity of the numerical oscillations are much less than at the margin, the temperature changes for Case 3 are well within the estimated limit.

For Case 4, where the numerical oscillations are negligible, the temperature increases at the margin are negligible (see Figures 5.11 and

5.19(b)). The spreading of the temperate ice zone is minimal due to the small temperature changes. This observation is in agreement with that of Clarke [14] who found that a thick layer of temperate basal ice does not form as a result of a surge. This is obviously contrary to Robin's [87] suggestion that a thick temperate basal ice layer forms during an instability.

Figure 5.20 shows the location of the dynamic divide as the surge propagates. It can be observed that near the end of a surge, the location of the dynamic divide approaches the position of the current divide for Cases 3 and 4. It should be noted that the shape of the BIC immediately after a surge as predicted by Model C for Case 2 (3 and 4), shown in Figure 5.18(f), is reasonable if one takes into account the melting of the margin and the long-term creep of the ice cap.

5.4 Summary

The dynamic behaviour of two major ice masses has been studied. For the Erebus Glacier Tongue, the emphasis has been placed on obtaining a suitable velocity field for a steady-state temperature analysis. Due to incompressibility it is shown that the influence of lateral spreading can be taken into account by doubling the relative vertical velocities. It is concluded that the ice cannot be frozen to the bedrock at the transition zone. The temperature simulations indicate that the temperature distribution depends on the upstream boundary conditions. Furthermore, the heat given off during freezing of ice at the base has a minimal effect on the temperature field.

For the Barnes Ice Cap, pre-surge temperature simulations indicate that a geothermal flux approaching 1.9 HFU is required to bring most of the south-west ice-bed interface to pressure-melting. The frozen margin that initially blocks a surge must yield plastically. Not enough frictional heat is dissipated to bring the ice near the margin to pressure melting. The results indicate that the initial conditions are very important to model instability. These conditions include the temperature distribution within the ice mass and the spatial variation of basal shear resistance. Although the following influences have not been considered, the flow relationship, non-homogeneity and non-isotropy of the ice mass may be important and need further investigation. The basal shear resistance model used in this study has been adopted for its simplicity and its ability to accomodate a time-dependent loss in its resistance.

This study demonstrates that surge simulations, which include the influences of temperature and basal instability, can be modelled by using the finite element method. Further research is required to determine more suitable sliding parameters to model surging of the Barnes Ice Cap. For the choice of parameters selected in this study the results obtained seem very reasonable. It is expected that a better choice of these parameters, determined on the basis of experiments or a parametric study, should yield more accurate results.

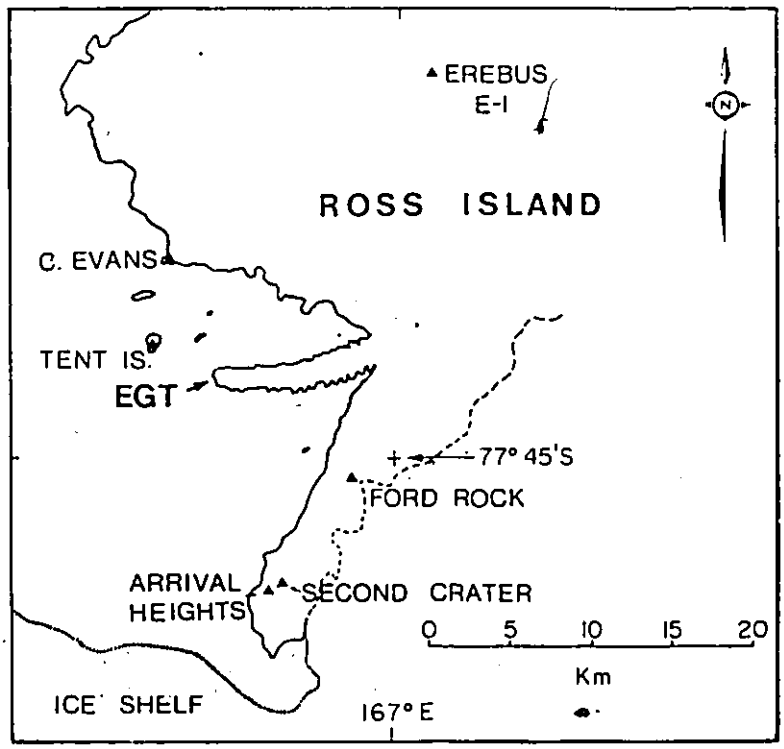

FIGURE 5.1 (a) EREBUS GLACIER TONGUE PROBLEM - Location, Holdsworth [42], and

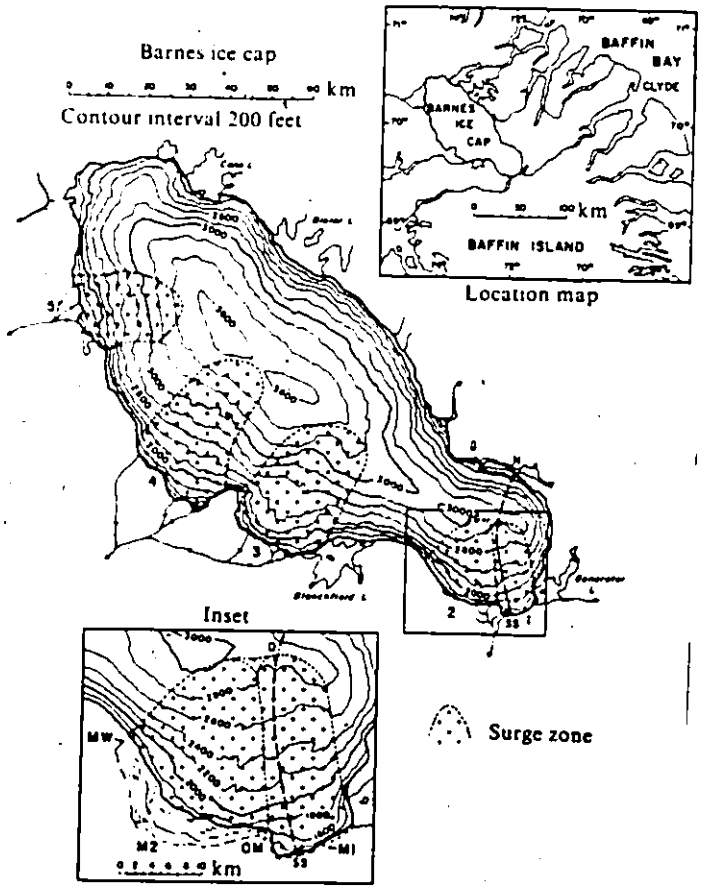

FIGURE 5.1 (b) BARNES ICE CAP PROBLEM - Location, Holdsworth [39].

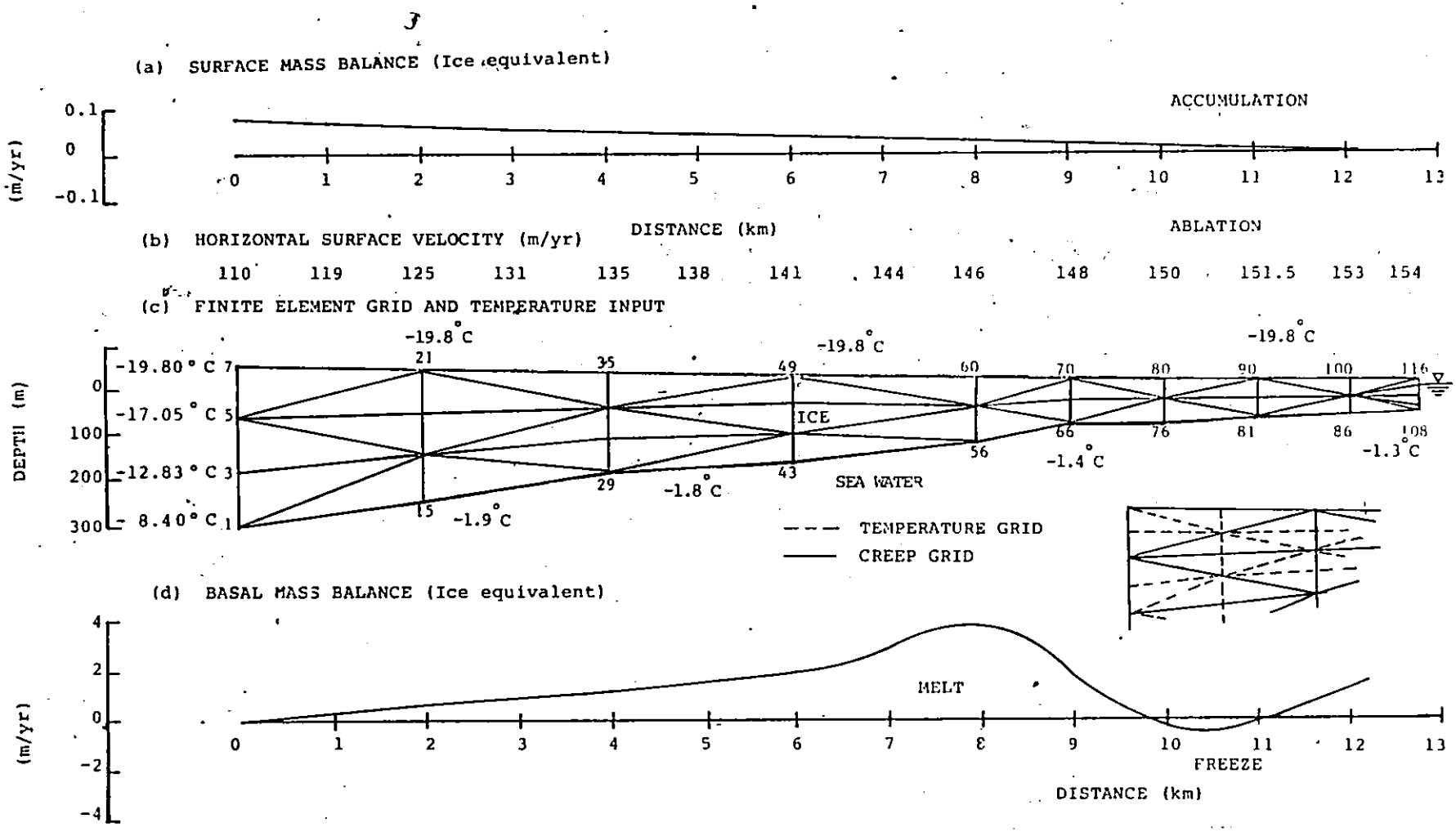

FIGURE 5.2 EREBUS GLACIER TONGUE PROBLEM - Finite element grid and summary of data [42].

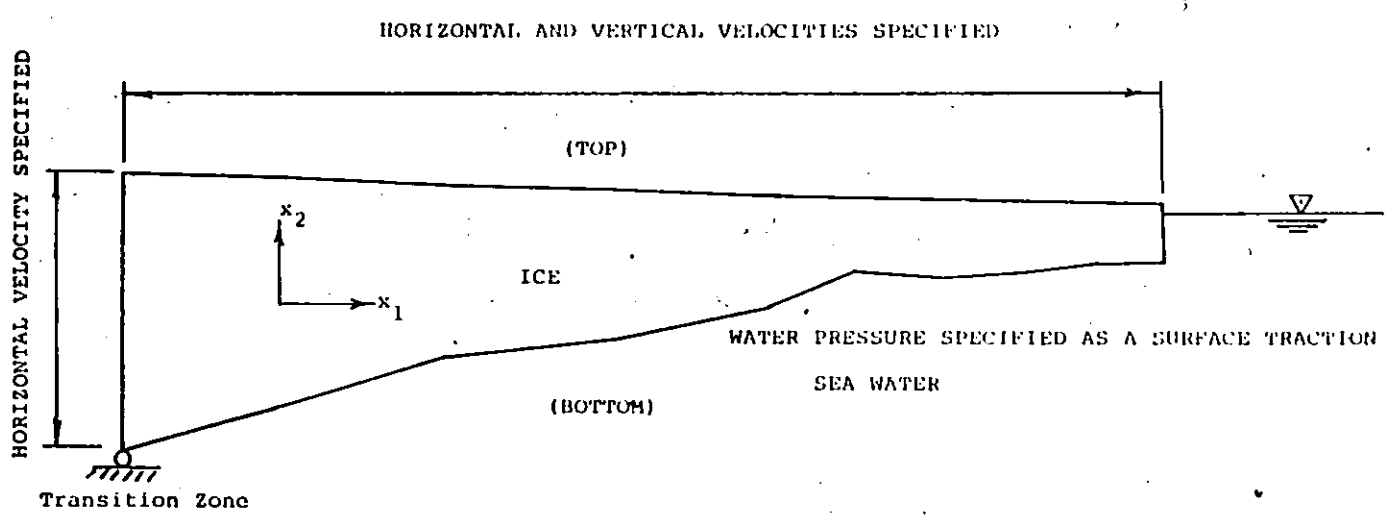

FIGURE 5.3 EREBUS GLACIER TONGUE PROBLEM - Boundary conditions for creep analysis.

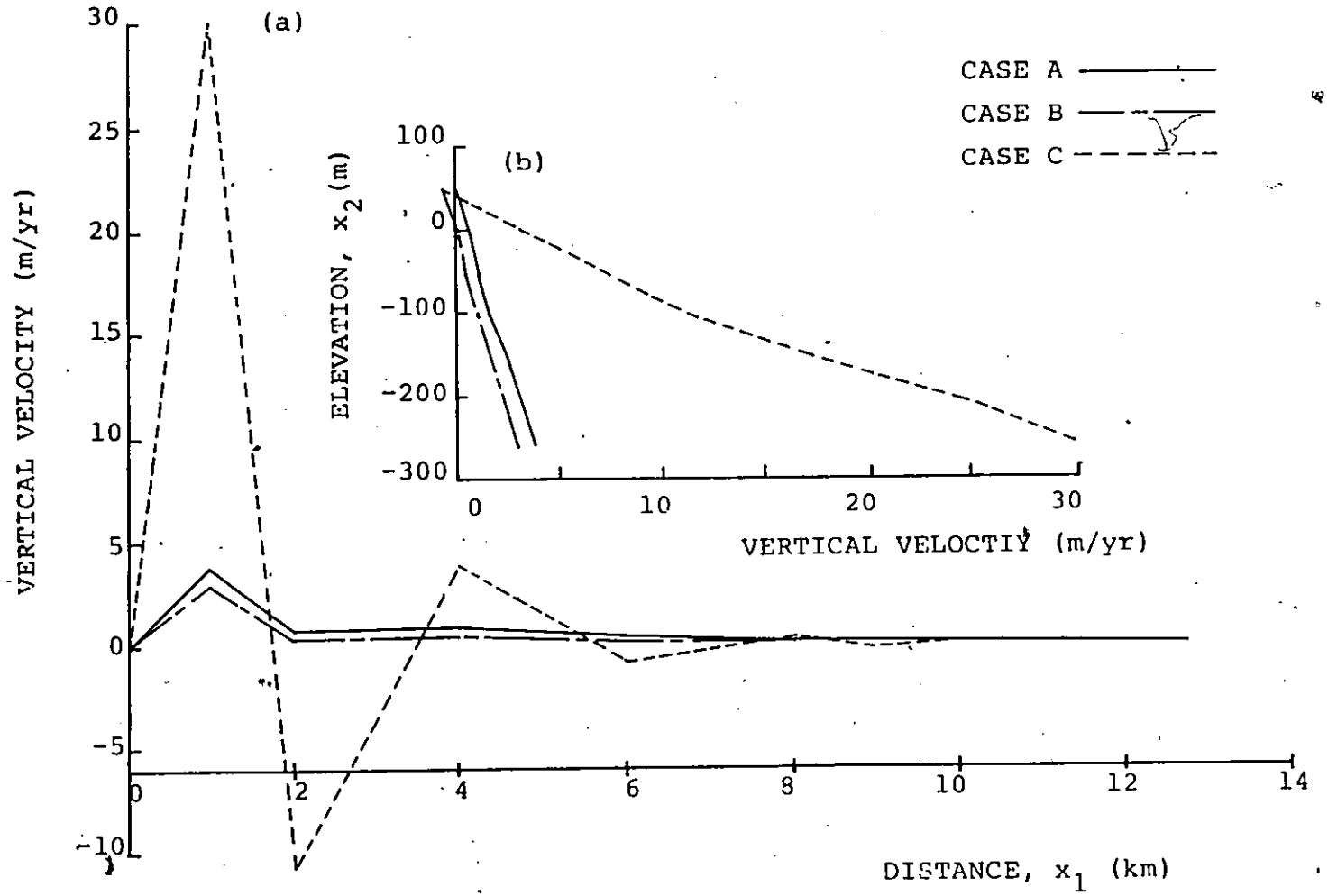

FIGURE 5.4 EREBUS GLACIER TONGUE PROBLEM: (a) Vertical velocity along bottom of glacier tongue, and (b) Vertical velocity profile at 1 km (Model A).

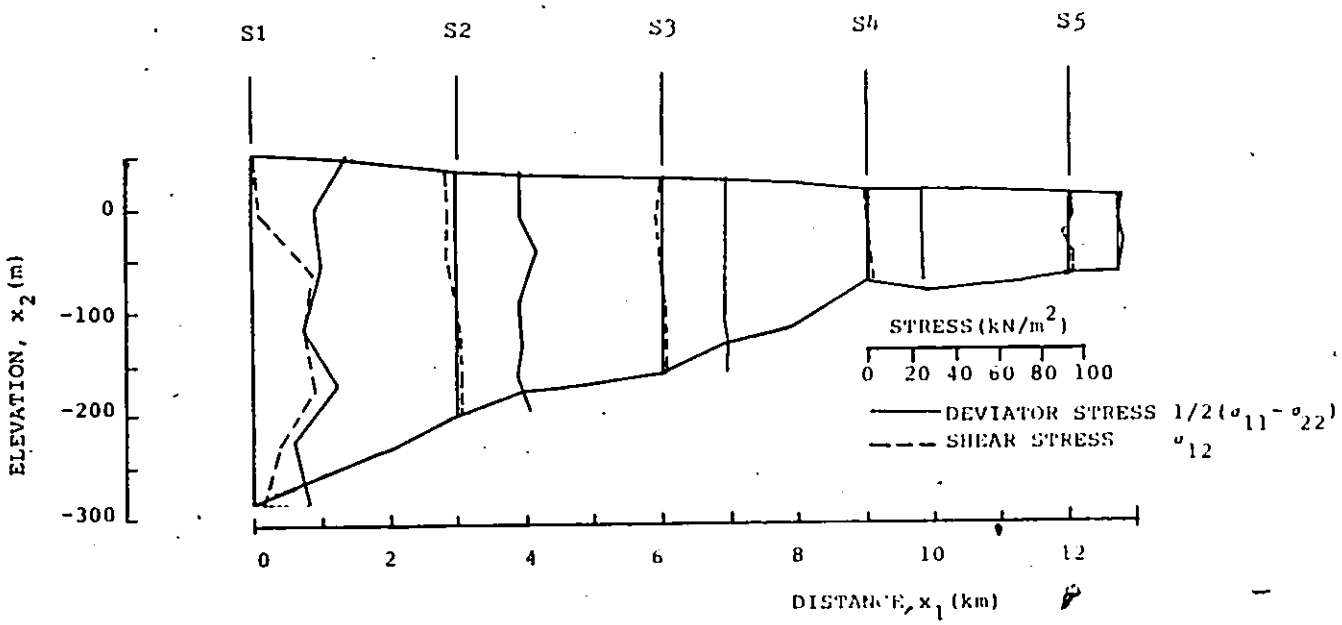

FIGURE 5.5 EREBUS GLACIER TONGUE PROBLEM - Equivalent stress and shear stress profiles along glacier tongue (Model A).

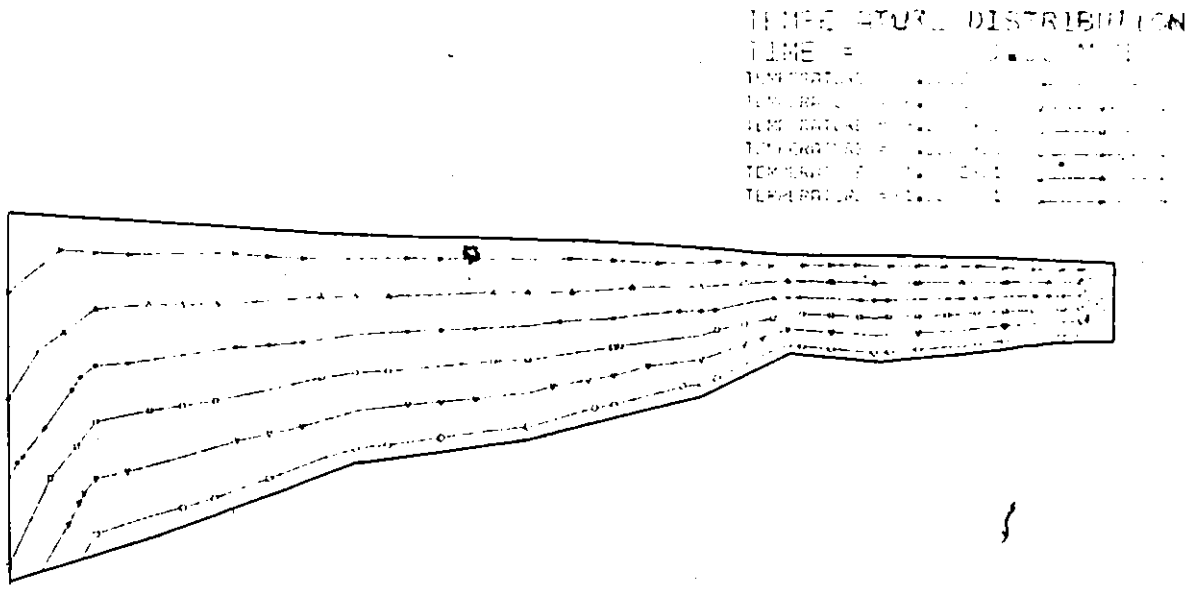

FIGURE 5.6 EREBUS GLACIER TONGUE PROBLEM - Temperature contours for: (a) Thermal analysis with conduction,

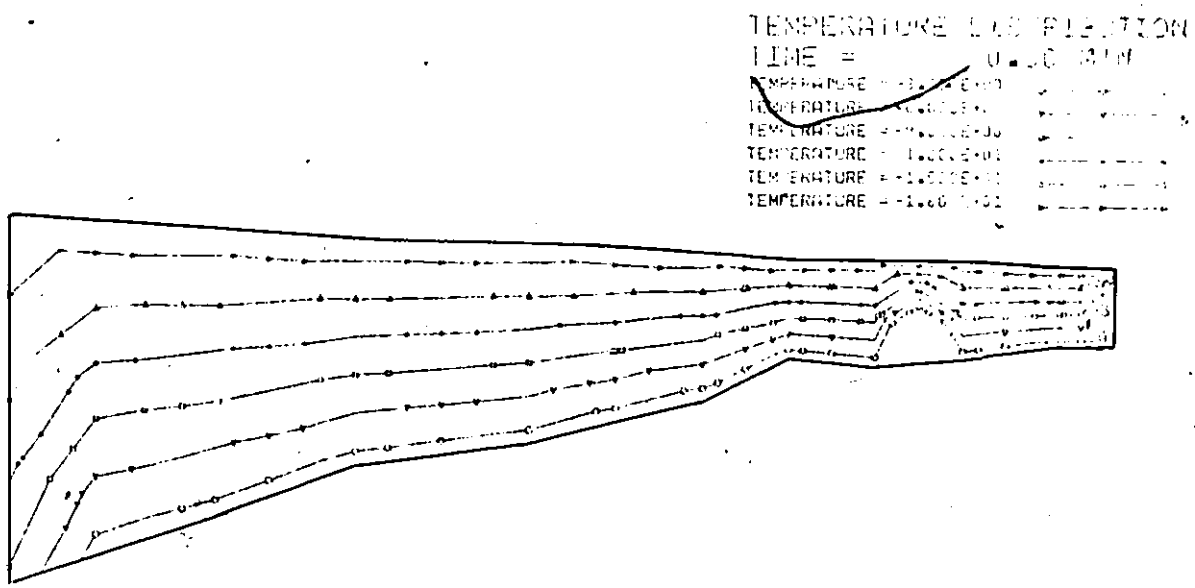

(b) Thermal analysis with conduction, strain heating and heat release due to freezing of seawater,

(cont'd on next page)

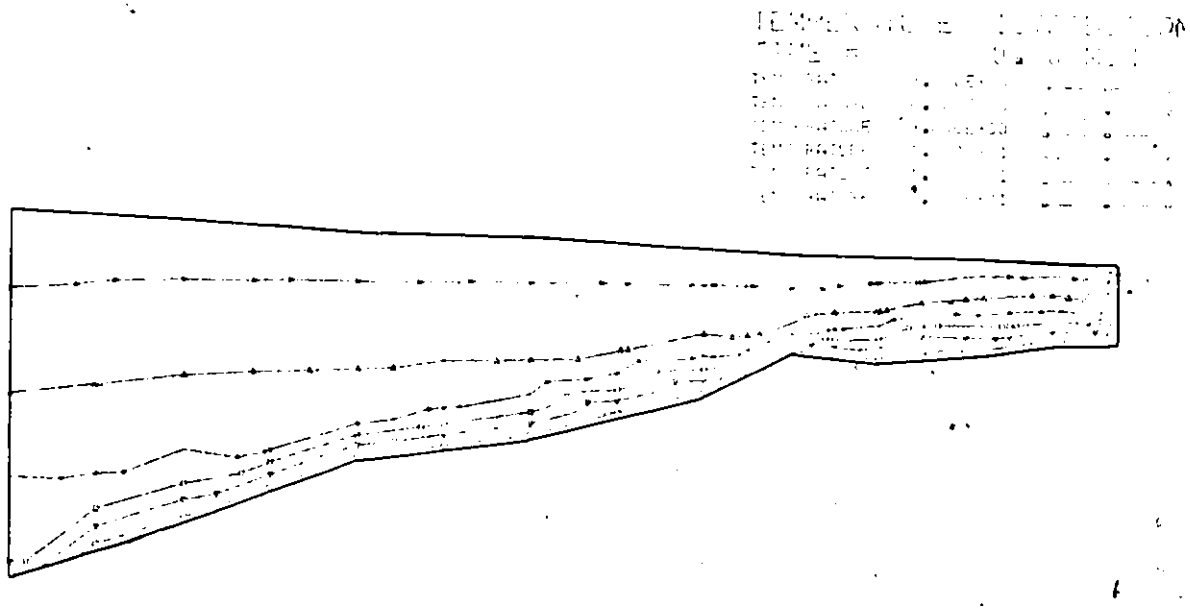

(c) Thermal analysis with conduction, strain heating, advection and heat release due to freezing of seawater,

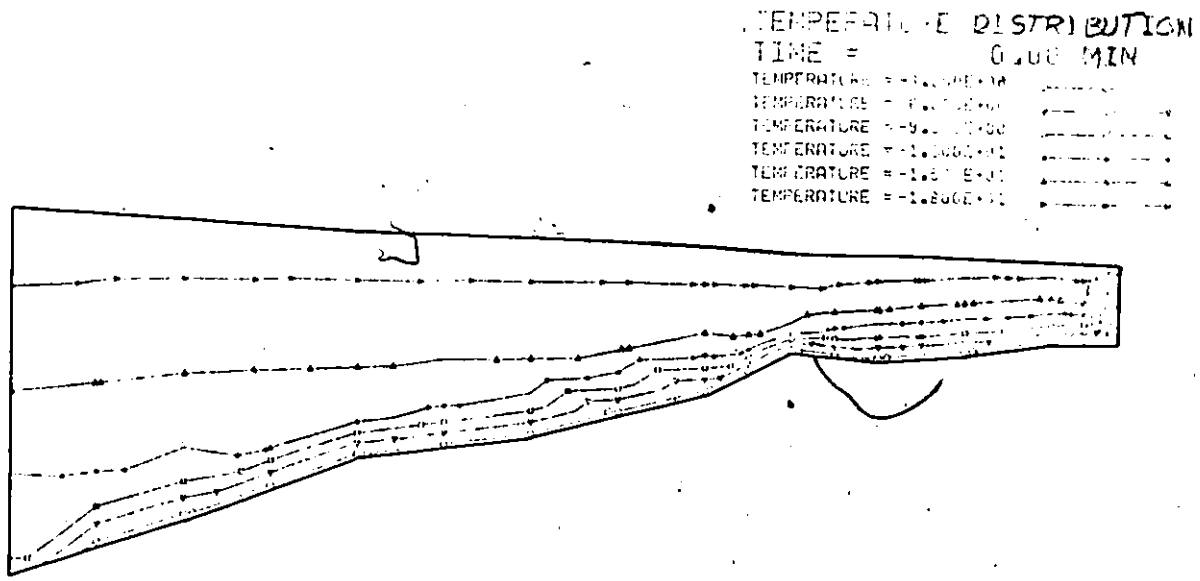

(d) Thermal analysis with conduction and advection, and

(cont'd on next page)

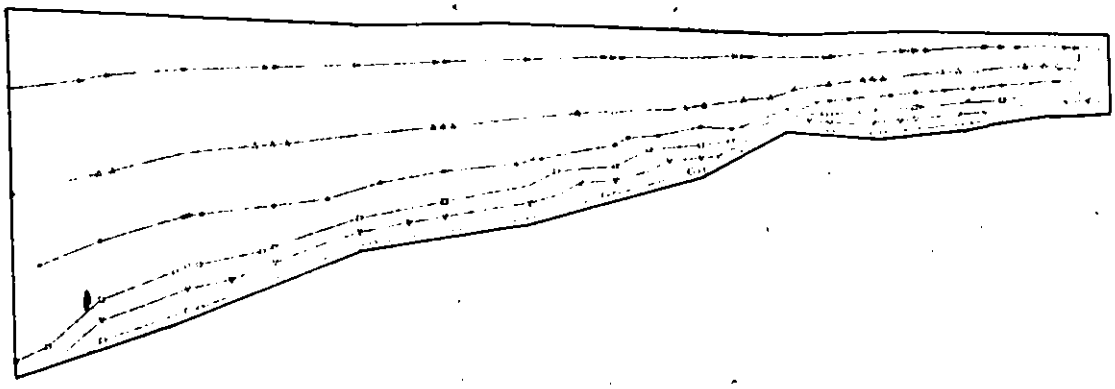

(e) Thermal analysis with conduction and advection where relative vertical velocity is doubled.

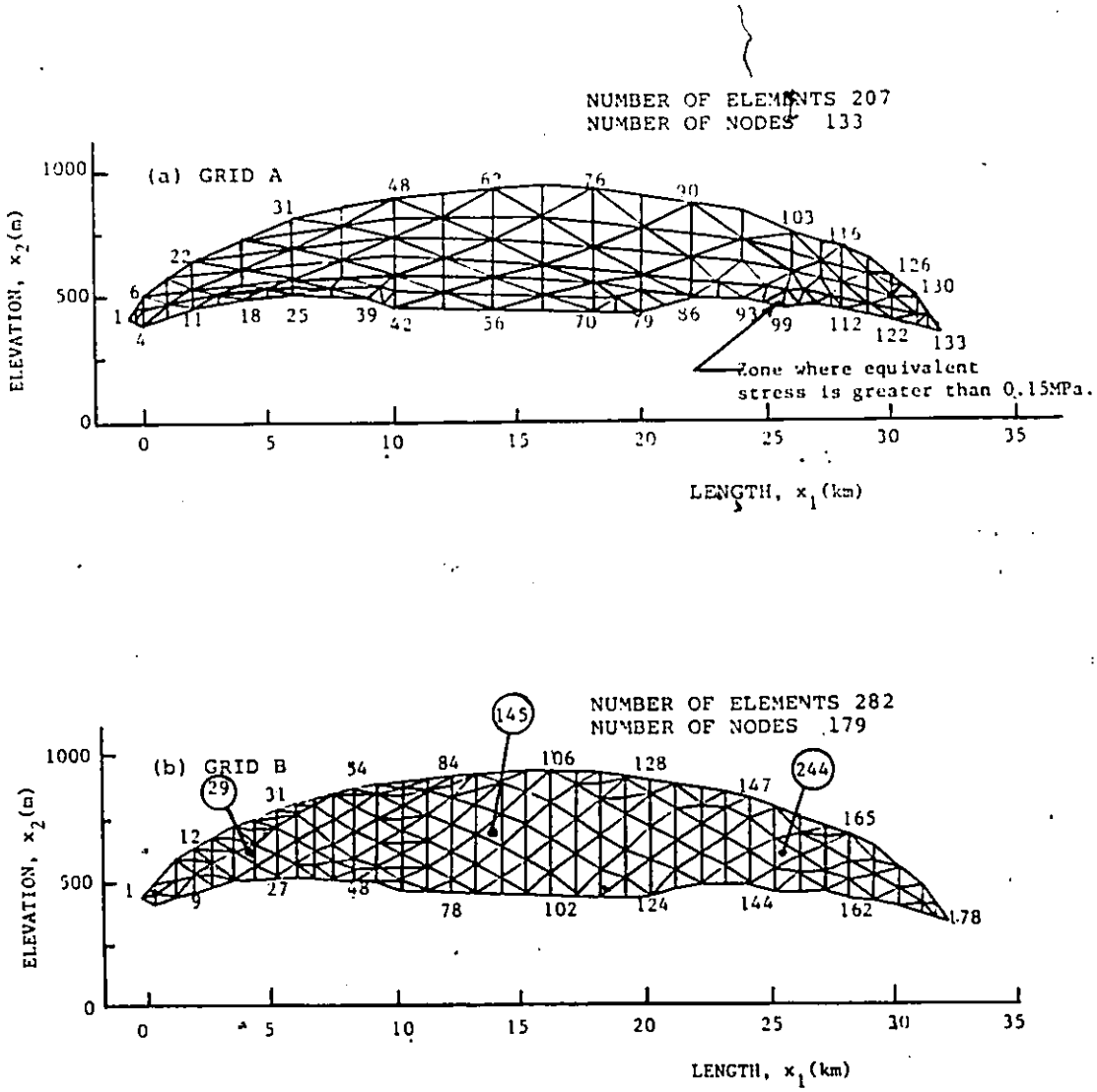

FIGURE 5.7 BARNES ICE CAP, SURGE PROBLEM - Finite element grids (Model C).

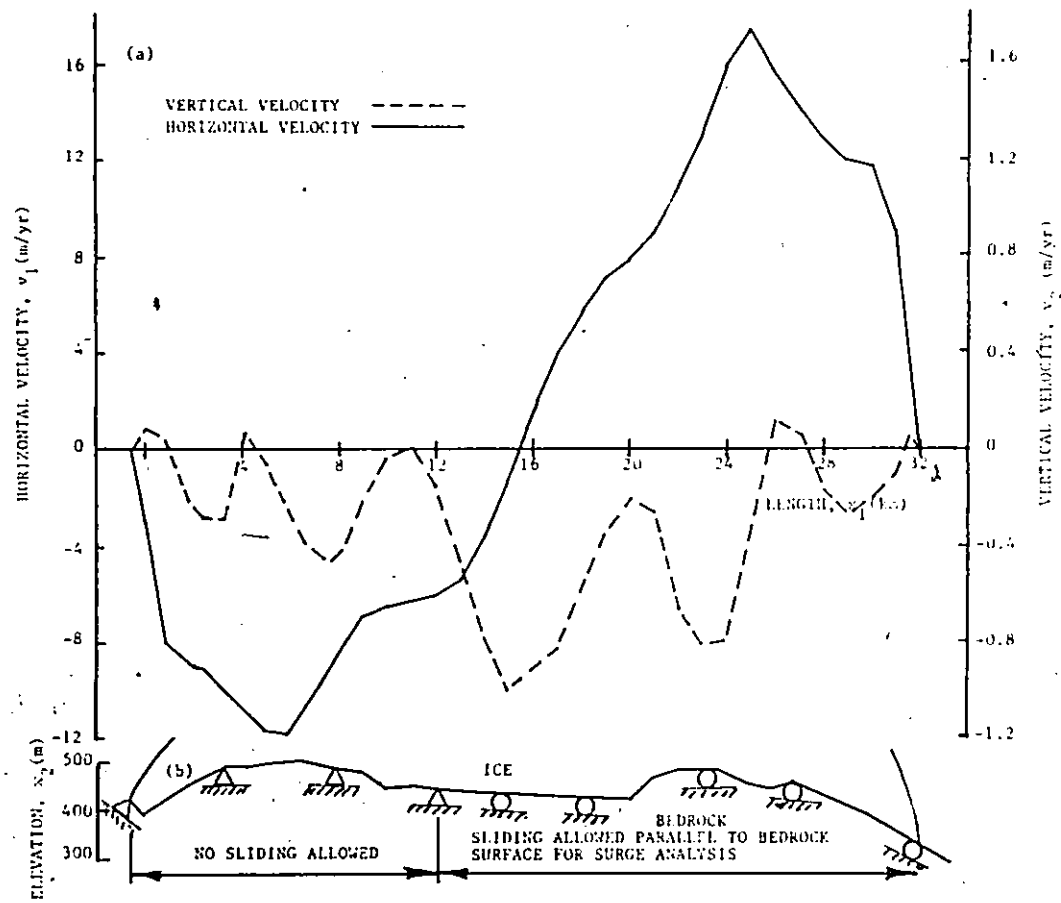

FIGURE 5.8 BARNES ICE CAP, SURGE PROBLEM: (a) Surface velocity variation from preliminary analysis, and (b) Non-variable basal boundary conditions for creep analysis.

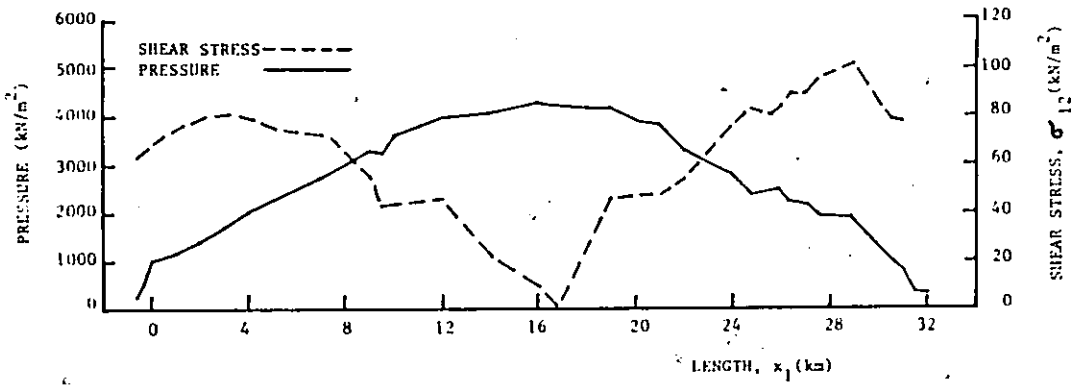

FIGURE 5.9 BARNES ICE CAP, SURGE PROBLEM - Average pressure and shear stress distributions within basal elements, preliminary analysis (Model C).

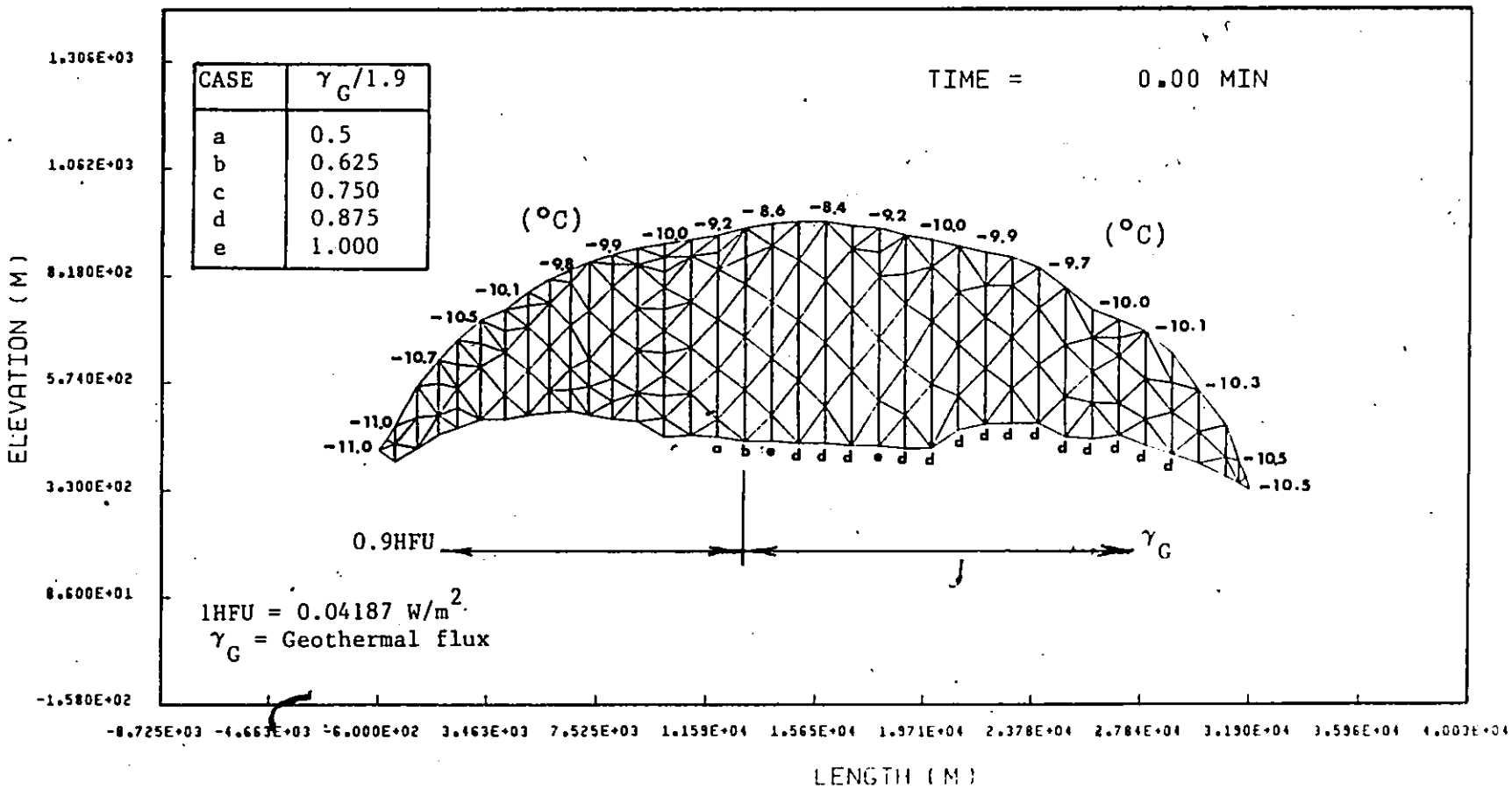

FIGURE 5.10 BARNES ICE CAP, SURGE PROBLEM - Thermal boundary conditions for preliminary analysis. Lower case letters at base give geothermal flux values when basal ice reaches pressure-melting temperatures.

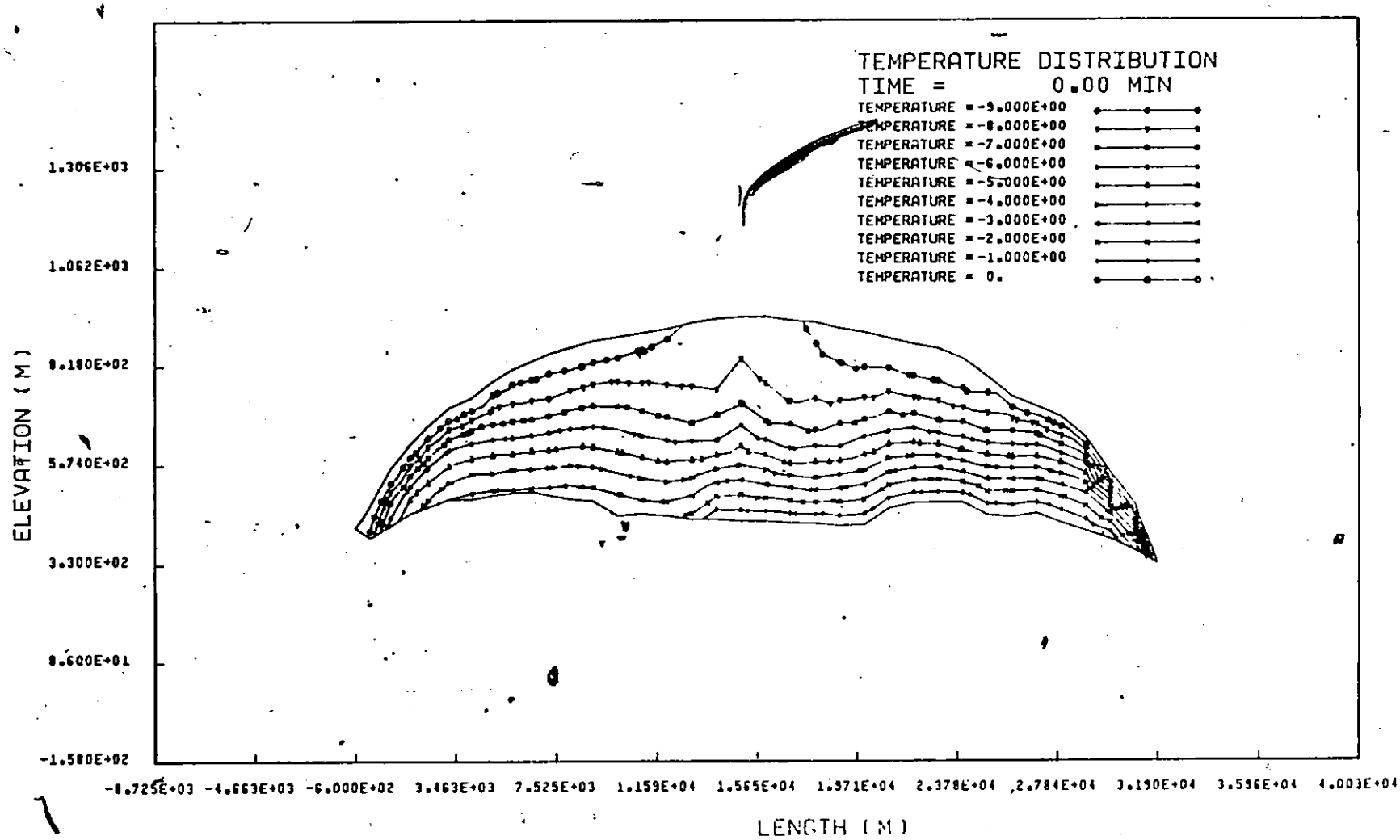

FIGURE 5.11 BARNES ICE CAP, SURGE PROBLEM - Steady-state temperature contours for γ_G = 1.9 HFU.

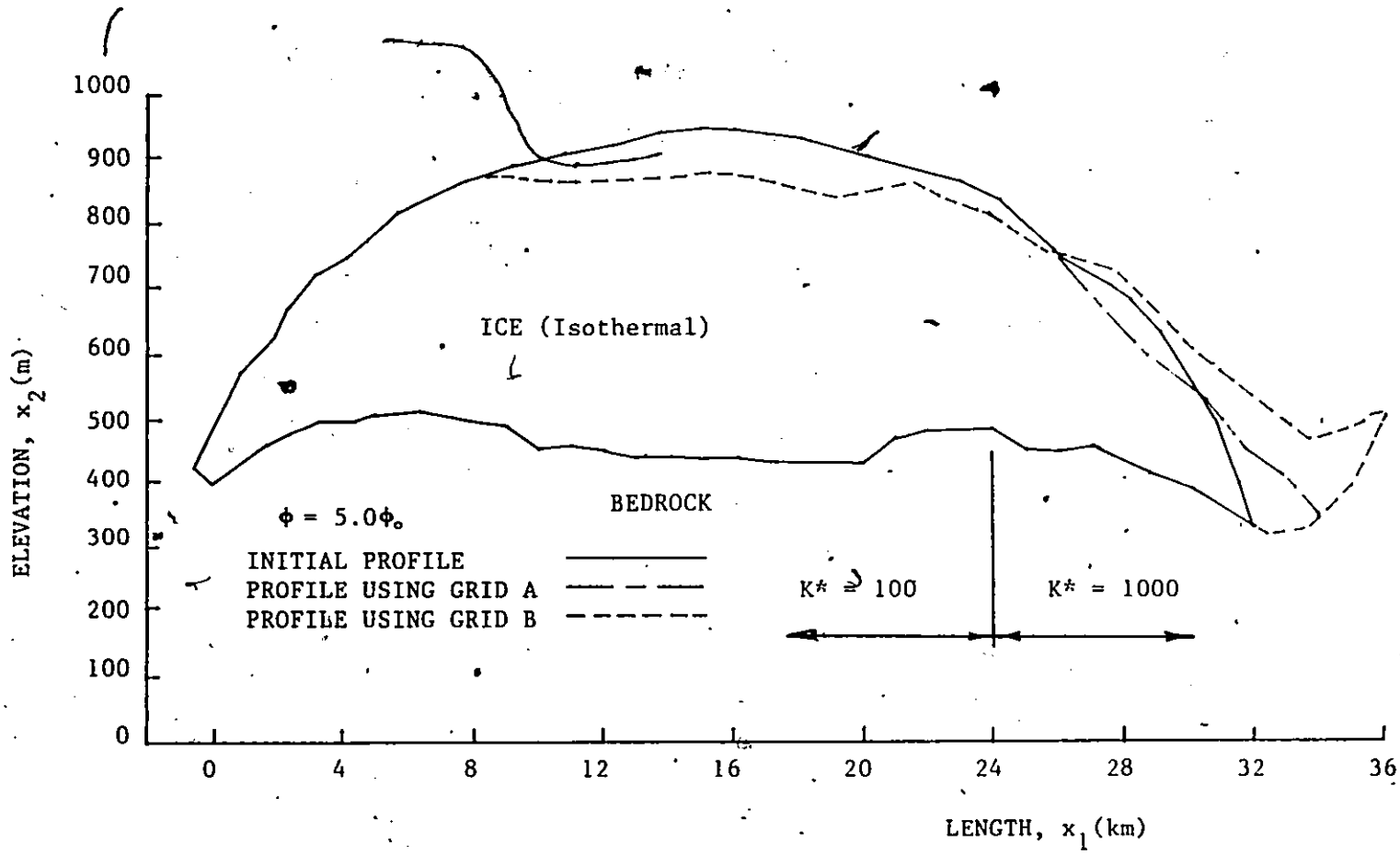

FIGURE 5.12 BARNES ICE CAP, SURGE PROBLEM - Ice cap profiles after surging 1.4 years. Comparison of solutions using Grids A and B (Model C).

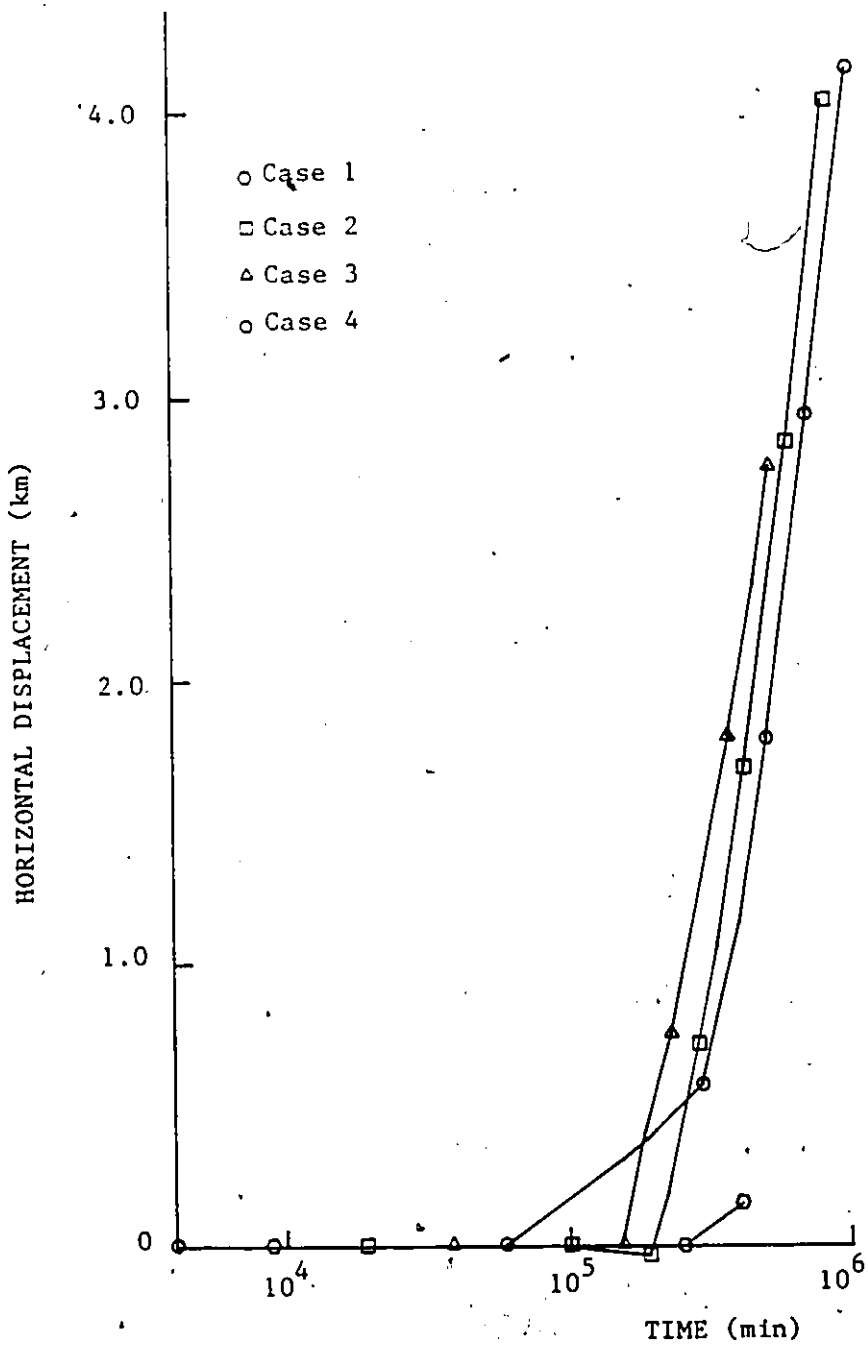

FIGURE 5.13 BARNES ICE CAP, SURGE PROBLEM - Advance of south-west margin (Model C).

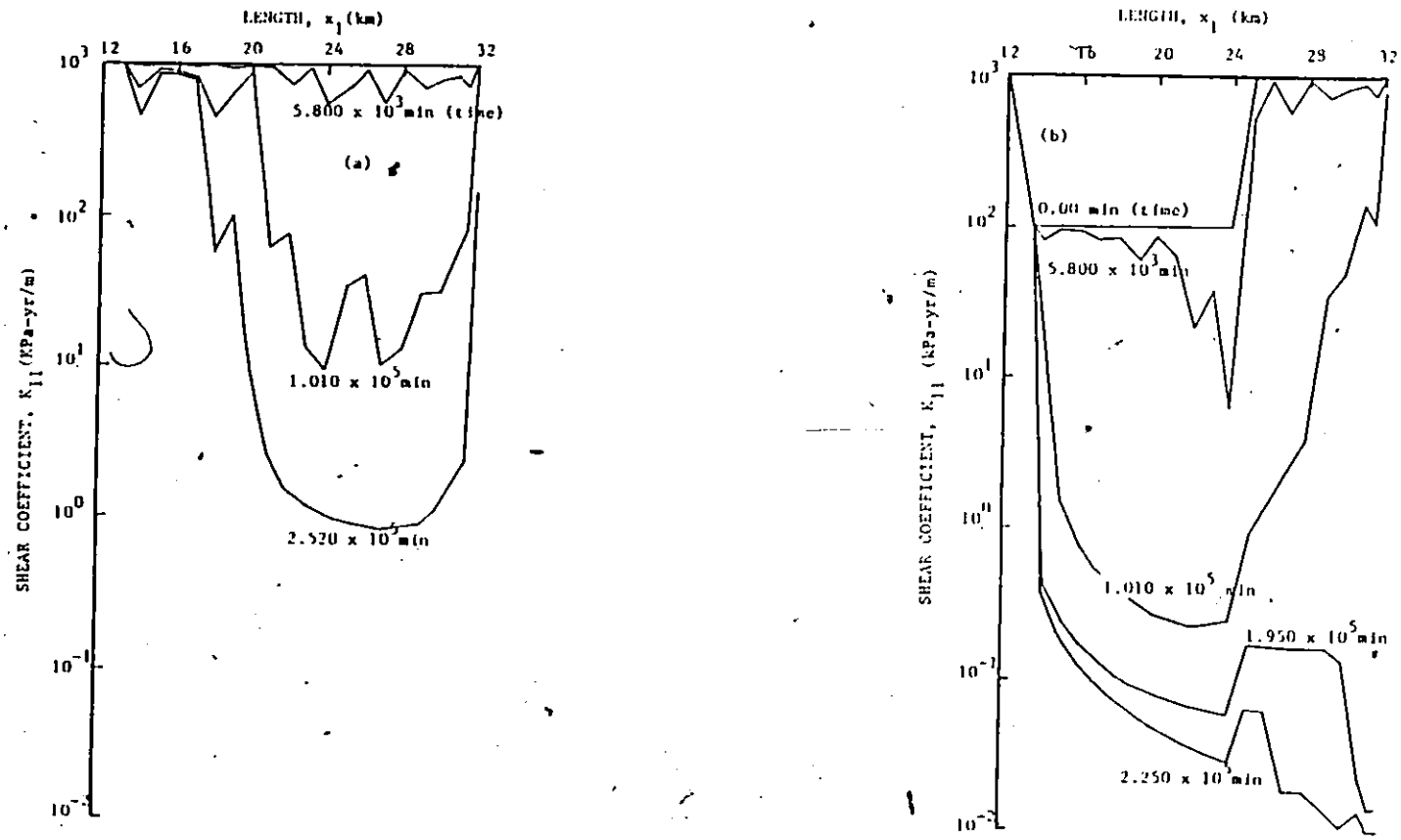

FIGURE 5.14, BARNES ICE CAP, SURGE PROBLEM - Remaining basal shear resistance in surge zone: (a) Case 1, (b) Case 2, (c) Case 3, and (d) Case 4 (Model C).

(cont'd on next page)

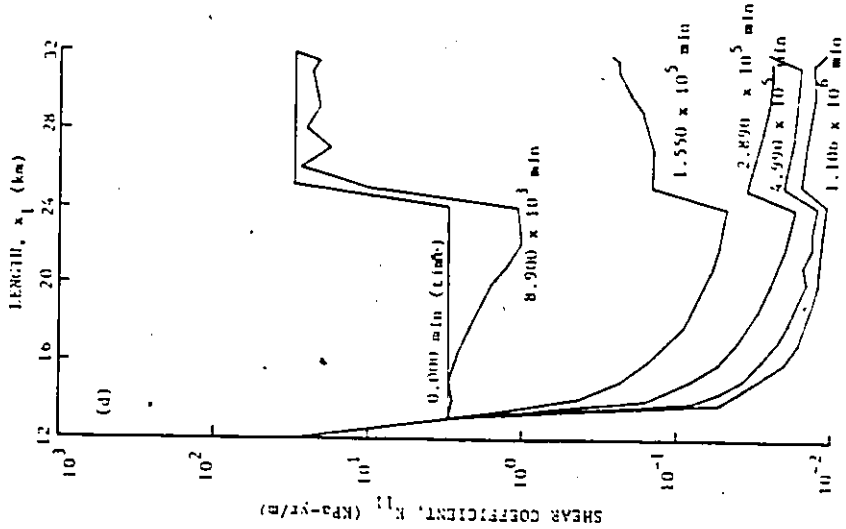
(d)
LENGTH, x_1 (km)
SHEAR COEFFICIENT, K_{11} (KPa-yr/m)
0.000 min (time)
8.900 x 10^3 min
1.550 x 10^5 min
2.890 x 10^5 min
4.990 x 10^5 min
1.100 x 10^6 min

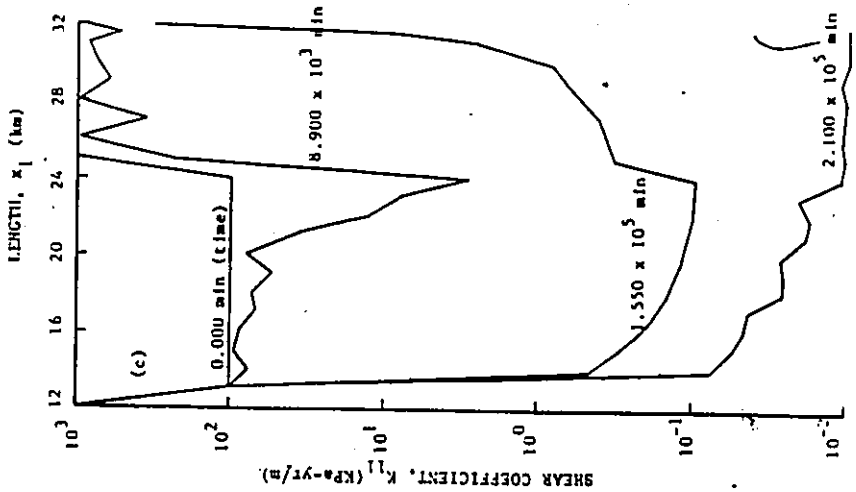
(c)
LENGTH, x_1 (km)
SHEAR COEFFICIENT, K_{11} (KPa-yr/m)
0.000 min (time)
8.900 x 10^3 min
1.550 x 10^5 min
2.100 x 10^5 min

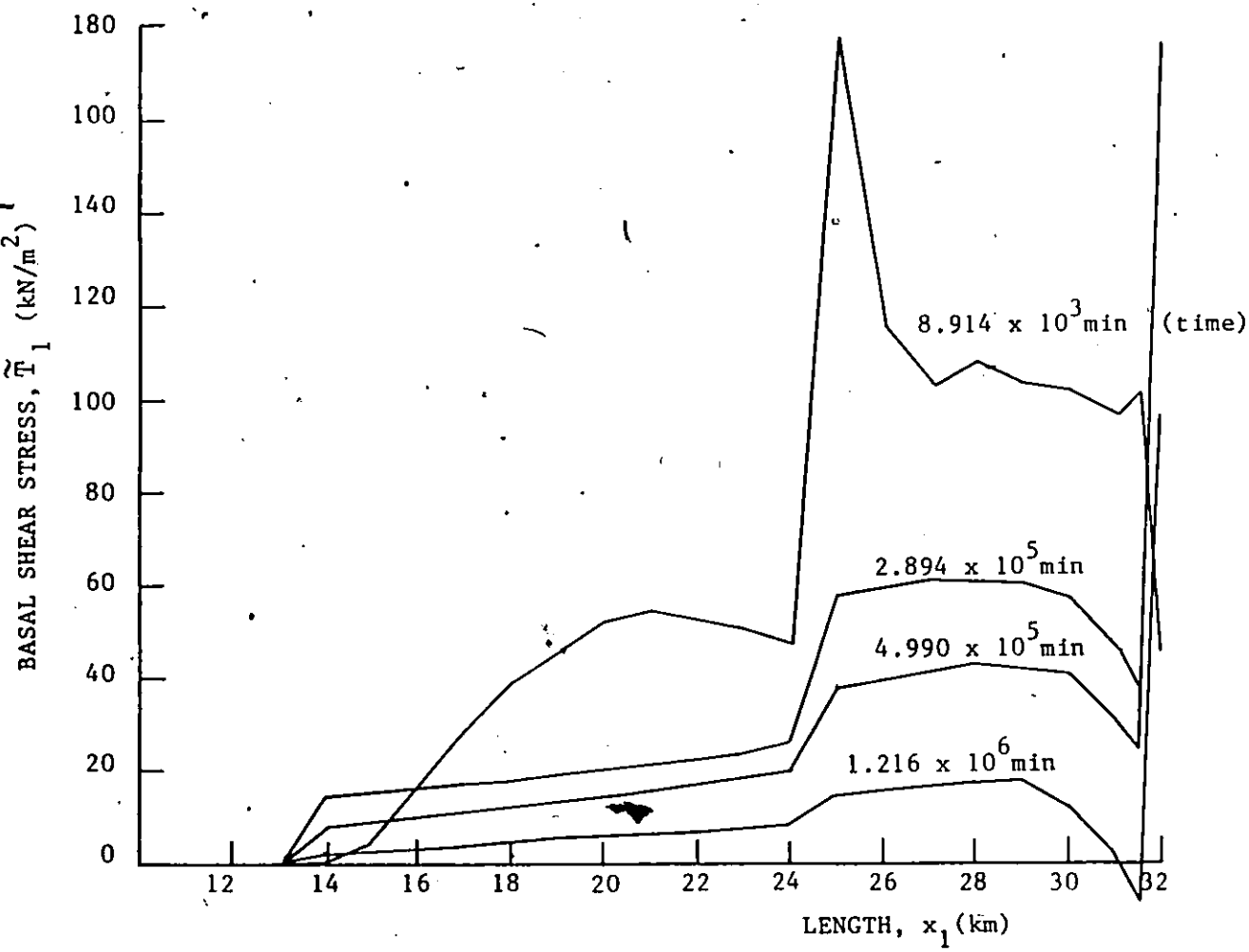

FIGURE 5.15 BARNES ICE CAP, SURGE PROBLEM - Basal shear stress variation during surging, Case 4 (Model C).

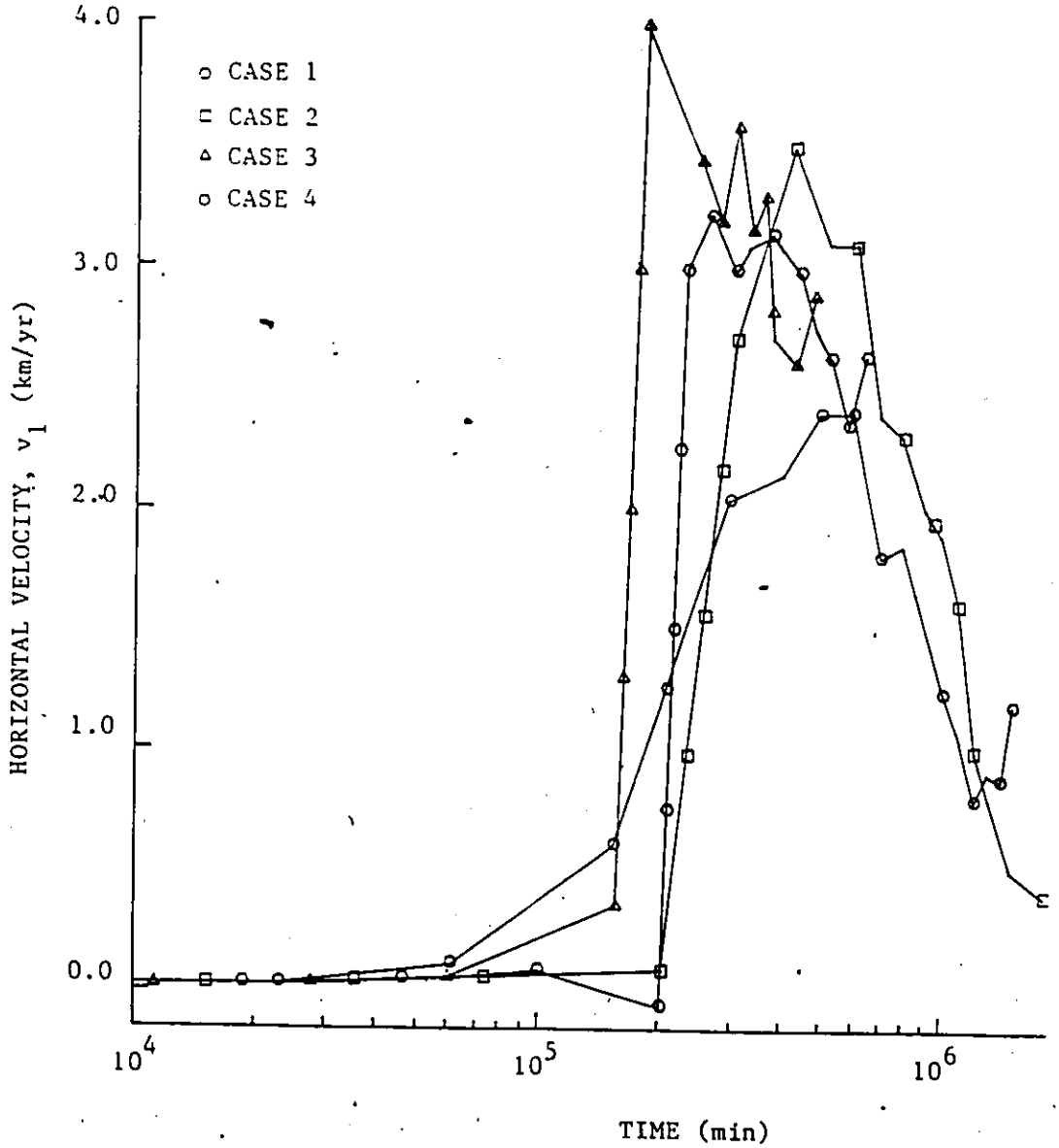

FIGURE 5.16 BARNES ICE CAP, SURGE PROBLEM - Horizontal surface velocity at node 165 with respect to time (Model C).

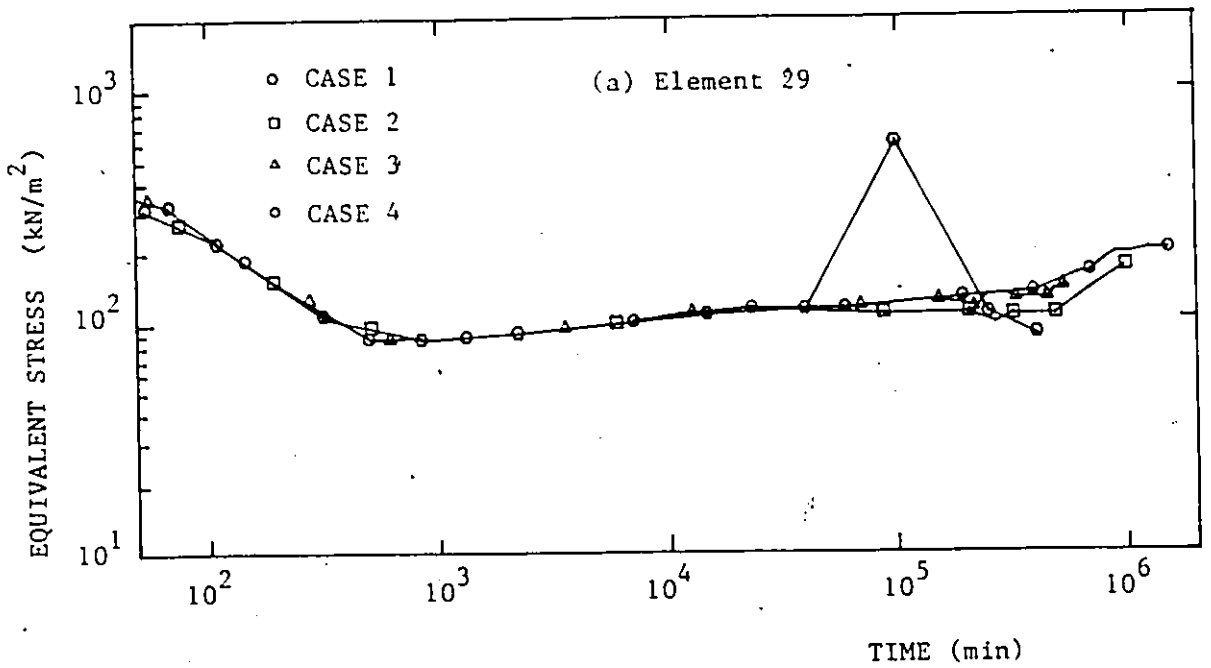

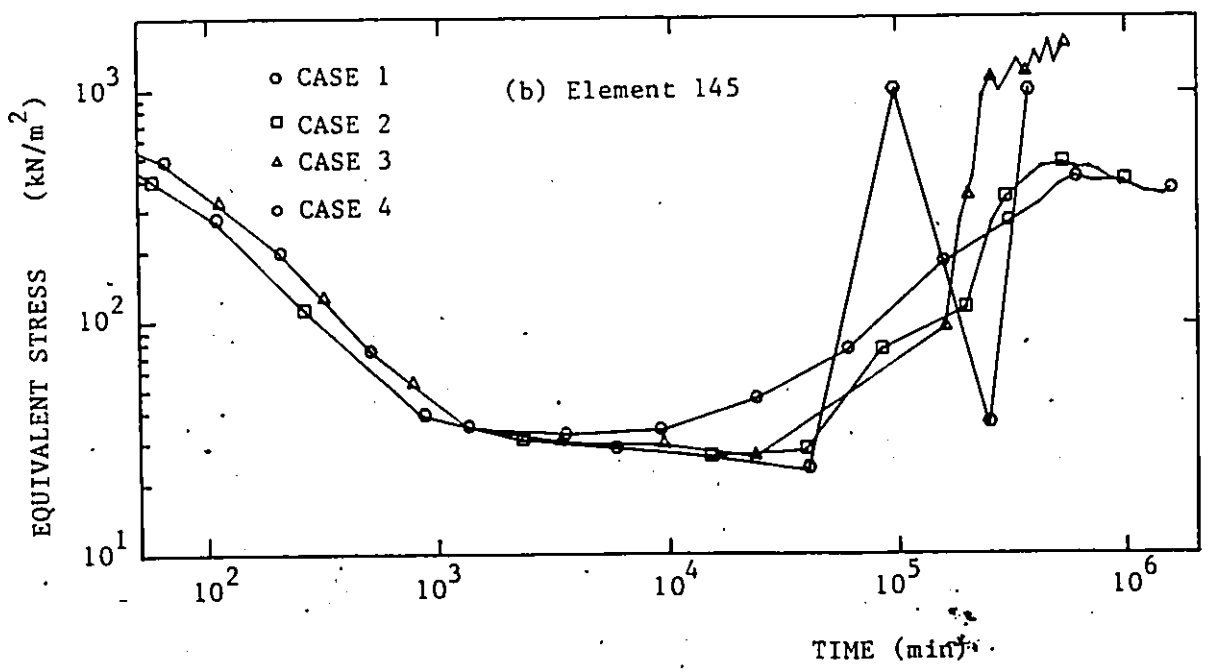

FIGURE 5.17 BARNES ICE CAP, SURGE PROBLEM - Equivalent stress with respect to time in: (a) element 29, (b) element 145, and (c) element 244 (Model C).

(cont'd on next page)

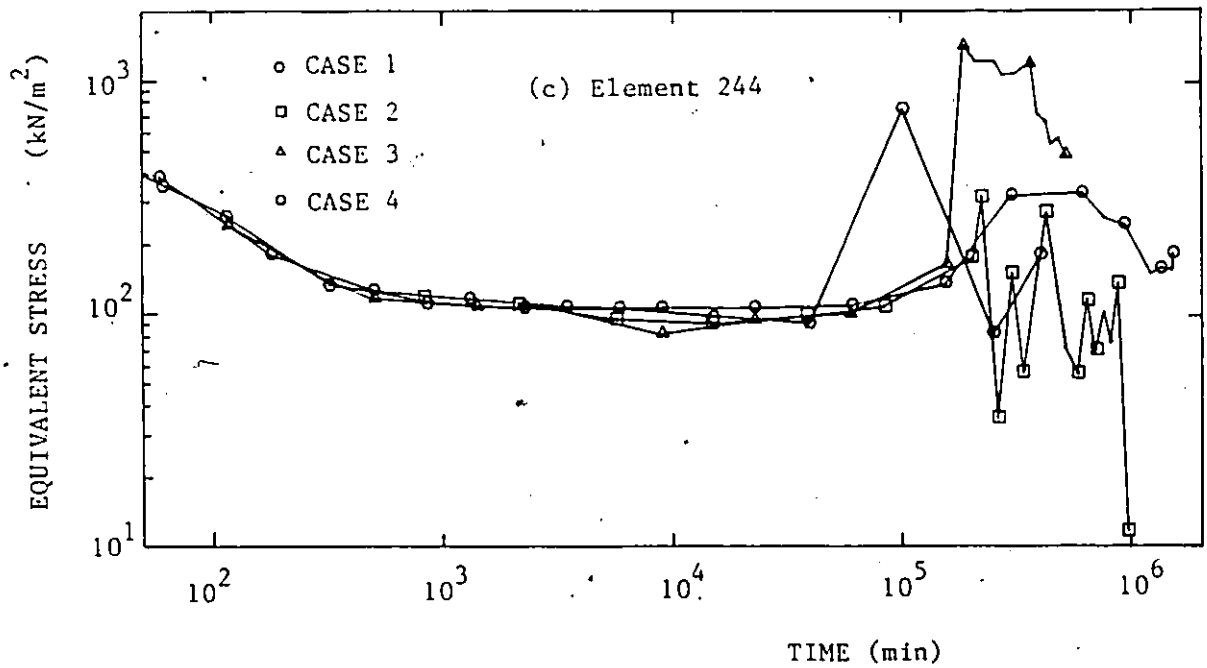
CASE 1
CASE 2
CASE 3
CASE 4
(c) Element 244
EQUIVALENT STRESS (kN/m^2)
10^3
10^2
10^1
10^2
10^3
10^4
10^5
10^6
TIME (min)

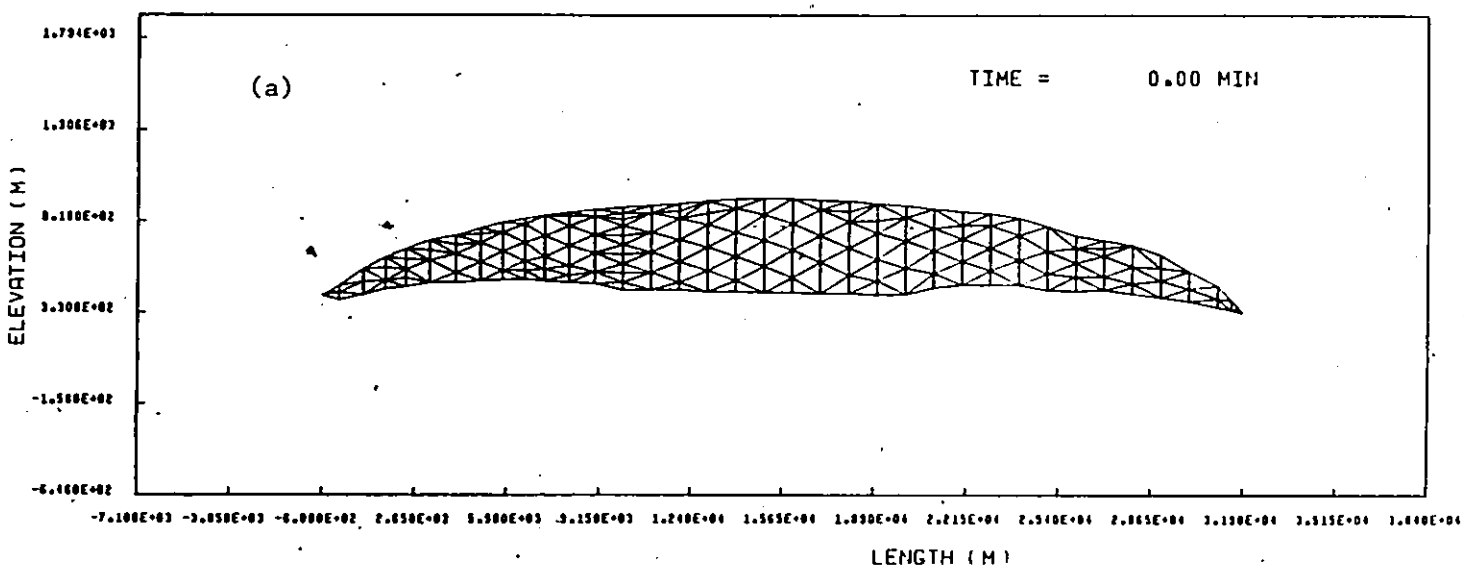

FIGURE 5.18 BARNES ICE CAP, SURGE PROBLEM - Profiles of ice cap for Case 2 at time: (a) 0.00 years, (b) 0.45 years, and (c) 2.29 years.

(cont'd on next page)

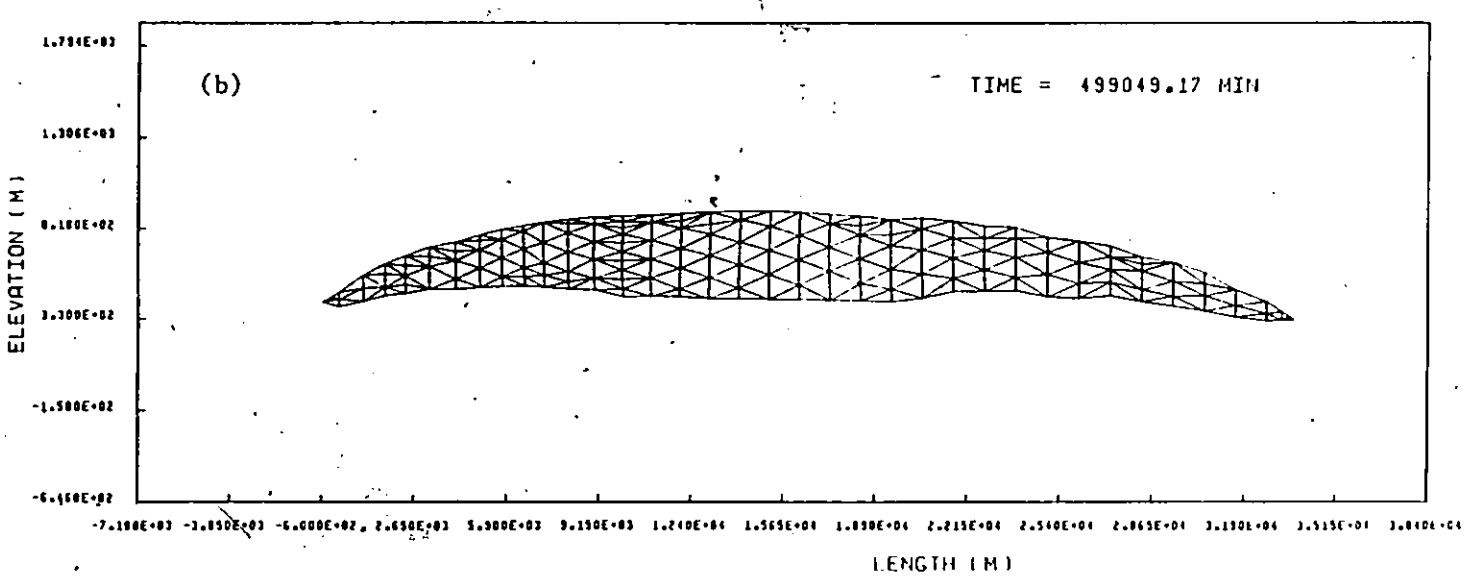

(cont'd on next page)

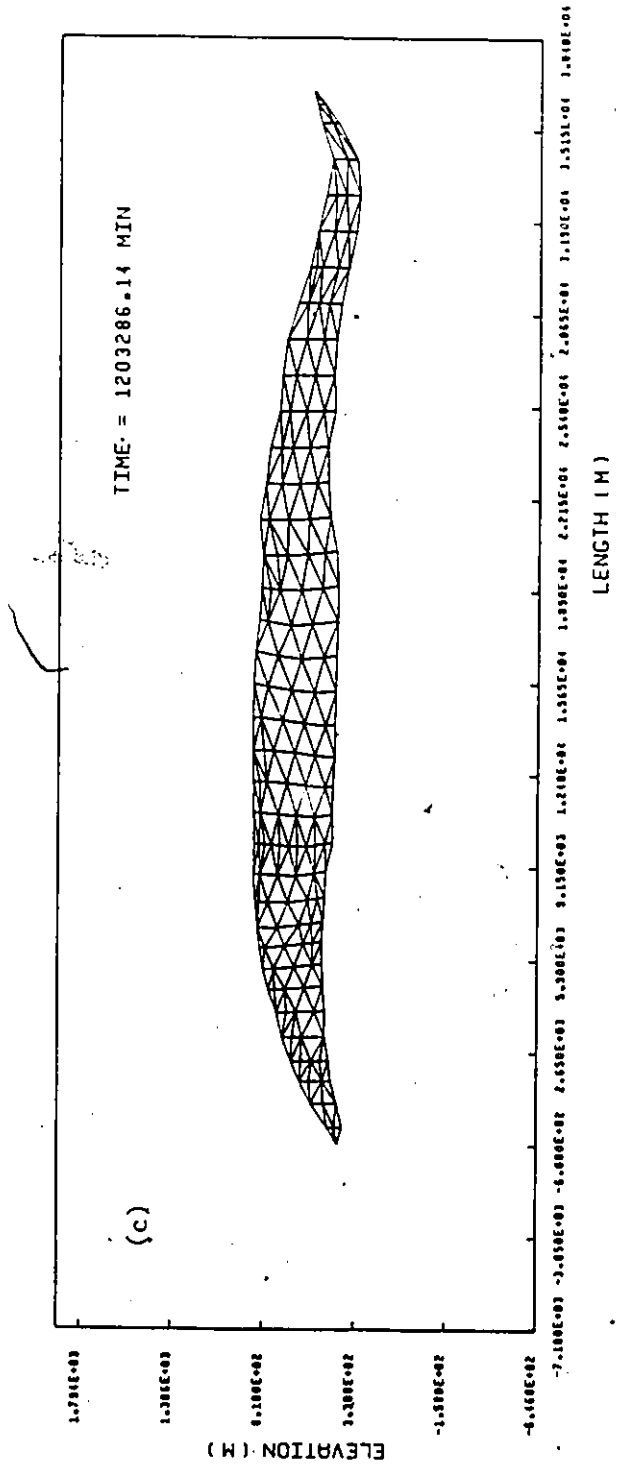
TIME = 1203286.14 MIN
(c)
ELEVATION (M)
LENGTH (M)

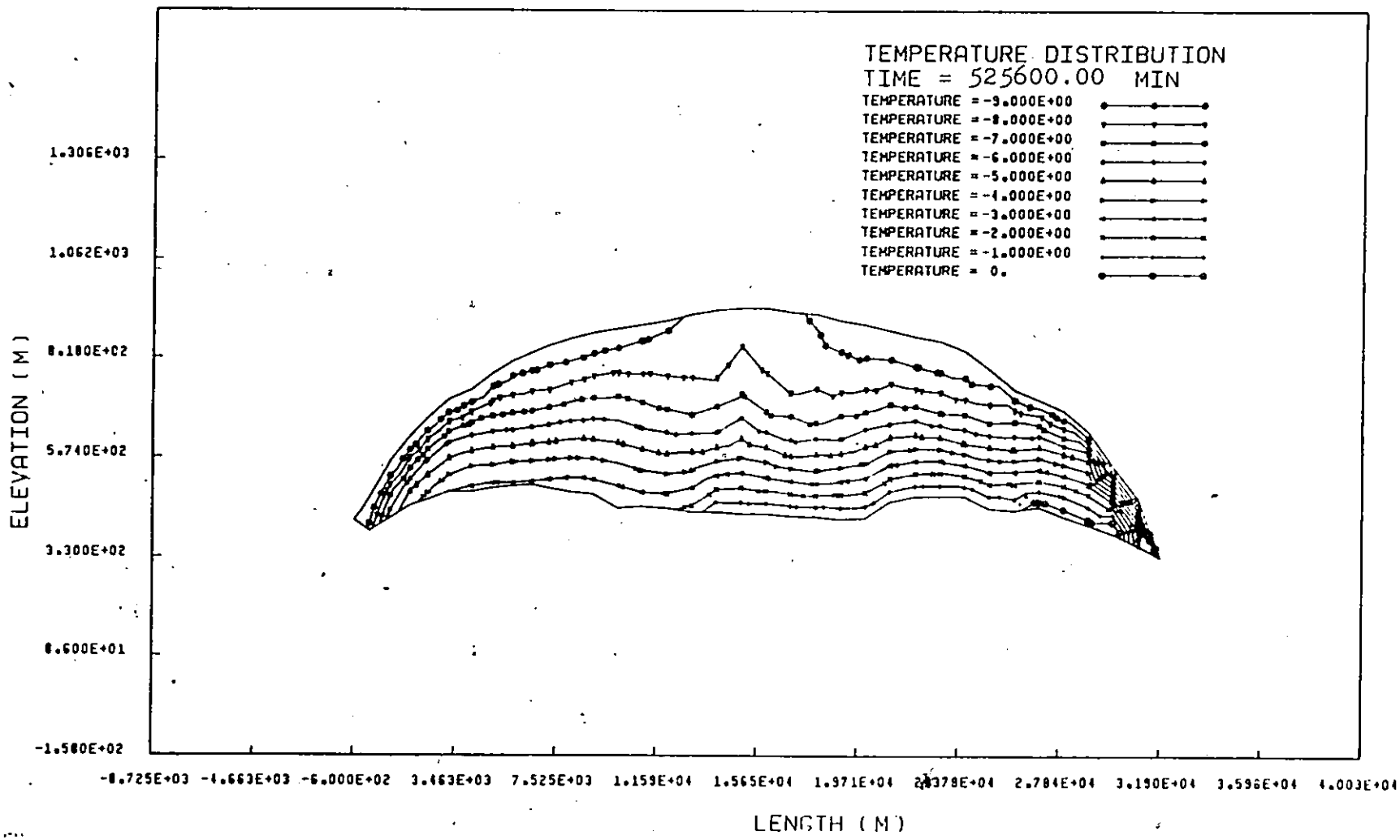

FIGURE 5.19 BARNES ICE CAP, SURGE PROBLEM - Temperature contours of ice cap: (a) Case 3 at 1.00 years (Model C), and

(cont'd on next page)

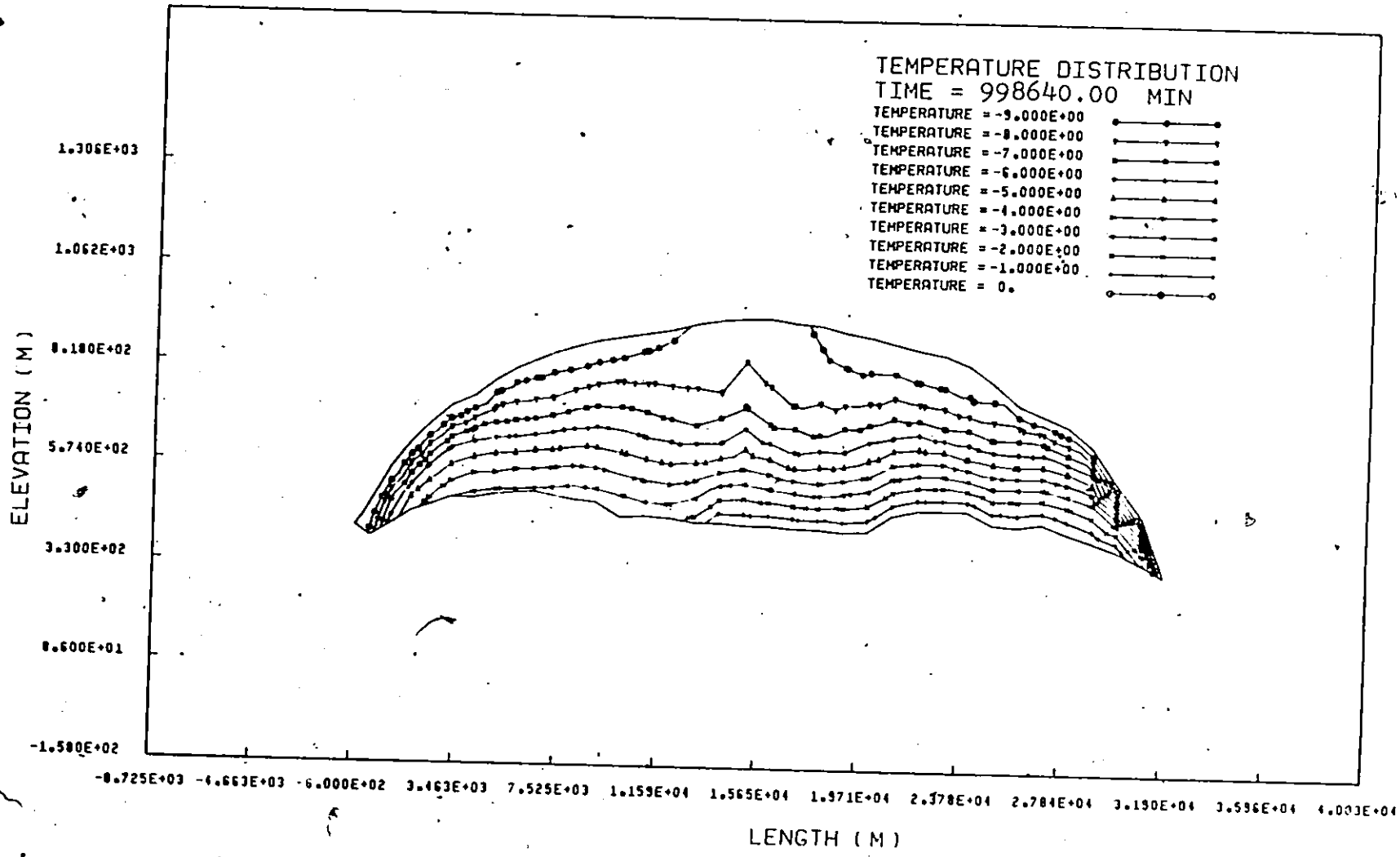

(b) Case 4 at 1.90 years (Model C).

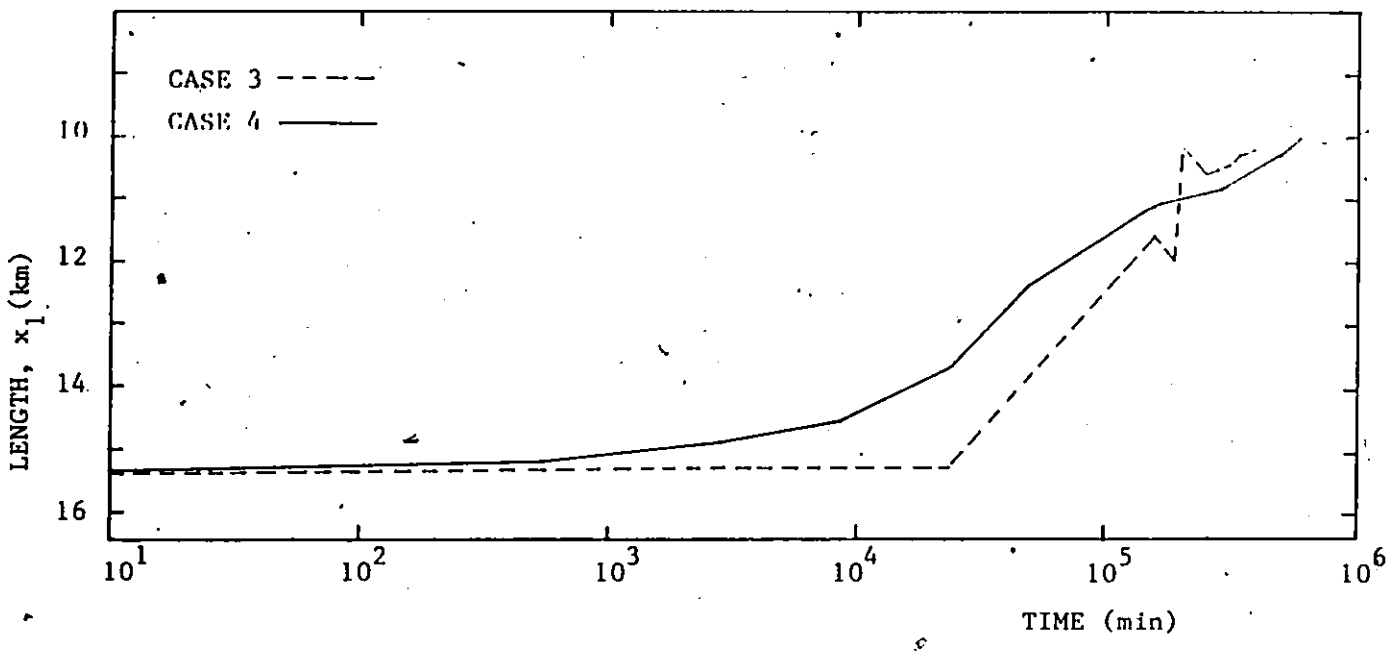

FIGURE 5.20 BARNES ICE CAP, SURGE PROBLEM - Change in position of dynamic divide during a surge.

CHAPTER 6

CONCLUSIONS

The finite element method is a powerful tool as has been demonstrated for temperature and creep analyses of large ice masses. Both steady-state and transient models have been presented. More important were the developments of the transient nonlinear creep and thermal analysis models which can solve problems where ice properties and boundary conditions may depend on time, stress and/or temperature. These transient models incorporate implicit time-marching schemes which improve the numerical stability of the algorithms when compared with the previous transient finite element models used in ice dynamics [24]. A time-dependent sliding element, also incorporating an implicit time-marching scheme, has also been developed. This element was used for sliding at the ice-bedrock interface. By allowing for time-dependent changes in the sliding resistance, the transient nonlinear creep model was used to study surging phenomenon based on basal instability. Thermal changes during creep were incorporated into the transient model through stepwise uncoupling of temperature and creep analyses.

When trying to model the temperature and velocity distributions of large ice massses, there are two major challenges: to develop a model that can describe the observed phenomena; and to determine suitable material properties for use in the model for analyzing large ice masses. Emphasis in this study has been placed on the modelling aspects. Suitable material properties were selected from the literature

whenever possible. For parameters which were not available in the literature, a parametric study was completed to determine their influence on the deformation and instability of large ice masses, especially the lubrication factor for basal instability.

It was demonstrated that transient creep analyses are not sensitive to initial stresses. For different initial stresses, all transient creep simulations converged rapidly to nearly the same velocity and stress fields for the double slope ice mass problem. Therefore, it can be concluded that the dynamic responses of large ice masses under self weight and over large periods of time depend only on the appropriate creep relationships, current temperature profiles and boundary conditions.

For most ice masses the temperature distributions are not well documented and uncertainty exists concerning the validity of steady-state conditions for computing temperature profiles. It was observed in this study that the transient thermal behaviour of large ice masses is very sensitive to initial temperature fields and insensitive to short-term temperature changes. A transient thermal study of the Barnes Ice Cap, presented in Appendix A5, demonstrated that it takes of the order of 10^3 years for the complete ice cap to adjust to new velocity fields and boundary conditions. Consequently the ability to accurately model the deformation of large ice masses also depends on one's ability to determine the ice body temperature profiles, whether through field explorations or numerical studies.

It was observed that the compressibility of a flow field due to elastic volumetric compliance had little influence on the computed velocities of a simple double slope ice mass with simple boundary conditions. However, the effect of compressibility was very noticeable when sliding was allowed along an irregular ice-bedrock interface of a more complex problem of Barnes Ice Cap presented in Appendix A5. Compressibility of the flow field appeared to reduce high velocity gradients which developed when enforcing compressibility. This suggested that it may be premature to assume that elastic strains are negligible even though they are small in magnitude when compared to creep strains. In general, computed velocities were very sensitive to the manner in which the basal boundary was handled.

The Erebus Glacier Tongue was studied to determine the temperature field within the glacier tongue. It was found that the upstream thermal and velocity boundary conditions were both very important for modelling this ice mass. The creep analysis was completed to approximate a very reasonable velocity field for advection in the thermal analysis. To incorporate thermal advection into the analysis, an upwinding scheme for triangular elements was incorporated. It was shown that reasonable velocity fields could only be achieved by assuming that the ice is not frozen to the bedrock at the transition between the land-based and the floating glacier. A gradual transition must exist to ensure that the ice does not fracture in the transition zone. Unlike the temperature field of the Barnes Ice Cap, which was very sensitive to vertical advection (see Appendix A5), the temperature field for the glacier tongue was dominated by the influence of nearly horizontal ther-

mal advection. The influence of horizontal advection was so strong that a large heat input due to the latent heat from freezing of sea water at the bottom boundary had little effect, even on the local temperature field.

Steady-state temperature simulations for the pre-surge profile of the Barnes Ice Cap indicated that a geothermal flux approaching 1.9 HFU is required to bring most of the south-west ice-bedrock interface to pressure melting. This conclusion is consistent with that by Holdsworth [41] who indicated that a high geothermal flux is required on the south-west side of the ice cap for it to surge due to basal instability. A few hypothetical surge simulations of the Barnes Ice Cap were completed to demonstrate the ability and the flexibility of the transient finite element model, developed herein, to solve practical problems. A limitation of these simulations was that the surge sliding parameters were not known and therefore had to be assumed. An attempt was made to choose these parameters in such a way as to ensure that most of a surge was completed during a two year period. For the parameters selected, the simulations appeared to be very reasonable. The transient model was able to predict the changes in velocity and stress fields that were anticipated to occur during a surge according to the trends reported in the literature. It was observed that the temperature changes due to increased frictional heating, as a result of surging, were negligible. The basal shear stresses at the margin, where the ice was frozen to the bedrock, were too low to cause any plastic yielding. This was attributed to the initial shear resistance distributions that were used in the analyses. Further investigation is required to determine parameters to

control yielding at the margin in accordance with the physics of the problem. While the lubrication factor was adjusted for rapid surging (within two years) the actual surge may have occurred over a longer period of time than was allowed in this study.

A major limitation of the transient creep model was due to the use of constant stress triangular elements. This element was responsible for inability of modelling high strain gradients when the mesh was too crude. Furthermore, due to creep incompressibility, normal stresses drifted and lead to undesirable constraints for some boundary conditions. These problems can be remedied through the use of higher order elements.

Based on this study, the following topics appear to require further investigation:

1. Although short-term creep simulations of large ice masses can be completed with the models developed herein, it is suggested that these models should be extended to include the influence of mass balance. By including mass balance, simulations can be carried out for much longer times. Thus, surge simulations can include both the initiation and propagation stages.
2. More field studies are required to determine relevant sliding parameters and constitutive relationships for the Barnes Ice Cap. These studies should include determination of the spatial distribution of parameters for sliding and creep flow laws.
3. Some of the difficulties of achieving close agreement between measured and computed surface velocities of the Barnes Ice Cap

have been attributed to anisotropy. Thus creep relationships should be extended to model anisotropy.

4. A major restriction of the models developed herein is that they apply only to planar flow. Provisions should be made to take into account strains in the lateral direction where it is not possible to identify planar flow situations.

Although the recommendations for future extensions of the models presented in this work are necessary, it is also important to appreciate that certain parameters have been identified. Hopefully their influence on the dynamics of large ice masses, reported in this study, will play relevant roles in future investigations.

APPENDIX A1

CHARACTERISTICS ASSOCIATED WITH CATASTROPHIC ADVANCES

Although limited information exists on the behaviour of surging ice masses during instability, some important observations noted by glaciologists are summarized below.

1. The geographic distribution of surging glaciers is not random, i.e. they are relatively common in some mountain regions but absent in others [83]. The environmental circumstances influencing their distribution are obscure. No specific climatic influence common to all regions has been found [65]. Based on the study of several surging glaciers in the Soviet Union, Dolgoushin and Osipova [20] indicated that these ice masses are concentrated in areas of recent glaciation.
2. The surging ice masses appear to reach instability in cycles of reasonably constant periods ranging between 10 and 100 years. The relatively constant periodicity and asynchronous behaviour of surging glaciers within a local area suggests that a surge is triggered internally [85]. During the quiescent phase the reservoir zone builds up and becomes more active while the ablation zone wastes away. This period of normal flow is followed by a relatively short active phase where the ice mass becomes unstable resulting in a large transfer of mass from the reservoir to the ablation zone [84]. The reservoir zone lowers on an average of 50 to 70 metres [20]. The accumulation and ablation

conditions have an influence on the duration and amplitude of the surge.

3. Weertman [95] indicates that rapid creep deformations within an ice mass do not alone account for the observed increase in velocity from the quiescent to the active phase, i.e. velocity increases from 10 to 100 times that observed in the quiescent phase. Based on current knowledge it is suggested that the propagation of surges involves drastic changes in bed friction which depends on the bed conditions and the interaction of the glacier sole with the subglacial hydraulic network at the ice-bed interface. For sliding to occur the ice-bed interface must be temperate.

4. Initially it was thought that surging glaciers are relatively long, i.e. from 15 to 30 kilometers [81]. More recent reports suggest that the length of a glacier does not appear to be a key factor associated with surging glaciers [20].

5. The advance of the glacier snout reaches approximately the same limits during each surge [87].

6. A number of surging glaciers lie along fault lines. There does not appear to be any correlation in space or time between the surges and the earthquakes in these areas [82].

APPENDIX A2

SURGE MECHANISMS

A2.1 General

Mechanisms contributing to ice mass instability are presented here. Three mechanisms are considered: material failure; thermal instability; and basal sliding instability. A fourth mechanism is discussed by Robin [87] and some description is provided here. He considers field conditions based on steady-state flow for which nonunique glacier configurations may exist. Robin suggests that a surge can be triggered when a glacier moves from one state of stress to another due to a buildup of ice in the reservoir zone. Unfortunately, he does not demonstrate that such conditions can be attained for unsteady flow. Weertman (in discussion to Robin [87]), indicates that such a mechanism can perhaps contribute to surge initiation, but is not responsible for surge propagation.

A2.2 Material Failure

Laboratory results for constant strain rate and constant stress tests suggest that instability may occur due to exceeding a maximum allowable yield stress or some critical strain as illustrated in Figures A2.1(a) and (b). Most experimental studies [28] have been completed for loading conditions not typical of conditions in natural ice masses. It is suggested that conditions under which the ice may undergo yielding

are likely to occur during a surge but not before a surge.

Microcracking in ice has been investigated by Gold [29, 30] in the laboratory and by Neave and Savage [69] out in the field. Laboratory experiments indicate that microcracking is highly sensitive to strain rate, temperature, type of loading, ice structure, etc. Neave and Savage investigated faulting at the base of the Athabaska Glacier, a location considered to be ideal for faulting due to high shear stresses and strain rates. Their field evidence suggested that most icequakes are near the surface (crevassing) and not within the basal layer.

Jonas and Müller [50] proposed that a surge can be initiated due to ice recrystallization either by rapid reduction in dislocation density or due to reorientation of basal planes more favourable to deformation. Experimental evidence indicates that recrystallization, in addition to microcracking, can lead to higher deformation rates and perhaps failure. In view of the long residence life of basal ice during which a preferred fabric can develop, it is questionable whether significant microstructural changes can occur to initiate a surge.

Material failure may be an important mechanism contributing to surge propagation. If appropriate creep rupture data is available, one can incorporate the influence of material failure into a surge model [22].

A2.3 Thermal Instability

Robin [86] first proposed a thermal runaway mechanism for instability of cold ice masses. He suggested that if the temperature at the base of a cold glacier can warm up slightly, this increase may be sufficient to initiate a positive-feedback cycle between energy dissipation and temperature at the base. When the temperature reaches pressure melting, the glacier will slide and become unstable. The ice mass will eventually slow down due to cold ice being advected downward. The slowing down of the surge is due to refreezing of the ice-bed interface. In a later version, Robin [87] suggested that the surge slows down for mechanical reasons.

Based on numerical modelling of thermal runaway, Clarke et al. [15] indicated: ablation tends to reduce stability while accumulation increases it; ablation increases growth time for instability whereas accumulation decreases it; a change from a frozen ice-bed interface to a temperate one can restore thermal stability; and growth times to reach instability are of the order of 10^2 - 10^3 years for glaciers and 10^3 - 10^4 years for large ice caps. Due to the length of time to develop a surge by thermal runaway, this mechanism cannot account for the instability of most surging glaciers. Clarke [14] indicated that even if the thermal mechanism is not responsible for surge initiation, the temperature distribution plays an important role in the timing of a surge cycle.

Most studies on thermal runaway, if not all, are purely thermal and do not account for the dynamic response of the ice mass.

A2.4 Instability Due to Basal Sliding

The most popular mechanism for catastrophic advances is the water-film mechanism proposed by Weertman [95, 97]. Emphasis in his theory is placed on the possibility of water collecting under a surging ice mass. This water reduces the basal sliding resistance to the extent that an instability can occur. Important features required for a surge to develop with this mechanism are: the basal ice must be at pressure melting; the bed must be watertight; and the excess water due to frictional heating must flow as a sheet.

Based on Weertman's mechanism, Robin and Weertman [88] developed a phenomenological model that describes a mechanism by which water of sufficient thickness can collect and cause instability. Their mechanism involves blocking of water flow at the ice-bedrock interface due to zero pressure gradients. The pressure gradients are related to changes in basal shear stress. Assumptions, in addition to those above, for the development of their model include: water pressure is given by Kamb's theory of sliding; water pressure is not strongly coupled with the subglacial hydraulic network; and Nye channels (incised into rock) are not well developed in the surge trigger zone. Even if all the assumptions at the ice-bed interface are valid before the surge, Kamb's theory for computing the pressure gradients is not valid once the water layer reaches an appreciable thickness. For such conditions the water pres-

sure becomes dependent on the regional hydraulic network [57].

Rather than placing emphasis on the development of a thick water layer, instability may be initiated due to extensive cavitation at the ice-bedrock interface. This instability due to cavitation has been suggested by Lliboutry [56]. The importance of cavity formation for surging is also discussed by Raymond [85]. Cavitation is generally expected in regions where the ice is thin and surface slopes are relatively steep. Cavitation may also occur under thick ice for more usual surface slopes when cavity water pressures exceed one half the ice overburden pressure [52]. Budd et al. [10] indicated that the cavity pressures at the ice-bedrock interface can approach seventy percent of the ice overburden pressure.

An important consideration proposed by Röthlisberger (in discussion to Weertman [97]) is that once a surge begins to propagate, a well developed subglacial hydraulic system may be destroyed and may contribute to the ice mass instability if water should spread out in the form of a sheet. Due to the complex nature of the conditions at the ice-bedrock interface, uncertainty exists regarding the role of the hydraulic system at the ice-bed interface in surging.

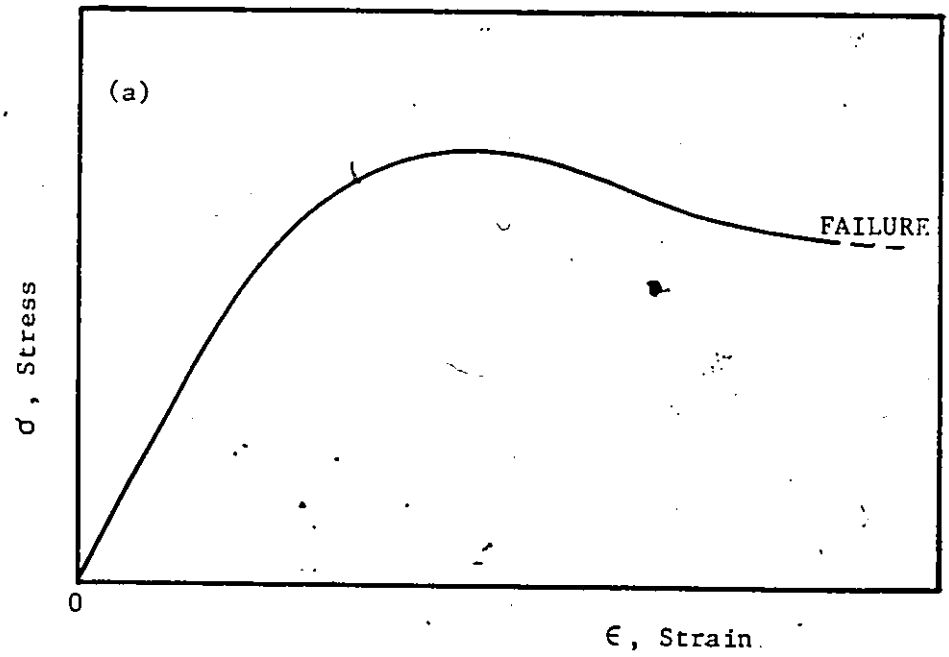

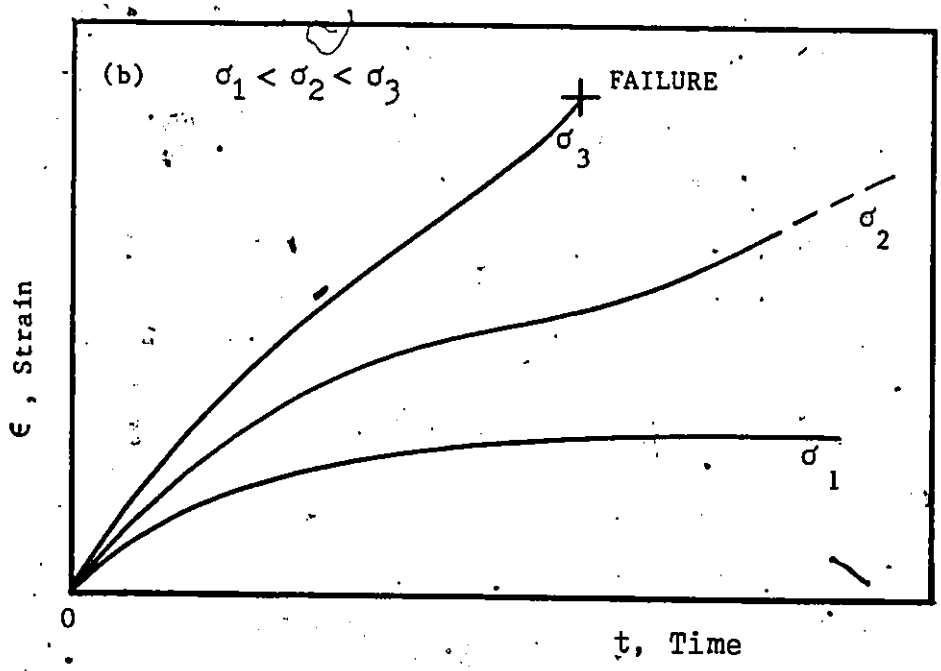

FIGURE A2.1 PLOTS FROM COMPRESSION TESTS: (a) Constant rate of strain, and (b) Constant stress (Schematics).

APPENDIX A3

STRENGTH PROPERTIES OF ICE

A3.1 General

Fresh water polycrystalline ice, although it has a common crystallographic structure, can have a wide range of material properties depending on: (1) test conditions, e.g., strain rate, temperature, specimen size and shape, etc.; (2) impurity and inclusion content; (3) texture; (4) fabric; (5) history of ice samples; (6) age of ice samples; and (7) crystal size. Other factors related to testing also influence the measured properties: (1) testing apparatus; (2) preparation techniques; and (3) sampling and storage conditions. With such a variety of factors influencing ice properties it is not expected that a close agreement among various studies on the properties of ice can be achieved. This has been recognized by many investigators [66].

The ultimate strengths of ice under high-loading rates and at -5°C have been quoted by Neave and Savage [69]: uniaxial tension, 15 bars (1.5 MPa); uniaxial compression, 35 bars; and shear, 7 bars. These ultimate strengths can vary by a factor of two or three. They also indicate that the above stresses are greater than those expected in ice masses. A summary of strengths are given in the following tables.

TABLE A3.1 COMPRESSIVE STRENGTH OF ICE

Reference	Temperature (°C)	Tensile Strength (MPa)	Ice Type
Butkovich [11]	-5 -20	2.8 3.4	Natural snow ice
Frederking [26]	-10	5.2 (uniaxial) 6.8 (plane-strain)	Granular-grained ice.

TABLE A3.2 TENSILE STRENGTH OF ICE

Reference	Temperature (°C)	Tensile Strength (MPa)	Ice Type	Type of Tests
Butkovich	-5	1.400	Artificial ice, grain randomly oriented	Uniaxial Tests
Kaplar	-6.5	1.296		
Jellinek	-4.5	1.517		
Carter	0 to -30	2.000		
Mellor & Hawkes	-7	[illegible]	Artificial ice, grain randomly oriented	Brazilian Tests
Butkovich	-5	0.4137		
Mellor & Hawkes	-7	0.378-0.678		
Hanson	-10	0.331-0.421		
Weeks	- 5	2.103-3.585	Sea ice	Ring Tests
Butkovich	-5 to -35	1.758-2.896	Artificial ice, Grain randomly oriented	
Mellor & Hawkes	-7	1.103-4.413		
Hanson	0 to -20	0.9998-3.206		
Frankenstein	0 to -5	1.413-1.896		

Tabulated by Nguyen [70].

TABLE A3.3 SHEAR STRENGTH OF ICE

Temperature (°C)	Shear Strength (MPa)	Type of Ice	Direction of Applied Stress
-5	0.8067	Lake ice; Grain with preferred orientation	//
-20	1.393		//
-5	1.345		⊥
-15	1.910		
-5	0.9791	Natural snow ice; Grain randomly oriented	
-20	1.076		

(Tabulated by Gold [30]).

Notation: // : parallel to long direction of grains
⊥ : perpendicular to long direction of grains.

APPENDIX A4

FINITE ELEMENT METHOD

A4.1 General

This appendix summarizes development of the finite element models for transient, non-linear creep. The displacement method is employed using the virtual work principle for planar elasticity and creep. The constant stress triangular element is used, but the method can be extended to include any higher order element. The continuum is subdivided into triangular elements of unit thickness as shown in Figure A4.1. The boundary for each body is approximated by straight lines joining the element nodes at the surface.

A4.2 Virtual Work Principle

Rather than working with a differential equation for equilibrium at a point, i.e.

$$\sigma_{ij,j} + b_i = 0 \qquad \text{(A4.1)}$$

equivalent integral statements which include the influence of boundary conditions are used when developing the finite element equations. For static equilibrium, the principle of virtual displacements is adopted, i.e. if a body under the action of a system of forces undergoes arbitrary virtual displacements during which forces do not change, the for-

ces will do zero work if and only if the forces are in equilibrium. The external work done by the forces can be shown to be equal to the internal work by using the divergence theorem. This is given by:

$$\int_{\Omega} \delta\varepsilon_{ij}\sigma_{ij}d\Omega - \int_{\Gamma_t} \delta u_i \bar{T}_i d\Gamma - \int_{\Omega} \delta u_i b_i d\Omega = 0 \qquad \text{(A4.2)}$$

where $\varepsilon_{ij} = \frac{1}{2}(u_{i,j} + u_{j,i})$ is the strain tensor

u_i = displacement in x_i direction

$\delta\varepsilon_{ij}$ = virtual strain tensor which is compatible with virtual displacements δu_i

σ_{ij} = stress tensor

b_i = body forces

$\bar{T}_i$ = $\sigma_{ij}\, n_j$ (specified traction on boundary Γ_0)

n_j = direction cosines of the unit outward normal to the boundary

Ω = volume of body

Γ_t = part of the boundary where the surface traction is applied.

On the boundaries where displacements are specified, the virtual displacements vanish. This principle is a statement of equilibrium and applies to linear and nonlinear problems.

A4.3 Discretized Equations

The entire problem domain Ω is divided into subdomains Ω_n (finite

elements) which are connected to each other at the nodal points. While the virtual work principle is a global statement, it is also applied to each element for formulating the discrete equilibrium equation. The displacement field within an element is approximated as:

$$\{u\} = [N]\ \{\delta\} \text{ or } u_i = \langle N_i \rangle\ \{\delta\} \qquad \text{(A4.3)}$$

where u_i is the displacement in the x_i direction, $\langle N_i \rangle$ is the ith row matrix of $[N]$ which contains the shape functions for u_i, and $\{\delta\}$ contains the nodal degrees of freedom (six for a constant stress triangular element).

$$\{\delta\}^T = \langle \delta_1, \delta_2, \ldots, \delta_6 \rangle \qquad \text{(A4.4)}$$

The shape functions are functions of position within the subdomain and are so chosen that the displacement compatibility between the elements is maintained.

For linear elastic problems, the stresses are related to the strains by the following constitutive equation,

$$\sigma_{ij} = D_{ijkl}\ \varepsilon_{kl} \quad \text{or} \quad \{\sigma\} = [D]\ \{\varepsilon\} \qquad \text{(A4.5)}$$

where $\{\varepsilon\} = [B]\{\delta\}$ and $[B]$ is commonly referred to as the strain matrix. The constitutive matrix $[D]$ can be found in most finite element texts [103]. For plane stress, it is given by

$$[D] = \frac{E}{1-\nu}\begin{bmatrix} 1 & \nu & 0 \\ \nu & 1 & 0 \\ 0 & 0 & \frac{(1-\nu)}{2} \end{bmatrix} \qquad (A4.6)$$

where E is the elastic modulus and ν, Poisson's ratio. The plane strain constitutive matrix can be obtained by replacing E and ν in Equation (A4.6) with $\frac{E}{1-\nu^2}$ and $\frac{\nu}{1-\nu}$, respectively.

Using Equations (A4.2) to (A4.5) and carrying out the usual finite element formulation gives

$$\delta\{\delta\}^T\left(\int_{\Omega_n} [B]^T[D][B]d\Omega\{\delta\} - \int_{\Gamma_{t_n}} [N]^T\{\bar{t}\}d\Gamma - \int_{\Omega_n} [N]^T\{b\}d\Omega\right) = \{0\} \qquad (A4.7)$$

where the subscript n refers to the nth element. For any arbitrary virtual displacement $\delta\{\delta\}^T$, Equation (A4.7) can only be satisfied if the equilibrium within the element is satisfied. By assembling the contributions from all of the elements and by imposing the appropriate compatibility of the nodal displacements, discretized equilibrium equations can be written in a compact form as follows;

$$[K]\{\Delta\} = \{P\} \qquad (A4.8.a)$$

where $\{\Delta\}$ contains all of the displacement global degrees of freedom that are unknown,

$$[K] = \sum_{1}^{N} \int_{\Omega_n} [B]^T [D][B] d\Omega \qquad \text{(A4.8.b)}$$

$$\{F\} = \sum_{1}^{N} \left(\int_{\Omega_n} [N]^T \{b\} d\Omega + \int_{\Gamma_{t_n}} [N]^T \{\bar{T}\} d\Gamma \right) \qquad \text{(A4.8.c)}$$

A4.4 Development of Plane Strain Elastic-Creep Compliance Matrix

In the implicit time-marching scheme adopted for this study, the plane strain conditions can only be imposed after all terms containing the stress increments $\{\Delta\sigma_n\}$ and the strain increments $\{\Delta\varepsilon_n\}$, during the nth creep iteration, have been expressed in the form of a constitutive relationship in the following form.

$$\begin{bmatrix} C_{11} & C_{12} & C_{13} & C_{14} \\ & C_{22} & C_{23} & C_{24} \\ \text{SYM} & & C_{33} & C_{34} \\ & & & C_{44} \end{bmatrix}_n \begin{Bmatrix} \Delta\sigma_{11} \\ \Delta\sigma_{22} \\ \Delta\sigma_{33} \\ \Delta\sigma_{12} \end{Bmatrix}_n = \begin{Bmatrix} \Delta\varepsilon_{11} \\ \Delta\varepsilon_{22} \\ \Delta\varepsilon_{33} \\ \Delta\gamma_{12} \end{Bmatrix}_n - \Delta t_n \begin{Bmatrix} \dot{\varepsilon}^c_{11} \\ \dot{\varepsilon}^c_{22} \\ \dot{\varepsilon}^c_{33} \\ \dot{\gamma}^c_{12} \end{Bmatrix}_n \qquad \text{(A4.9.a)}$$

The plane strain condition is enforced by allowing the total strain increment $\Delta\varepsilon_{33}$ to vanish in the form of a constraint. The effective compliance matrix is given by

$$[C_n] = [D] + \theta\Delta t_n [H_n] \qquad \text{(A4.9.b)}$$

where

$$[D]^{-1} = \frac{1}{E}\begin{bmatrix} 1 & -\nu & -\nu & 0 \\ & 1 & -\nu & 0 \\ \text{SYM} & & 1 & 0 \\ & & & 2(1+\nu) \end{bmatrix} \qquad \text{(A4.9.c)}$$

and

$$[H_n] = \phi_{1_n}\begin{bmatrix} a^2 & ab & ac & ad \\ & b^2 & bc & bd \\ \text{SYM} & & c^2 & cd \\ & & & d^2 \end{bmatrix}_n + \phi_{2_n}\begin{bmatrix} 2 & -1 & -1 & 0 \\ & 2 & -1 & 0 \\ \text{SYM} & & 2 & 0 \\ & & & 6 \end{bmatrix} \qquad \text{(A4.9.d)}$$

The symbols are defined as follows:

$$\phi_{1_n} = \left(\frac{\partial \dot{\varepsilon}_e^{\,c}}{\partial \sigma_e} - \frac{\dot{\varepsilon}_e^{\,c}}{\sigma_e}\right)_n, \qquad \phi_{2_n} = \left(\frac{1}{2}\frac{\dot{\varepsilon}_e^{\,c}}{\sigma_e}\right)_n$$

θ = degree of implicitness, Δt_n = time increment at time t_n

$\{\Delta\varepsilon_n\}$ = total strain increment vector, $\{\dot{\varepsilon}_n^{\,c}\}$ = creep strain-rate vector

σ_e = equivalent stress, $\dot{\varepsilon}_e^{\,c}$ = equivalent creep strain rate

$$a = \frac{\partial\sigma_e}{\partial\sigma_{11}} = \frac{1}{2\sigma_e}(2\sigma_{11} - \sigma_{22} - \sigma_{33}), \quad b = \frac{\partial\sigma_e}{\partial\sigma_{22}} = \frac{1}{2\sigma_e}(2\sigma_{22} - \sigma_{11} - \sigma_{33})$$

$$c = \frac{\partial\sigma_e}{\partial\sigma_{33}} = \frac{1}{2\sigma_e}(2\sigma_{33} - \sigma_{11} - \sigma_{22}), \quad d = \frac{\partial\sigma_e}{\partial\sigma_{12}} = 3\,\frac{\sigma_{12}}{\sigma_e}$$

$$\dot{\gamma}_{12}{}^{c} = 2\dot{\varepsilon}_{12}{}^{c}, \quad \Delta\gamma_{12} = 2\Delta\varepsilon_{12}.$$

Equation (A4.9.a) is condensed by removing the third row of this matrix equation and by replacing $\Delta\sigma_{33}$ in the remaining three equations with

$$\Delta\sigma_{33} = \frac{1}{C_{33}}[\Delta\varepsilon_{33} - \Delta t_n\dot{\varepsilon}_{33}{}^{c} - (C_{13}\Delta\sigma_{11} + C_{23}\Delta\sigma_{22} + C_{43}\Delta\sigma_{12})]_n. \quad \text{(A4.10.a)}$$

Before substituting for $\Delta\sigma_{33}$, the plane strain constraint ($\Delta\varepsilon_{33} = 0$) and creep incompressibility ($\dot{\varepsilon}_{ii}{}^{c} = 0$) are applied to Equation (A4.10.a), yielding

$$\Delta\sigma_{33} = \frac{1}{C_{33}}[(\dot{\varepsilon}_{11} + \dot{\varepsilon}_{22})\Delta t_n - (C_{13}\Delta\sigma_{11} + C_{23}\Delta\sigma_{22} + C_{43}\Delta\sigma_{12})]_n. \quad \text{(A4.10.b)}$$

After substituting Equation (A4.10.b) into (A4.9.a) and collecting all like terms, the constitutive relationship for plane strain creep deformation can be written in a condensed form as follows.

$$[C_n^*] \begin{Bmatrix} \Delta\sigma_{11} \\ \Delta\sigma_{22} \\ \Delta\sigma_{12} \end{Bmatrix}_n = \begin{Bmatrix} \Delta\varepsilon_{11} \\ \Delta\varepsilon_{22} \\ \Delta\gamma_{12} \end{Bmatrix}_n - \Delta t_n [\beta_n] \begin{Bmatrix} \dot{\varepsilon}_{11}{}^c \\ \dot{\varepsilon}_{22}{}^c \\ \dot{\gamma}_{12}{}^c \end{Bmatrix}_n \tag{A4.11.a}$$

The condensed effective compliance matrix $[C_n^*]$ is given by

$$[C_n^*] = \begin{bmatrix} C_{11} - \frac{C_{13}C_{13}}{C_{33}} & C_{12} - \frac{C_{23}C_{13}}{C_{33}} & C_{14} - \frac{C_{43}C_{13}}{C_{33}} \\ & C_{22} - \frac{C_{23}C_{23}}{C_{33}} & C_{24} - \frac{C_{43}C_{23}}{C_{33}} \\ \text{SYM} & & C_{44} - \frac{C_{43}C_{43}}{C_{33}} \end{bmatrix}_n \tag{A4.11.b}$$

and

$$[\beta_n] = \begin{bmatrix} 1 + \frac{C_{13}}{C_{33}} & \frac{C_{13}}{C_{33}} & 0 \\ \frac{C_{23}}{C_{33}} & 1 + \frac{C_{23}}{C_{33}} & 0 \\ \frac{C_{34}}{C_{33}} & \frac{C_{34}}{C_{33}} & 1 \end{bmatrix}_n \tag{A4.11.c}$$

An important property of the effective compliance matrix is that it remains symmetric after being condensed for plane strain creep deformations. This is because an associative flow law has been used. The inversion of Equation (A4.11.b) is completed numerically.

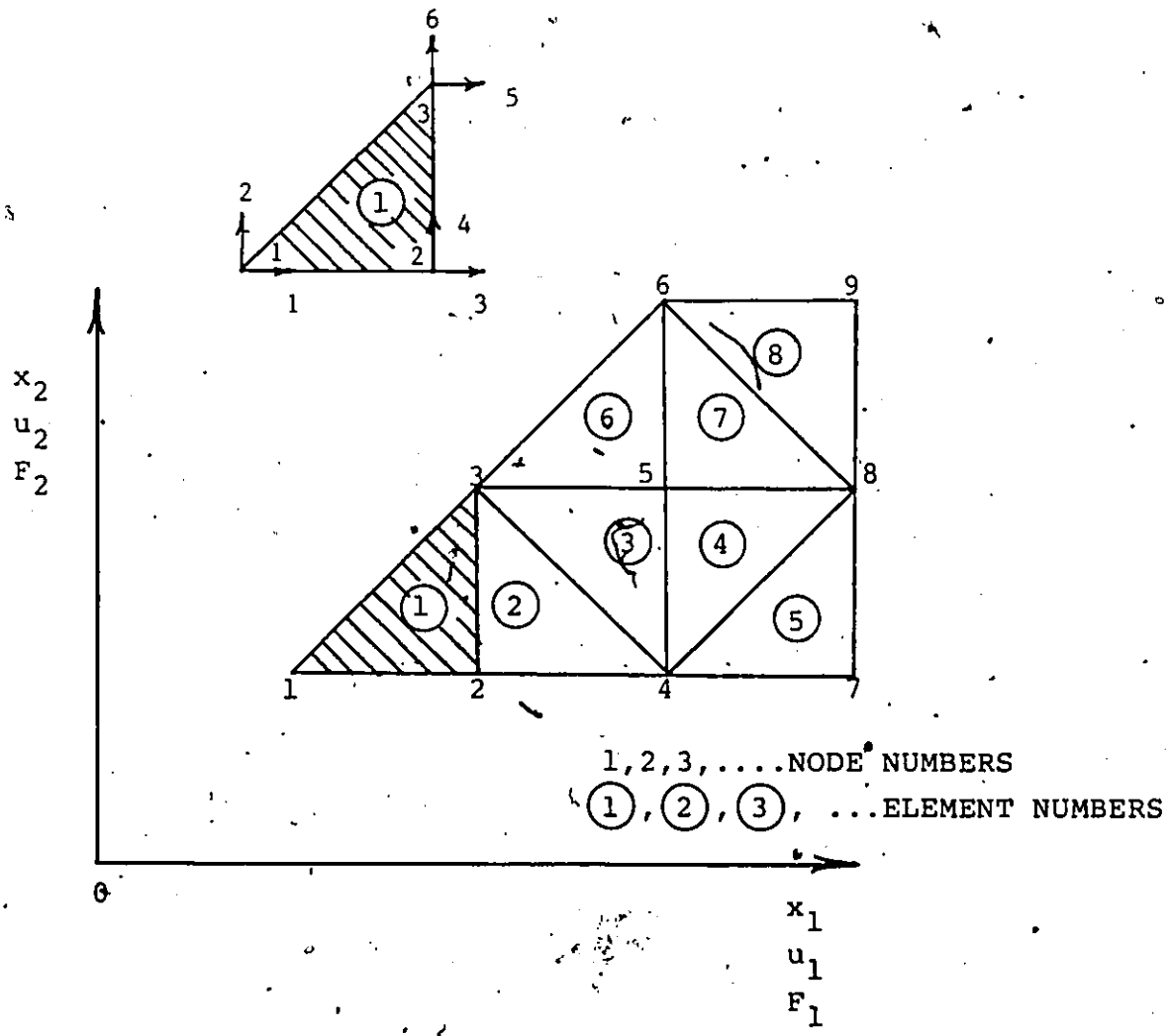

FIGURE A4.1 TRIANGULAR FINITE ELEMENT DIVISION OF A PLANAR REGION.

APPENDIX A5

BARNES ICE CAP (BIC) (POST-SURGE)

A5.1 Overview of Problem

Three factors, influencing creep behaviour of large ice masses, are considered: material properties; temperature field; and boundary conditions.

The index of the power law for ice creep of BIC determined from bore holes and tunnel investigation by Hooke [44] is approximately 1.65. Through numerical simulations of the north-east margin, Hooke et al. [46] indicated that an index of 2.6 gives better agreement between the computed and measured the horizontal surface velocities. Holdsworth [36] determined a much higher index of 4.2 from his surface velocity measurements taken along section N-O. The material properties adopted in this study are those used by Emery and Mirza [24], see Table A5.1. The linear creep law used for one of the double slope examples is also employed for some BIC simulations. While it is known that the ice cap is neither homogeneous nor isotropic, these simplifying assumptions are used in order to study the factors that influence the overall dynamics of section N-O-SS. A comparison of the computed flow response completed by Hooke et al. [46], in which the variation of the ice structure is incorporated and that completed in the current study, will clearly demonstrate how the assumption of homogeneity affects the prediction of creep behaviour within an ice mass.

TABLE A5.1 MATERIAL PROPERTIES USED FOR BARNES ICE CAP SIMULATIONS

Unit Weight:	$\gamma = 8.952\ kN/m^3$
Modulus of Elasticity:	$E = 9.075 \times 10^6\ kN/m^2$
Poisson's Ratio:	$\nu = 0.34$
Flow Laws(1)	Hooke's Parameters: $\dot{\varepsilon}_e^c = 0.0327\ \sigma_e^{1.65}$
	Nye's Parameters: $\dot{\varepsilon}_e^c = 0.0374\ \sigma_e^{3.07}$
	Meier's Parameters: $\dot{\varepsilon}_e^c = 0.012\ \sigma_e + 0.006\ \sigma_e^{4.5}$

Flow Law Including Temperature Variation(2):

$$\dot{\varepsilon}_e^c = f(\sigma_e)\ \exp\left(\frac{-Q}{RT}\right)$$

$Q = 78$ kJ/mol for $T > -8°C$

$Q = 120$ kJ/mol for $T < -8°C$

Sliding Law(3): $\hat{T}_1 = 3.00\ \hat{v}_1$

Thermal Conductivity: $K = 2.1\ W \cdot m^{-1} \cdot °C^{-1}$

Heat Capacity: $C = C_\rho \rho = 2.1 \times 10^6\ W \cdot sec \cdot m^{-3} \cdot °C^{-1}$

(1) All flow laws are expressed in terms of Dorn's definitions for equivalent stress and strain. Units for stress and strain rate are bars (0.1 MPa) and per annum, respectively.

(2) All constants for flow laws are adjusted to correspond to appropriate values at -8°C.

(3) Units for shear stress and basal sliding velocity are kPa and meters per annum, respectively.

Field studies by Classen [16] along the south-west slope revealed a temperate basal ice layer of approximately 30 m thick within the core of the ice cap. The margins were found to be frozen to the bedrock. Hooke [45] estimated the basal temperatures beneath the north-east side of the south dome for several values of geothermal flux. He indicated that the basal ice is frozen to the bed for geothermal flux values less than 1.4 HFU. Figure A5.1 shows both the estimated and the measured temperature contours provided by Holdsworth [41]. The surface temperatures shown in Figure A5.1 are the values at a depth of 17 m from the surface. These temperatures have been used as the boundary condition on the surface in thermal simulations of BIC.

The overall temperature-creep response of BIC is not in steady-state. Field studies by Holdsworth [39] have shown that the north-east side is in close dynamic equilibrium while the south-west side is rapidly wasting away. The greater ablation rate when compared with the vertical emergence velocity [39] is consistent with the post-surge events for surge type glaciers.

The temperature study herein has been limited to determining the sensitivity of the BIC temperature field to geothermal flux, pressure melting, velocity field and changes in boundary conditions. The creep study of the post-surge profile of BIC only addresses the short term flow behaviour. The development of the sliding element has allowed for simulation of high deformation gradients at the ice-bed interface which is considered to be important beneath the south-west side of the ice cap.

The maximum possible time step for the transient creep analyses is given by Equation (3.29.b) with F = 250. This factor helps allow for time steps large enough to yield a reasonable solution with minimal computational effort. Simulation periods for BIC are generally limited to two years. Longer periods lead to a divergence of the ice cap response from the expected response which is believed to be due to round-off errors and an accumulation of errors associated with the residual creep load vector when checking the overall equilibrium. Much larger factors are possible for simpler problems with less complex boundaries.

A5.2 Finite Element Idealizations of BIC

Three different finite element idealizations shown in Figures A5.2(a), (b) and (c) are used when studying dynamic responses of the Barnes Ice Cap. The grid shown in Figure A5.2(a) is used for simulations with Models A and B while those in Figures A5.2(b) and (c) are used for Model C. The two idealizations in Figures A5.2(a) and (b) are compatible with one another in that they have the same nodes (four CST elements approximate one LST element). A direct comparison can thus be made between the predicted response given by the various models for the same number of displacement or velocity degrees of freedom. An additional simulation is completed by modelling only the response on the south-west side of the ice cap by using Grid C to the right of the topographic divide.

A comparison of the computed horizontal surface velocity distributions, using Model C, for the different finite element grids is shown in Figure A5.3. These simulations are completed assuming isothermal temperatures, using Hooke's flow parameters and allowing no basal sliding. Agreement among the results from different grids is generally good except where longitudinal strains appear to dominate, i.e. near to the divide. The effect of a coarser grid is to predict lower velocities in this region due to lack of sensitivity of the finite element grid to the changing longitudinal deviatoric stresses. Very little difference in the computed horizontal surface velocity distribution is observed when only the south-west portion of the ice cap is modelled. It should be noted that based on the simulations for the complete ice mass profile, the dynamic divide is approximately 150 m north-east of the topographic divide.

A5.3 Influence of Flow Parameters

In the study of the influence of flow parameters it is assumed that the ice is homogeneous, isotropic and isothermal. Furthermore no sliding was allowed at the ice-bed interface. The creep relationships used for the double slope problem are also used for the current BIC simulations since these cover a fairly wide range of creep responses. All of the simulations which are presented in this section are completed with Model A. A comparison of the creep responses predicted by each model is given in the next section.

The computed horizontal surface velocities for different flow parameters vary considerably over the entire length of the ice cap as shown in Figure A5.4. While the magnitude of the velocities depends on the creep law, a similar qualitative behaviour is observed regardless of the flow law. Of particular importance is the increased sensitivity of the strain rate to the equivalent stress for larger powers, as anticipated. The velocity variation predicted when using Nye's parameters suggests that on the average equivalent stress on the south-west side of the divide is lower than that on the north-east side.

Because of lack of sliding at the base on the south-west side, the computed horizontal velocities are obviously not close to the measured horizontal velocities. This is expected as sliding at the base is believed to dominate the creep flow behaviour on the south-west side. Hooke et al. [46] achieved a good agreement between the measured and the computed velocities on the north-east side by taking into account the changes in ice structure. It should be pointed out that there is no sliding on this side as the ice is frozen to the bedrock. They included the influence of the white ice band, adjusted the flow constant to account for the change in ice fabric when moving away from the divide and allowed for a non-isothermal temperature field. Figure A5.5 illustrates the influence of the nonhomogeneity of the ice cap properties on the horizontal surface velocity. The peak velocity can be made to decrease and shift toward the margin by allowing for nonhomogeneous properties through using different flow laws.

A5.4 Comparison of Models A, B, C and the Influence of Basal Sliding

The finite element simulations discussed in this section are completed by assuming an isothermal temperature field and by using Hooke's flow parameters to characterize the ice rheology. On the north-east side where no basal sliding is allowed, all of the models predict similar surface velocity distributions as shown in Figure A5.6.

There are two important considerations to account for when comparing the measured and the computed surface velocities on the south-west side: horizontal velocity due to internal deformation; and horizontal velocity due to basal sliding. The contribution from each component can only be deduced from field measurements in reality. Unfortunately this information is not available currently. In order to account for sliding, a power law can be used to characterize the sliding response at the ice-bedrock interface. However, for simplicity, a linear sliding law is used for all subsequent analyses.

Reasonable horizontal surface velocities are computed on the south-west side by assuming that the sliding parameter is constant along most of the south-west ice-bedrock interface. It has been found that the sliding law,

$$\tilde{T}_1 = 3.0\ \tilde{v}_1 \qquad \text{(A5.1)}$$

can account for the high horizontal surface velocities that are observed

along section O-SS. Equation (A5.1) is neither unique nor is it considered to be the most optimum form that characterizes the sliding beneath BIC. To attain an optimum relationship for sliding, spatial variations for the creep and sliding relationships must be considered. During the preliminary studies it was found that velocity reversals at the base can be induced by a sharp transition from sliding to no sliding or vice versa. Thus the transition between no sliding and sliding has been spread over an interval. Figure (A5.6) gives the two basal sliding schedules that have been used for the BIC study. The high shear resistance at the toe is intended to account for the margin being frozen to bedrock.

For Schedule A, Models B and C, which allow for some compressibility, predict similar horizontal surface velocity variations on the south-west side while Model A predicts an entirely different response between the 10 and 28 km sections (see Figure A5.6(a)). The introduction of compressibility appears to smooth out the high velocity gradients. By increasing the transition interval of no sliding to sliding, Schedule B, the peak horizontal surface velocity predicted by Model A is greatly reduced and better agreement of velocities predicted by Models A and B is observed, Figure (A5.6(b)). It appears that both the compressibility and the smaller gradients for basal shear resistance have the effect of dissipating energy hence suppressing the larger velocity gradients. These observations clearly indicate that the predicted creep response of an ice mass is very sensitive to the manner in which the basal boundary is handled and the model chosen for analysis. It should be mentioned that the same surface velocities are computed for Schedules

A and B north-east of the 10 km section and south-west of the 28 km section. Figure A5.7 shows some computed horizontal velocity profiles along the ice cap, when using Schedule A for basal shear resistance. Figure A5.8 clearly demonstrates the short period of time required for BIC to reach a steady-state flow after having started the simulation from an elastic state of stress. The short transient period shown in this figure is consistent with the conclusions in Section 4.2.2.

A5.5 Velocity Field for Temperature Simulations

To obtain reasonable velocity fields for different temperature simulations which involve thermal advection, steady-state creep analyses are completed by fixing the vertical surface velocities at their measured values using Model A (non-Newtonian creeping flow with incompressibility). For the case where all of the vertical surface degrees of freedom in velocity are specified, the dynamic divide shifts three kilometers south-west of the current divide. When only a few degrees of freedom are specified, the influence on the velocity field is only local. To achieve a close agreement between the measured and the computed velocities, proper characterization of the ice properties and boundary conditions are needed.

The surface velocities specified for the thermal analyses are shown in Figures A5.9(a) and (b). Figure A5.10 indicates the approximate particle paths that are estimated by using a nonlinear streamline finite element model [101]. Assuming that the ice flow characteristics

can be modelled reasonably, the streamline analysis can also be used for tracing particle paths when attempting to speculate the age of ice at various depths for establishing the chronology of geological events of the earth's surface [40].

A comparison of the measured and the computed surface velocity variations indicates that the qualitative behaviour is good even without a close agreement, Figure A5.9. The larger computed negative vertical velocities north-east of the 14 km section reflect an overestimation of longitudinal extension due to the creep law used. South-west of this section, the extreme values of the computed vertical velocities indicate an increase in sensitivity of the vertical velocity to the flow of ice over the bedrock undulations when sliding is allowed. To attain a closer agreement between the computed and the measured velocities, adjustments must be made to both the creep and the basal sliding relationships.

A5.6 Temperature Simulations of BIC

This section deals with the steady-state simulations that illustrate the sensitivity of the temperature distribution within an ice mass to such key factors as pressure melting, strain heating, thermal advection and the geothermal flux. The thermal properties used for these analyses are given in Table A5.1 and the boundary conditions are shown in Figure A5.1.

The results shown in Figures A5.11(a) to A5.12(c) are summarized

below.

1. When the influence of pressure melting is not included, the zero isotherm extends well into the south-west core of the ice cap, Figure A5.11(a). The influence of pressure melting is to suppress the penetration of the zero isotherm as shown in Figure A5.11(b). The pressure field for determining the pressure melting temperature is approximated from the isothermal creep simulation by using Model A. It has been assumed that the pressure field is not too sensitive to changes in boundary conditions or creep flow properties.
2. The influence of strain heating is to expand the zone of temperate ice as anticipated. The strain heating field is also approximated using the creep simulation.
3. Thermal advection lowers the temperature of the ice cap, thus substantially decreasing the extent of the temperate ice zone. The temperature contours shift both in the vertical and horizontal directions. A comparison of the streamlines shown in Figure A5.10 with the temperature contours in Figure A5.12(a) clearly demonstrates the correspondence between the particle path and the temperature distribution for an ice mass in which thermal advection is important.
4. With decreasing geothermal flux beneath the south[illegible]st slope, the ice mass becomes colder as anticipated. The computed temperature fields are generally colder than the temperature distribution shown in Figure A5.1 which was provided by G. Holdsworth of Environment Canada [41].

While most of the ice mass is predicted to be colder, the south-west tip is shown to be at the pressure melting point when a geothermal flux of 1.9 HFU is assumed. This result is not consistent with Classen's [16] observation that the margins are frozen to the bedrock. Based on this inconsistency, it is suggested that the geothermal flux in this area is less than 1.9 HFU. For a geothermal flux of 1.4 HFU the entire basal ice layer becomes frozen to the bedrock.

Due to the extreme sensitivity of the ice temperature to thermal advection, a good estimate for the velocity field is required to get a reasonable agreement between the measured and the computed temperatures; that is assuming that the ice mass has adjusted to steady-state conditions. Near to the divide the the[illegible]advection is dominant in both vertical and horizontal directions. All simulations suggest that while a geothermal flux of 1.9 HFU is too high to account for the measured temperature distributions, 1.4 HFU is too low. If the extent and magnitude of the percolating melt-water near the surface were known, it would have been a simple matter to introduce the influence of latent heat into the finite element thermal analysis.

The temperature distribution shown in Figure A5.11(b) is used for the temperature-dependent creep simulations. The other temperature fields are considered to be either much too warm or too cold for the non-isothermal creep analyses.

A5.7 Creep Flow in a Non-Isothermal Temperature Field

The Arrhenius relationship is used to take into account the influence of temperature on creep. All creep laws are adjusted to correspond to temperature conditions at -8°C in order to allow for the changes in activation energy above and below this temperature [3]. The horizontal and vertical surface velocity distributions, for the isothermal and non-isothermal simulations, are shown in Figures A5.13(a) and (b), respectively. These velocity distributions correspond to the nearly steady-state conditions that are attained before the mean normal stresses begin to diverge. The results clearly indicate that the temperature field influences overall creep response, as anticipated. Care must be taken when interpreting these results since the predicted behaviours are not in steady-state and may also be subject to some numerical drift.

The shear stress and pressure variations within the basal ice layer are shown in Figures A5.14(a) and (b), respectively. A change in the temperature field has a negligible effect on both the shear stress and pressure distributions beneath most of the ice cap. However, sliding beneath the south-west side of the ice cap does influence the stress state at the ice-bed interface. The shear stresses appear to be more sensitive to sliding than pressures. The pressure distribution, given in Figure A5.14(b) appears to reflect the overburden stresses due to self weight of the ice. It is observed that the pressures from Model C are generally lower than those from Model A. This is attributed to the constant stresses in the CST elements which are meaningful only at the

centroids of the elements rather than at the nodes where the stress averages are computed.

If the bed is relatively impermeable and the ice is at pressure melting, water should collect in the local minimum pressure zones. The collection of water would reduce the basal sliding resistance which could lead to sliding instabilty. Since the ice cap in its current configuration appears to be stable, it is believed that meltwater runoff must occur at the ice-bed interface.

A5.8 Transient Thermal Analysis

The numerical examples of thermal analysis presented so far involved steady-state situations. A full transient temperature-creep analysis of BIC has been completed for the following initial and boundary conditions: the initial temperature field is the same as given in Figure A5.11(b); the initial stress field is linear elastic and due to self weight; the geothermal flux beneath the south-west side of the ice cap is 1.02 HFU; the remaining temperature boundary conditions are the same as shown in Figure A5.1; and the south-west side of the ice cap is allowed to slide (Schedule A). Strain heating and the heat due to frictional sliding at the base from the creep analysis are included as additional heat input. The temperature-dependent version of Meier's law is used to characterize the ice rheology.

It is observed that the creep response seems very reasonable up to 5×10^5 minutes (347 days). Thereafter, the response starts to

diverge from the expected behaviour. However, the divergence does not lead to numerical instability. This problem can be eliminated through a better choice of finite element. Figure A5.15 shows the horizontal surface velocity variation at different times. The change in the geometry of the ice mass is not sufficient to explain the changes in the velocity distribution. The decrease in velocity is attributed to the difficulties with the CST element, discussed in Section 4.2.2, when a nearly steady-state of stress is attained; i.e. $\sigma_{33} = 1/2(\sigma_{11} + \sigma_{22})$. Since no sliding is allowed at the ice-bed interface north-east of the 12 km section, the incompressibility problems appeared to have spread throughout the ice mass.

Although the velocities diverge, the temperature changes remain stable. The changes in temperature over the thirty-four year simulation period are negligible. A separate transient analysis, in which dynamic changes are not included, is completed to establish the thermal response time for BIC to adjust to a new velocity field and geothermal flux distribution. The temperature boundary conditions are the same as for the previous analysis. The velocity field, strain heating distribution and the heat due to frictional sliding at the base computed in the previous analysis are used for the transient thermal analysis.

The first noticeable changes in temperature appear near the bedrock as illustrated in Figure A5.16. Farther away from this boundary the temperature changes are much smaller. It is interesting to note that the temperature at node 56 initially increases due to the temperature gradients of the initial temperature distribution. This increase

in temperature occurs over an eighty-four year period, after which the temperature decreases due to the lower geothermal flux. The increase in temperature above pressure melting is not physically possible. The influence of pressure melting was not taken into account for this simulation. Had the pressure melting state been accounted for, the temperature should have remained relatively constant over the first 84 years rather than having increased.

The time for the ice mass to adjust to its new boundary conditions and flow field is of the order of 10^4 years. This example clearly demonstrates the complex response of an ice mass due to locked-in temperature gradients and the difficulty in trying to get close agreement between the computed and the measured temperatures. In order to achieve realistic temperature simulations, the influence of temperature histories must be included. However, if the temperature field is known, say through field measurements, the velocity field can be computed more easily as long as reasonable flow parameters are used. The long time period for BIC to fully realize the new boundary conditions is consistent with the conclusions on thermal response times for ice caps by other investigators [15]. If the thermal instability was important for the surge of BIC as speculated by Classen [16], the surge initiation must have occurred over a number of centuries and not decades.

Contour plots are given in Figures A5.17(a) and (b) to illustrate the changes in the temperature distribution with time. Figures A5.18(a) and (b) show temperature profiles within the BIC at the 14 km and 29 km sections, respectively. It is clear from these profiles

that the initial temperature field reflects conditions when heat conduction dominates. In Figure A5.18(a) it is also observed that the ice near the bed is initially at pressure melting. A change in the curvature of the temperature profiles is observed with time which also indicates the influence of thermal advection.

A5.9 Summary

The post-surge simulations of the Barnes Ice Cap (BIC) indicate that basal sliding can account for the high horizontal surface velocities that have been measured on the south-west side of the ice cap. A comparison of the measured and the computed vertical velocities suggests that the amount of sliding that is allowed in the finite element simulations is too high. Consequently in addition to sliding, it is believed that nonhomogeneous and anisotropic conditions also contribute to the observed dynamic behaviour of BIC. It has been shown that BIC takes approximately 10^4 years to adjust to changes that influence the temperature field within the ice cap.

It has been shown that the compressibility, due to changes in the elastic strains, is important for determining the creep velocity field. This indicates that it may be premature to assume that the influence of elastic strains is negligible, although these are small when compared with the magnitudes of the creep strains. For conditions when shear flow dominates, compressibility is not important and the elastic influence can be neglected. For analyses of flow over bedrock

undulations, where longitudinal strains are important, elastic compressibility should be included.

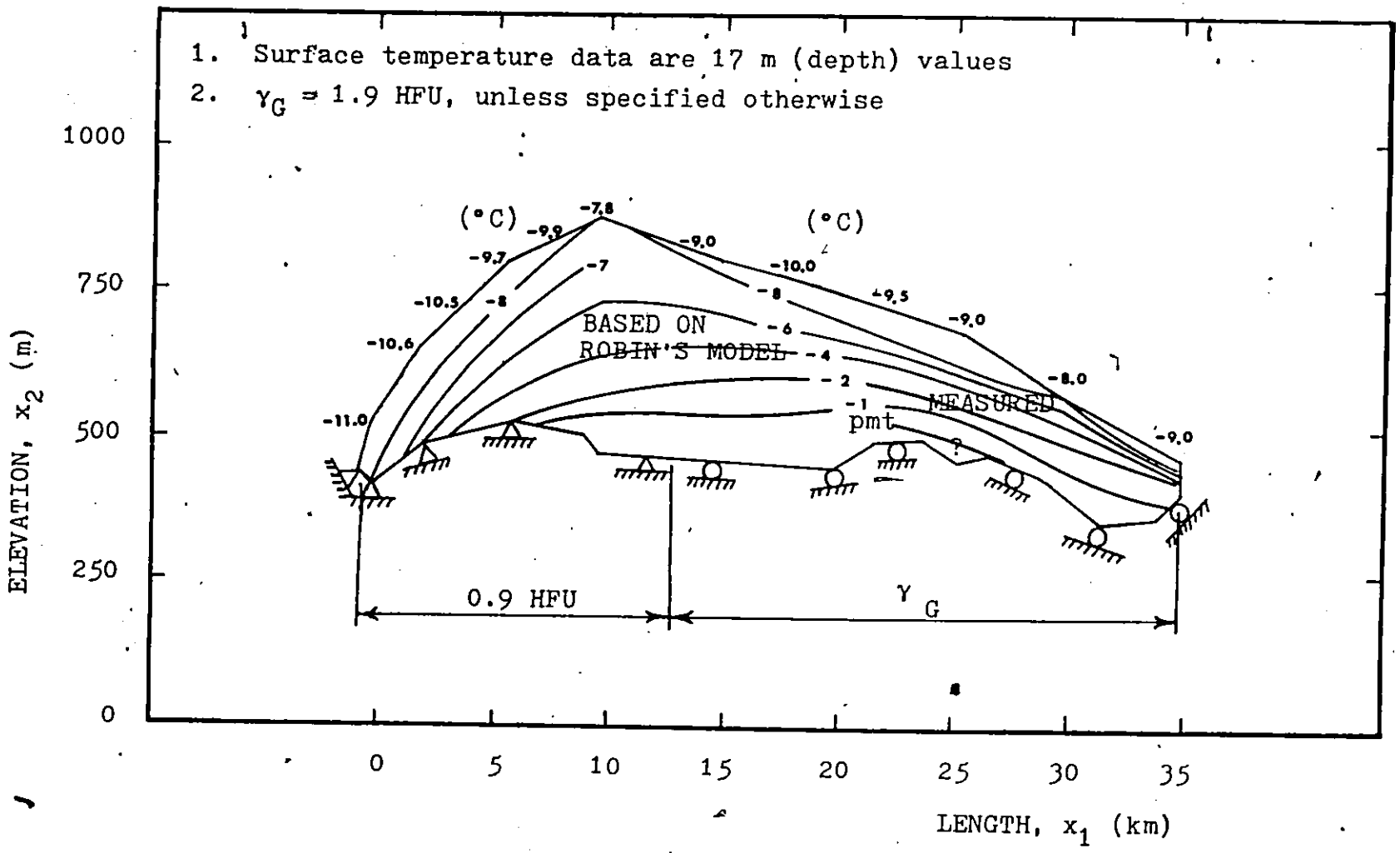

FIGURE A5.1 BARNES ICE CAP PROBLEM - Temperature data by Holdsworth [41] and non variable basal boundary conditions for creep analysis

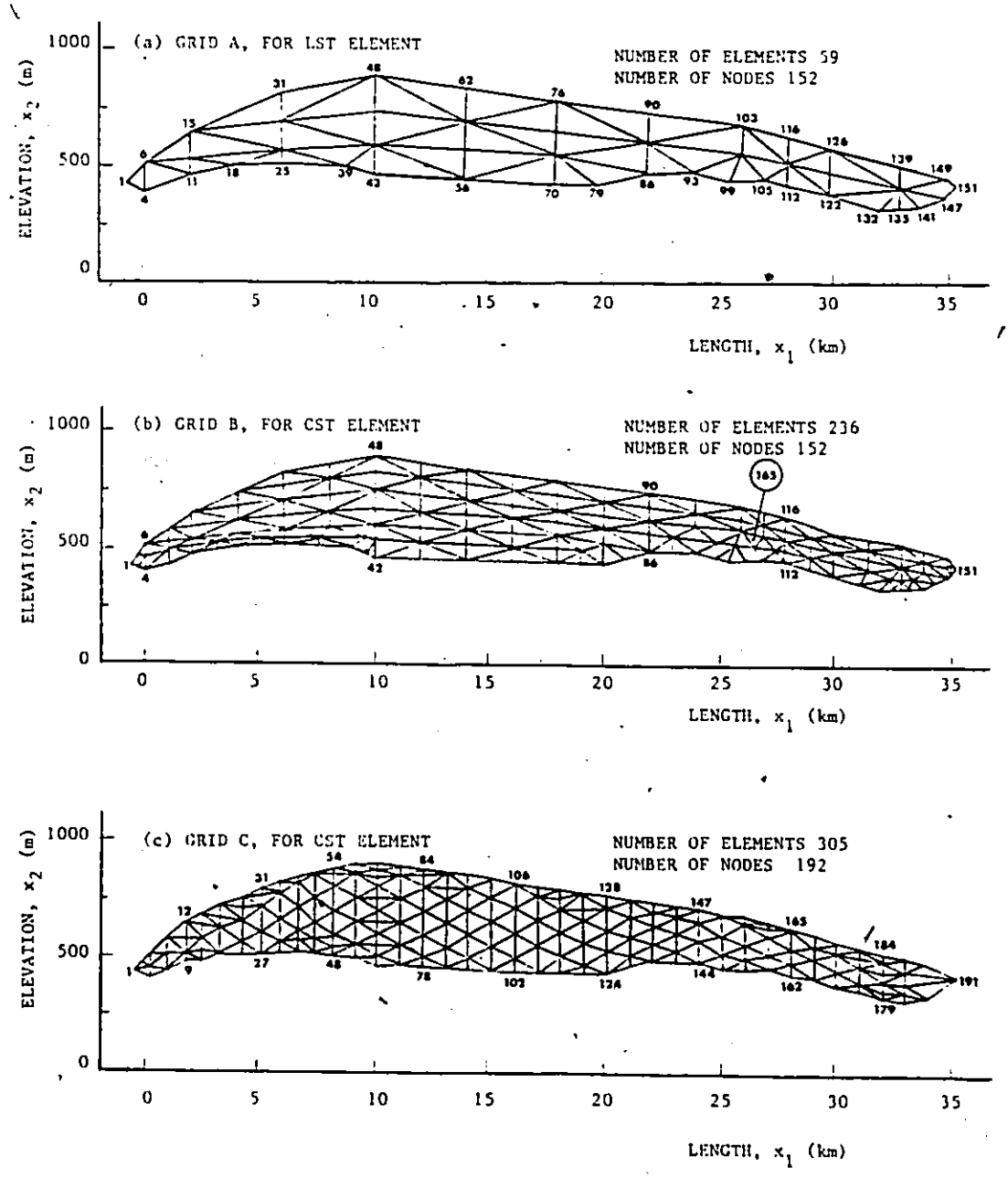

FIGURE A5.2 BARNES ICE CAP PROBLEM - Finite element grids.

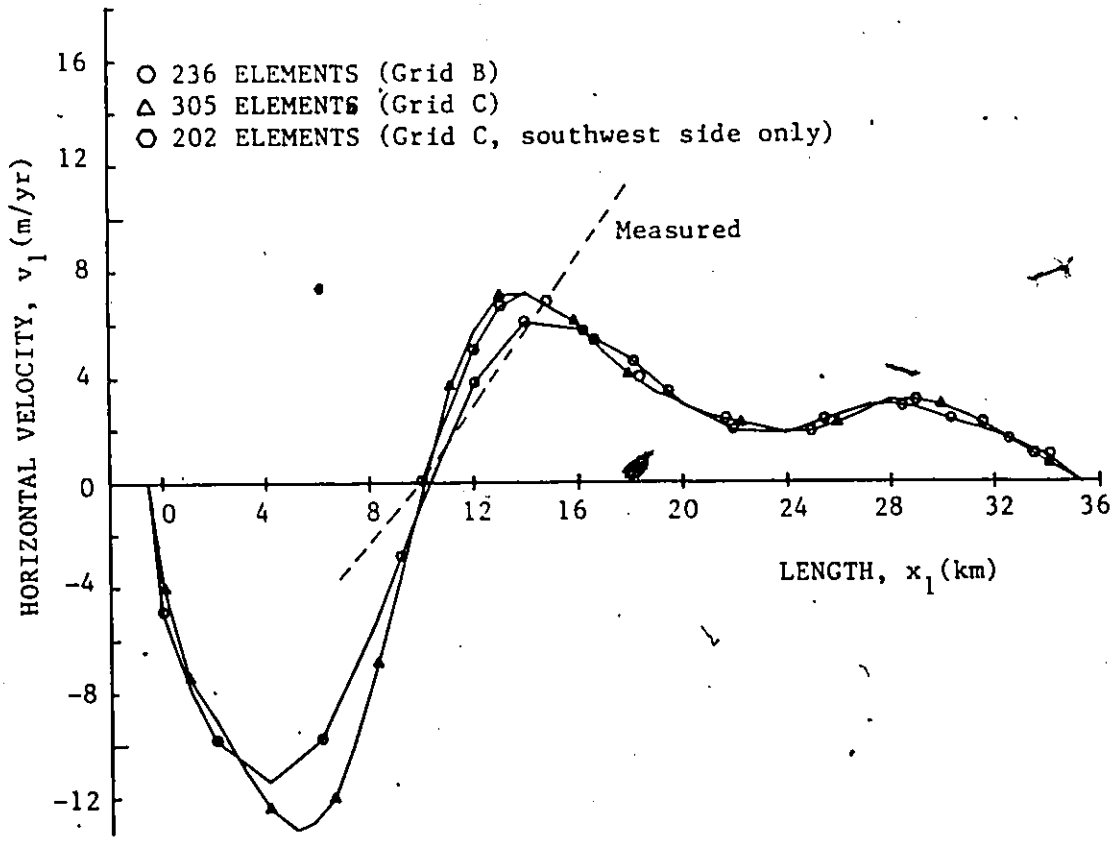

FIGURE A5.3 BARNES ICE CAP PROBLEM - Horizontal surface velocity variations for different grids (Model C).

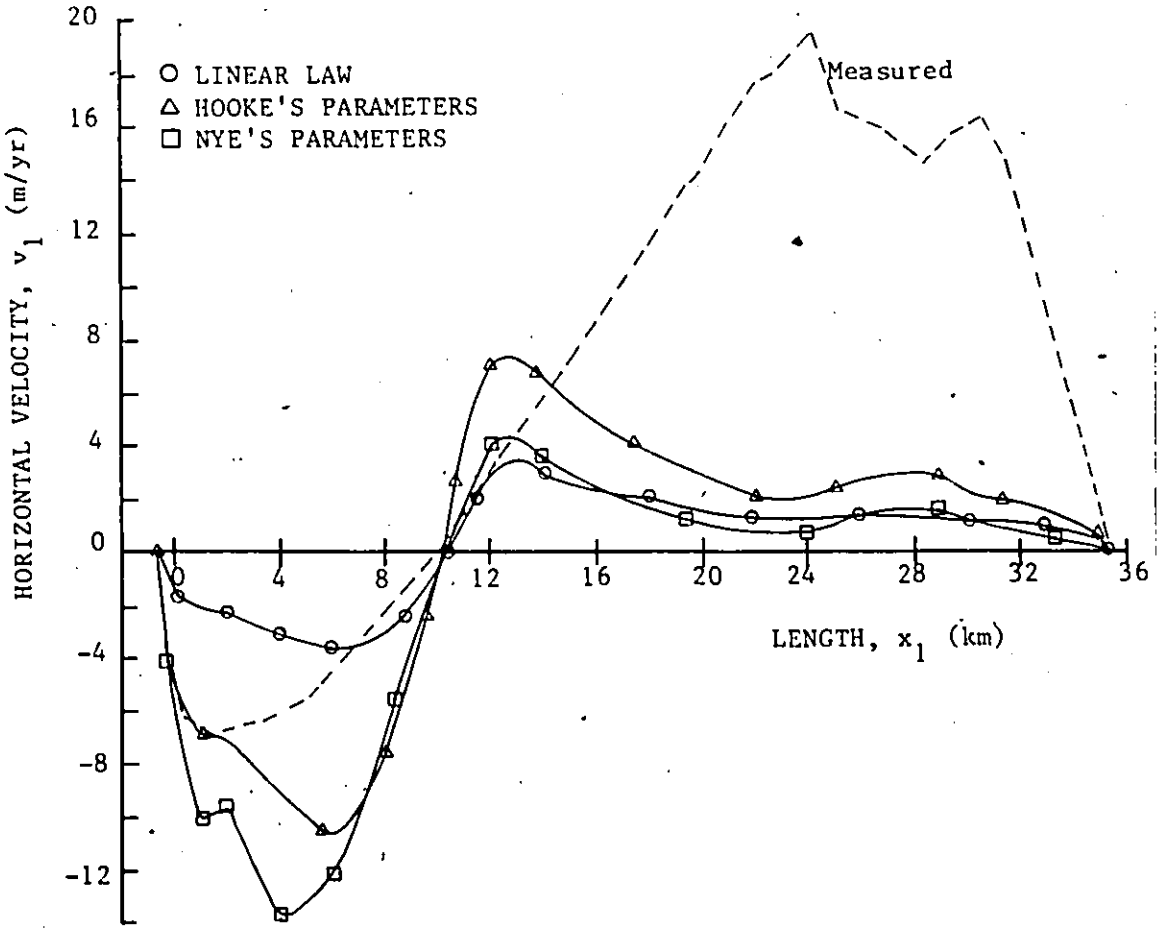

FIGURE A5.4 BARNES ICE CAP PROBLEM - Horizontal surface velocity variations for different creep laws (Model A).

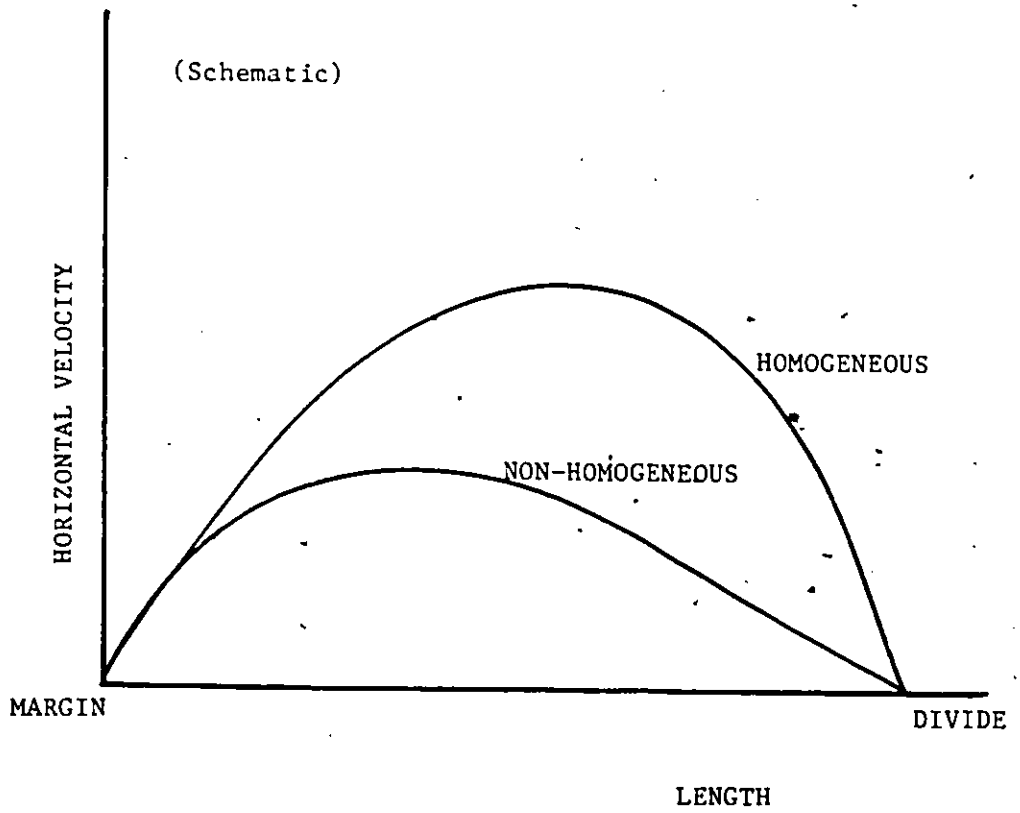

FIGURE A5.5 CHANGE IN SURFACE VELOCITIES DUE TO NON HOMOGENEOUS MATERIAL PROPERTIES

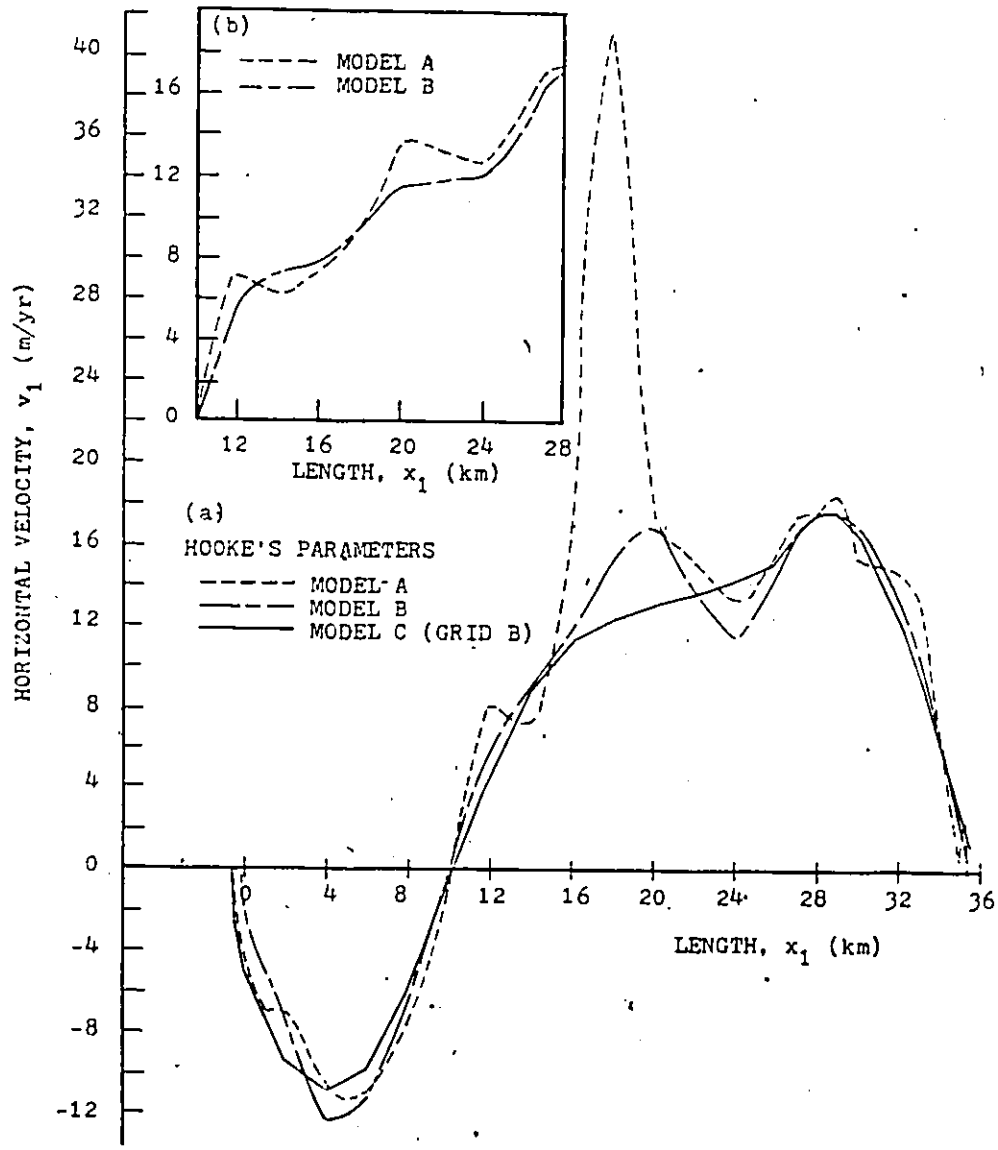

BASAL SHEAR COEFFICIENT ($\tilde{k}_{11}$) VARIATION ALONG GLACIER

LENGTH, x_1 (km)	10	12	14	16	18	20	35	35.15	35.3
SCHEDULE A	10^4	10^3	10^2	10^1	3.0	3.0 →	3.0	10^2	10^3
SCHEDULE B	10^4	10^3	10^2	25	10^1	3.0 →	3.0	10^2	10^3

FIGURE A5.6 BARNES ICE CAP PROBLEM - Comparison of horizontal surface velocity variations from Models A, B and C, when basal sliding is allowed. Surface velocities for (a) Schedule A, and (b) Schedule B.

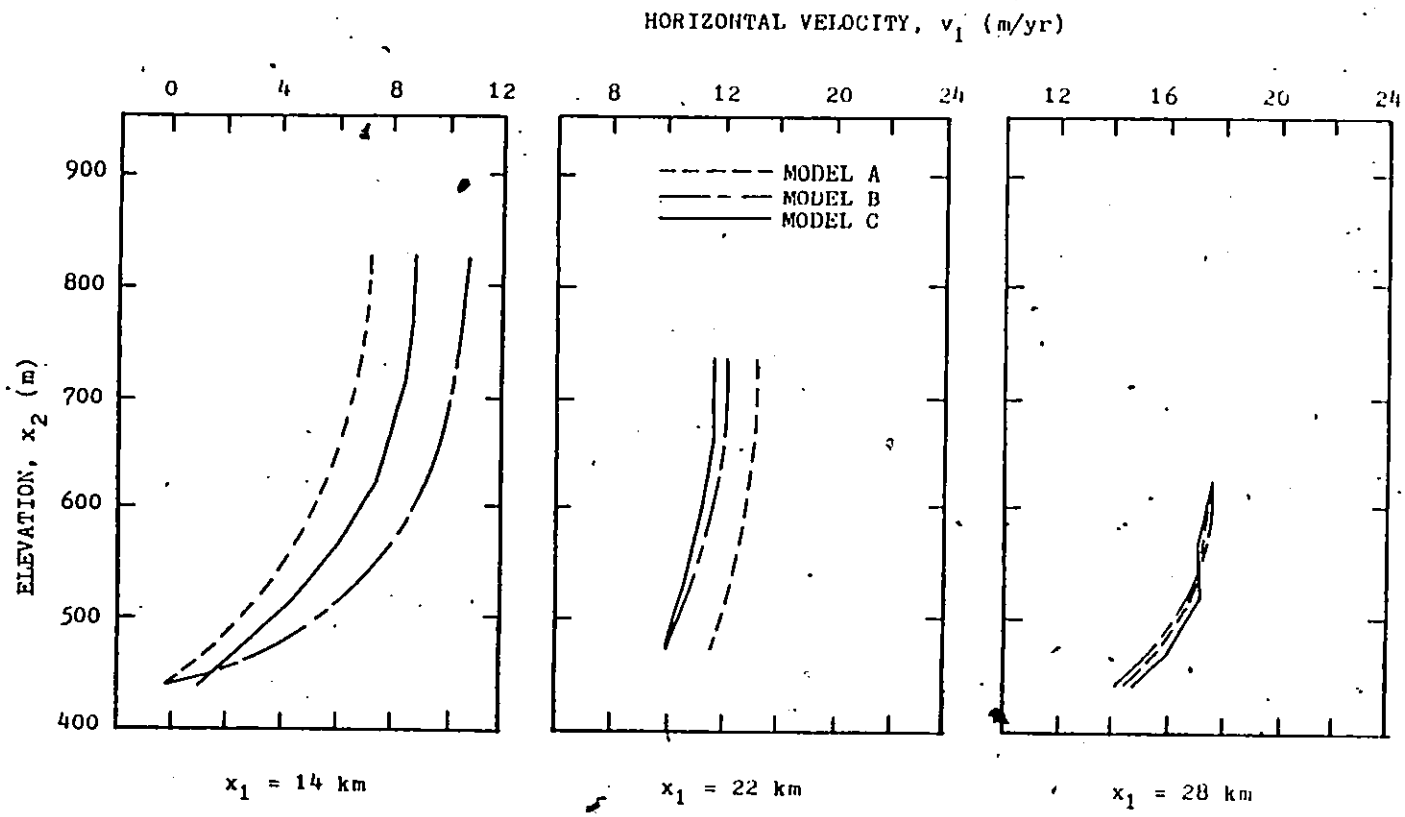

FIGURE A5.7 BARNES ICE CAP PROBLEM - Horizontal velocity profiles at various cross-sections.

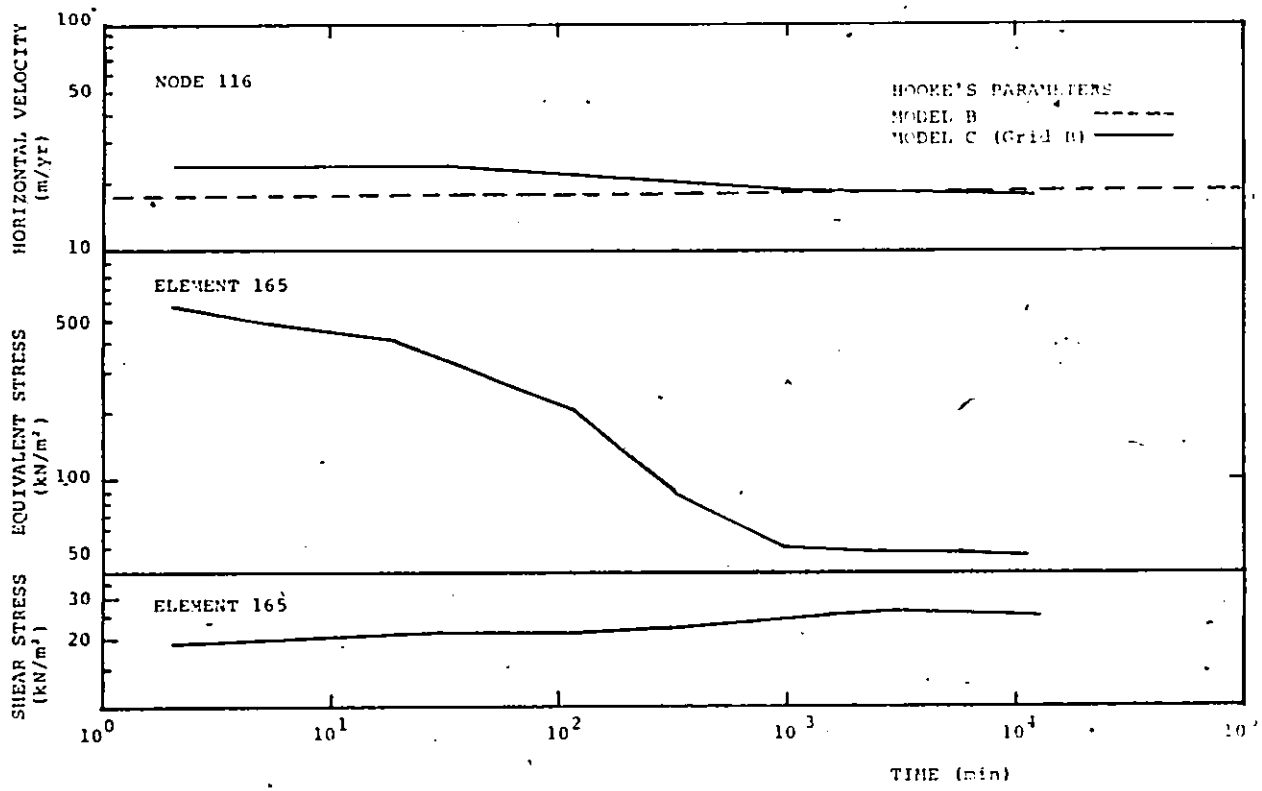

FIGURE A5.8 BARNES ICE CAP PROBLEM - Time-dependent changes in horizontal velocity at node 116 and in stresses of element 165 (Model C, Grid B).

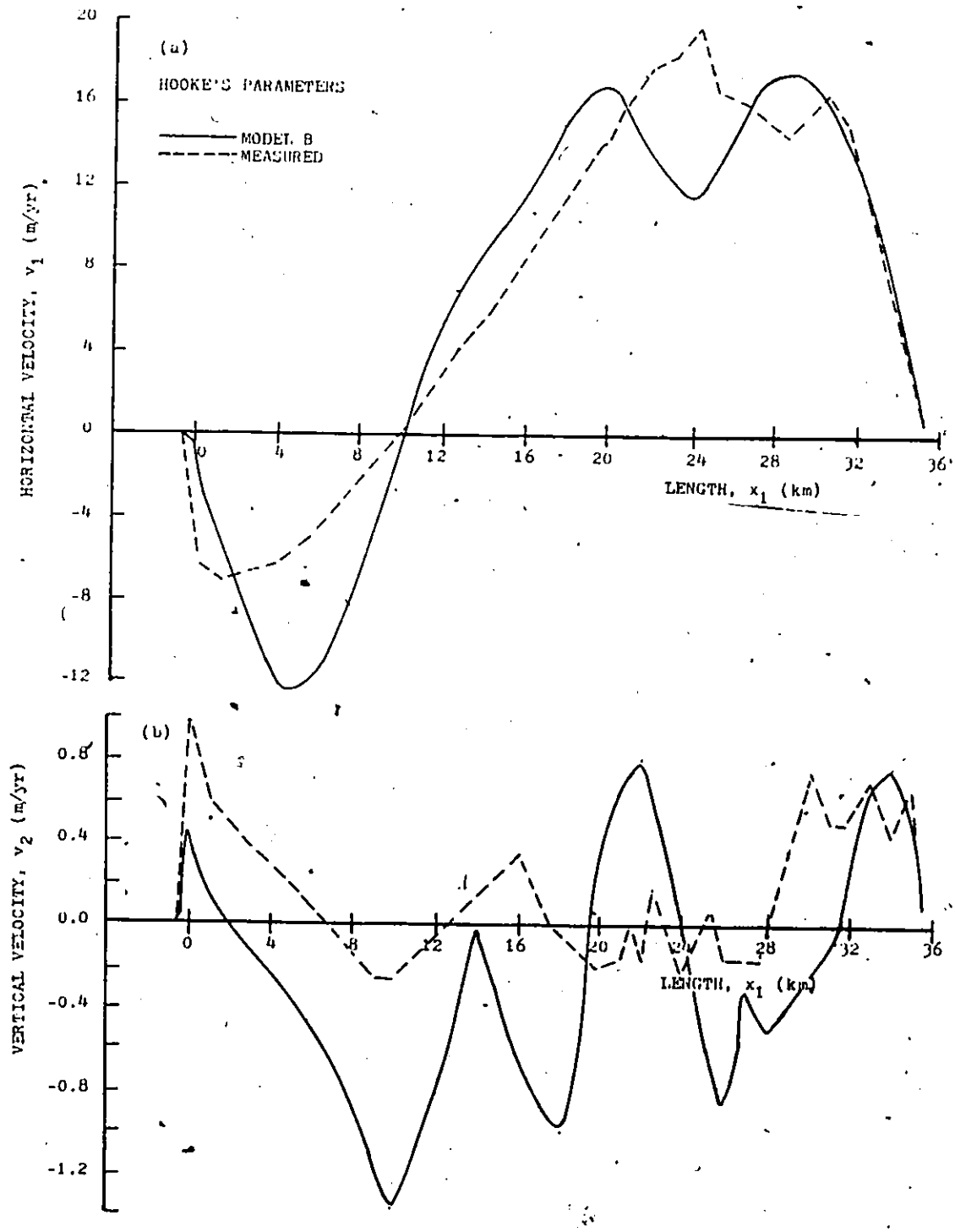

FIGURE A5.9 BARNES ICE CAP PROBLEM: (a) Horizontal surface velocity variation (same as shown in Figure A5.6, Schedule A), and (b) Vertical surface velocity variation, for the steady-state thermal analysis (Model B).

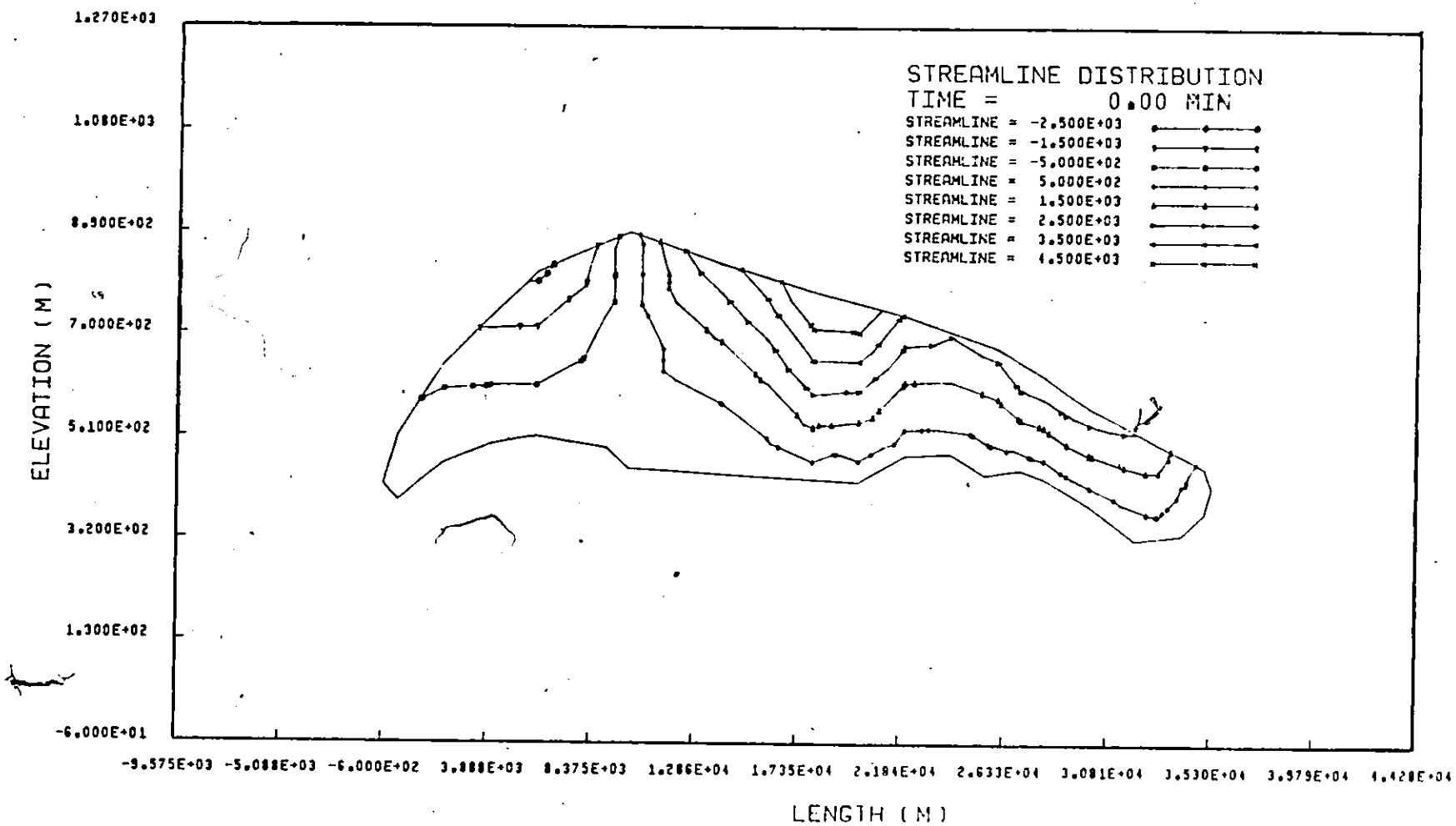

FIGURE A5.10 BARNES ICE CAP PROBLEM - Streamlines of velocity field used for the steady-state thermal analysis (Model B).

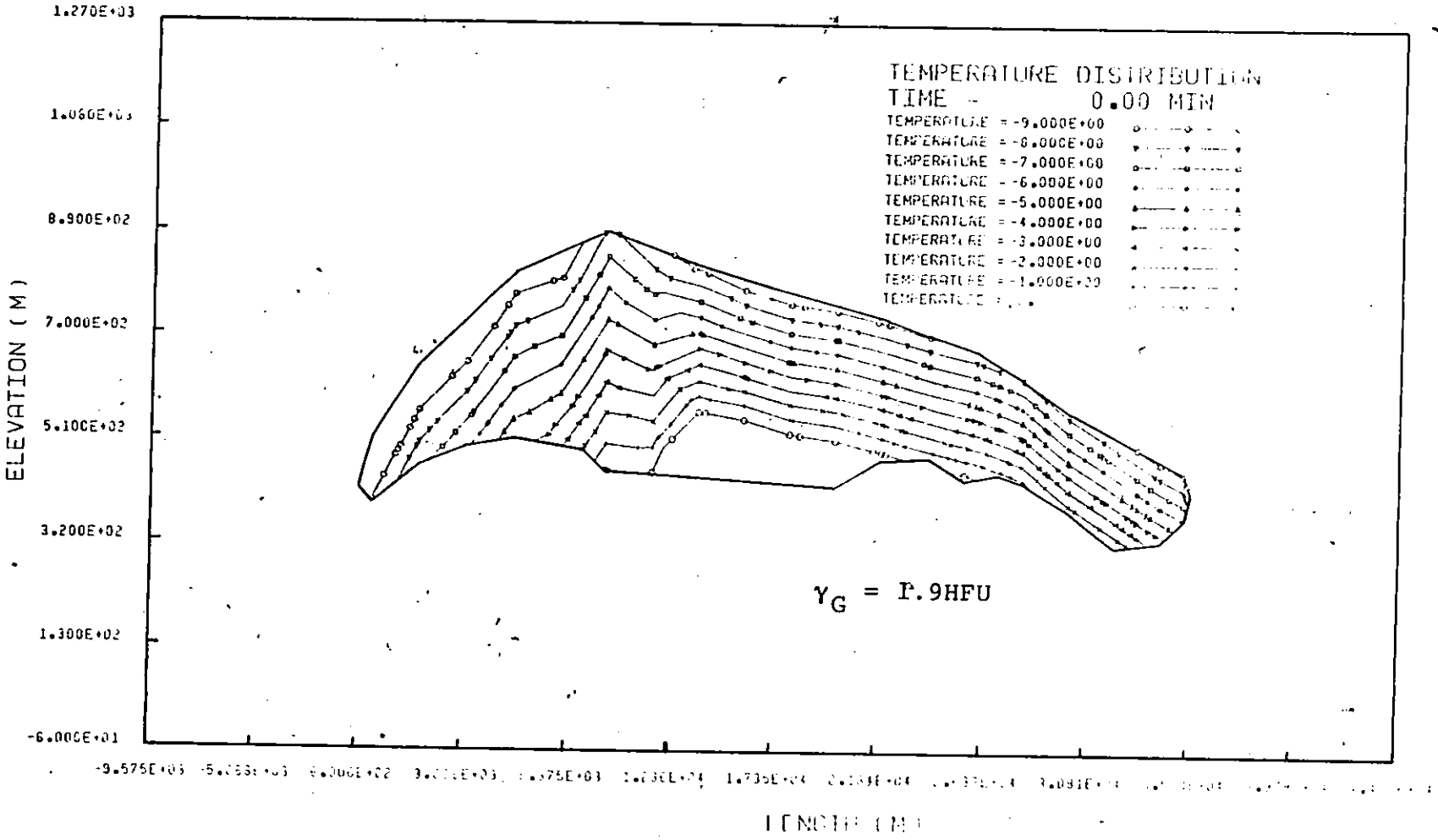

FIGURE A5.11 BARNES ICE CAP PROBLEM - Plots of temperature contours for: (a) Conduction only,

(cont'd on next page)

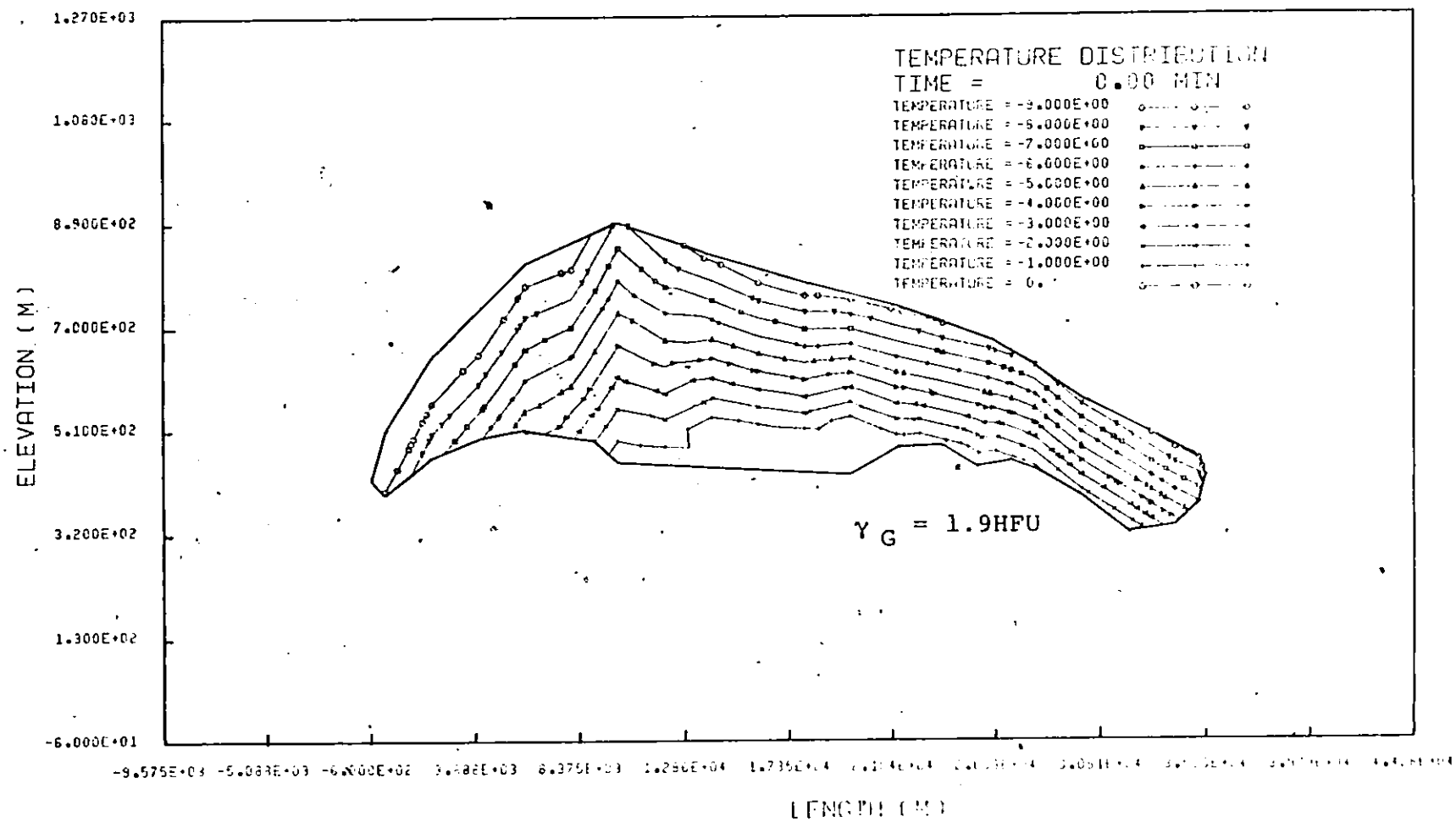

(b) Conduction with pressure melting influence, and

(cont'd on next page)

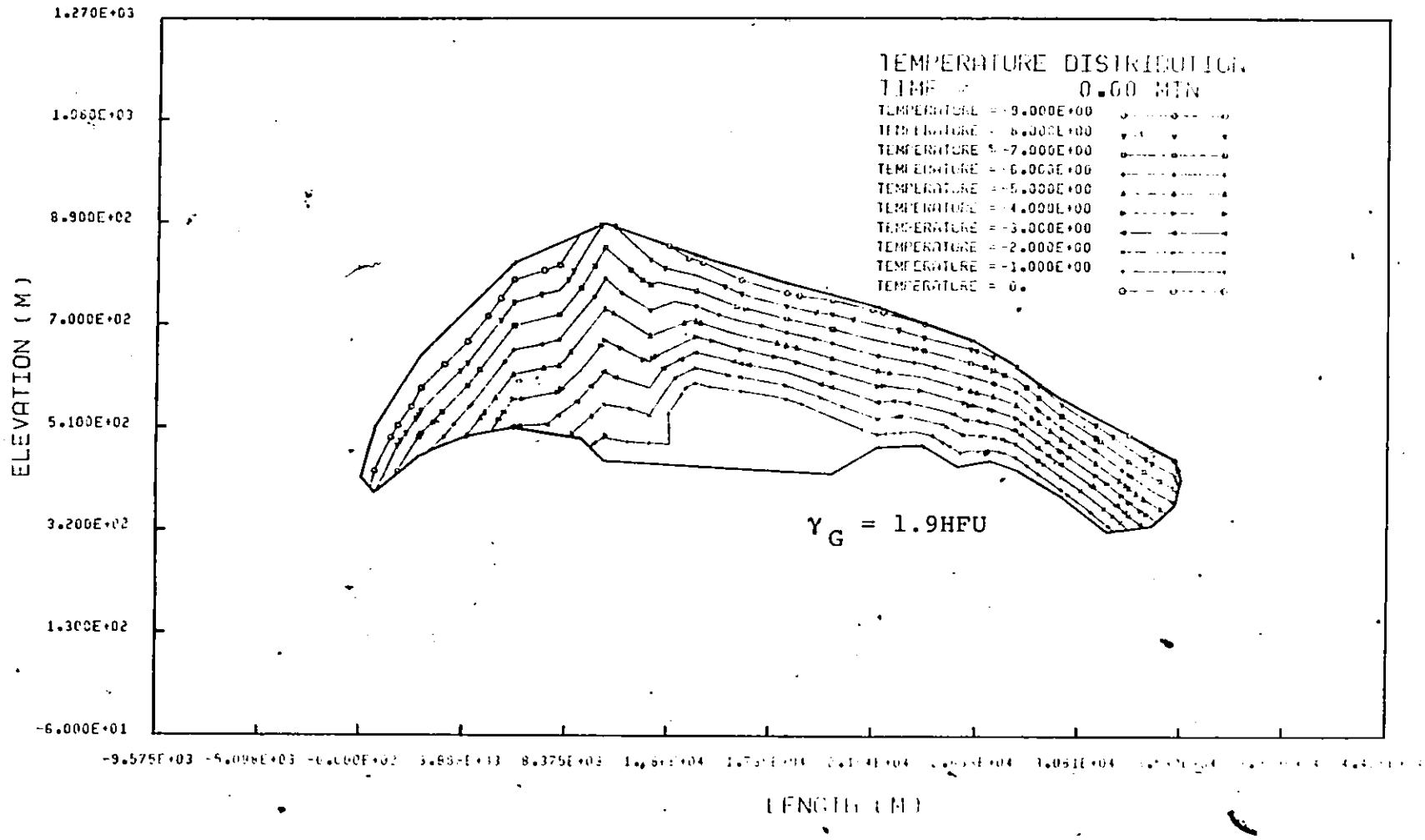

(c) Conduction and strain heating with pressure melting influence.

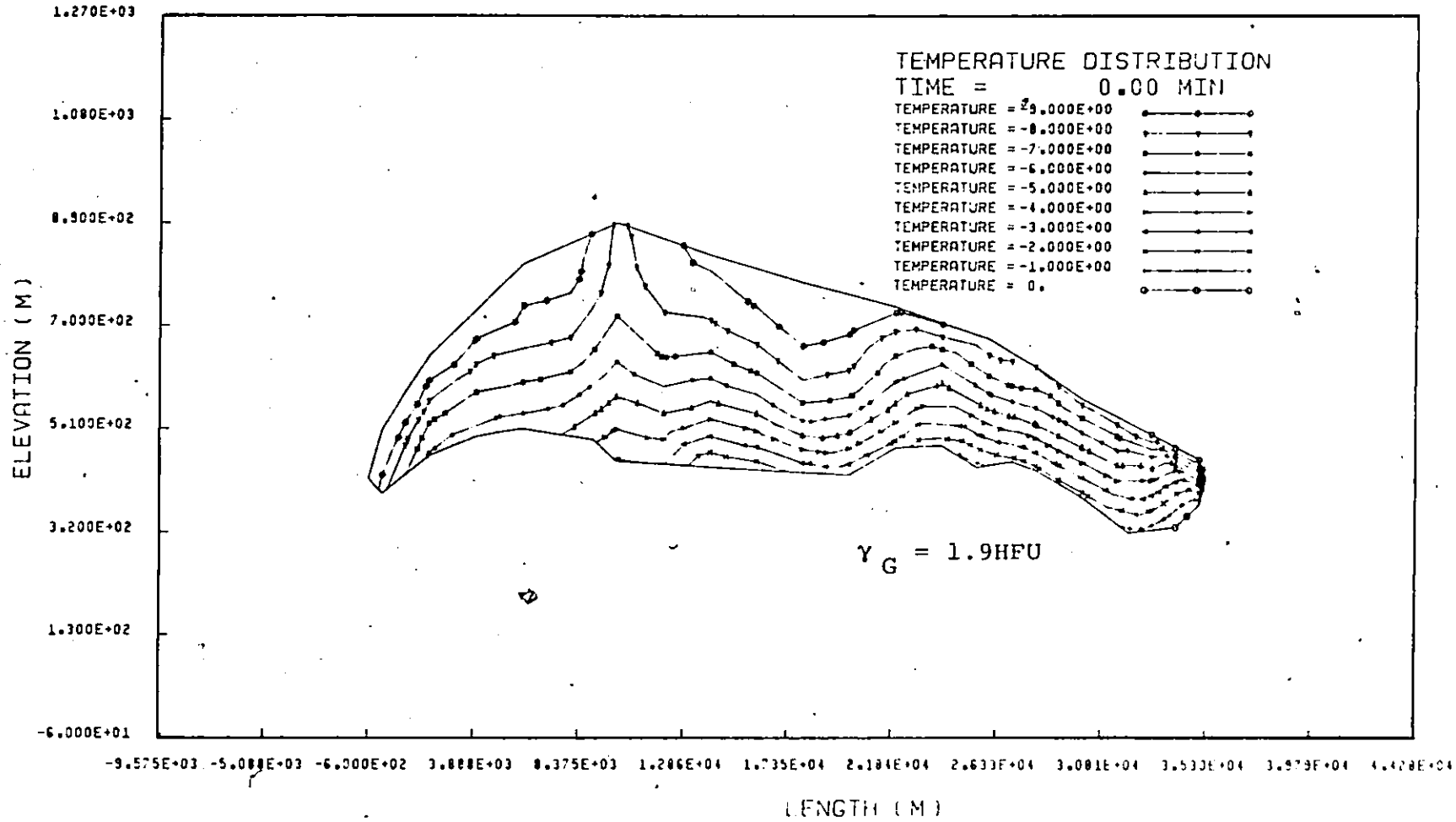

FIGURE A5.12 BARNES ICE CAP PROBLEM - Plots of temperature contours where thermal analysis includes the influence of conduction, advection, strain heating and pressure melting: (a) γ_G = 1.9 HFU,

(cont'd on next page)

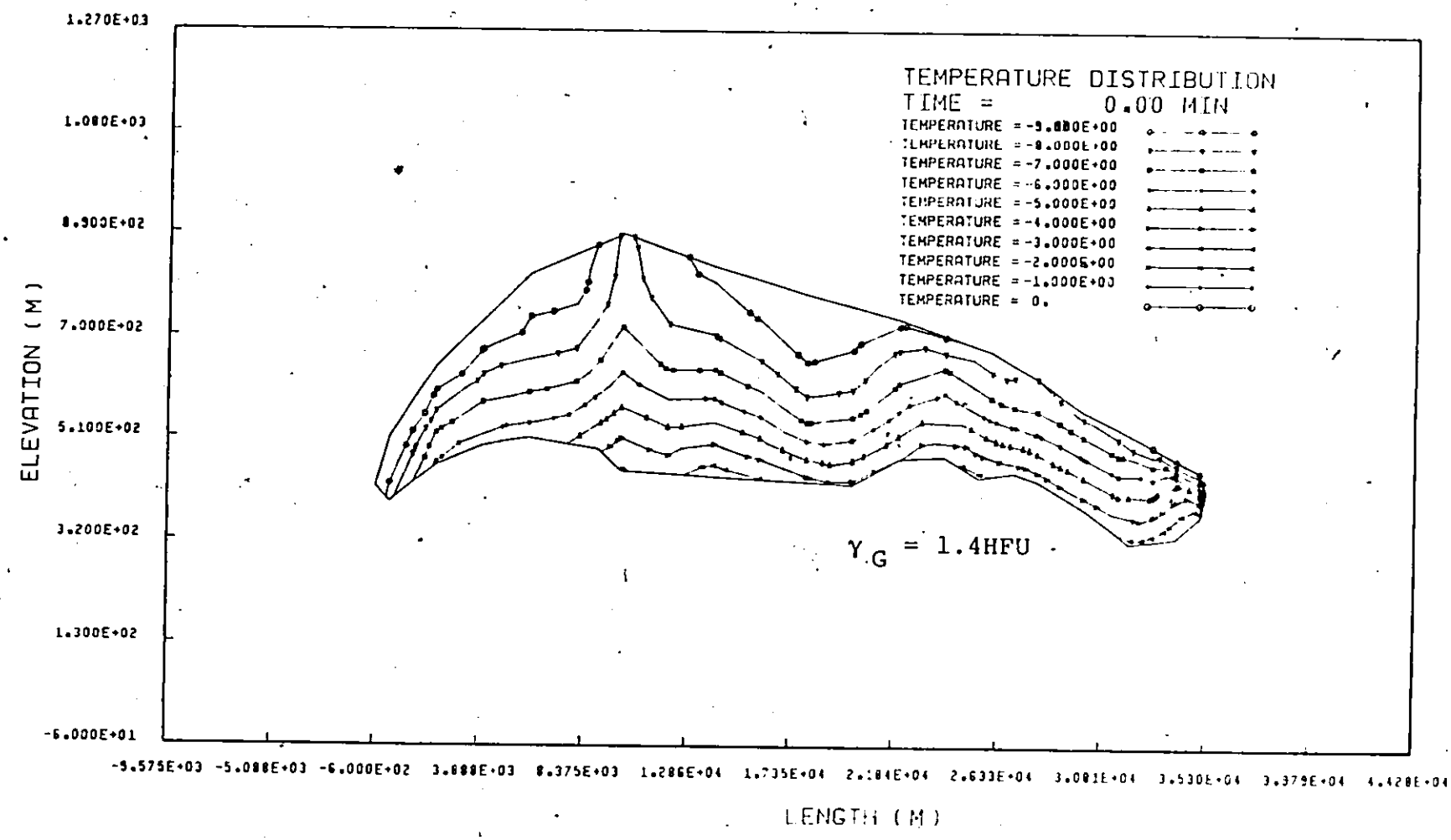

(b) γ_G = 1.4 HFU, and

(cont'd on next page)

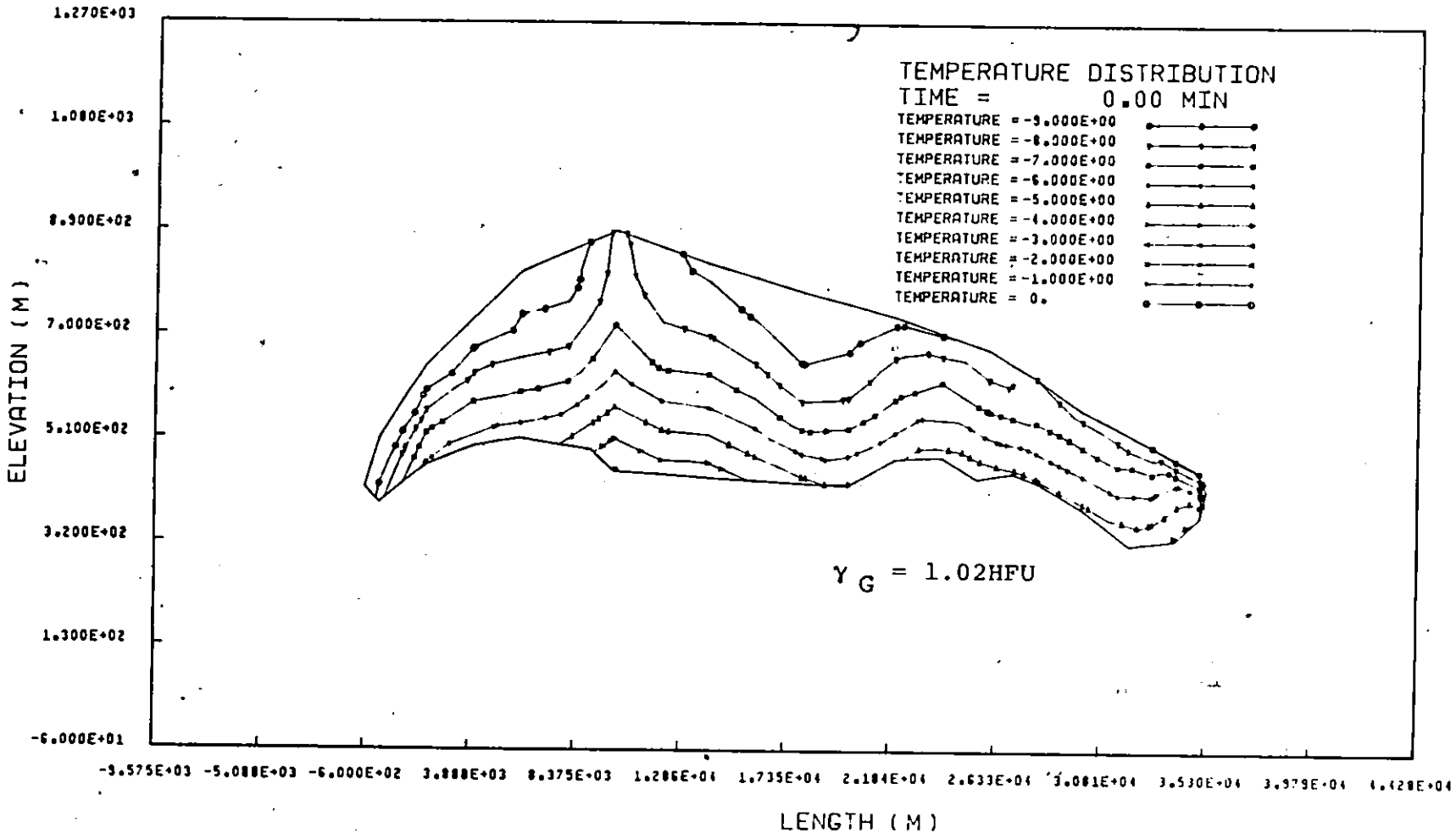

(c) γ_G = 1.02 HFU.

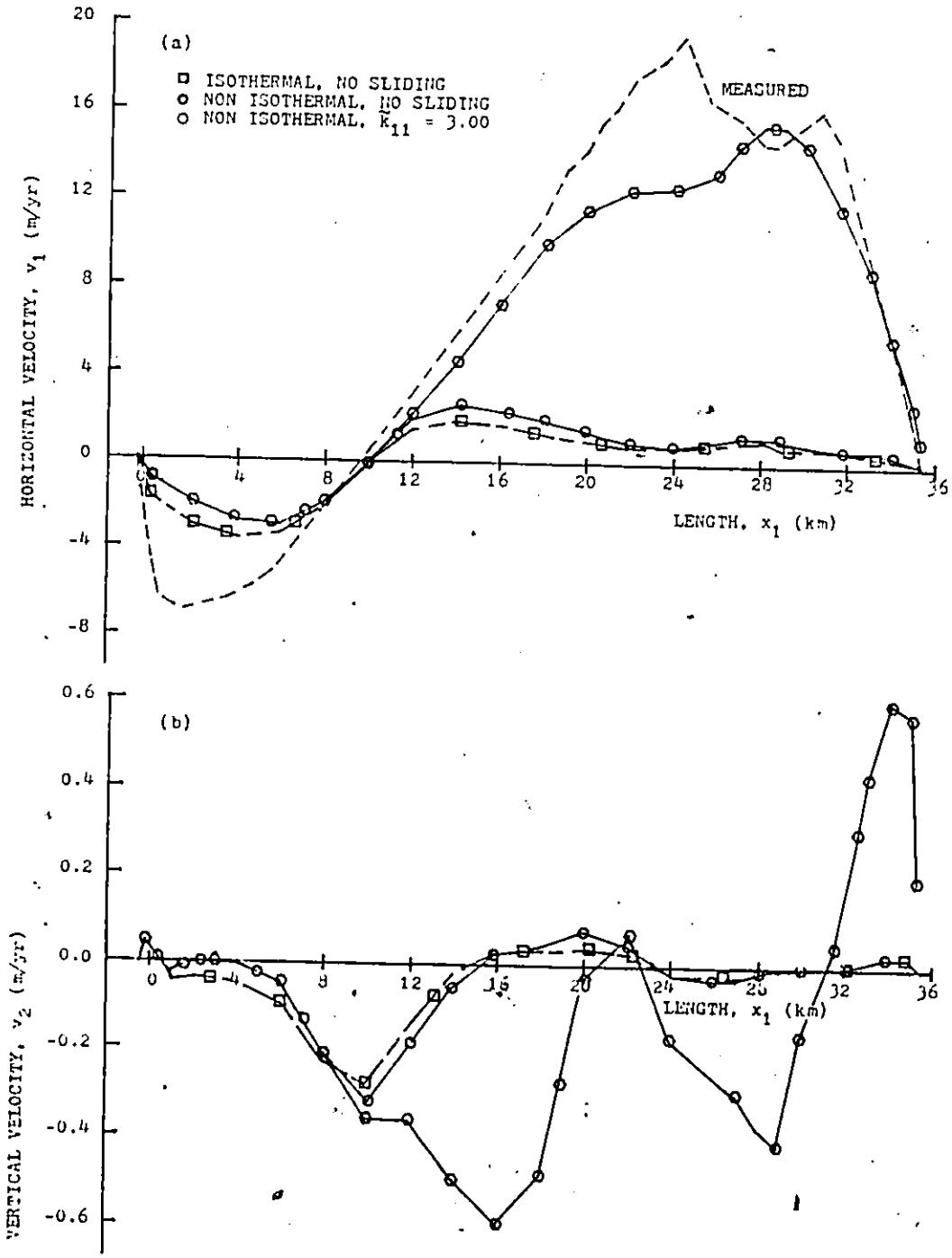

FIGURE A5.13 BARNES ICE CAP PROBLEM: (a) Horizontal surface velocity variations, and (b) Vertical surface velocity variations, using Meier's Law (Model C, Grid B).

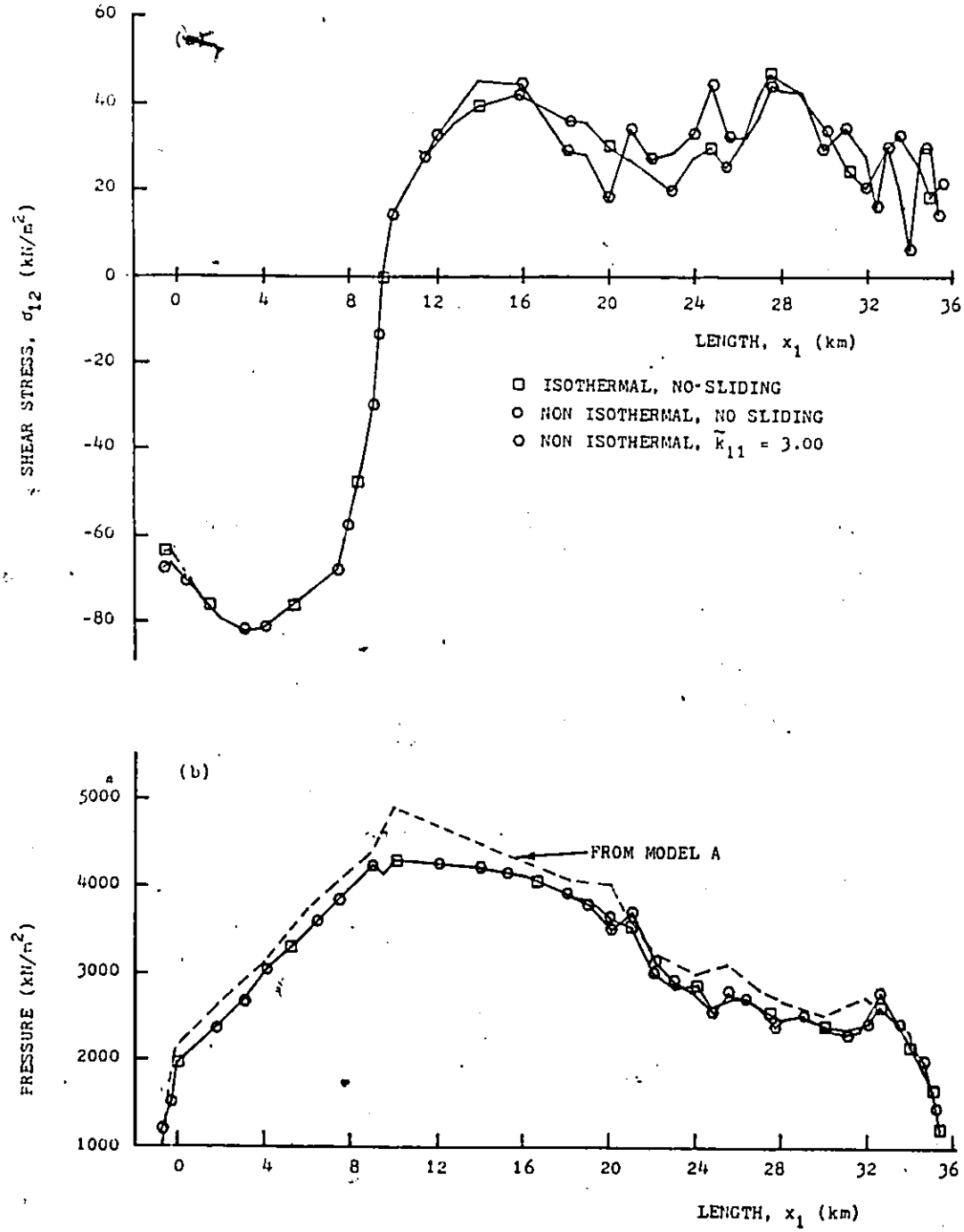

FIGURE A5.14 BARNES ICE CAP PROBLEM - Variation of: (a) Shear stress, and (b) Pressure in basal layer of ice cap, using Meier's Law (Model C, Grid B).

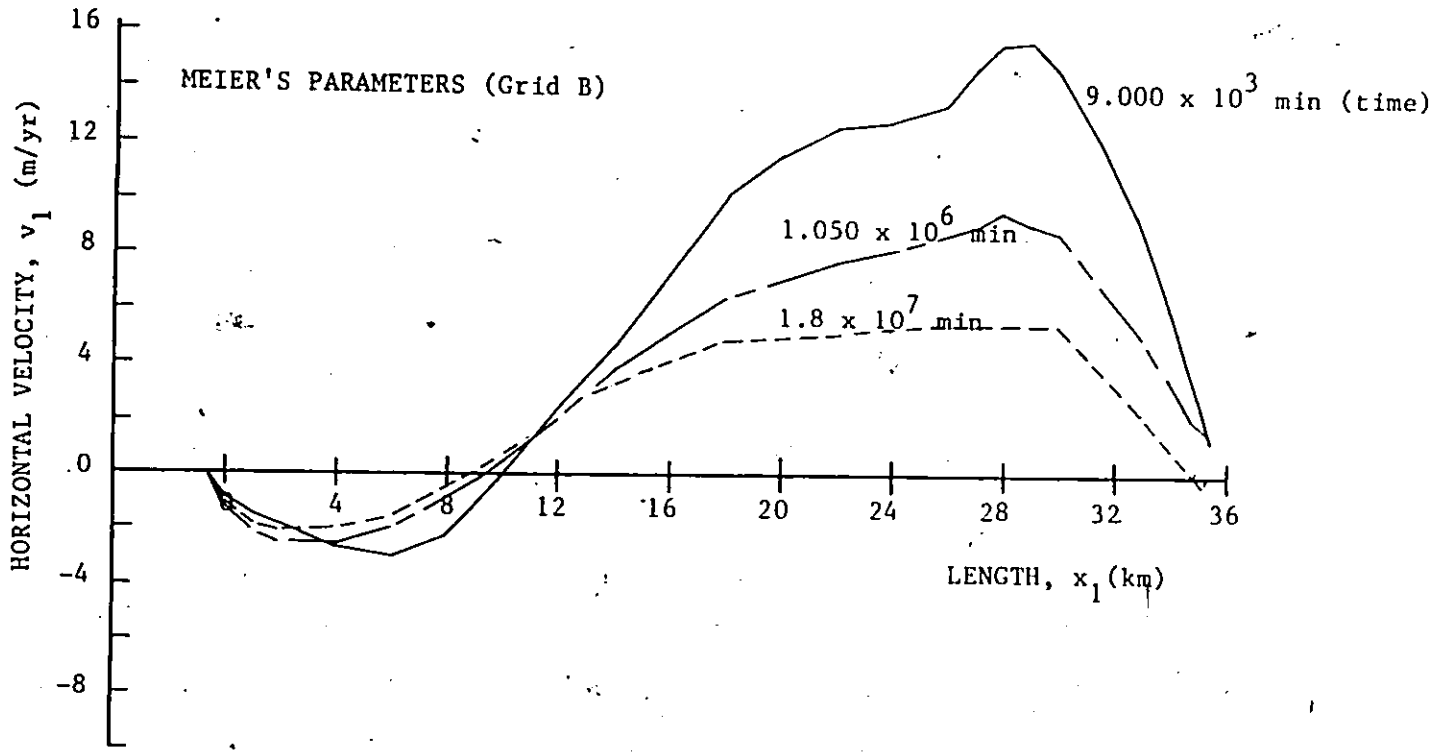

FIGURE A5.15 BARNES ICE CAP PROBLEM - Horizontal velocity variation at different stages during creep, using Meier's Law (Model C, Grid B)

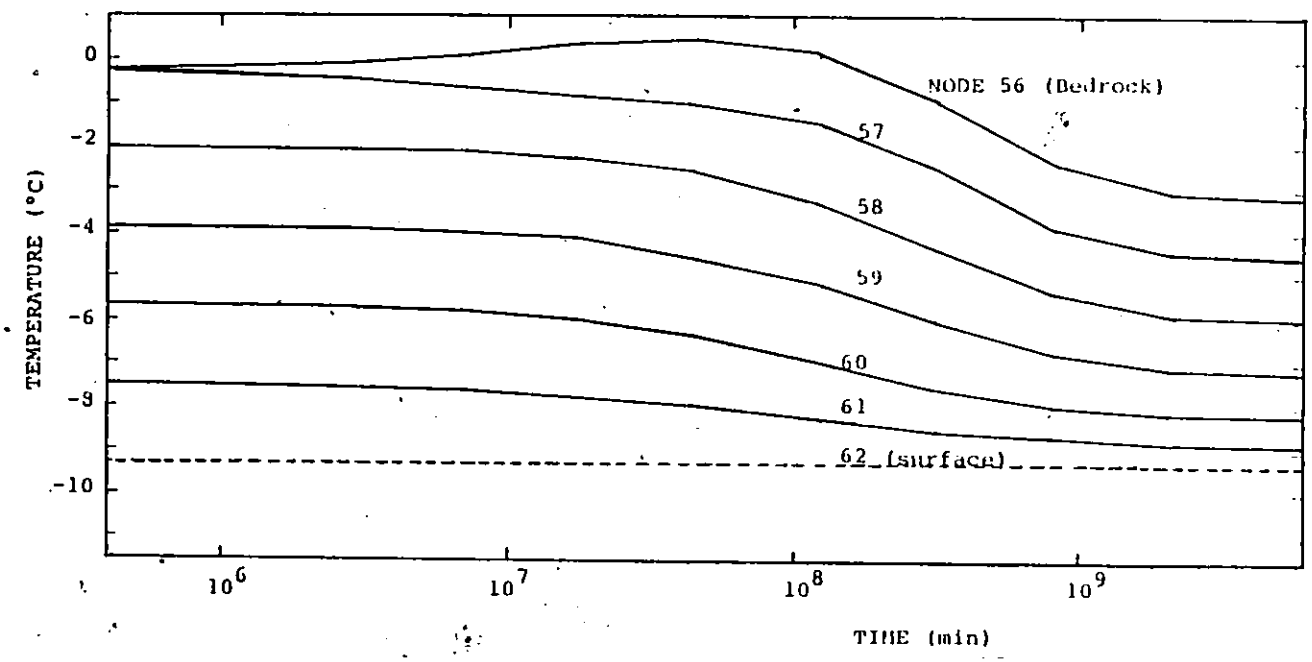

FIGURE A5.16 BARNES ICE CAP PROBLEM - Change in temperature with respect to time at x_1 = 14 km section. Initial temperature field for analysis is given in Figure A5.13(b). Velocity field for analysis is obtained from creep analysis using Meier's Law and allowing for sliding.

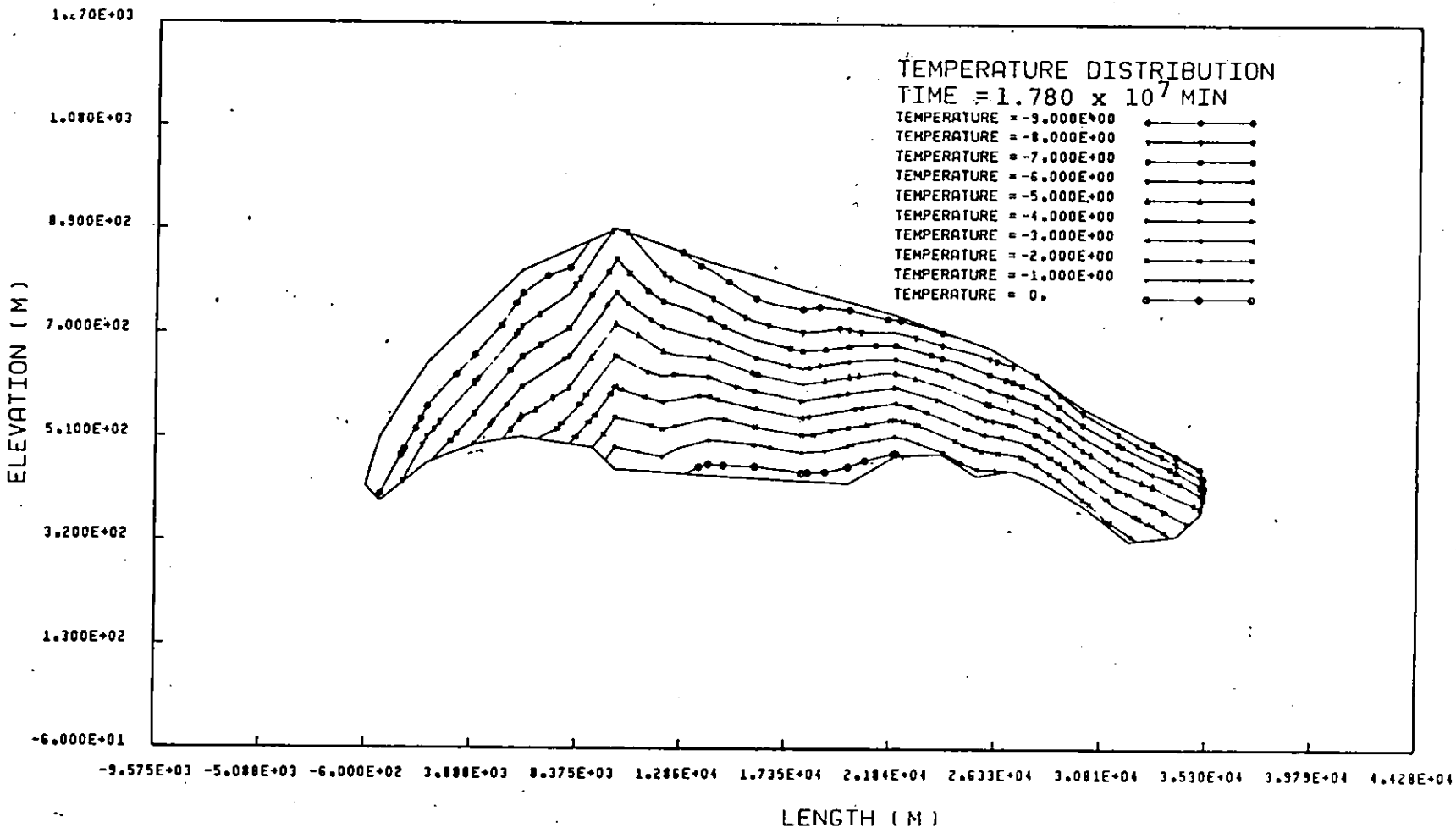

FIGURE A5.17 BARNES ICE CAP PROBLEM: (a) Temperature contours at 33.87 years (γ_G = 1.02 HFU), and

(cont'd on next page)

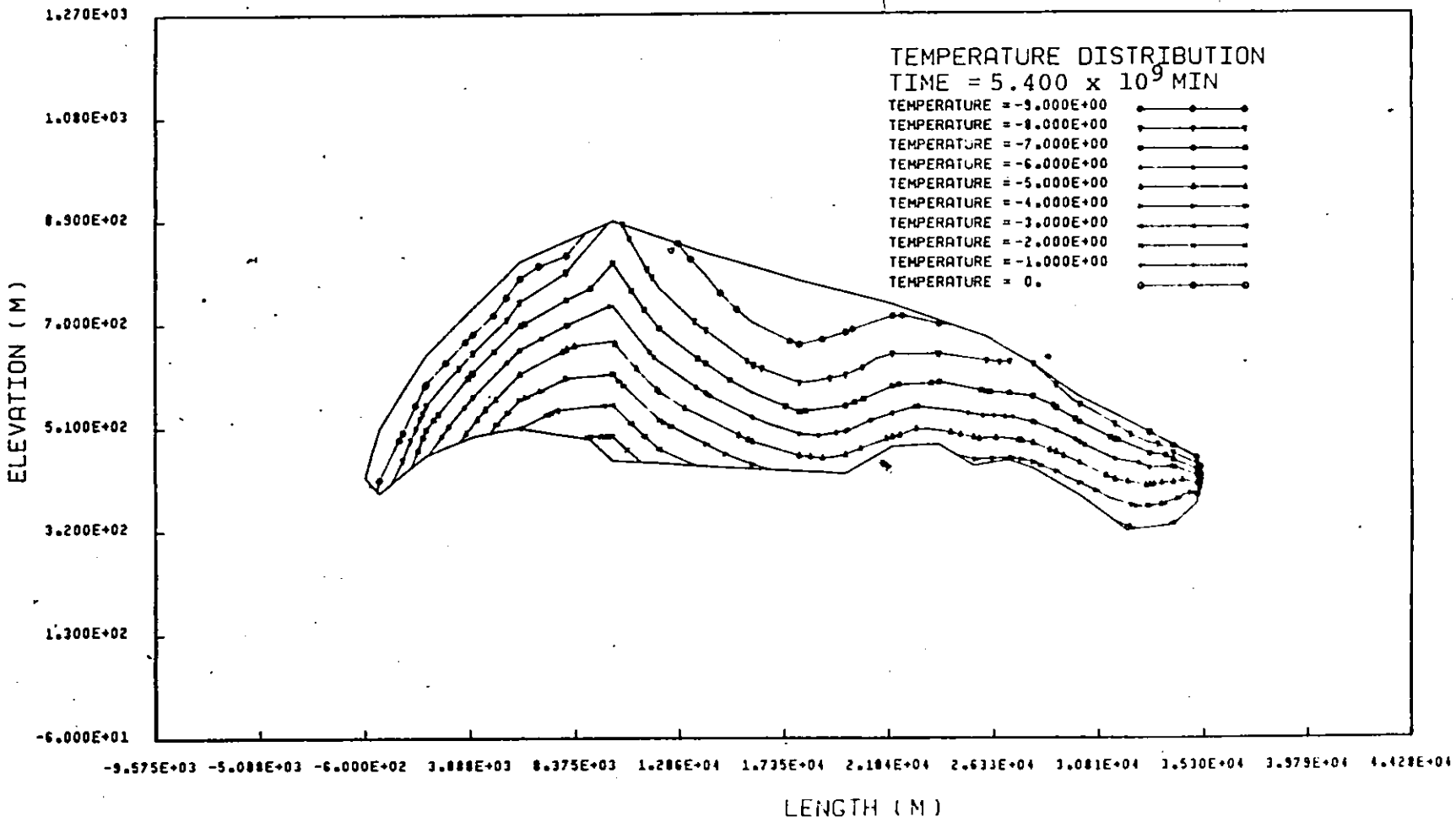

(b) Temperature contours at 1027.40 years (γ_G = 1.02 HFU).

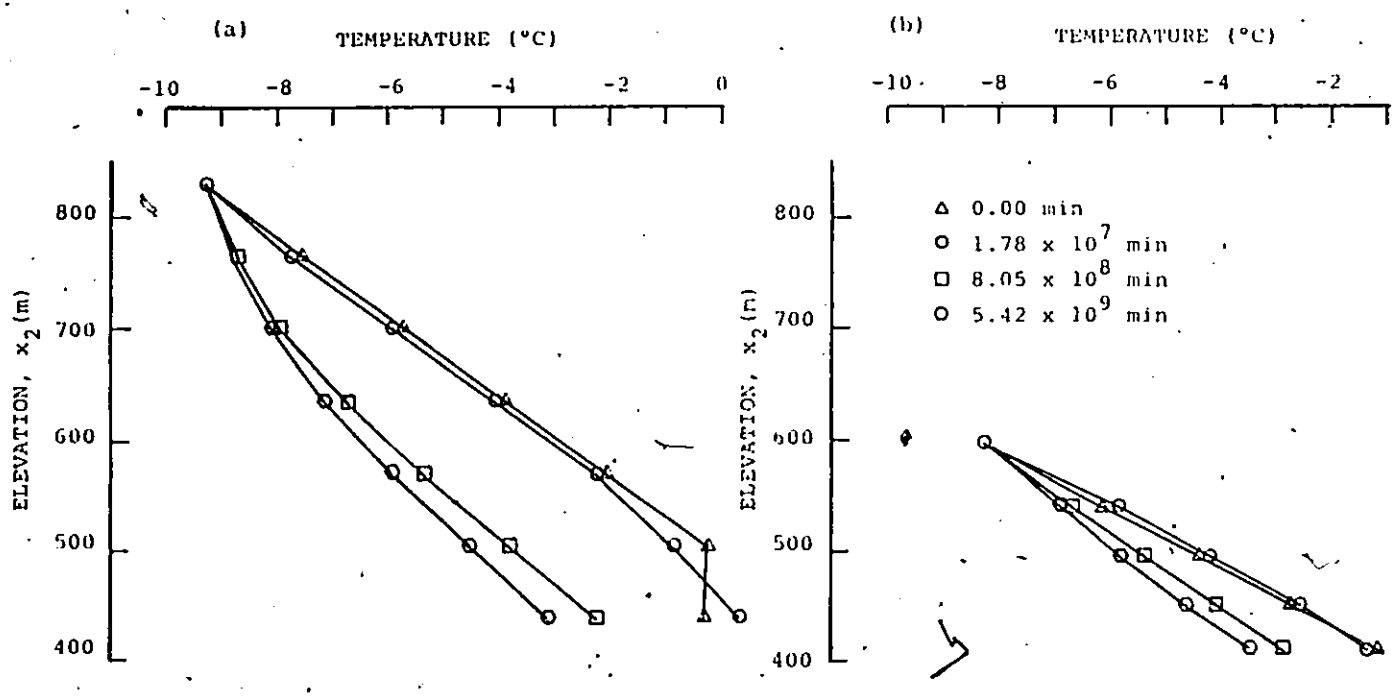

FIGURE A5.18 BARNES ICE CAP PROBLEM - Temperature profiles at different stages during thermal analysis: (a) x_1 = 14 km, and (b) x_1 = 29 km.

APPENDIX A6

BARNES ICE CAP INFORMATION (HOLDSWORTH [41])

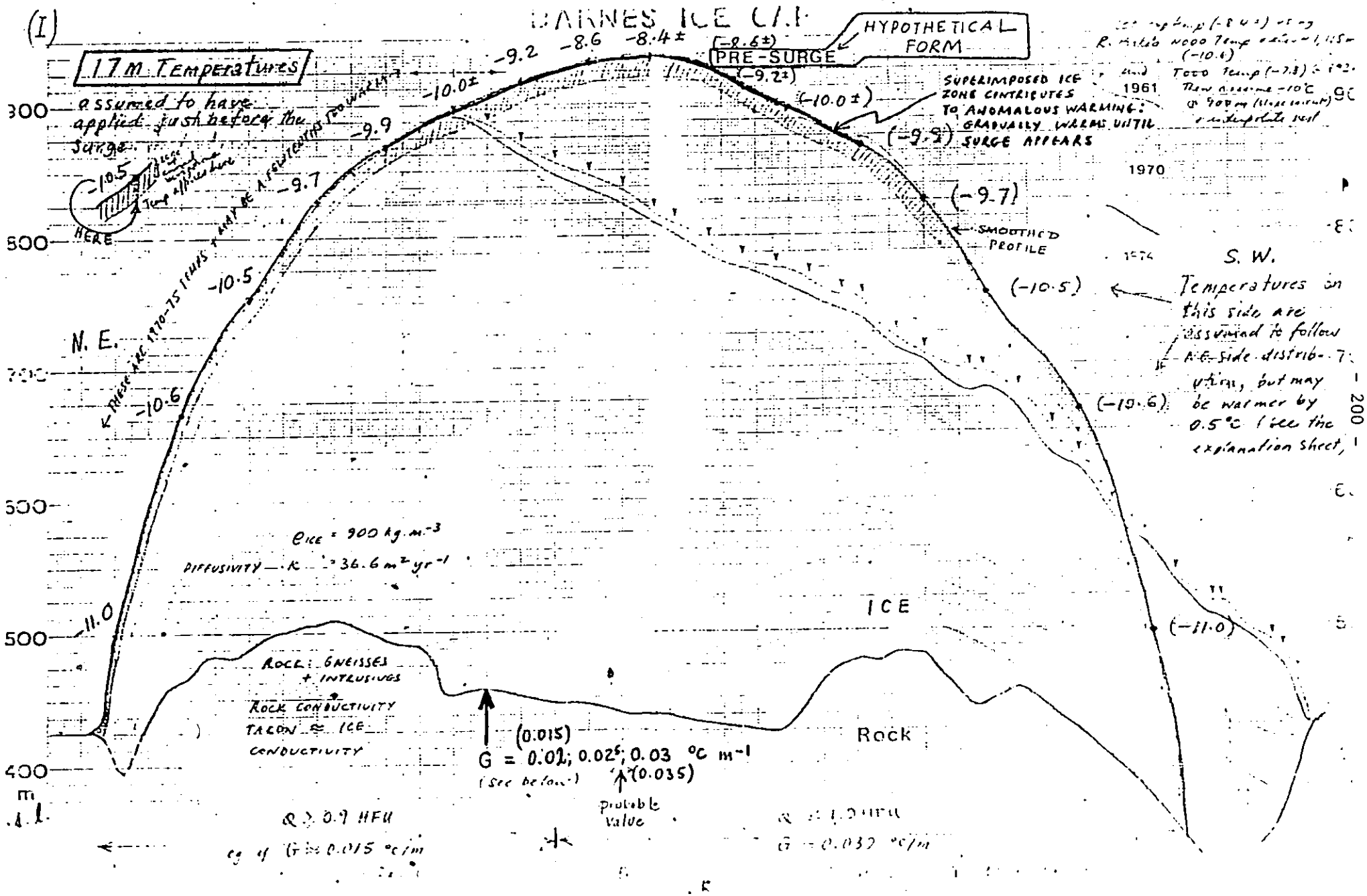

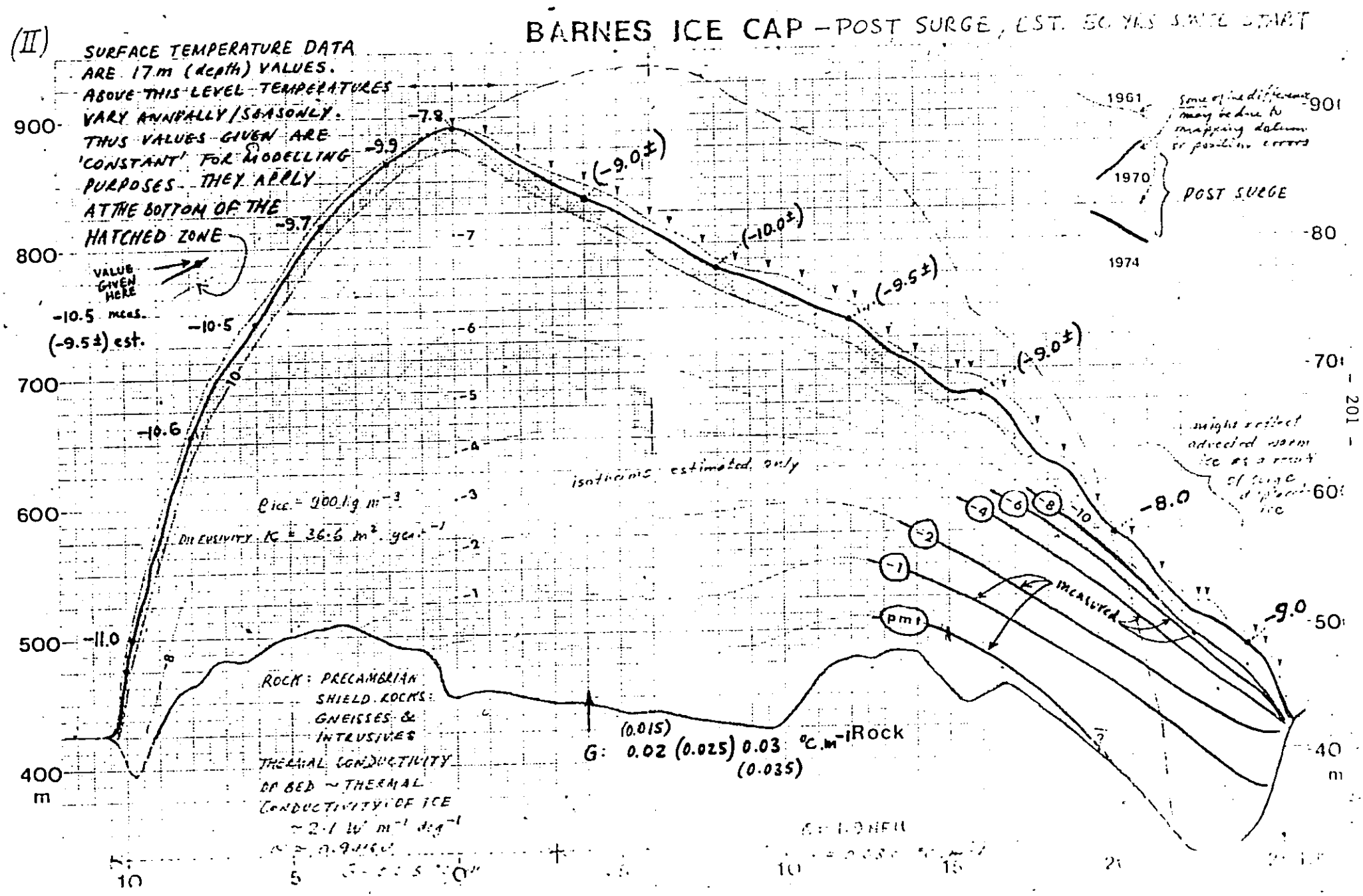

REFERENCES

[1] Anderson, C.A. and Bridwell, R.J., "A Finite element method for studying the transient nonlinear thermal creep of geological structures", International Journal for Numerical and Analytical Methods in Geomechanics, Vol. 4, 1980, 255-76.

[2] Argyris, J.H., Dunne, P.C., Angelopoulos, T. and Bichat, B., "Large natural strains and some difficulties due to nonlinearity and incompressibility in finite elements", Computer Methods in Applied Mechanics and Engineering, Vol. 4, 1974, 219-78.

[3] Barnes, P., Tabor, D. and Walker, J.C.F., "The friction and creep of polycrystalline ice", Proceedings of the Royal Society, Ser. A, Vol. 324, 1971, 127-155.

[4] Bathe, K.J. and Wilson, E.L., Numerical Methods in Finite Element Analysis, Prentice-Hall Inc., New Jersey, 1976.

[5] Boulton, G.S. and Jones, A.S., "Stability of temperate ice caps and ice sheets resting on beds of deformable sediment", Journal of Glaciology, Vol. 24, 1979, 29-43.

[6] Boulton, G.S., Morris, E.M, Armstrong, A.A. and Thomas, A., "Direct measurement of stress at the base of a glacier", Journal of Glaciology, Vol. 22, 1979, 3-24.

[7] Budd, W.F., "The dynamics of ice masses", Anare Scientific Reports, Series A(IV) Glaciology, Publication No. 108, Australia, 1969.

[8] Budd, W.F., "The longitudinal stress and strain-rate gradients in ice masses", Journal of Glaciology, Vol. 9, 1970, 19-27.

[9] Budd, W.F., " A first simple model for periodically self-surging glaciers", Journal of Glaciology, Vol. 14, 1975, 3-21.

[10] Budd, W.F., Keage, P.L. and Blundy, N.A., "Empirical studies of ice sliding", Journal of Glaciology, Vol. 23, 1979, 157-170.

[11] Butkovich, T.R., "Ultimate strength of ice", Cold Regions Research and Engineering Laboratory (C.R.R.E.L.), Research Report No. 11, Hanover, New Hampshire, 1954.

[12] Chan, D.H., "Creep and Fracture Simulation of Ice Using the Finite Element Method", M. Eng. Thesis, McMaster University, Hamilton, 1981.

[13] Christie, D., Griffiths, D.F., Mitchell, A.R. and Zienkiewicz, O.C., "Finite element methods for second order differential equations, with significant first derivatives", International Journal for Numerical Methods in Engineering, Vol. 10, 1976, 1389-96.

[14] Clarke, G.K.C., "Thermal regulation of glacier surging", Journal of Glaciology, Vol. 16, 1976, 231-59.

[15] Clarke, G.K.C., Nitsan, U. and Paterson, W.S.B., "Strain heating and creep instability in glaciers and ice sheets", Reviews of Geophysics and Space Physics, Vol. 15, 1977, 235-47.

[16] Classen, D.F., "Temperature profiles for the Barnes Ice Cap surge zone", Journal of Glaciology, Vol. 18, 1977, 391-405.

[17] Colbeck, S.C., Dynamics of Snow and Ice Masses, Academic Press Inc, London, New York, 1980.

[18] Collins, I.F., "On the use of the equilibrium equations and flow law in relating the surface and bed topography of glaciers

and ice sheets", Journal of Glaciology, Vol. 7, 1968, 199-204.

[19] Cormeau, I., "Numerical stability in quasi-static elasto/visco-plasticity", International Journal for Numerical Methods in Engineering, Vol. 9, 1975, 109-127.

[20] Dolgoushin, L.D. and Osipova, G.B., "Glacier surges and the problems of their forecasting:, Snow and Ice Symposium (Proceedings of the Moscow Symposium, Aug. 1971), International Association of Scientific Hydrology, Publication No. 104, 1975, 292-304.

[21] Donea, J., "On the accuracy of finite element solutions to the transient heat-conduction equation", International Journal for Numerical Methods in Engineering, Vol. 8, 1974, 103-110.

[22] Emery, J.J., "Finite Element Analysis of Creep Problems in Soil Mechanics", Ph.D. Thesis, University of British Columbia, Vancouver, June 1971.

[23] Emery, J.J. and Nguyen, T.Q., "Simulation of ice flow prob lems", Second Symposium - Applications of Solid Mechanics, Hamilton, June 17 and 18, 1974.

[24] Emery, J.J. and Mirza, F.A., "Finite element method simulation of large ice mass flow behaviour", International Union of Theoretical and Applied Mechanics Symposium on the Physics and Mechanics of Ice, Copenhagen, Denmark, Aug. 6-10, 1979.

[25] Fowler, A.C., "A mathematical approach to the theory of glacier sliding", Journal of Glaciology, Vol. 23, 1979, 131-41.

[26] Frederking, R., "Plane-strain compressive strength of columnar-grained and granular-snow ice", Journal of Glaciology, Vol.

18, 1977, 505-16.

[27] Glen, J.W., "Experiments on the deformation of ice", Journal of Glaciology, Vol. 2, 1952, 111-14.

[28] Glen, J.W., The creep of polycrystalline ice", Proceedings of the Royal Society, Ser. A., Vol. 228, 1955, 518-38.

[29] Gold, L.W., "Deformation mechanisms in ice", Research Paper No. 193, National Research Council, Division of Building Research, Ottawa, Canada, 1963.

[30] Gold, L.W., "Elastic and strength properties of fresh water ice", Technical Paper No. 283, National Research Council of Canada, Ottawa, 1968.

[31] Gold, L.W., "The failure of ice", Research Paper No. 516, National Research Council, Division of Building Research, Ottawa, Canada, 1972.

[32] Gold, L.W., "Engineering properties of fresh-water ice", Journal of Glaciology, Vol. 19, 1977, 197-212.

[33] Goodman, R.E., Taylor, R.L., and Brekke, T.L., "A model for the mechanics of jointed rock", Journal of the Soil Mechanics and Foundations Division, Proceedings of the American Society of Civil Engineers, Vol. 93, 1968, 637-59.

[34] Heinrich, J.C., Huyakorn, P.S., Zienkiewicz, O.C. and Mitchell, A.R., "An 'upwind' finite element scheme for two-dimensional convective transport equation", International Journal for Numerical Methods in Engineering, Vol. 11, 1977, 131-43.

[35] Herrmann, L.R., "Elasticity equations for incompressible and nearly incompressible materials by a variational theorem", Journal of the American Institute of Aeronautics and Astro-

nautics, Vol. 3, 1965, 1896-1900.

[36] Holdworth, G., "Evidence of a surge on Barnes Ice Cap, Baffin Island", Canadian Journal of Earth Sciences, Vol. 10, 1973, 1565-74.

[37] Holdsworth, G., "Erebus Glacier Tongue, McMurdo Sound, Antarctica", Journal of Glaciology, Vol. 13, 1974, 27-35.

[38] Holdsworth, G., "Deformation and flow of Barnes Ice Cap, Baffin Island", Scientific Ser. No. 52, Inland Waters Directorate, Water Resources Branch, Ottawa, Canada, 1975.

[39] Holdsworth, G., "Surge activity on the Barnes Ice Cap", Nature, Vol. 269, 1977, 588-90.

[40] Holdsworth, G., "Mount Logan (Yukon Territory) Field Report", Glaciology Division, Department of the Environment, Ottawa, Canada, Sept. 1978.

[41] Holdsworth, G., "Barnes Ice Cap thermal regime-outline", Private Communication, 1978.

[42] Holdsworth, G., "Erebus Glacier Tongue", Private Communication, 1981.

[43] Homer, D.R. and Glen, J.W., "The creep activation energies of ice", Journal of Glaciology, Vol. 21, 1978, 429-44.

[44] Hooke, R.L., "Structure and flow in the margin of the Barnes Ice Cap, Baffin Island, N.W.T., Canada", Journal of Glaciology, Vol. 12, 1973, 423-38.

[45] Hooke, R.L., "Pleistocene ice at the base of the Barnes Ice Cap, Baffin Island, N.W.T., Canada", Journal of Glaciology, Vol. 17, 1976, 49-59.

[46] Hooke, R.L., Raymond, C.F., Hotchkiss, R.L. and Gustafson, R.I.,

"Calculations of velocity and temperature in a polar glacier using the finite element method", Journal of Glaciology, Vol. 24, 1979, 131-45.

[47] Hughes, T.J.R., "A simple scheme for developing upwind finite elements", International Journal for Numerical Methods in Engineering, Vol. 12, 1979, 1359-65.

[48] Hutter, K., Legerer, F. and Spring, U., "First-order stresses and deformations in glaciers and ice sheets", Journal of Glaciology, Vol. 27, 1981, 227-70.

[49] Johnson, W. and Mellor, P.B., Engineering Plasticity, Van Nostrand Reinhold Co., London, New York, 1978.

[50] Jonas, J.J. and Müller, F., "Deformation of ice under high internal shear stresses", Canadian Journal of Earth Sciences, Vol. 6, 1969, 963-967.

[51] Kamb, B. and LaChapelle, E., "Direct observation of the mechanism of glacier sliding over bedrock", Journal of Glaciology, Vol. 5, 1964, 159-72.

[52] Kamb, B., "Sliding motion of glaciers: Theory and observations", Reviews of Geophysics and Space Physics, Vol. 8, Nov. 1970, 673-728.

[53] Kanachi, M.B., Zienkiewicz, O.C. and Owen, D.R.J., "The visco-plastic approach to problems of plasticity and creep involving geometric nonlinear effects", International Journal for Numerical Methods in Engineering, Vol. 12, 1978, 169-81.

[54] Liestol, O., "Glacier surges in West Spitzbergen", Canadian Journal of Earth Sciences, Vol. 6, 1969, 895-97.

[55] Lliboutry, L.A., "Une théorie du frottement du glacier sur son lit", Annales de Géophysique, Vol. 15, 1959, 250-65.

[56] Lliboutry, L.A., "General theory of subglacial cavitation and sliding of temperate glaciers", Journal of Glaciology, Vol. 7., 1968, 21-58.

[57] Lliboutry, L.A., "Local friction laws for glaciers: A critical review and new openings", Journal of Glaciology, Vol. 23, 1979, 67-95.

[58] Loken, O.H. and Andrews, J.T., "Glaciology and chronology of fluctuations of the ice margin at the south end of the Barnes Ice Cap, Baffin Island, N.W.T.", Geographical Bulletin, Vol. 8, 1966, 341-59.

[59] Loken, O.H., "Evidence of surges on the Barnes Ice Cap, Baffin Island", Canadian Journal of Earth Sciences, Vol. 6, 1969, 899-901.

[60] Mahaffy, M.W., "A three-dimensional numerical model of ice sheets: Tests on the Barnes Ice Cap, N.W.T.", Journal of Geophysical Research, Vol. 81, 1976, 1055-66.

[61] Malvern, L.E., Introduction to the Mechanics of a Continuous Medium, Prentice-Hall Inc., New Jersey, 1969.

[62] McMeeking, R.M. and Rice, J.R., "Finite-element formations for problems of large elastic-plastic deformation", International Journal of Solids and Structures, Vol. 2, 1975, 601-16.

[63] Meier, M.F., "Model of flow of Saskatchewan glacier, Alberta, Canada", United States Geological Survey Professional Paper 351, 1960.

[64] Meier, M.F., "Seminar on the causes and mechanics of glacier

surges, St. Hilaire, Canada, Sept. 10-11, 1968: A summary", Canadian Journal of Earth Sciences, Vol. 6, 1969, 987-89.

[65] Meier, M.F. and Post, A., "What are glacier surges?", Canadian Journal of Earth Sciences, Vol. 16, 1969, 807-17.

[66] Mellor, M., "Mechanical properties of polycrystalline ice", International Union of Theoretical and Applied Mechanics Symposium on the Physics and Mechanics of Ice, Copenhagen, Denmark, Aug. 6-10, 1979.

[67] Michel, B., Ice Mechanics, Les Press De L'Université Laval, Quebec City, 1978.

[68] Mirza, F.A., "Convergence of Mixed Methods in Continuum Mechanics and Finite Element Analysis", Ph.D. Thesis, University of British Columbia, Vancouver, 1977.

[69] Neave, K.G. and Savage, J.C., "Icequakes on the Athabasca Glacier", Journal of Geophysical Research, Vol. 75, 1970, 1351-62.

[70] Nguyen, T.A., "Simulation of Ice Flow Using the Finite Element Method", M. Eng. Thesis, McMaster University, Hamilton, 1976.

[71] Nye, J.F., "The flow of glaciers and ice sheets as a problem in plasticity", Proceeding of the Royal Society, Ser. A, Vol. 207, 1951, 554-72.

[72] Nye, J.F., "The mechanics of glacier flow", Journal of Glaciology, Vol. 2, 1952, 82-93.

[73] Nye, J.F., "The flow of ice from measurements in glacier tunnels, Laboratory experiments and the Jungfraufirn bore hole experiment", Proceedings of the Royal Society, Ser. A, Vol. 219, 1953, 477-89.

[74] Nye, J.F., "The distribution of stress and velocity in glaciers and ice-sheets", Proceedings of the Royal Society, Ser. A, Vol. 239, 1957, 113-33.

[75] Nye, J.F., "The effect of longitudinal stress on the shear stress at the base of an ice sheet", Journal of Glaciology, Vol. 8, 1969, 207-13.

[76] Nye, J.F., "A calculation on the sliding of ice over a wavy surface using a Newtonian viscous approximation", Proceedings of the Royal Society, Ser. A, Vol. 311, 1969, 445-67.

[77] Nye, J.F., "Glacier sliding without cavitation in a linear viscous approximation", Proceedings of the Royal Society, Ser. A, Vol. 315, 1970, 381-403.

[78] Orwon, E., "Joint Meeting of the British Glaciological Society, the British Rheologists' Club and the Institute of Metals", Journal of Glaciology, Vol. 1, 1949, 231-40.

[79] Paterson, W.S.B., The Physics of Glaciers, Permagon Press, London, 1969.

[80] Paterson, W.S.B., "Ice sheets and ice shelves", In Dynamics of Snow and Ice, Ed. by S.C. Colbeck, Academic Press, London, New York, 1980, 1-78.

[81] Post, A.S., "The exceptional advances of the Muldrow, Black Rapids and Sustina glaciers", Journal of Geophysical Research, Vol. 65, 1960, 3703-12.

[82] Post, A.S., "Alaskan glacier: Recent observations in respect to earthquake-advance theory", Science, Vol. 148, 1965, 366-68.

[83] Post, A.S., "Distributions of surging glaciers in western North America", Journal of Glaciology, Vol. 8, 1969, 229-40.

[84] Raymond, C.F., "Mechanics of glacier Movement", In Rocksdides and Avalanches, Vol. 1, Natural Phenomena, Ed. by B. Voight, Developments in Geotechnical Engineering, Elsevier, Scientific Pub. Co., New York, 1978, 793-833.

[85] Raymond, C.F., "Temperate valley glaciers", In Dynamics of Snow and Ice Masses, Ed. by S.C. Colbeck, Academic Press, London, New York, 1980, 70-139.

[86] Robin, G. de Q., "Ice movement and temperature distributions in glaciers and ice sheets", Journal of Glaciology, Vol. 2, 1955, 523-32.

[87] Robin, G. de Q., "Initiation of glacier surges", Canadian Journal of Earth Sciences, Vol. 6, 1969, 919-27.

[88] Robin, G. de Q. and Weertman, "Cyclic surging of glaciers", Journal of Glaciology, Vol. 12, 1973, 3-18.

[89] Sanderson, T.J.O., "Equilibrium profile of ice shelves", Journal of Glaciology, Vol. 22, 1979, 435-59.

[90] Sanderson, T.J.O. and Doake, C.S.M., "Is vertical shear in an ice shelf negligible?", Journal of Glaciology, Vol. 22, 1979, 285-92.

[91] Schytt, V., "Some comments on glacier surges in eastern Svalbard", Canadian Journal of Earth Sciences, Vol. 6, 1969, 867-73.

[92] Thorarinsson, S., "Glacier surges in Iceland with special reference to surges of Bruarjokall", Canadian Journal of Earth Sciences, Vol. 6, 1969, 876-82.

[93] Weertman, J., "On the sliding of glaciers", Journal of Glaciology, Vol. 3, 1957, 33-38.

[94] Weertman, J., "Deformation of floating ice shelves", Journal of Glaciology, Vol. 3, 1957, 38-42.

[95] Weertman, J., "Catastrophic glacier advances", In Commission des Neiges et Glaces, Colloque d'Obergurgl, Sept. 10-18, 1962, International Union of Geodesy and Geophysics, International Association of Scientific Hydrology, Vol. 8, 1962, 31-39.

[96] Weertman, J., "The theory of glacier sliding", Journal of Glaciology, Vol. 15, 1964, 287-303.

[97] Weertman, J., "Water lubrication mechanism of glacier surges", Canadian Journal of Earth Sciences, Vol. 6, 1969, 929-42.

[98] Weertman, J., "General theory of water flow at the base of a glacier or ice sheet", Reviews of Geophysics and Space Physics, Vol. 10, 1972, 287-333.

[99] Weertman, J., "The unsolved general glacier sliding problem", Journal of Glaciology, Vol. 23, 1979, 97-115.

[100] Zienkiewicz, O.C. and Parekh, C.J., "Transient field problems: Two-dimensional and three-dimensional analysis by isoparametric finite elements", International Journal for Numerical Methods in Engineering, Vol. 2, 1970, 61-71.

[101] Zienkiewicz, O.C. and Godbole, P.N., "Viscous, incompressible flow with special reference to non-Newtonian (plastic) fluids", In Finite Elements in Fluids, Vol. 1, Viscous Flow and Hydrodynamics, Ed. by Gallagher et al, J. Wiley and Sons, London, New York, 1974.

[102] Zienkiewicz, O.C., Gallagher, R.H. and Hood, P., "Newtonian and non-Newtonian viscous incompressible flow. Temperature reduced flows. Finite element solutions.", In the Mathe-

matics of Finite Elements and Applications II, Ed. by J. Whiteman, Academic Press, London, New York, 1975, 235-67.

[103] Zienkiewicz, O.C., "The Finite Element Method", Third Edition, McGraw-Hill Book Co. Ltd., London, 1977.

[104] Zlámal, Milos, "Finite element methods in heat conduction problems", In the Mathematics of Finite Elements and Applications II, Ed. by J. Whiteman, Academic Press, London, New York, 1975.